Simulation of Pre-Planetesimal Collisions with Smoothed Particle Hydrodynamics

Dissertation
der Mathematisch-Naturwissenschaftlichen Fakultät
der Eberhard Karls Universität Tübingen
zur Erlangung des Grades eines
Doktors der Naturwissenschaften
(Dr. rer. nat.)

vorgelegt von

Ralf J. Geretshauser

aus Regensburg

Tübingen
2011

Tag der mündlichen Qualifikation:	8. November 2011
Dekan:	Prof. Dr. Wolfgang Rosenstiel
1. Berichterstatter:	PD Dr. Roland Speith
2. Berichterstatter:	Prof. Dr. Wilhelm Kley

Abstract

In the coagulation scenario of planet formation, planets are assembled by subsequent collisions starting from micron sized dust grains in protoplanetary discs. Three stages can be distinguished: firstly, the dust grains stick by van-der-Waals forces after collision. Millimetre-sized, highly porous dust aggregates are produced as a result. In the second growth step, from millimetre to kilometre size, the dust aggregates are referred to as pre-planetesimals. This step is problematic and addressed in the thesis at hand: pre-planetesimal growth is endangered by disruptive collisions (fragmentation barrier) and may be halted at centimetre sizes by compaction and consequential rebound (bouncing barrier). The sticking mechanism in the pre-planetesimal regime is unknown. The investigation of the second step in global dust coagulation models is difficult since data on the outcome of pre-planetesimal collisions are missing and laboratory experiments on these are infeasible beyond centimetre size. However, once a sufficient population of kilometre-sized planetesimals has formed, planet formation is ensured by gravity-aided accretion in the third growth step.

Since laboratory experiments with large pre-planetesimals are hard to carry out, in this thesis a realistic numerical model for the simulation of porous pre-planetesimal material is developed and thoroughly calibrated with by means of laboratory benchmark experiments. Smoothed particle hydrodynamics (SPH) is adopted as a numerical method together with extensions for the simulation of solid media. A preexisting porosity model is enhanced by more realistic material equations, an improved treatment of tensile forces and a damage model based on the inhomogeneity of dust aggregates. As a result, the calibration process yields the only numerical model currently available, which can reproduce compaction, fragmentation, and bouncing of SiO_2 dust aggregates quantitatively correct. Additionally, material relations, which are hard to measure in the laboratory, such as the dynamic compressive and shear strength as well as the bulk modulus are determined.

The four-population model is presented in this thesis as a new classification scheme for pre-planetesimal collisions. This is a collision data transfer format accurate enough to capture all combinations of sticking, bouncing, and fragmentation processes in pre-planetesimal collisions and at the same time simple enough to be implemented in dust coagulation models. It distinguishes between the largest and second largest fragment, a fragment class whose mass distribution is modelled by a power-law, and a class which indicates the limit of the numerical resolution.

As an application of the calibrated numerical porosity model this thesis investigates the influence of hard shells of dust aggregates on the occurrence of bouncing collisions. It is shown that hard shells lead to bouncing events only for low collision velocities. The probability of bouncing events might be overestimated by current collision statistics due to experimental artefacts involving hard shells. As a consequence, bouncing might be less dangerous for planet formation than currently assumed.

After several collisions in a protoplanetary disc, pre-planetesimals feature a collisional history and thus are very likely to be inhomogeneous. By means of the inhomogeneity damage model it is shown, that inhomogeneous pre-planetesimals are weaker than their homogeneous equivalents. The larger the degree of inhomogeneity the smaller are the fragments in a fragmenting collision.

As major application of the numerical porosity model a large set data set of the outcomes of collisions between homogeneous aggregates of low, medium, and high porosity is presented. It is shown, that the threshold velocities for bouncing and fragmentation depend on the object porosity and object size, which are both often neglected in current investigations of planetesimal formation.

Zusammenfassung

Dem Koagulationsszenario der Planetenentstehung zufolge entstehen Planeten durch sukzessive Kollisionen in protoplanetaren Scheiben beginnend mit mikrometergroßen Staubkörnern. Dabei kann man drei Phasen unterscheiden: Anfangs haften die Staubkörner durch van-der-Waals Kräfte nach einem Zusammenstoß. Als Resultat entstehen millimetergroße, hochporöse Staubaggregate. Im zweiten Größenschritt, der von einigen Millimetern bis hin zu Kilometern reicht, bezeichnet man die Staubaggregate als Präplanetesimale. Diesem problematischen Schritt widmet sich die vorliegende Arbeit. Das Wachstum von Präplanetesimalen ist einerseits durch Kollisionen bedroht, in denen die Aggregate zerstört werden (Fragemtationsbarriere), und andererseits angehalten bei Größen von einigen Zentimetern durch Aggregatverdichtung und daraus folgendem gegenseitigen Abprallen (Abprallbarriere). Der Haftmechanismus im Größenbereich der Präplanetesimale ist unbekannt. Die nähere Untersuchung dieses zweiten Größenschritts mittels globalen Staubkoagulationssimulationen gestaltet sich schwierig, denn die nötigen Daten von Prä-Planetesimalkollisionen stehen nicht zur Verfügung und Laborexperimente, um diese zu gewinnen, sind jenseits von Größen von einigen Zentimetern nicht realisierbar. Hat sich jedoch eine ausreichende Population von kilometergroßen Planetesimalen gebildet, ist die Entstehung von Planeten durch den Mechanismus der gravitationsverstärkten Akkretion im dritten Wachstumsschritt sichergestellt.

Da Laborexperimente mit großen Präplanetesimalen schwer durchzuführen sind, wird in der vorliegenden Arbeit ein numerisches Modell für die realistische Simulation des porösen Materials entwickelt, aus dem Präplanetesimale bestehen. Dieses Modell wird mit Hilfe von Labortestexperimenten sorgfältig kalibiert. Als numerische Methode wird Smoothed Particle Hydrodynamics (SPH) mit Erweiterungen für die Simulation von Festkörpern verwendet. Ein bestehendes Porositätsmodell wird durch realistischere Materialgleichungen, eine verbesserte Behandlung von Zugkräften und ein Schadensmodell erweitert, das auf der Inhomogenität von Staubaggregaten beruht. Das Endergebnis der Kalibrierung ist das gegenwärtig einzige numerische Modell, das Verdichtung, Fragmentierung und gegenseitiges Abprallen von SiO_2 Staubaggregaten quantitativ reproduzieren kann. Zusätzlich wurden Materialbeziehungen gewonnen, die im Experiment schwer messbar sind, wie etwa die dynamische Kompressions- und Scherfestigkeit sowie das Kompressionsmodul.

In dieser Arbeit wird zudem das Four-Population Modell als neues Klassifikationsschema für Prä-Planetesimalkollisionen vorgestellt. Dabei handelt es sich um ein Format zum Austausch von Kollisionsdaten, das zum einen genau genug ist, um jegliche Kombination von Haftungs-, Abprall- und Fragmentierungsprozessen in Präplanetesimalkollisionen abzubilden, und andererseits aber auch einfach genug ist, um in globale Staubkoagulationsmodelle implementiert zu werden. In diesem Modell werden nach ihrer Masse unterschieden: das größte und zweitgrößte Fragment, eine Fragmentklasse, deren Massenverteilung durch ein Exponentialgesetz dargestellt wird, und eine Klasse für die numerische Auflösungsgrenze.

Als Anwendung des kalibrierten numerischen Porositätsmodells untersucht diese Arbeit den Einfluss von kompakten Schalen von Staubaggregaten auf das Auftreten von gegenseitigem Abprallen. Es wird gezeigt, dass das Vorhandensein von kompakten Schalen nur bei niedrigen Geschwindigkeiten zum Abprallen führt. Die Wahrscheinlichkeit von gegenseitigem Abprallen in derzeitigen Kollisionsstatistiken könnte durch experimentelle Artefakte überschätzt sein, die auf das Vorhandensein von kompakten Schalen zurückzuführen sind. Folglich könnte gegenseitiges Abprallen weniger bedrohlich für die Planetenentstehung sein als bisher angenommen.

Nach mehreren Stößen in einer protoplanetaren Scheibe weisen die Präplanetesimale eine Kollisionsgeschichte auf und sind daher sehr wahrscheinlich inhomogen. Mit Hilfe des Inhomogenitätsschadensmodells wird gezeigt, dass inhomogene Präplanetesimale fragiler sind als ihre homogenen Äquivalente. Je höher der Inhomogenitätsgrad ist, desto kleiner sind die Fragmente nach einer fragmentierenden Kollision.

Als Hauptanwendung des numerischen Porositätsmodells wird ein Datensatz von Kollisionen zwischen homogenen Präplanetesimalen mit niedriger, mittlerer und hoher Porosität vorgestellt. Es wird gezeigt,

dass die Grenzgeschwindigkeiten für Abprallen und Fragmentierung von der Porosität der Objekte und deren Größe abhängen, was in derzeitigen Untersuchungen von Planetesimalentstehung oft vernachlässigt wird.

Contents

1. Introduction **13**

2. Planet Formation **15**
- 2.1. Protoplanetary discs . . . 15
  - 2.1.1. Formation of star and disc . . . 15
  - 2.1.2. Observational constraints . . . 17
  - 2.1.3. Disc models . . . 19
  - 2.1.4. Turbulence and inner disc dynamics . . . 22
- 2.2. Dust coagulation . . . 24
  - 2.2.1. Dust grain properties . . . 24
  - 2.2.2. Particle gas dynamics . . . 25
  - 2.2.3. Conditions for dust coagulation . . . 27
  - 2.2.4. Dust coagulation in the disc . . . 28
- 2.3. Collision or Collapse? - Growing Planetesimals . . . 34
  - 2.3.1. The coagulation scenario . . . 34
  - 2.3.2. The gravitational instability scenario . . . 41
- 2.4. Gravity Takes Over - Growing Planets . . . 44
  - 2.4.1. Methods and characteristic quantities . . . 44
  - 2.4.2. Orderly growth . . . 46
  - 2.4.3. Runaway growth . . . 46
  - 2.4.4. Oligarchic growth . . . 47
  - 2.4.5. Final stages . . . 48
- 2.5. The Focus of this Thesis: Planetesimal Formation . . . 49

3. Investigating Planetesimal Formation - A Selection of Methods **51**
- 3.1. Dust Growth in the Laboratory . . . 51
  - 3.1.1. Basic concepts . . . 51
  - 3.1.2. Results . . . 52
  - 3.1.3. Limitations . . . 54
- 3.2. Molecular Dynamics Simulations . . . 55
  - 3.2.1. Basic concepts . . . 55
  - 3.2.2. Results . . . 55
  - 3.2.3. Limitations . . . 57
- 3.3. Dust Coagulation Models . . . 57
  - 3.3.1. Basic concepts . . . 57
  - 3.3.2. Results . . . 58
  - 3.3.3. Limitations . . . 59
- 3.4. The method used in this thesis: Collisions with solid body mechanics . . . 60
  - 3.4.1. Methodological motivation . . . 60

3.4.2. Drawbacks and solutions 61
3.4.3. Advantages over other methods 62

4. Smoothed Particle Hydrodynamics and Solid Bodies 63
4.1. Basics 63
4.1.1. Kernel interpolation and discretisation 65
4.2. Hydrodynamics 68
4.2.1. Equation of Continuity 68
4.2.2. Euler and Navier-Stokes Equations 69
4.2.3. Energy equation 72
4.2.4. Equation of motion 72
4.3. Solid Body Mechanics 73
4.3.1. Elastic behaviour of solid bodies 73
4.3.2. Plastic behaviour of solid bodies 82
4.3.3. Equations of state 84
4.3.4. The porosity model 87
4.3.5. Damage models 96
4.4. Numerical Issues 99
4.4.1. The kernel function 99
4.4.2. Artificial viscosity 99
4.4.3. Tensile instability and artificial stress 101
4.4.4. Rotational instability and correction factors 102

5. Calibration 103
5.1. Benchmark Experiments 104
5.1.1. Compaction setup 104
5.1.2. Bouncing setup 107
5.1.3. Fragmentation setup 110
5.2. Numerical Setting 113
5.2.1. Computational domain and boundary conditions 115
5.2.2. Resolution and convergence 116
5.2.3. Geometrical difference of 2D and 3D setups 121
5.2.4. Artificial viscosity and other numerical parameters 123
5.3. Adopting and Adapting Empirical Material Parameters 126
5.3.1. Tensile Strength 127
5.3.2. Shear Strength 127
5.3.3. Compressive Strength 130
5.3.4. Comparing the plastic properties with benchmark experiments 138
5.3.5. Bulk Modulus 142
5.4. Summary 149

6. Pre-Planetesimal Collisions 153
6.1. Four-population model 153
6.1.1. Reproducing sticking, bouncing, and fragmentation collision types 154
6.1.2. A new model for mapping collision outcome 158
6.1.3. Applying the new model to simulation data 164

6.1.4. Discussion and Outlook 177
6.2. Inhomogeneity damage model 179
6.2.1. Implementation issues 179
6.2.2. Simulation results 182
6.2.3. Discussion and Outlook 191
6.3. Hard shells and aggregate bouncing 194
6.3.1. Homogeneous dust aggregates 194
6.3.2. Hard shell dust aggregates 199
6.3.3. Discussion and outlook 203
6.4. Head-on Collisions with Equal Porosity 204
6.4.1. Numerical setting and evaluation 205
6.4.2. Simulation results 207
6.4.3. Discussion and outlook 217

7. Conclusions 221
7.1. Summary and discussion 221
7.2. Outlook 224

A. Computer programs and evaluation tools 227
A.1. Particle distribution evaluation tool `sph3Deval` 227
A.2. Fragment distribution evaluation tool `fragment` 227
A.3. Particle distribution tool initgrid 228
A.4. Parallel SPH code `parasph` 229

List of Figures 233

List of Tables 235

1. Introduction

Pre-planetesimals are the millimetre- to kilometre-sized building blocks of planets. Their predecessors in size are micrometre to millimetre sized fractal dust aggregates which hit each other and stick by van der Waals forces. The successors of pre-planetesimals are kilometre sized planetesimals for which their self-gravity acts as an enhancing mechanism for accretion. The subject of this thesis is the development of a numerical model for the simulation of porous pre-planetesimal dust material to determine the outcome of two-body collisions at parameter ranges inaccessible to laboratory experiments. The collision statistics are to be determined depending on parameters such as object size and porosity, collision velocity and impact parameter. The results are intended for the use in global dust coagulation models. Based on this purpose the outline of this thesis is as follows.

In Ch. 2 I describe the astrophysical context of this thesis: the role of planetesimals in planet formation. In Sec. 2.1 protoplanetary discs are introduced as the environment of planet formation. Observational constraints are discussed as well as theoretical modelling of discs, their inner structure, and internal motions of the disc components, which are gas and dust. Section 2.2 is devoted to the evolution of the fractal dust aggregates. Starting from the properties of protoplanetary dust grains, their motions in the disc due to particle-gas-interaction, and the conditions for dust growth, I explain the assembly and properties of the end products of this step: highly porous, fluffy pre-planetesimals of millimetre to centimetre size, which are the objects to be simulated in this thesis. The next growth step to planetesimals is problematic and discussed in Sec. 2.3. Two hypotheses are presented as possible solutions: the coagulation and the gravitational instability scenario. I treat the advantages as well as the drawbacks of each scenario and explain how each of them can profit from the work presented here. In particular the fragmentation barrier and bouncing barrier of the coagulation hypothesis are addressed in this thesis. Assuming a sufficient population of planetesimals, Sec. 2.4 outlines the further path to planets through the stages of orderly, runaway, and oligarchic growth. Section 2.5 concludes this chapter by integrating this thesis into the broad picture of planetesimal formation.

Chapter 3 briefly introduces various methods contributing to the investigation of planetesimal formation. This is to assess the benefits and limitations of the neighbouring disciplines of this thesis and possible information exchange. Section 3.1 is devoted to laboratory experiments which provide material parameters and the laboratory reference for the benchmark experiments of this thesis. Molecular dynamics simulations are discussed in Sec. 3.2. This method may provide empirically inaccessible material parameters in future collaborations. The dust coagulation models of Sec. 3.3 are the addressee of the results of this thesis. They combine the dust evolution with the internal dynamics of the disc and require profound two-body collision statistics. Section 3.4 justifies the smoothed particle hydrodynamics (SPH) numerical scheme as a suitable methodological choice for the given topic. This arises from the requirements and drawbacks of the neighbouring methods.

The numerical method SPH is presented in detail in Ch. 4 with special respect to the simulation of solid bodies. Section 4.1 describes the fundamental ideas of SPH such as the kernel interpolation and discretisation. The equations of hydrodynamics and their SPH representation are briefly reviewed in Sec. 4.2. Since solid body mechanics is rarely used in the astrophysical context, I derive its basic equations in more detail in Sec. 4.3 and present the SPH representations used in this thesis. This includes the theories of elasticity and plasticity as well as some equations of state. The porosity and damage models developed for this work require special attention in this section. The chapter is concluded with some numerical issues in Sec. 4.4.

The heart of this thesis is the extensive calibration and validation process of the porosity model (Ch. 5). The benchmark experiments which are carried out numerically in this thesis and at the same time in the laboratory by collaborators are presented in Sec. 5.1. To establish a profound basis for the calibration I settle some specific numerical issues such as resolution and convergence in Sec. 5.2. Section 5.3 describes the calibration of the material relations tensile strength, shear strength, compressive strength, and bulk modulus as well as their numerical determination where they are not available from laboratory measurements. The results are compared with the experimental reference. Section 5.4 summarises the calibration process.

Chapter 6 is devoted to pre-planetesimal collisions and a suitable mapping format. In Sec. 6.1 I develop a new classification scheme for pre-planetesimal collision outcome: the four-population model. In detail I describe the benefits of this quantitative approach over other categorisation attempts and show that other mapping models are encompassed by the new method. To demonstrate its functionality I utilise it to classify my simulation data. In addition, the porosity model is shown to reproduce all sticking, bouncing, and fragmentation types seen in laboratory experiments. To improve the realistic simulation of dust aggregates I present results from simulations with my inhomogeneity damage model in Sec. 6.2. It is shown that inhomogeneous aggregates are more fragile than homogeneous aggregates and smaller fragments are produced for a higher degree of inhomogeneity. Section 6.3 addresses the bouncing barrier: experimental results might overestimate the occurrence of rebound in aggregate collisions. It is also demonstrated how hard shells influence the bouncing properties of pre-planetesimals. To conclude this chapter, I present the results of a large number of head-on collisions in Sec. 6.4. Transition threshold velocities between positive, neutral, and negative growth are determined for homogeneous aggregates of high, intermediate, and low porosity. The study emphasises the dependence of these thresholds on projectile size and filling factor.

In the conclusions chapter (Ch. 7), I summarise and discuss the results of this thesis (Sec. 7.1) and give an outlook on future work (Sec. 7.2).

2. Planet Formation

2.1. Protoplanetary discs - The stage for planet formation

2.1.1. Formation of star and disc

Before planets can form, the environment for planet formation has to be established. Planets are thought to be formed in circumstellar discs around a central star. This is the essential setup for planet formation and it also represents the initial conditions for the evolution of our own solar system. For the sake of simplicity, the following discussion carries on with this simple starting point in mind leaving aside other conceivable environments such as discs around binaries. In this section the formation of the central star and its surrounding disc will be explained. The passage follows the extensive review articles by Larson (2003) and McKee and Ostriker (2007), which describe this vast topic in adequate detail. Recent advances in understanding star and disk formation have been made by Stamatellos et al. (2007) and Tscharnuter et al. (2009).

Stars form from molecular clouds which are massive and dense subregions in spiral arms of galaxies or in galactic nuclei. These clouds consist mainly of hydrogen and helium in molecular form and a very small fraction of other material, which is referred to as *metallic* in astrophysical terminology. Initially, these objects have a nearly uniform density.

metallic material

In an widely accepted scenario, which can be traced back to Newton, small density fluctuations in the almost homogeneous medium are amplified by gravitational forces and, eventually, the molecular cloud becomes gravitationally unstable. As a consequence, gravitational attraction exceeds thermal pressure forces and the cloud collapses in a runaway process. The spherical collapse can, e.g. be modelled based on initial states similar to a *Bonnor-Ebert sphere* (after the works of Bonnor 1956 and Ebert 1957), which is an equilibrium isothermal sphere of finite size. Temperature and boundary pressures are fixed. A stability analysis reveals that this configuration is unstable to collapse if the following critical values for the sphere's radius $R_{\rm BE}$ and mass $M_{\rm BE}$ exceed the values

Bonnor-Ebert sphere

$$R_{\rm BE} = \frac{0.48\, c_{\rm s}^2}{\sqrt{G P_{\rm b}}} \tag{2.1}$$

$$M_{\rm BE} = \frac{1.18\, c_{\rm s}^4}{\sqrt{G^3 P_{\rm b}}}\,, \tag{2.2}$$

where $c_{\rm s}$ is a fixed sound speed, $P_{\rm b}$ the boundary pressure and G the gravitational constant. Neglecting an outward pressure gradient, which develops during the collapse, a uniform sphere of gas requires the free-fall time $t_{\rm ff}$ to develop from a state of rest to an infinite density peak. Despite of its simplifying assumptions, the *free-fall time* remains a good approximation and it is given by

free-fall time

$$t_{\rm ff} = \left(\frac{3\pi}{32\, G \rho_{\rm mc}}\right)^{1/2}, \tag{2.3}$$

where ρ_{mc} is the initial density distribution. However, no matter what initial or boundary conditions are chosen, an outward pressure gradient appears at the boundary when the collapse begins. The collapse is assumed to proceed isothermally. The gradient propagates inward as rarefaction wave with the speed of sound and causes the collapse to be highly non-uniform. This is because the collapse of the outer layers are slowed by the outward pressure gradient compared to the inner layers. In general, it can be said that the collapse is characterised by a runaway growth of a central density peak which occurs in a non-uniform way.

protostar

second collapse

In the centre of the collapsing molecular cloud a cloud core forms and increasing thermal pressure counteracts gravitational forces. Therefore, the core must have a minimum mass so that gravitational forces always exceed thermal counter-forces and an object of stellar density, an embryonic star or *protostar*, can be formed. This process, which lasts only a few thousand years, can be divided into two substages. The first core grows in mass and heats up until the temperature reaches 2000 K. Then the molecular hydrogen starts to dissociate. Now the energy delivered by contraction under gravitational forces does not only heat the core but also dissociates hydrogen; at this point the *second collapse* starts. The further process is a complex interplay between thermodynamics, redistribution of angular momentum, and energy transport. The second collapse lasts until nearly all hydrogen has been dissociated and it decelerates when the stellar density reaches $\rho \sim 10^{-3}\,\mathrm{g/cm^3}$ and the temperature rises above $T \sim 10000\,\mathrm{K}$.

Bondi(-Hoyle) accretion

star classification

In this process, the protostar gains only a small fraction of its final stellar mass by direct collapse from the molecular cloud core. At the end of the collapse process it has reached less then 10^{-2} solar masses. Most of the mass of the cloud core stays behind in an extended in-falling envelope. From now on, the protostar acquires its mass by gravitational accretion from this surrounding envelope, which is referred to as *Bondi accretion* if the accreting object is stationary and *Bondi-Hoyle accretion* of the object is moving. Accretion proceeds in different stages which can be distinguished according to the dominant wavelengths in the emitted spectrum of the evolving star: a Class 0 object features sub-millimetre wavelengths which indicates an early phase of rapid accretion. This phase lasts some 10^4 years. The main accretion phase (Class I) lasts a few times 10^5 years and is characterised by a spectrum dominated by far-infrared wavelengths, which gives rise to the presence of a circumstellar disc. A pronounced near-infrared spectrum points to a Class II object which represents a classical T Tauri star with considerable circumstellar dust and an accretion phase lasting up to 10^6 years. Finally, a Class III object emits mostly at visible wavelengths and is similar to a weak line T Tauri star with no significant circumstellar material and accretion.

circumstellar disc

angular momentum transport

After this short description about the formation of the central star I turn the focus to the formation of the *circumstellar disc*, which is the location where planet formation actually takes place. These discs are formed as a byproduct of stars during the collapse of isothermal axisymmetric molecular clouds, where the cloud is rotating slowly. Their existence is a consequence of the conservation of angular momentum. It has been shown, that rotation does not prevent the formation of a density singularity during collapse, but most of the mass of the cloud ends up in a centrifugally supported disc around the singularity. For the star to grow in mass, material has to be transported inwards in the disc and accreted by the star, while angular momentum must be removed or transported outwards. This is only possible if the disc is somehow viscous. Although it has been clear for a long time, that molecular viscosity is much too small to cause efficient outward transportation of angular momentum, a mechanism that creates sufficient viscosity of the disc still has to be identified. A complicated interplay between magnetohydrodynmics (MHD), radiative transfer, chemistry, and also solid state physics is in discussion to aid the accretion process. Shakura and Sunyaev (1973), Lynden-Bell and Pringle (1974), and others avoided the problem of exactly determining the viscosity mechanism by introducing a phenomenological description. In their *alpha prescription* for angular momentum transport, which is based on dimensional grounds, the effective kinematic (or turbulent) viscosity ν of the disc has to obey

alpha prescription

$$\nu \equiv \alpha \frac{c_\mathrm{s}^2}{\Omega_\mathrm{K}} = \alpha c_\mathrm{s} H\,, \tag{2.4}$$

where c_s is the sound speed, Ω_K the Keplerian angular velocity and H the scale height of the disc defined as $H = c_\mathrm{s}/\Omega_\mathrm{K}$. With this model, disc evolution can be studied with pure hydrodynamics and α represents the strength of turbulence in the disc. Typical values of α range between 10^{-3} and a few 10^{-2} (see, e.g. Johansen and Klahr 2005, Dzyurkevich et al. 2010).

Theory, simulations, and observations suggest that circumstellar discs are a very frequent, if not inevitable, byproduct of star formation (Hartmann 2009). Hence, the basic environment where planets form can be expected around nearly every forming star. Therefore, I will stress the aspect of them as the location of planet formation and call them *protoplanetary discs* in the further discussion. Average protoplanetary disc sizes are ~ 200 AU and at most 1000 AU (e.g. Andrews and Williams 2007). Disc masses of T Tauri systems range from ~ 10^{-3} to 10^{-1} solar masses with a median at 5×10^{-3} solar masses (e.g. Andrews and Williams 2005). The largest mass fraction of a protoplanetary disc is gas mainly in form of molecular hydrogen H_2, but also He, CO, CO_2, N_2 and CH_4. The smaller fraction consists of solid dust particles of initially micrometre size. They are mostly compounds of C, Si, and O. Water is also present in the gas phase in the inner regions and as water ice in the outer regions of the disc. The gas and dust material of the former protoplanetary disc of our solar system is the material that planets, gas giants, moons, Kuiper belt objects, and all other massive objects orbiting around the sun are made of. Now that the stage for planet formation is set, I focus on the actual planet formation process itself. This process is closely linked to the dynamics in the disc, which, in turn, is linked to the underlying disc model. The next sections are devoted to this topic.

protoplanetary discs

2.1.2. Observational constraints for protoplanetary discs

Over the past two decades, inventions and improvements of various observational techniques have amplified our insight into the structure and dynamics of protoplanetary discs. With the aid of *spectral energy distributions (SED)* more and more realistic disc models can be constructed and constraints for planet formation can be derived. In the first part of this section, the available observational data and its interpretation will be summarised following the review articles by Natta et al. (2007), Dullemond et al. (2007), and references therein.

SED

Protoplanetary discs can be found around young, optically visible pre-main sequence stars. Their structure can, e.g. be analysed with the aid of scattered light measurements at visual and infrared wavelengths, mid-infrared spectroscopy and millimetre interferometry.

A first look on the disc is provided at visible and near-infrared wavelengths, where a dark disc silhouette presents itself against the background light originating from the star and scattered by the disc surface. These images, first of all, demonstrate that a disc shaped object has formed around the young star. Secondly, the object is optically thick at visible and near-infrared wavelengths.

Further investigation of the disc already involves model assumptions of the disc: the emitted spectrum of the disc is mainly determined by its temperature. A balance is established between heating through stellar irradiation and cooling by thermal emission of the dust grains. Under the assumption that the dust temperature is equal to the gas temperature, the temperature profile of the disc can be computed using dust radiative transfer methods and disc model assumptions presented in the next part of this section. The temperature profile finally determines the SED. Many possible SEDs are computed by a parameter study and the suitable disc parameters are chosen as a best fit of computed and observed SED.

SED domains

The SED can be divided into three wavelength regions (see Fig. 2.1): the *energetic domain* contains the largest fraction of emitted energy. Its constraining wavelengths (~ 1.5 µm – 100 µm) are determined by the minimum and maximum temperatures of the dust. Smaller wavelengths are referred to as the *Wien domain*. For wavelengths greater than 100 µm, in the *Rayleigh-Jeans domain*, the SED drops in a steep, nearly power law fashion, whose slope depends on the grain properties and optical depth of the disc.

Wien domain

In the left panel of figure 2.1 the features of a model disc are connected with the according features in the SED. The bump at near-infrared wavelengths indicates that the disc has an inner rim. In the inner regions very close to the star dust is evaporated and, hence, this region is dust free. Further outward, somewhere within 1 AU (depending on the luminosity of the star) the dust condensation radius is located (see Fig. 2.1, right panel). Here, the disc starts off with a relatively sharp inner edge. This edge possibly is puffed up compared to the remaining vertical profile of the disc. The region within 1 AU is particularly interesting for the energy balance of the disc, since a huge amount of energy is set free there. However, for planet formation it plays a minor role. Therefore, I refer the interested reader to the review article by Dullemond and Monnier (2010) for an extensive discussion.

energetic domain

The infrared dust features in the energetic domain originate from emission of the hot dust surface layer (see Fig. 2.1, right panel). The dust grains in the surface layers are exposed to stellar irradiation. Therefore, they have a higher temperature than the dust in the interior and emit at shorter wavelengths. The near and mid infrared emission typically originate from small disc radii. The far infrared flux (Rayleigh-Jeans domain) comes from the outer regions of the disc. Here, a shallow SED slope indicates a flaring disc geometry, i.e. the disc is “double-bowl-shaped”. This is because with a flaring geometry a large portion of the stellar irradiation is captured and reemitted at the cool outer regions of the disc. For a deeper look into the disc, one has to go to even longer wavelengths and perform millimetre up to centimetre interferometry. At these wavelengths more and more regions of the disc become optically thin, which reveals the bulk of the dust mass in the disc down to the disc’s midplane. These observations provide the strongest evidence that *dust growth* by coagulation and dust settling to the midplane take place in protoplanetary discs. This is regarded as the initial step of planet formation. Particularly the following facts (Natta et al. 2007) are relevant for modelling this process:

Rayleigh-Jeans domain

dust growth

1. Grains in the disc are in average much larger than in the interstellar medium (ISM) and in molecular clouds. Dust has aggregated to millimetre and centimetre sizes in many of the observed discs.
2. There is evidence for a vertical stratification of the dust. Small grains at micron sizes exist closer to the disc’s surface. The largest fraction of dust exists as pebbles in the midplane of the disc. Hence, most of the solid mass is concentrated in centimetre sized aggregates once the star becomes optically visible.
3. Grain properties do not show any correlation with star or disc parameter, i.e. all kinds of discs around all kinds of stars potentially can and normally do process grains.

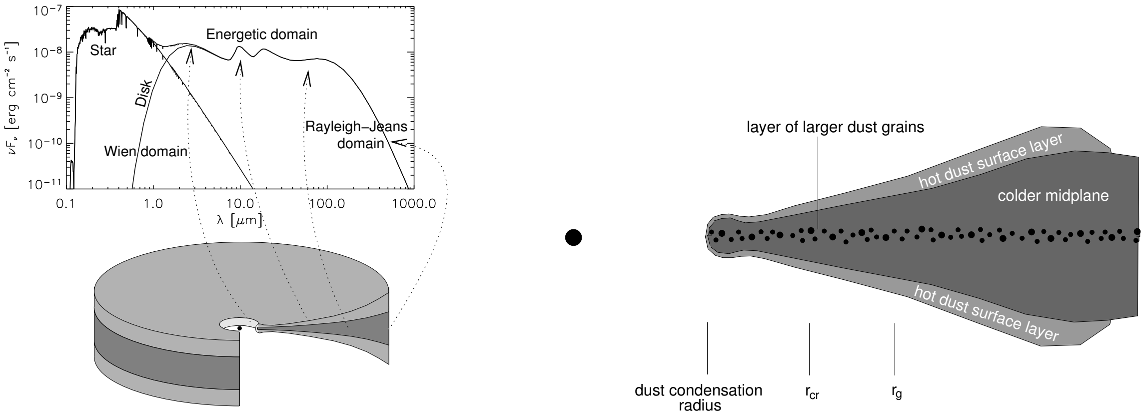

Figure 2.1. *Build-up of the SED of a protoplanetary disc* (left). The near-infrared feature comes from the inner rim, the mid-infrared bump indicates dust in the warm outer layers of a flaring disc, and the far infrared flux originates from deeper, cooler regions around the midplane of the disc. *Vertical cut trough the dust structure of a protoplanetary disc* (right). The region beyond the dust condensation radius is puffed up. The surface layers of the disc are heated by stellar irradiation. Dust pebbles accumulate near the midplane of the disc (figures from Dullemond et al. 2007).

4. Grain properties also do not seem to vary with time. Processed grains are found around the youngest and oldest pre-main sequence stars.

As valuable as these findings are, they have to be interpreted with caution. When collecting the data from which the above results are derived, today's millimetre interferometers act at their sensitivity and resolution limits. In principle grain properties in the upper layers can also be derived from the polarisation of scattered light at visible and near-infrared wavelengths. However, this is technically very challenging and data therefrom is still scarce. Furthermore, regions between the dust condensation radius and a few AU are optically thick even at very long wavelengths and, thus, the grain properties at the midplane are inaccessible there. Independent of the observational technique, kilometre-size planetesimals can only be detected through the perturbations they create, but pre-planetesimals in the size range between centimetres and kilometres cannot be detected at all.

To summarise, current observations provide plenty of information about the structure and dynamics of protoplanetary discs. It could even be shown that grain growth and processing, the initial step of planet formation, takes place in nearly every disc. However, essential steps of the planet formation process are still not accessible to contemporary observational instruments and techniques. Therefore, modelling of the gas and dust dynamics inside the disc is inevitable for a deeper insight into the genesis of planets. In the next part the basis for this will be laid: the model of a protoplanetary disc.

2.1.3. The construction of disc models

This part, again following review articles by Natta et al. (2007), Dullemond et al. (2007), and references therein, is devoted to the basic disc parameters which represent the cornerstone of each disc model and its influence on the dynamics in the disc. Because of the disc's radial symmetry, the surface density $\Sigma(r)$ is introduced for its description. For a disc with constant accretion rate $\dot{M}$ onto the host star (*steady state accretion disc*, Shakura and Sunyaev 1973, Pringle 1981) and sufficiently large radii

steady state disc

$$\Sigma(r) = \frac{\dot{M}}{3\pi\nu}\,, \tag{2.5}$$

with the kinematic viscosity ν from Eq. (2.4). With the scale height $H = c_{\mathrm{s}}/\Omega_{\mathrm{K}}$, the temperature at the midplane $T_{\mathrm{c}}(r)$, and some constant K the *surface density* reads

surface density

$$\Sigma(r) = \mathrm{K}\frac{\dot{M}}{r^{3/2}\alpha T_{\mathrm{c}}(r)}\,. \tag{2.6}$$

Hence, the radial dependence of the surface density critically depends on the radial dependence of the temperature structure of the disc and this is where the main complexity of the disc model lies. The *vertical density distribution* $\rho(r,z)$ generally is assumed to be gaussian

vertical density distribution

$$\rho(z,r) = \frac{\Sigma(r)}{\sqrt{2\pi}H}\exp\left(-\frac{z^2}{2H^2}\right)\,. \tag{2.7}$$

Elaborate models distinguish between surface density of the gas $\Sigma_{\mathrm{g}}(r)$ and surface density of the dust $\Sigma_{\mathrm{d}}(r)$ as well as their corresponding vertical density profiles $\rho_{\mathrm{g}}(r,z)$ and $\rho_{\mathrm{d}}(r,z)$. The treatment of gas and dust also differs in their corresponding scale heights, where the dust scale height depends on the settling and diffusion of the dust (for details see, e.g. Cuzzi and Weidenschilling 2006).

In the literature, three different models, mainly differing in the choice of the gas surface density $\Sigma_{\mathrm{g}}(r)$, have been proposed and used. Following the nomenclature of Zsom et al. (2010), I will briefly introduce and discuss the *low density model*, the *minimum mass solar nebular (MMSN) model*, and the *high density model*.

low density model

The low density model has been introduced by Brauer et al. (2008a). On the basis of recent millimetre dust emission maps observed by Andrews and Williams (2007) they chose the gas surface density profile to be

$$\Sigma_{\mathrm{g}}(r) = 45\,\mathrm{g/cm^2}\left(\frac{r}{\mathrm{AU}}\right)^{\delta}\,. \tag{2.8}$$

profile slope

Their disk extends from 0.03 AU to 150 AU and its mass is $0.01\,\mathrm{M}_{\odot}$. The choice of the *slope* of the profile δ, which is -0.8 in this case, is the key issue of all disc models. Although the observations by Andrews and Williams (2007) have their median at an exponent of -0.5, Brauer et al. (2008a) justify their slightly steeper choice by the argument that dust emission observations are restricted to the outer parts of the disc, where dust growth proceeds slower than in the inner parts. This effect makes gas density profiles seem shallower than they are. Cuzzi and Weidenschilling (2006) additionally note that the disc mass will be underestimated once particles have grown past millimetre size since larger particles are hardly detectable. Despite these corrections the low mass model features the smallest power law exponent of all presented models. Its density in the midplane at 1 AU is $2.4 \times 10^{-11}\,\mathrm{g/cm^3}$.

MMSN model

The MMSN model is the oldest of the three models and it is most widely used as a reference model. It was introduced by Weidenschilling (1977a) and improved by Hayashi (1981) and Hayashi et al. (1985). Their gas surface density reads

$$\Sigma_\mathrm{g}(r) = 1700\,\mathrm{g/cm^2}\left(\frac{r}{\mathrm{AU}}\right)^{\delta}\ , \tag{2.9}$$

with $\delta = -1.5$. This was derived from today's solar system properties. The model assumes that the planets have formed at their present positions. Weidenschilling (1977a) augments the planets with H and He such that solar composition is restored and spreads out the augmented planetary masses over annuli centred on the planets' orbits. The main idea of this construction is that planet formation is somehow the reverse process of the spreading. Hayashi (1981) and Hayashi et al. (1985) took into account where different solids, especially water ice, have their condensation radii. The surface density is computed by dividing the augmented mass by the surface area of its corresponding annulus. The total mass of the MMSN is $0.01\,\mathrm{M}_\odot$ and it reaches from 0.4 AU (Mercury orbit) to 30 AU (Neptune orbit).

However, the MMSN model has some drawbacks (see, e.g. Desch 2007). First, it assumes that all solid mass of the protoplanetary disc was incorporated in the planets. It does not take into account that a substantial amount of solid mass could be lost into the sun or otherwise removed from the planet formation process. Therefore, as already noted by Weidenschilling (1977a), the disc mass is actually the lower bound of the mass of the original nebula. Second, the MMSN is only a snapshot, leaving aside that protoplanetary discs evolve with time. Despite these critics the MMSN model has widely been used as benchmark model.

high density model
Nice model

The last model of importance is the high density model proposed by Desch (2007). In a sense, it is a revision of the MMSN model. It is also based on our solar system, but it assumes that the planets have migrated after their formation. This is suggested by the *Nice model* (Tsiganis et al. 2005, Gomes et al. 2005, Morbidelli et al. 2005), which places the starting points of the giant planets between 5 AU and 15 AU and shows that Uranus and Neptune probably switched places during their orbital evolution because Jupiter and Saturn crossed their mutual 2:1 mean motion resonance (MMR) causing chaotic behaviour in the solar system. The Nice model explains a variety of phenomena of the solar system such as the late heavy bombardment (Gomes et al. 2005), the existence of the Kuiper belt, and the trapping of the Jovian Trojans (Morbidelli et al. 2005). Consequently, the planet configuration of the Nice model requires a much more compact solar nebular. Hence, the surface density has a steeper profile. The original profile by Desch (2007) depends on the fraction of the mass of all solids that is locked up in planetesimals. It was adopted by Zsom et al. (2010) as

$$\Sigma_\mathrm{g}(r) = 5.1\times10^{4}\,\mathrm{g/cm^2}\left(\frac{r}{\mathrm{AU}}\right)^{-2.2}\ . \tag{2.10}$$

This profile is inconsistent with a steady state accretion disc (Eq. 2.5), but it is consistent with a photo-evaporated decretion disc. Although $\Sigma_\mathrm{g}(r)$ was originally designed for the outer solar system, it can be extrapolated to 1 AU where the density in the midplane is $2.7\times10^{-8}\,\mathrm{g/cm^3}$.

After presenting the most commonly used disc models, the question arises how the choice of the disc model affects the process of planet formation. Brauer et al. (2008a) and Zsom et al. (2010) have studied this issue. Summarising, they find that depending on the disc model, dust aggregates have higher (low mass model) or lower (high mass model) relative velocities (see figure 2.2). This is because the higher the gas density the stronger the coupling between gas and dust. This

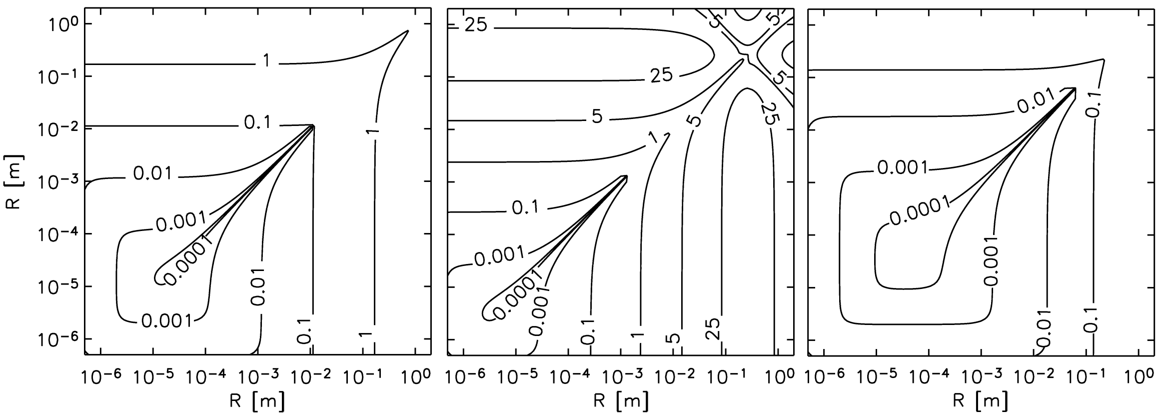

Figure 2.2. *Collision velocities for various disc models.* Relative velocities (labelled contour lines) for collisions between dust aggregates of different sizes (axes) at 1 AU in the disc midplane. All considered disc models are laminar ($\alpha = 10^{-5}$). Surface densities are chosen according to the minimum mass solar nebula (MMSN) model (left), low density model (middle), high density model (right) (figure after Weidling et al. 2009).

leads to the effect that the planet formation is stalled at different grain sizes. This problem will be discussed extensively in section 2.3.1. Before treating the onset of dust growth by coagulation, some words have to be said about the inner dynamics of a protoplanetary disc.

2.1.4. Turbulence and inner disc dynamics

As already mentioned at the end of section 2.1.1, protoplanetary discs have to be somehow viscous in order to transport angular momentum outwards and material inwards, where it is accreted by the star. The presented alpha prescription for angular momentum transport (Eq. 2.4) is solely a phenomenological approach to the problem. Since molecular viscosity is far too low to explain the observed mass accretion rates, turbulence is believed to be responsible for angular momentum transport. The source of turbulence, however, is still a matter of debate (see, e.g. McKee and Ostriker 2007).

magnetic stresses

MRI

dead zone

The most promising candidates for angular momentum transport are *magnetic stresses.* If the differentially rotating gas in the protoplanetary disc is moderately or even weakly ionised, a local instability, the *magneto-rotational instability (MRI)* (Balbus and Hawley 1991), develops. With the aid of recent elaborate magnetohydrodynamics (MHD) simulations (e.g. Johansen and Klahr 2005, Ilgner and Nelson 2006, Flaig et al. 2009, Dzyurkevich et al. 2010), the α value caused by MRI is estimated to be $\sim 10^{-3} - 10^{-2}$. It has to be underlined that turbulence can only be produced by MRI if the gas is sufficiently ionised and dust plays an important role in this process since it acts as an electron absorber. Therefore, Gammie (1996) has suggested a layered accretion disc model: a *dead zone* around the midplane, where the MRI is not active, is enclosed between two sufficiently ionised, accreting layers. The exact size of this dead zone depends on the dust distribution in the nebular and detailed chemistry. Based on the dust properties of the ISM, Ilgner and Nelson (2006) have shown that there is no turbulence caused by MRI in large parts of the disc.

Even in an almost laminar protoplanetary disc, i.e. with very low α values around 10^{-5}, or in dead zones there can be turbulence generated by *Reynolds stresses*. This can be generated by the following mechanism: observations suggest that there is vertical stratification in the protoplanetary disc (see end of section 2.1.2). Particles accumulate near the midplane and form a dense dust-rich particle layer there. In regions above and below this particle layer the dust to gas ratio is much lower. Goldreich and Ward (1973), Weidenschilling (1977b), and Cuzzi et al. (1993), amongst others, demonstrate that the particle layer rotates slightly faster than its adjacent gas layers. This is because there exists an outward pressure gradient of the gas. The centripetal acceleration of the gas is generated by the gravitational attraction as an inward force and an outward force by the pressure gradient. As already noted by Whipple (1972) large enough dust particles do not feel the pressure support, hence, they tend to pursue their orbits with Keplerian velocity $V_\mathrm{d} = V_\mathrm{K} = \Omega_\mathrm{K} r = \sqrt{GM_* r^{-1}}$, where M_* is the mass of the star. Because dust particles dominate the motion in the midplane, the dense particle layer as a whole rotates at Keplerian speed. The orbital velocity of the gas layers above and below is given by

Reynolds stresses

$$V_\mathrm{g} = \left(1 + \frac{r}{2\rho_\mathrm{g} V_\mathrm{K}^2} \frac{\partial p}{\partial r}\right) V_\mathrm{K}\,, \tag{2.11}$$

where the pressure gradient is outward, i.e. $\partial p/\partial r < 0$. This vertical velocity gradient generates a shear flow between both layers. Numerical investigations by Cuzzi et al. (1993) and Johansen et al. (2006a) have demonstrated that such shear flows are subject to *Kelvin-Helmholtz instability*, which causes turbulence. Weidenschilling (1980) was the first to showed by scaling arguments that also the particle layer itself becomes turbulent. This effect puffs up the particle layer until gravity, which lets dust settle to the midplane, and turbulence, that stirs the dust to upper layers, generate a steady state. The latter determines the final thickness of the layer. However, with respect to angular momentum transport, Stone and Balbus (1996) have shown that this kind of turbulence as well as convection due to vertical or radial entropy gradients tends to transport angular momentum inwards instead of the desired outward direction.

Kelvin-Helmholtz instability

For the sake of completeness, *gravitational stresses* have to be mentioned as third source for turbulence in a protoplanetary disc. Because of the constant evolution of the discs due to accretion flows, gravitational energy is constantly released. This energy on its own can also maintain turbulent motions (see, e.g. Cuzzi and Weidenschilling 2006, McKee and Ostriker 2007, and references therein).

gravitational stresses

I close this section by drawing the readers attention to the crucial interdependence of dust evolution on the one hand and disc model and dynamics on the other hand. The density and size distribution of dust in the disc influences angular momentum transport and, hence, accretion dynamics by generating turbulence via shear instabilities as well as inhibiting MRI by acting as electron absorber causing low ionisation in large parts of the disc. Furthermore, dust is of major importance for the thermal structure since dust opacity dominates over gas opacity and, thus, dust can shield parts of the disc from stellar or cosmic irradiation. However, turbulent motions in the disc co-determine relative velocities between dust grains and aggregates and, thus, influence the evolution of the dust density and size distribution, which finally ends up in planets. The physics of dust agglomerates and their evolution is, therefore, of major importance for disc dynamics and planet formation. Consequently, the next section deals with the first step of planet formation: with the genesis of dust aggregates from dust grains.

2.2. Dust coagulation - The first phase of planet formation

After the short introduction to the properties of protoplanetary discs as the vast stage of planet formation, I will now focus on the microscopic building blocks of planet formation: the dust grains. Entrained in the disc's gas their relative motions lead to mutual collisions. The outcome of the collisions, in turn, depends on the sticking properties of the grains and the collision energy. Consequently, I will first discuss the microscopic properties of the dust grains, then I will turn to their interaction with the gas and the sources of relative velocities, and finally I will describe the process of dust coagulation as the first step of planet formation.

2.2.1. Dust grain properties

As we have already seen in section 2.1.2, observational techniques are capable of providing us with plenty of information about the dust grain properties and distribution in protoplanetary discs. According to these measurements, these show no dependence on star or disc parameters (Natta et al. 2007). Weidenschilling (2000) conjectured that dust already started coagulating while the protoplanetary disc was forming from a molecular cloud. (This process was discussed in section 2.1.1). Using a very elaborate dust coagulation model, Ormel et al. (2009) have demonstrated recently with numerical simulations that, if cloud lifetimes are restricted to free-fall times (see Eq. 2.3), this effect has little influence on the dust size distribution. Hence, at the onset of planet formation the grain size distribution in protoplanetary discs must have been similar to the ISM. Mathis et al. (1977), Li and Greenberg (1997), and Clayton et al. (2003) derive grain sizes of $0.1 - 1\mu m$ from extinction and polarisation measurements.

chemical composition

The *chemical composition* of dust grains is a topic of ongoing astrochemical and astromineralogical research. It is clear (Henning and Meeus 2010) that the bulk of dust material consists of silicates and carbonaceous material. In particular, silicates such as Mg_2SiO_4 (forsterite), $Mg_2Si_2O_6$ (enstatite), and carbon compounds such as CO (carbon monoxide), SiC (silicon carbide), CN (cyanine), and Polycyclic Aromatic Hydrocarbons (PAHs) play an important role as constituents of dust grains in the warm regions of the inner protoplanetary disc. In the cold outer regions the grains consist of, or are coated by, H (hydrogen) and H_2O (water ice). Hence, in general, protoplanetary dust is assumed to be nonmagnetic, uncharged, solid, and electrically insulating. The dust material features a high sublimation temperature, great hardness, high Young's moduli, and intermediate or high density (Poppe et al. 2000, Blum and Wurm 2008). Nevertheless, it is a matter of debate wether long-range forces such as magnetic and electric forces are relevant for the planet formation process (Dominik et al. 2007).

Wurm (2003) underlines the importance of knowing as much as possible about the properties of the individual dust grains as well as their initial distribution. This is because these initial conditions might determine the overall fate of growth. Some conditions possibly promote, others possibly inhibit planet formation. This raises the key question of how dust grains stick together to form bigger aggregates. This process is synonymously called *dust agglomeration*, *aggregation*, or *coagulation* (Blum and Wurm 2008). Poppe et al. (2000) have shown in laboratory experiments with diamond (C), silica (SiO_2), enstatite ($Mg_2Si_2O_6$), and silicon carbide (SiC) that it is rather the grain shape, size, and roughness, which determines the sticking probability, than the grain material.

dust agglomeration, aggregation, coagulation

For the dust agglomeration process it is crucial to know, which collision energies lead to sticking between two grains[1], a grain and an agglomerate[2] (i.e. particle-cluster-aggregation, PCA), and two agglomerates (i.e. cluster-cluster-aggregation, CCA). Therefore, laboratory experiments (see, e.g. Blum and Wurm 2008, Güttler et al. 2010, and section 3.1 for an overview) and numerical simulations, in particular molecular dynamics (MD) simulations (see section 3.2 for an overview) have to be carried out to determine the sticking probability for various aggregate sizes and collision velocities. Since realistic protoplanetary material is lacking, hard and expensive to produce, or difficult in its numerical treatment, protoplanetary *dust analogues* with similar properties are chosen. Although there have been experiments with oxides, metals, silicates, and organic materials, the only systematic study has been carried out with silica (SiO_2) (see Blum and Wurm 2008, and references therein). This material is rather unimportant in astrochemistry (Gail 2004), but it features grain sizes of ~ 1 µm and all other properties listed in the penultimate paragraph. In particular, mono-disperse spherical SiO_2 consists of smooth spheres, which makes it an ideal candidate for analytical and numerical modelling. Precise knowledge of the properties of this dust analogue is crucial for understanding the planet formation process in the warm inner regions of the protoplanetary disc. Recently, progress has also been made in numerical studies of the aggregation of water ice grains (Wada et al. 2007, 2008, 2009, Suyama et al. 2008), which may be important for planet formation in the cold outer regions of a disc. However, laboratory experiments are rather sparse in this field.

dust analogues

In case of SiO_2 induced electric dipoles, i.e. *van der Waals forces*, and in case of water ice *static electric dipoles* make individual grains stick to each other because of dipole-dipole interaction between the molecules constituting the grains (e.g. Dominik et al. 2007, Blum and Wurm 2008). Hereby, static dipole forces are much stronger than induced dipole (van der Waals) forces. In a simple model of two spherical 1µm grains, this attraction causes the two particles to come in contact with each other. At the contact area both grains will be elastically deformed until an equilibrium state between attraction and repulsion has been established. This process has been studied analytically by Johnson et al. (1971), Chokshi et al. (1993) and Dominik and Tielens (1996) and in the laboratory by Heim et al. (1999).

static dipoles

van der Waals forces

As a summary of this section it can be said that the microscopic reason for sticking, and hence for dust agglomeration, are dipole-dipole interactions. Individual dust grains establish contacts to each other, which can be modified in six degrees of freedom (see section 3.2). Hereby, particles in larger aggregates can be rearranged without breaking the individual grains. Energy can be dissipated through irreversible rearrangement of the dust grains. The microscopic, and thus also the macroscopic, behaviour of dust aggregates is determined by grain size and morphology.

2.2.2. Particle gas dynamics

Dust grains are entrained in the gas of a protoplanetary disc. They follow its motions and, hereby, gain relative velocities, which leads to mutual collisions and aggregate growth. Therefore, the coupling between dust and gas plays an eminent role in the planet formation process. In this section I will present some quantities which have been used throughout the past decades of research in this field (e.g. Whipple 1972, Weidenschilling 1977b, Cuzzi et al. 1993, Dullemond and Dominik 2004, Cuzzi and Weidenschilling 2006, Dominik et al. 2007).

---

[1] A dust grain is a chemically homogeneous solid monomer of spherical or irregular shape. It is the smallest building block of a dust agglomerate.

[2] A dust agglomerate consists of several dust grains, which are bound together by static or induced dipole-dipole forces. The agglomerate has porous or fractal structure.

Knudsen number

The first quantity to introduce is the ratio between mean free path length λ_{mfp} of the gas and the radius R_{d} of a dust particle: the *Knudsen number* is given by

$$\mathrm{Kn} = \frac{\lambda_{\mathrm{mfp}}}{R_{\mathrm{d}}} . \tag{2.12}$$

Reynolds number

For high gas densities or large particle radii it follows $\mathrm{Kn} \ll 1$ and the particles are in the *Stokes regime* (e.g. Weidenschilling 1977b). For low gas densities or small particle radii ($\mathrm{Kn} \gg 1$) the particles move in the *Epstein regime* (e.g. Weidenschilling 1977b). The transition between both regimes is found at $\mathrm{Kn} = 4/9$ for *Reynolds numbers* $\mathrm{Re} < 1$. The latter is defined as

$$\mathrm{Re} = \frac{2\rho_{\mathrm{g}} R_{\mathrm{d}} v_{\mathrm{gd}}}{\eta} , \tag{2.13}$$

stopping time

where ρ_{g} is the gas density, v_{gd} the relative velocity between the gas and dust particle and η the gas viscosity. Weidenschilling (1977b) distinguishes between three different Stokes regimes depending on Re. However, for most applications the first Stokes regime ($\mathrm{Re} < 1$) is sufficient.
For both regimes the interaction between gas and dust particles is characterised by the *stopping time*, or sometimes also called *friction time*. It is defined as

$$\tau_{\mathrm{s}} = \frac{m_{\mathrm{d}} v_{\mathrm{gd}}}{|F_{\mathrm{f}}|} , \tag{2.14}$$

Epstein regime

where m_{d} is the mass of the dust particle and F_{f} is the friction force. According to Weidenschilling (1977b) the stopping time τ_{s} is the time in which v_{gd} is reduced by a factor of e by a constant friction force F_{f}. It can be interpreted as the time a particle needs to dissipate its kinetic energy of its relative motion to the gas (Kempf et al. 1999) or as the time the particle equilibrates with a gas moving at the relative velocity v_{gd}.
In the Epstein regime the stopping time τ_{s} is given by

$$\tau_{\mathrm{s,Ep}} = \frac{3}{4} \frac{m_{\mathrm{d}}}{\sigma_{\mathrm{d}}} \frac{1}{\rho_{\mathrm{g}} c_{\mathrm{s}}} , \tag{2.15}$$

Stokes regime

where $\sigma_{\mathrm{d}} = R_{\mathrm{d}}^2 \pi$ is the cross section of the dust particle and c_{s} the sound speed of the gas. Whereas in the Stokes regime

$$\tau_{\mathrm{s,St}} = \tau_{\mathrm{s,Ep}} \times \frac{4}{9} \frac{R_{\mathrm{d}}}{\lambda_{\mathrm{mfp}}} = \frac{3}{4} \frac{m_{\mathrm{d}}}{\sigma_{\mathrm{d}}} \frac{1}{\rho_{\mathrm{g}} c_{\mathrm{s}}} \times \frac{4}{9} \frac{R_{\mathrm{d}}}{\lambda_{\mathrm{mfp}}} , \tag{2.16}$$

as stated by Zsom et al. (2010). It should be noted that both quantities depend on the ratio of dust particle mass and cross section $m_{\mathrm{d}}/\sigma_{\mathrm{d}}$. This will be of major importance for dust coagulation.
So far, the motions of a dust particle have been characterised for laminar flow. For turbulent motions in the protoplanetary disc the turbulence parameter α has been introduced in Eq. (2.4). Now, turbulent eddies have a typical velocity v_{edd}. The parameterisation of this quantity is still under debate. Here, I follow Dullemond and Dominik (2004) who state

$$v_{\mathrm{edd}} = \alpha^q c_{\mathrm{s}} , \tag{2.17}$$

where q is a turbulence parameter with $0 < q < 1$. Dullemond and Dominik (2004) set $q = 1/2$.

With the typical largest eddy size $l_{\mathrm{edd}} = \alpha^{1-q} H$ the eddy turn over time $\tau_{\mathrm{edd}} \equiv l_{\mathrm{edd}}/v_{\mathrm{edd}} = \alpha^{1-2q}/\Omega_{\mathrm{K}}$ can be defined. Finally, the motion of dust particles in a turbulent environment can be characterised by the *Stokes number*

Stokes number

$$\mathrm{St} \equiv \frac{\tau_{\mathrm{s,Ep}}}{\tau_{\mathrm{edd}}} = \frac{3}{4}\frac{m_{\mathrm{d}}}{\sigma_{\mathrm{d}}}\frac{\Omega_{\mathrm{K}}}{\rho_{\mathrm{g}} c_{\mathrm{s}} \alpha^{1-2q}} \,. \tag{2.18}$$

It has to be noted that the choice of this quantity varies in the literature (e.g. Cuzzi and Weidenschilling 2006, Brauer et al. 2008a). However, again the coupling to turbulent eddies expressed by the Stokes number depends on the ratio of mass and cross section of the dust particle $m_{\mathrm{d}}/\sigma_{\mathrm{d}}$.
The interaction with gas has a great influence on the relative velocities of individual dust particles and aggregates. These lead to mutual collisions and their result, in turn, depends on threshold velocities for sticking, bouncing and fragmentation. These thresholds have to be determined experimentally in the laboratory or by molecular dynamics simulations, which, again, rely on measured microscopic properties. Thus, before I discuss how dust aggregate growth proceeds, I will shortly review the conditions for dust coagulation.

2.2.3. Conditions for dust coagulation

For the description of the conditions for dust coagulation, I distinguish three different cases: collisions of two individual grains (*particle-particle aggregation, PPA*), which is clearly the beginning of dust coagulation, collisions between a single particle and a dust agglomerate (*particle-cluster aggregation, PCA*), and collisions between two dust aggregates (*cluster-cluster aggregation, CCA*).
In the literature (e.g. Dominik et al. 2007, Paszun and Dominik 2009, Ormel et al. 2009) PCA and CCA also denote two limiting cases of aggregate growth: PCA describes the collision of a single grain with a large multi-monomer aggregate, whereas CCA denotes the collision of two almost equally sized multi-monomer aggregates. Sometimes aggregates themselves are characterised by the aggregation process (PCA, CCA) they were formed from.

PPA

For the sticking condition of PPA Poppe et al. (2000) performed collisions of dust grains with radii $R_{\mathrm{d}} = 0.07 - 0.6\,\mu\mathrm{m}$ and impact velocities of $v_{\mathrm{i}} = 0 - 100\,\mathrm{m/s}$ on smooth large targets. They found, that in most cases the sticking probability can be described by a *capture velocity* below which dust grains always stick and above which particles always bounce. This capture velocity is in the range of $v_{\mathrm{c}} = 1.2 - 2.5\,\mathrm{m/s}$. It is higher for irregular shaped grains and lower for spherical grains. Additionally, the capture velocity decreases with increasing grain size. Irregular sized grains even have a non-zero sticking probability for $v_{\mathrm{i}} > 10\,\mathrm{m/s}$. Dominik and Tielens (1997) theoretically derive a capture velocity of

capture velocity

$$v_{\mathrm{c,theo}} \propto \frac{\gamma^{5/6}}{(2R_{\mathrm{d}})^{5/6}\rho_0^{1/2}} \tag{2.19}$$

where γ is the surface energy of the dust grains and ρ_0 the bulk density of the dust material. Blum and Wurm (2000) show that this theoretical relation is in excellent agreement with results from experiments.

between PCA and CCA

In the following paragraph I will discuss growth conditions for aggregate-aggregate collisions in the regime between the limiting cases PCA and CCA. Dominik and Tielens (1997) showed that these collisions are best characterised by the (effective) impact energy (E_{eff}) of the collision, which is essentially the impact energy using the reduced mass of the collision partners, the energy necessary to break a monomer contact (E_break) and the energy necessary to roll a contact a quarter of a monomer's circumference (E_roll). The following recipe was confirmed and extended in 2D and 3D simulations by Paszun and Dominik (2006, 2009) and Wada et al. (2007, 2008).

fractal growth

For low impact energies ($E_\mathrm{eff} < 5E_\mathrm{roll}$), fractal aggregates (see section 2.2.4 for details) are formed by a simple hit-and-stick mechanism. In this regime, no restructuration of the chain-like aggregates takes place. Wurm and Blum (1998) and Blum and Wurm (2000) confirm these findings and find *fractal hit-and-stick growth* for $v_\mathrm{i} < 0.2\,\mathrm{m/s}$ with SiO_2 dust aggregates. The sticking efficiency was unity. Dominik and Tielens (1997) argue that rolling is the main reason for aggregate restructuring, twisting is probably important for small grains, and sliding can be neglected (for a description of these degrees of freedom see section 3.2).

compaction

For higher impact energies ($E_\mathrm{eff} > 5E_\mathrm{roll}$), the chain-like structures are more and more *compacted* such that the mass to cross section ratio $m_\mathrm{d}/\sigma_\mathrm{d}$ decreases (see also Fig. 2.4). The importance of this quantity for the dust aggregates' motion in the protoplanetary disc was discussed in section 2.2.2. Blum and Wurm (2000) find the onset of compaction for $v_\mathrm{i} \sim 0.7\,\mathrm{m/s}$. Maximum compaction is reached for $E_\mathrm{eff} \sim n_\mathrm{c} E_\mathrm{roll}$ (Dominik and Tielens 1997), where n_c is the number of contacts in the aggregate. However, Wada et al. (2007) find that the maximum compression depends on the ratio of rolling to breaking energy. They conclude that ice aggregates have a higher maximum compaction than SiO_2. Dominik and Tielens (1997) underline the fact that aggregate compaction provides an important energy sink for the collisional evolution in the protoplanetary disc.

catastrophic disruption

With ($E_\mathrm{eff} > 3n_\mathrm{c}E_\mathrm{break}$) or $v_\mathrm{i} \sim 1.2\,\mathrm{m/s}$ (Blum and Wurm 2000) the aggregates lose single monomers during collision and collisions with $E_\mathrm{eff} > 10n_\mathrm{c}E_\mathrm{break}$ ($v_\mathrm{i} \sim 1.9\,\mathrm{m/s}$) lead to *catastrophic disruption*. This represents the limit for aggregate-aggregate growth for SiO_2 dust aggregates. Wada et al. (2009) point out that this threshold velocity is raised to $\sim 50\,\mathrm{m/s}$ for ice aggregates.

So far, only head-on collisions have been considered. Simulations by Paszun and Dominik (2006) suggest that also rotation plays a role in aggregate-aggregate collisions. Wada et al. (2007) add the collision offset and Paszun and Dominik (2009) the compactness of aggregates to the list of parameters that might influence the collisional outcome. A systematic study of these parameters is far from being complete.

2.2.4. Dust coagulation in the disc

After the discussion of the general growth conditions of dust aggregates in collisions, these now have to be applied to the dynamics inside the protoplanetary disc. For collisions, some mechanism has to generate relative velocities between the individual dust aggregates. In the literature, four important mechanisms are mentioned: Brownian motion, differential settling, radial drift, and turbulence. These act all on dust aggregates at all times in the disc. However, it turns out that because of a strong dependence on surface and mass of the aggregates these mechanisms govern growth in distinct size regimes. For the subsequent discussion I will follow the review articles by Wurm (2003), Cuzzi and Weidenschilling (2006), Dominik et al. (2007), and Blum and Wurm (2008).

Brownian motion

At the beginning of the coagulation process there are only single dust grains or small aggregates consisting of a few monomers in the protoplanetary disc (Ormel et al. 2009). Because of their small mass, these particles have a very small stopping time τ_s (Eqns. 2.15 and 2.16), i.e. they

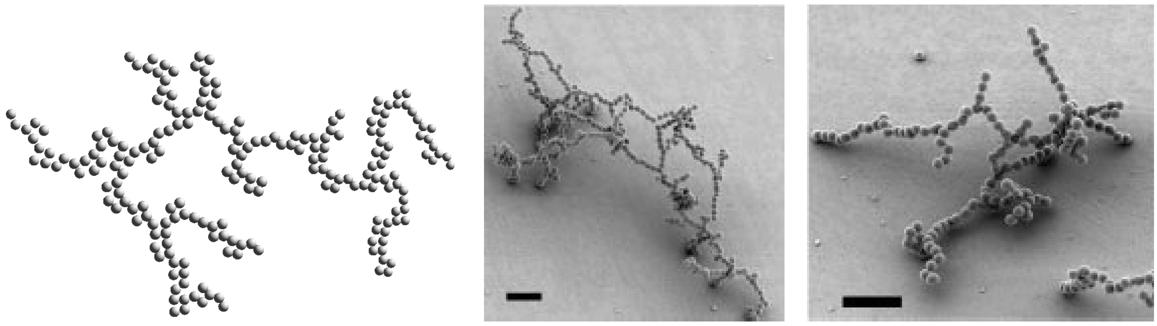

Figure 2.3. *Fractal aggregates.* Examples for fractal dust aggregates in molecular dynamics simulations (left, S. Carstens, unpublished data) and in coagulation experiments (middle and left, J. Blum, unpublished data, black bar represents 1 µm).

couple very well to the gas. Depending on the disc model (see section 2.1.3), for a 1 µm particle $\tau_s < 1$ s at 1 AU (Wurm 2003). The relative velocity induced by Brownian motion is given by

Brownian relative velocity

$$\Delta v_B = \sqrt{\frac{8kT(m_{d,1} + m_{d,2})}{\pi m_{d,1} m_{d,2}}}\,, \tag{2.20}$$

where k is the Boltzmann constant, T is the temperature of the gas, and $m_{d,1}$ and $m_{d,1}$ are the masses of the collision partners. Hence, typical collision velocities of micron-sized dust grains are of the order $v_B \sim 10\,\mathrm{mm/s}$. This is well below the capture velocity $v_c \sim 1\,\mathrm{m/s}$ from the previous section. Because Brownian motion provides the largest relative velocities in this size regime, collisions will always result in sticking. The mean collision time is about 10 yr.

For very small aggregates, the collision velocities are even below the threshold of restructuration. Therefore, aggregate growth first proceeds in a fractal way, producing chain like structures (see figure 2.3). In the case of solid spheres, the mass increases with radius in a cubic fashion ($m_d \propto R_d^3$) and the cross section depends on the radius quadratically ($\sigma_d \propto R_d^2$). In contrast, fractal growth is characterised by a *fractal dimension* D_f such that

fractal dimension

$$m_d \propto \sigma_d \propto R_d^{D_f}\,. \tag{2.21}$$

In general the fractal dimension for mass and cross section are not identical, but on empirical grounds Wurm (2003) argues that for $D_f \leq 2$ they can be set equal.The growth of fractal aggregates with $D_f \sim 1.4$ has been shown experimentally in microgravity experiments (Blum et al. 1998, Blum and Wurm 2000, Blum et al. 2002, Krause and Blum 2004). Deviations from results of MD simulations (Kempf et al. 1999) could be explained after the effect of Brownian rotation was taken into account (Blum et al. 2006a, Paszun and Dominik 2006). Even elaborate coagulation codes such as Ormel et al. (2007) can simulate fractal growth in protoplanetary disc environments.

Turbulent mixing

The role of turbulence in the growth process is still under debate. This is because the sources, their strength, and above all the contribution of local and global turbulence is unknown and is a field of ongoing research (see section 2.1.4 and references therein). Some dust coagulation models (Ormel et al. 2007, Brauer et al. 2008a, Zsom et al. 2010) assume global turbulence (generated, e.g. by MRI) and its interaction with dust by the formalism presented in section 2.2.2. Others (e.g. Weidenschilling 2010) assume a laminar protoplanetary disc or a dead zone and only model (local) shear induced turbulence around the midplane. Therefore, it is difficult to assess how turbulence influences dust growth. For example, Ormel et al. (2007) find that the second stage after Brownian motion is governed by turbulence. Due to the assumption of global turbulence also the dust growth in the upper layers of the disc is affected. If only local turbulence around the midplane is assumed, particles have to settle to the midplane before they can be affected by turbulence. As a consequence, differential settling becomes the intermediate growth step between Brownian motion and turbulent mixing. With these conceptional problems in mind, only a rough picture of dust coagulation by turbulence can be given.

In a simple explanation (Cuzzi and Weidenschilling 2006), the coupling of a dust aggregate is analogous to the response of an oscillator to periodic forces of different frequency. The oscillator, the analogue to the dust particle, responds well to forces varying more slowly than its natural response time. For dust particles, this is the stopping time τ_s. Therefore, dust aggregates are entrained in *turbulent eddies* with $\tau_\mathrm{edd} > \tau_\mathrm{s}$.

turbulent eddies

Relative velocities due to turbulent motions depend on many parameters such as the stopping times of the dust particles τ_s, the eddy turn over time τ_edd, the typical eddy velocity v_edd and the Kepler time $\tau_\mathrm{K} = {}^{2\pi}/_{\Omega_\mathrm{K}}$ (see also Sec. 2.2.2). The relative velocities were computed numerically by Völk et al. (1980) and Mizuno et al. (1988), analytical fit formulae were derived by Weidenschilling (1984) from their results. These formulae have been used by a number of coagulation codes (e.g. Dullemond and Dominik 2005, Ormel et al. 2007). Finally, Ormel and Cuzzi (2007) have presented new formulae which correct the behaviour for particles with large Stokes numbers, which were used by Brauer et al. (2008a). In a regime where the stopping times of two particles are small (i.e. small mass to cross section ratio) $\tau_\mathrm{s} < \tau_\mathrm{edd}$ and $\tau_\mathrm{s,1} \sim \tau_\mathrm{s,2}$, the relative velocity induced by turbulence is negligible. This is the reason why Brownian motion is still dominating the growth for dust grains and fractal dust aggregates. However, for a *dispersion* in stopping times $\tau_\mathrm{s,1} \neq \tau_\mathrm{s,2}$, i.e. a dispersion in ${}^{m_\mathrm{d}}/_{\sigma_\mathrm{d}}$ and $\tau_\mathrm{s,1,2} < \tau_\mathrm{edd}$, relative velocities will be increased because of turbulence. For $\tau_\mathrm{s} > \tau_\mathrm{edd}$, relative velocities no longer depend on $\tau_\mathrm{s,1} - \tau_\mathrm{s,2}$, but scale with $\sqrt{{}^{m_\mathrm{d}}/_{\sigma_\mathrm{d}}}$ of the largest collision partner. In this regime, turbulence creates relative velocities between equally sized collision partners, which would not collide because of differential settling or radial drift as discussed below. Ormel et al. (2007) find collision velocities of the order 0.1 m/s in the first regime and 10 m/s in the second regime.

stopping time dispersion

This means that for small particles growth can proceed, because relative velocities due to turbulence are still below the capture velocity v_c. The growth even proceeds in a fractal way because the restructuring limit is exceeded. However, for increasing aggregate sizes, compaction takes place and the mass to cross section ratio changes. This leads to a dispersion in stopping times, which again promotes collisions at higher velocities. These velocities may exceed the limit of catastrophic disruption, which produces small dust grains again, which can be swept up by larger aggregates. Turbulence growth can proceed up to centimetre sizes.

As a conclusion it can be said that turbulence acts as a background mechanism in the regimes of differential settling and radial drift, which increases collision velocities and collision rates, in particular between equally sized bodies. Turbulence is active on a large size scale roughly ranging from millimetre to metre until larger bodies fully decouple from the gas motions. Turbulence promotes growth for small aggregates, but for larger bodies it can also lead to catastrophic collisions.

Differential settling

In section 2.1.2 it was already mentioned that there is observational evidence for a vertical stratification of the disc and, hence, settling of larger dust aggregates to the midplane. The reason for settling is the vertical component of gravity acting on the dust, which is not supported by the gas pressure (Dominik et al. 2007). In the literature, various expressions with differing complexity can be found for the description of dust settling. Wurm (2003) simply states

dust settling velocities

$$v_{\mathrm{sett}} = g_z \tau_{\mathrm{s}} \tag{2.22}$$

where g_z is the vertical component of gravitational acceleration in a laminar disc. Brauer et al. (2008a) assume that the settling velocity cannot exceed the vertically projected Kepler velocity. Additionally, via the Stokes number (Eq. 2.18) they take turbulent effects into account and derive

$$v_{\mathrm{sett}} = \frac{z \mathrm{St} \Omega_{\mathrm{K}}}{1 + \mathrm{St}} \tag{2.23}$$

where z is the height of the dust particle above the midplane. From these expressions it becomes clear, why the settling motion is *differential.* Small particles with small τ_{s} or St, respectively, settle slower than large particles. As a consequence, the disc becomes vertically stratified with small particles remaining in the upper layers and larger particles which accumulate near the midplane. Wurm (2003) estimates that for single dust grains ($R_{\mathrm{d}} \sim 1\,\mu\mathrm{m}$) $v_{\mathrm{sett}} \sim 10^{-3}\,\mathrm{m/s}$ and settling to the midplane would take $\sim 10^{6}$ yr which is in the order of the lifetime of the disk. Therefore, Brownian motion and turbulence have to grow aggregates with larger τ_{s}. However, during the first growth phases collision velocities hardly exceed the restructuring limit ($\sim 0.2\,\mathrm{m/s}$, see section 2.2.3). In this velocity regime fractal growth with $D_{\mathrm{f}} < 2$ dominates and, thus, mass and cross section depend on the dust radius R_{d} with the same fractal dimension D_{f} (Eq. 2.21). Therefore, $\tau_{\mathrm{s}}(m_{\mathrm{d}}/\sigma_{\mathrm{d}})$ and also $\mathrm{St}(m_{\mathrm{d}}/\sigma_{\mathrm{d}})$ hardly change in this regime (Wurm 2003). Consequently, aggregates with $D_{\mathrm{f}} < 2$ settle almost as slowly as the initial dust grain population.

differential settling

Nevertheless, there are small differences in the distribution of the fractal dimension, which are about 10 % (Kempf et al. 1999). This leads to a dispersion in τ_{s} and St. Wurm (2003) estimates that for 100 μm particles relative velocities due to differences in v_{sett} will exceed velocity differences caused by Brownian motion. Thus, differential settling is the most important source for collisions of sub-millimetre aggregates (at least in a laminar disc or a dead zone). Growth will proceed in a fractal way until the aggregates have reached some centimetres in size and settle to the midplane with speeds comparable to those of the initial dust grains. Small relative velocities below v_{c} ensure continuous growth. It has to be noted, however, that with increasing aggregate mass the impact energy also increases, although collision velocities remain rather constant. Larger aggregates get more and more compacted and their mass to cross section ratio increases (see figure 2.4).

compaction

Finally, at centimetre sizes, collision velocities due to settling get larger and larger and growth is no longer fractal. Now, the dust aggregates grow like spheres, where $m_{\mathrm{d}} \propto R_{\mathrm{d}}^3$ and $\sigma_{\mathrm{d}} \propto R_{\mathrm{d}}^2$. Hence, stopping times are increasing with $\tau_{\mathrm{s}} \propto R_{\mathrm{d}}$ and collisions between small dust grains and large aggregates are more frequent. Collision velocities reach a few m/s (Dominik et al. 2007) and small dust grains are simply swept up by the rapidly growing aggregates. The more these large aggregates grow, the faster they can collect smaller ones. This inevitably leads to a runaway process, which is known as *rain-out* of dust particles because of its similarity with the formation

rain-out

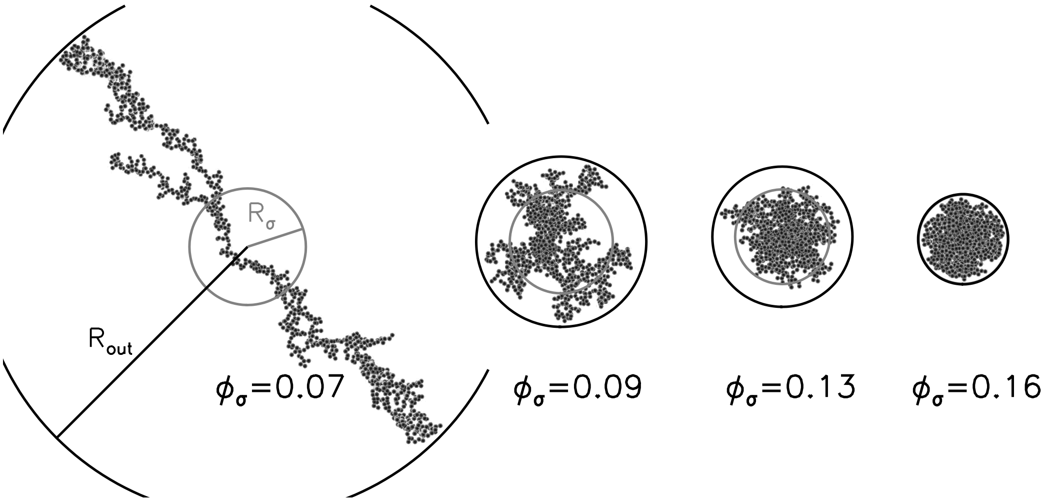

Figure 2.4. *Aggregate compaction.* Each agglomerate consists of 1,000 monomers. The geometrical filling factor ϕ_σ is a measure for the compactness of the object, R_σ is the projected surface equivalent radius, whereas R_{out} is the outer radius of the aggregate. Collisions above the restructuring limit lead to an increasing compaction (from left to right) of the aggregate. This increases the mass to cross section ratio $m_\text{d}/\sigma_\text{d}$ and, hereby, stopping time τ_s and Stokes number St (figure from Paszun and Dominik 2009).

of rain drops in clouds. It has been investigated with the aid of more and more sophisticated coagulation simulations (e.g. Weidenschilling 1980, 1984, 2000, Dullemond and Dominik 2005, Ormel et al. 2007). Particularly Ormel et al. (2007) emphasise that the porous, i.e. fractal, nature of the dust aggregates in the initial growth stages must not be neglected. They find (with respect to their MMSN disc model) that compact grains, which grow as spheres, rain out with masses of 10^{-4} g while porous grains reach the midplane with 1 g. For spherical compact particles this is equivalent to a factor ~ 20 in size, for porous aggregates even larger. Dust settling happens extremely fast. It takes ~ 10^3 yr in the inner regions and ~ 10^4 yr in the outer regions of the protoplanetary disc. The important mechanism here is the sweeping of small dust grains and aggregates by larger ones. Blum and Wurm (2008) find in laboratory experiments that collisions of two millimetre sized particles never lead to sticking, but rather bouncing at low collision energies or fragmentation at high collision energies. They favour growth by a large aggregate collecting smaller aggregates and dust grains for the build-up of centimetre sized objects and larger. However, this will be subject to closer investigation within this thesis.

As a summary it can be said that dust settling is (maybe together with the uncertain impact of turbulent mixing) the dominant growth mechanism for aggregate sizes between the sub-millimetre and centimetre regime. Initially the process is slow because of the fractal nature of growth, the rather small dispersion of stopping times, and the resulting small differences in relative velocities. But the more the aggregates get compacted and the more the mass to cross section ratio increases, the faster the aggregates settle to the midplane increasing collision rates with smaller grains and aggregates, which they sweep up. Eventually, they rain out in a runaway growth process which is halted once they settle around the midplane.

Radial drift

The larger the particles get, the more their stopping time increases, i.e. the more they decouple from the surrounding gas, and accelerate to nearly Keplerian velocity because they lack the pressure support from the gas. The gas, however, is rotating at sub-Keplerian speed (as discussed in section 2.1.4, in particular Eq. 2.11). Hence, the particles feel a *headwind* (Whipple 1972, Weidenschilling 1977b), which saps their angular momentum. As a consequence, the orbits of the dust aggregates decay and they drift radially inwards. Additionally, the gas itself flows inwards because it is being accreted by the star. Hence, the inward drift velocity given by (e.g. Brauer et al. 2008a)

headwind

$$v_{\mathrm{drift}} = -\frac{c_{\mathrm{s}}^2\,(\delta + 7/4)}{V_{\mathrm{K}}\,(\mathrm{St} + 1/\mathrm{St})} - \frac{3\alpha c_{\mathrm{s}}^2\,(3/2 - \delta)}{V_{\mathrm{K}}\left(1 + \mathrm{St}^2\right)}\,, \tag{2.24}$$

where c_{s} is the sound speed of the gas, δ the exponent of the gas surface density profile (Eqns. 2.8, 2.9, and 2.10), V_{K} the Keplerian velocity, and α the turbulence parameter (Eq. 2.4). The first term accounts for the head wind and the second term for gas accretion. Just like in the case of differential settling, relative velocities are generated by a dispersion of St or τ_{s}, equivalently. Again, dust aggregates of similar size have almost vanishing relative velocities due to radial drift. However, drift velocities reach a few m/s for centimetre sized particles (Cuzzi and Weidenschilling 2006) and growth can proceed as for differential settling. Drift velocities reach their maximum for St = 1. In the MMSN model this is equivalent to metre sized objects, which drift into the host star within 100 yr. Hence, they are lost very quickly for planet formation. This problem is known as *metre size barrier* and will be addressed in section 2.3.

metre size barrier

Conclusion

From the observational, experimental, and theoretical point of view it is clear that dust agglomeration takes place in protoplanetary discs. An initial micrometre sized dust grain population can grow up to centimetre sizes by mutual collisions and sticking due to van der Waals forces (SiO_2) or static electric dipoles (water ice). Relative velocities are first generated by Brownian motion, then, as aggregates grow and increase their mass to cross section ratio, relative velocities are generated by velocity differences in turbulent mixing, differential settling, and radial drift. Because of their porous structure, they stay in the outer layers of the disc for a long time, but eventually they settle to the midplane. The growth mechanisms beyond centimetre size, however, are far from being clear. Collision velocities increase and fragmentation becomes more and more frequent. Additionally, they exceed the escape velocity unless objects have grown roughly to kilometre size. As a consequence, fragments cannot be bound gravitationally as a rubble pile and net growth cannot be achieved. Radial drift velocities also increase and a considerable amount of material is probably lost into the star or is photo-evaporated in regions close to the star. These and other problems and possible solutions for the next phase of planet formation will be presented in the next section.

2.3. Collision or Collapse? - Growing Planetesimals

planetesimals
pre-planetesimals
core accretion
gravitational instability

This section is dedicated to an intermediate growth step, which has to bridge a size regime from centimetre sized pebbles to kilometre sized *planetesimals*. This is also the thematic location of the thesis at hand. I will call the objects of this intermediate size regime *pre-planetesimals*. The dominant growth mechanism of the first regime is characterised by mutual collisions and sticking by dipole-dipole interaction. In the planetesimal regime gravitational forces become dominant and typical collision velocities are below the escape velocity of the planetesimal. This growth step will be discussed in section 2.4. However, it is a matter of a ongoing and lively debate how pre-planetesimals grow to planetesimals. In the literature, two main ways of planetesimal formation have been proposed so far: the *coagulation* or *core accretion scenario* and the *gravitational instability scenario*. The first one is a direct continuation of the hit-and-stick mechanism of the first growth step. As an alternative, the gravitational instability hypothesis assumes that regions of the protoplanetary disc become unstable enough to collapse into planetesimals or even larger objects under their self-gravity. Both scenarios have appealing aspects as well as drawbacks. Therefore, in recent years there have been many attempts to refine and even combine both theories. This section will give a brief overview of both paths to planetesimals.

2.3.1. The coagulation scenario

fragmentation barrier
drift barrier
bouncing barrier

In its most basic version, the coagulation scenario assumes that planetesimals form by a continuous hit-and-stick mechanism from micrometre to kilometre sizes. Indeed, if coagulation models assume a sticking probability of unity (perfect sticking assumption) then growth proceeds quickly to planetesimals (see, e.g. Dullemond and Dominik 2005). As we have already seen in section 2.2.3, this is highly unrealistic, even for small aggregates and impact velocities of a few m/s. For objects of a few metres to some hundred metres relative collision velocities reach some tens of m/s depending on the disc model (see, e.g. Weidenschilling and Cuzzi 1993, Brauer et al. 2008a). Turbulence increases collision velocities even more for metre sized bodies (Cuzzi and Weidenschilling 2006). The most serious obstacle to the coagulation scenario therefore is a *fragmentation barrier* (Zsom et al. 2010). The fragmentation condition mainly depends on two quantities: the material properties of the colliding objects, in particular the material strength, and the collision velocities. Consequently, opponents of the coagulation hypothesis argue that impact velocities are too high and pre-planetesimals are too weak, while supporters try to find mechanisms to reduce collision velocities and argue for material properties that promote sticking. As a second obstacle, objects of metre size have the highest drift velocities towards the star, and are therefore endangered to be lost quickly for the planetesimal formation process (*drift barrier*). Recently, Zsom et al. (2010) included the effect of restitution (bouncing) in their coagulation simulations, which lead to the discovery of a possible *bouncing barrier* at centimetre sizes. All of these barriers emerge roughly around the metre size. Therefore, they are often subsumed as the *metre size barrier* in the literature. In the following, I will shortly describe these obstacles and solutions for them, if available.

Fragmentation barrier

rock-like brittle material

Youdin and Shu (2002) and Youdin (2004) suggest that pre-planetesimals in the early solar system were like rocks. In their pioneering work, Benz and Asphaug (1994, 1995) developed a smooth particle hydrodynamics (SPH) code for the simulation of *rock-like brittle material*. With their code they performed high (some km/s, Benz and Asphaug 1999) and low velocity collisions (5 – 40 ms, Benz 2000) of rocky pre-planetesimals and planetesimals (sizes of 1 m to 10 km). The results of Benz (2000) are of particular interest in this context. He finds, that collisions at low velocity are even more disruptive than at high velocity and in all cases the largest remnants were smaller than the large target. Thus, no net growth occurred in these collisions. For bodies of 1 m – 1 km, critical destruction velocities range from 3.2 mm/s (!) to 3.2 m/s with increasing size. Evidently, rock-like pre-planetesimals are very easy to disrupt and growth by mutual collisions is impossible, since collision velocities always exceed the disruption threshold.

porous structure

Simply assuming an increased material strength does not provide a way out of this issue for two reasons. Material with increased strength is unlikely to be analogous to protoplanetary dust material and even if it was, this does not mean that two collision partners stick to each other. As a consequence, either collision velocities have to be lower or an efficient way of dissipating energy has to be found. Weidenschilling (1977b) already conjectured that if the internal structure of pre-planetesimals was somewhat porous, smaller particles could be embedded in larger particles by collision. Here, the *porous structure* provides an efficient energy dissipation mechanism. Indeed, as we have seen in section 2.2 the objects formed in the first step of the coagulation process are very likely to be porous. Blum and Schräpler (2004) and Blum et al. (2006b) have generated highly porous decimetre sized aggregates by a random ballistic deposition (RBD) process with their dust analogous (SiO_2). They measured the aggregates' material strengths, which mainly depend on the filling factor, the ratio of filled volume to total volume (discussed in detail in 4.3.4). Sirono (2004) has shown in simulations of porous ice aggregates that, if the compressive strength (see also section 4.3.4) is smaller than the other strength components (shear strength and tensile strength), collisional growth is possible. Also Ormel et al. (2007) has stressed the key importance of porosity for the formation of pre-planetesimals. Such objects can be generated by a hit-and-stick mechanism below the restructuring limit (Blum and Wurm 2008). Langkowski et al. (2008) show, that for collisions between millimetre sized projectiles and centimetre sized highly porous targets at velocities below 3 m/s, the projectile almost always sticks to the target by partial or full incorporation.

high porosity
fragility

Compressing *highly porous* dust aggregates is an efficient energy dissipation mechanism, but it comes with a drawback, which is pointed out by Youdin (2004): they are very *fragile*. This has been shown by Wurm et al. (2005b). In this reference impacts between dusty small (mm) projectiles and porous dusty targets (cm) at several tens of m/s never lead to sticking but to cratering and ejection of fragments of more than the projectile's mass. Collisions with these velocities are realistic and frequent for similar sizes in the protoplanetary disc. Even if they were rare events, a single catastrophic disruption is sufficient to destroy the whole pre-planetesimal (Benz 2000).

compaction

As a second drawback, porous aggregates get *compacted* in non-catastrophic collisions. Compact aggregates have a higher compressive and tensile strength, which makes them more robust, but at the same time their ability to absorb kinetic energy decreases. Weidling et al. (2009) observed that highly porous aggregates can get compacted to higher filling factors in collisions with ~ 0.2 m/s. Blum and Münch (1993) found that compact aggregates never stick for collision velocities above 4 m/s but instead they fragment (Wurm and Blum 2000). As a consequence of these findings, highly porous aggregates either fragment in high velocity collisions, or they get compacted in low velocity collisions and, hence, lose their ability to absorb kinetic energy, and then fragment in intermediate velocity collisions, or bounce in low velocity collisions. In any case, no sticking and net growth is observed.

intermediate porosity

partial sticking

re-accretion by aerodynamical effects

grinding growth model

Pre-planetesimal growth does not necessarily start with highly porous dust aggregates but with objects of *intermediate porosity*. Teiser and Wurm (2009b) have shown that compact decimetre sized objects can form by accumulation of 100 µm sized dust projectiles well above the restructuring limit (~ 7.7 m/s). Collisions between compact millimetre projectiles and compact centimetre to decimetre targets at very large impact velocities (a few tens of m/s) do not always lead to fragmentation, but to *partial sticking* of the projectile (Wurm et al. 2005b, Paraskov et al. 2007, Teiser and Wurm 2009a). In these experiments the total mass of the ejected fragments was even smaller than the projectile mass and, hence, high velocity collisions can lead to net growth. Wurm et al. (2001a,b) and Wurm et al. (2004) suggest that even the fragments are not lost for planetesimal growth but can be *re-accreted by aerodynamical effects*: in the primary impact a large amount of energy is dissipated by compaction and friction. Hence, fragments ejected from the surface of an aggregate in a primary collision possess a low ejection velocity (Wurm et al. 2005b, Paraskov et al. 2007). Because of gas flows around and through the porous aggregate the small ejecta are forced back onto the aggregate's surface and stick in a secondary collision. Based on this idea Teiser and Wurm (2009a) suggest the following *grinding growth model* (see figure 2.5): the onset of planetesimal growth is fractal as described in section 2.2.4 and produces centimetre to decimetre sized bodies which get compacted. Collisions between these objects are destructive and provide a reservoir for millimetre sized objects. When millimetre sized projectiles collide with centimetre sized targets there will be a lot of rebound and erosion with few or no net growth in the primary collision. In the secondary collision, the sub-millimetre ejecta can be re-accreted and planetesimals of kilometre size can form.

grain removal from midplane

However, recent findings indicate that collisions between single grains and large targets may be erosive at high velocities (Blum and Wurm 2008). A much stronger counterargument comes from the dynamics in a turbulent protoplanetary disc: centimetre sized dust aggregates have already settled to the midplane of the disc. There, catastrophic disruptions between them account for the grinding process that provides sub-millimetre particles, which can be re-accreted. Johansen et al. (2008) show that the time scales for turbulent diffusion of these small particles are much shorter than collision time scales. Hence, ejecta are *removed* from the midplane very efficiently, which hinders re-accretion. It has to be mentioned, however, that Johansen et al. (2008) neglect aerodynamically enhanced sticking as suggested by Wurm et al. (2001a,b) and Wurm et al. (2004).

Nevertheless, this example shows that results from laboratory experiments have to be joined with protoplanetary disc models and dynamics. Of course it is impossible for dust coagulation models to simulate the collisional physics for each collision taking place in the disc in full detail. Therefore, thresholds for sticking, bouncing, and fragmentation as well as fragmentation statistics have to be provided from laboratory experiments. Where laboratory experiments no longer suffice, data from computer simulations of collisions have to bridge the gap. The thesis at hand contributes to this approach.

fragmentation threshold

Mostly, coagulation simulations simply assume a *fragmentation threshold* of 1 m/s (Blum and Münch 1993) for disruptive events and neglect its dependence on porosity or size of the aggre-

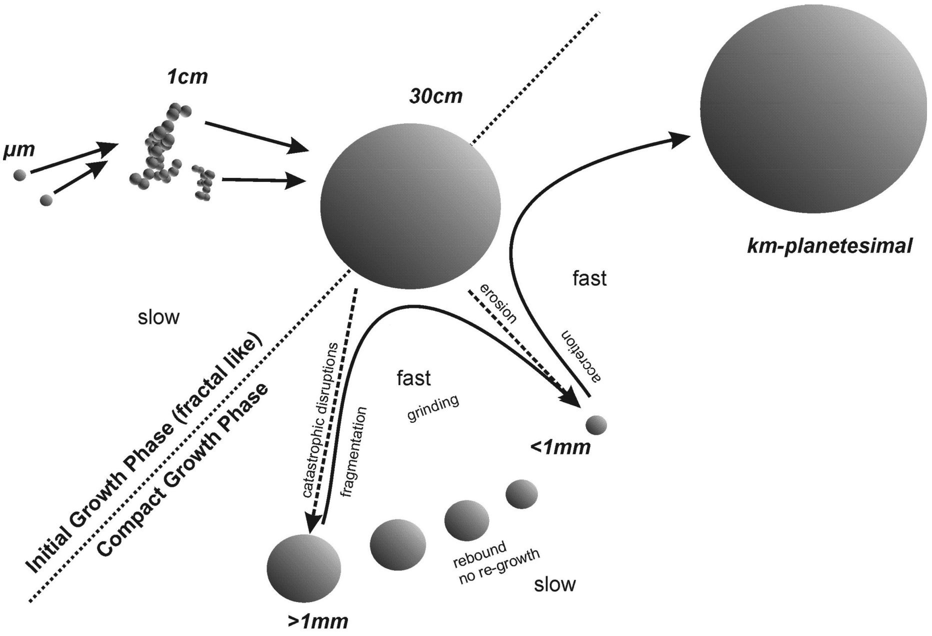

Figure 2.5. *Grinding growth model.* The beginning of dust growth is fractal. Centimetre sized pebbles are either compacted in bouncing collisions, ground down to dust grains again, or they accrete debris grains and, hereby, grow to planetesimals (figure from Teiser and Wurm 2009a).

gates. The resulting *fragment distribution* of these collision is then described as a power law

fragment distribution

$$n(m)\mathrm{d}m \propto m^{-\xi}\mathrm{d}m \tag{2.25}$$

where $n(m)$ is the number of particles per unit volume within the mass range $[m, m+\mathrm{d}m]$. ξ is the fragmentation parameter which has been determined experimentally and ranges between 1.3 and 2 (Mathis et al. 1977, Davis and Ryan 1990, Blum and Münch 1993, Güttler et al. 2010). With these assumptions, Brauer et al. (2008a) find that, depending on the disc model, dust coagulation is halted at centimetre or even millimetre size. Only if an unrealistic fragmentation threshold of 30 m/s is assumed particles start to break through the fragmentation barrier and grow to planetesimals. Also a very sophisticated sticking, bouncing, and fragmentation model by Güttler et al. (2010) and Zsom et al. (2010) comes to the conclusion that planetesimal formation is halted at centimetre sizes. By means of numerical aggregate collision simulations, it is one of the main purposes of this thesis to provide sticking, bouncing, and fragmentation thresholds and fragment distributions which are not accessible to laboratory experiments.

An attempt, to raise the fragmentation threshold to this value is to assume that planetesimals formed from ices or ice-dust mixtures. Wada et al. (2009) find in molecular dynamics simulations that ice has a disruption threshold velocity of 50 m/s. On the other hand, experiments by Supulver et al. (1997) indicate that ice is not much stickier than dust aggregates. In any case, this mechanism is only applicable for the outer regions of the protoplanetary disc, where it is sufficiently cold for water to freeze out.

Recently, Weidenschilling (2010) has argued against the high collision velocities in laminar discs *collective effects*

or dead zones: as already outlined in section 2.1.4 the settling of dust aggregates to the disc's midplane enhances the concentration of solids there. As a consequence, gas in the midplane is dragged to Kepler velocity and turbulence is generated between the midplane and the slower rotating adjacent layers above and below. *Collective effects* due to this turbulence now increase relative velocities between small particles and decrease them for larger particles. Hence, collisions are less disruptive and larger particles can break through the fragmentation barrier.

sticking mechanism

Despite of all these attempts to make planetesimal formation by coagulation possible, I will close the section with the fact noted by supporters (Weidenschilling 2000) and opponents (Youdin 2004) of the coagulation theory: the *sticking mechanism* for macroscopic bodies is still unclear.

Drift barrier

headwind

drift velocities

The drift barrier is one of the oldest arguments against planetesimal formation by coagulation. It was discovered by Weidenschilling (1977b). As already explained in section 2.2.4, the larger the dust aggregates become, the more they tend to orbit with Keplerian velocity because they lack the pressure support of the gas. Hence, they feel a *headwind* from the gas which orbits at sub-Keplerian speed. As a consequence, they loose angular momentum and drift radially inwards. As indicated by Eq. 2.24 this drift velocity depends on the disc model and the Stokes number St (Eq. 2.18). The latter again depends on the mass to cross section ratio $m_\mathrm{d}/\sigma_\mathrm{d}$ of the particle and on the gas density ρ_g and, thus, on the location in the disc. Typical drift velocities for variations of the MMSN model are displayed in figure 2.6. Evidently, *drift velocities* for the MMSN model are the highest ($\sim 10-100\,\mathrm{m/s}$) for bodies of roughly metre size. In general, radial drift reaches its maximum for particles with $\mathrm{St}=1$. As a matter of fact, metre sized bodies drift into the star from 1 AU in about 100 yr. In contrast millimetre and kilometre sized objects have drift times of $\sim 10^5$ yr. This is because small objects couple well to the gas and follow its motions and big objects sufficiently decouple from the gas and are only weakly perturbed by the headwind. The radial drift velocity reaches its peak in the transition between these regimes. This short drift time scale puts a hard constraint on the time of planetesimal formation. Metre sized objects originating at 1 AU must grow to kilometre size within a century to escape accretion (or photo-evaporation) by the host star.

collective effects

Several ways have been proposed to circumvent or, at least, diminish the problems caused by the radial drift barrier. *Collective effects* in the midplane of non-turbulent discs or dead zones in turbulent discs, which already helped to reduce collision velocities, may be a possible solution. If the particle density in the midplane becomes sufficiently high, the gas is dragged towards Kepler velocity and the effect of the headwind felt by metre sized bodies is alleviated. Consequently, inward drift is slowed considerably (e.g. Cuzzi et al. 1993, Dominik et al. 2007, Weidenschilling 2010).

local pressure maxima

However, in sufficiently turbulent discs small particles may be stirred up from the midplane, decreasing dust density there, which in turn decreases the collective effect of gas dragging and increases the headwind. In this case, dust and also metre sized boulders are efficiently trapped in *local pressure maxima* (Whipple 1972). The reason for this can be seen from Eq. 2.11: the headwind is essentially caused by the fact that the pressure supported gas rotates at a sub-Keplerian velocity and pressure support comes from an outward pressure gradient $\partial p_\mathrm{g}/\partial r < 0$. If locally $\partial p_\mathrm{g}/\partial r = 0$ on a long timescale, then the gas rotates at Kepler velocity and particles feel no head wind. Furthermore, if this is a pressure maximum particles will accumulate in this region. This is because particles move away from local pressure minima and accumulate at local pressure max-

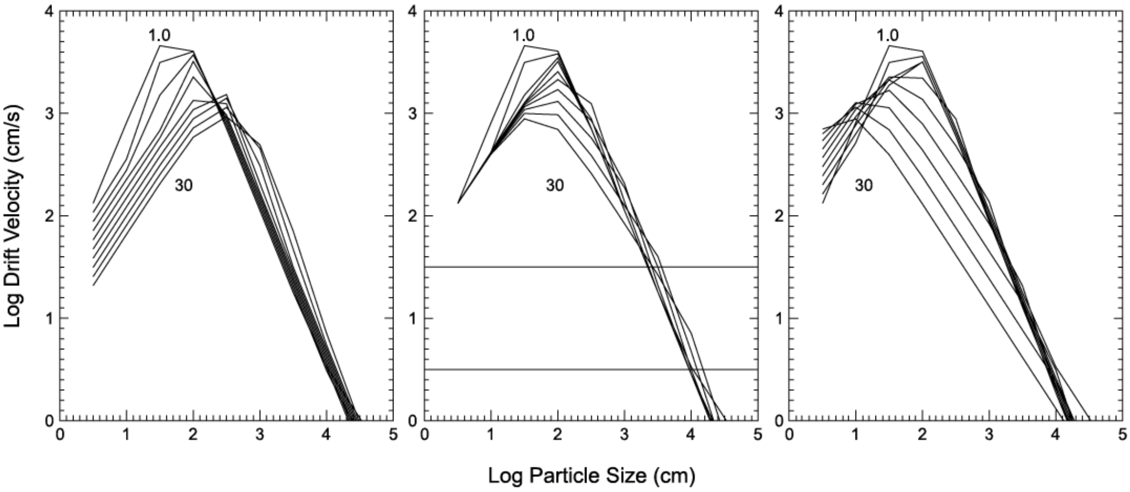

Figure 2.6. *Radial drift velocities.* Drift velocities are plotted as functions of particle radius for the MMSN (Eq. 2.9 with $\delta = -0.5$ (left), -1.0 (middle), and -1.5 (right). The curves are labelled according to the location in the disc 1 – 30 AU (figure from Cuzzi and Weidenschilling 2006).

ima. The reason is the following: for $r > 0$ let $\partial p_{\mathrm{g}}/\partial|_{r_0} r = 0$ and r_0 a local maximum. Then for $\Delta r > 0$: $\partial p_{\mathrm{g}}/\partial|_{r_0-\Delta r} r > 0$ and consequently according to Eq. 2.11 the gas rotates locally at super-Keplerian velocity. Hence, the particles feel a tailwind which drags them outwards, towards the maximum. On the other hand, $\partial p_{\mathrm{g}}/\partial|_{r_0+\Delta r} r < 0$ and the gas rotates locally at a sub-Keplerian velocity. Thus, the particles feel a headwind, which drags them inwards, again back to the maximum. For local pressure minima the contrary takes place. Possible reasons for local pressure maxima (sometimes called pressure bumps) are, e.g. sublimation processes near the snow line (Kretke and Lin 2007, Brauer et al. 2008b), gaseous spiral arms (Rice et al. 2004), or MRI generated turbulence (Johansen et al. 2006b).

Bouncing barrier

The so-called bouncing barrier was introduced recently based on global coagulation simulations by Zsom et al. (2010). For this approach, Güttler et al. (2010) have compiled and categorised all available experimental data for dust aggregate collisions into several types of sticking, fragmentation, and also bouncing. The data for bouncing rely on studies by Blum and Münch (1993), Heißelmann et al. (2007), Langkowski et al. (2008), Weidling et al. (2009), Güttler et al. (2010). Zsom et al. (2010) implemented these findings into their coagulation code, distinguishing between small and large, porous and compact dust aggregates and simulated dust coagulation for the three model discs presented in section 2.1.3. For the *low density model* (Eq. 2.8) they found that within the first 300 yr aggregates grow by the hit-and-stick mechanism through van der Waals forces (see section 2.2.4). In a second phase growth is halted by bouncing collisions in which the dust aggregates mainly get compacted. No sticking or fragmentation occurs in this phase. In the *MMSN model* the onset of dust growth is the same, but in the second phase some mass transfer in bouncing collisions and some sticking occurs. In the *high density model* the first phase is again dominated by hit-and-stick collisions, but it lasts only 200 yr. Then bouncing with mass transfer dominates and halts dust growth at aggregate masses of 1 g. It is remarkable that fragmentation never occurs for all disc models. So far, no counterarguments or ways around the bouncing barrier have been found. This issue will be addressed in the thesis at hand.

The grain retention and late pebble problems

grain retention problem

The aforementioned barriers stress the problem that planetesimal formation may be halted at a certain size limit. The *grain retention problem* deals with the issue that planetesimal formation might be too efficient. It was already mentioned earlier (section 2.1.2, see also Natta et al. 2007) that (sub-)micron sized dust is present in the outer layers of the disc for a very long time (10^6 yr or even longer). With their coagulation code, Dullemond and Dominik (2005) computed the dust distribution for various disc ages at every location in the disc using all basic dust coagulation mechanisms, excluding fragmentation. Subsequently, they fed the acquired data into a continuum radiative transfer code and calculated the resulting spectral energy distributions (SED, see Sec. 2.1.2). Finally, these were compared with observational data from T Tauri discs. As a result, they found that the process of planetesimal formation is too quick to mach the observational data. Without fragmentation, the outer regions of the disc are depleted of small grains within 10^3 yr. Dullemond and Dominik (2005) suppose that this inconsistency could be resolved, when collisions in the disc midplane do not result in perfect sticking only but (sub-)millimetre dust is generated continuously by (at least partially) destructive collisions of larger bodies. The small dust aggregates are then transported back to the upper layers of the disc by turbulent diffusion. However, small dust grains are also swept up by larger bodies (see Teiser and Wurm 2009a and figure 2.5) and, therefore, removed again from the disc. Consequently, the processes of grain retention by fragmentation (or photo-evaporation and re-condensation, see Ormel et al. 2007) and grain depletion by planetesimal growth have to reach a stable equilibrium for 10^6 yr. Ormel et al. (2007) found that in the case of porous particles, the problem is even more severe, since coagulation and, consequently, grain removal is accelerated because of the increased geometrical cross section of porous aggregates. To reproduce the SED of T Tauri discs, in all cases the protoplanetary disc has to be nearly laminar ($\alpha \sim 10^{-6}$) which contradicts the observed accretion rates onto the host star and the resulting dynamic turbulent viscosity (see section 2.4). As a follow-up on the work of Dullemond and Dominik (2005), Birnstiel et al. (2009, 2010) simulated the coagulation in protoplanetary discs with different fragmentation properties and tried to constrain the required parameters that allow for a suitable growth-fragmentation steady state. They found, that low values for the fragmentation parameter ξ (see Eq. 2.25) and fragmentation threshold velocities of some m/s reproduce the T Tauri SED observations. Zsom et al. (2010) suggest that dust production in partially destructive bouncing collisions could also provide a reservoir for dust grains. To conclude this issue, it has to be stressed that fragmentation does not only endanger planetesimal formation. A suitable amount of fragmentation even seems to be required to explain the appearance of disc observations. Therefore, a detailed investigation of dust production in sticking, bouncing, and completely disruptive collisions between porous dust aggregates is crucial for understanding a planet formation process which is consistent with the observations. This is one of the issues which are a central topic of this thesis.

late pebble problem

The *late pebble problem* is closely related to the grain retention problem. It was investigated by Brauer et al. (2007) and refers to the observational result (e.g. Natta et al. 2007) that not only (sub-)millimetre sized dust but also centimetre sized pebbles are present in the outer regions of the disc. These objects are estimated to drift inwards in time scales of 10^5 yr. In contrast, observations suggest that they are present over $5-10\times10^6$ yr in the outer disc. Brauer et al. (2007) found that this can only be explained for very high and very low disc masses. The remaining time of pebbles in outer regions is also augmented by high porosities. Collective effects like dragging the gas to nearly Keplerian speed in the midplane slow down the drift rates but are not sufficient to resolve this problem. Low turbulence values ($\alpha \sim 10^{-6}$) also reduce the drift rate considerably. Therefore, dead zones could provide a way out of this issue.

Other barriers and loopholes

Barge and Sommeria (1995), Klahr and Henning (1997), and Klahr and Bodenheimer (2006) suggested that *particle trapping in vortices* could enhance growth rates of pre-planetesimals, such that they could grow their way through the metre size barrier more quickly before they are lost into the host star. These vortices are large, slow, two-dimensional circulation patterns with turnover times similar to the orbital period. They are able to capture metre sized bodies near their centre. Note that they have to be distinguished from turbulent eddies originating from homogeneous, isotropic, three-dimensional turbulence (Cuzzi et al. 2001). However, it is unclear wether these eddies live long enough to capture pre-planetesimals until they have grown to planetesimals.

particle trapping in vortices

Youdin and Shu (2002) bring forward a counterargument from investigating meteorites. They argue, that if the coagulation hypothesis was true, particles of a size range spanning from micron sizes to metre sizes should be found in the most primitive meteorites. Instead, the maximum sizes found do not exceed centimetre sizes. Youdin and Shu (2002) conclude, that the solar system failed to generate pre-planetesimals larger then centimetre size. Therefore, they propose a growth mechanism that quickly and directly generates planetesimals from pebbles: the gravitational instability scenario.

2.3.2. The gravitational instability scenario

The gravitational instability (GI) scenario is older than the coagulation scenario. It was proposed independently by Safronov (1969) and Goldreich and Ward (1973). They hypothesise that planetesimals or even small planets have formed by a gravitational instability. The process is a miniature version of the star formation process presented in section 2.1.1. After dust aggregates have settled to the midplane (see section 2.2.4) this particle layer becomes dense enough to collapse under its own gravitational attraction. As a quantitative criterion the *Toomre parameter* Q_d has to fulfil

Toomre parameter

$$Q_\mathrm{d} = \frac{\Omega_\mathrm{K}\bar{v}_\mathrm{d}}{\pi G \Sigma_\mathrm{d}} < 1 \tag{2.26}$$

(Toomre 1964), where Σ_d and $\bar{v}_\mathrm{d}$ denote the surface density and velocity dispersion of the dust aggregates, respectively. Equivalently, Sekiya (1998) proposed particularly for stratified fluids that the density in the midplane $\rho_\mathrm{c} = \rho_\mathrm{g} + \rho_\mathrm{p}$ of a protoplanetary disc around a star with mass M_* has to exceed the *Roche limit* ρ_R

Roche limit

$$\rho_\mathrm{c} > \rho_\mathrm{R} = \frac{0.62 M_*}{r^3} \tag{2.27}$$

Kelvin-Helmholtz instability

for a GI to occur. Until the 1980's, it was considered to be sure that planets form via gravitational collapse of parts of the disc. However, Weidenschilling (1980, 1984, 1995) noted that because of the *Kelvin-Helmholtz instability* created by the velocity shear between the faster rotating midplane and the slower rotating adjacent layers (see section 2.1.4) even laminar discs become turbulent. This turbulence stirs up particles from the midplane and puffs up the midplane layer. As a consequence, the density in the midplane never exceeds the critical limit and no GI will develop. This result has been confirmed by Cuzzi et al. (1993) and Dobrovolskis et al. (1999) with even more elaborate models and by Sekiya (1998) with a linear stability analysis.

enhanced dust-to-gas ratio

gas removal

particle pile-up

Nevertheless, in recent years there has been renewed interest in planet(esimal) formation by gravitational instability. Sekiya (1998) pointed out that GI could occur if the *dust-to-gas ratio* was *enhanced* over the protosolar value. This increases Σ_{d} in Eq. 2.26. Chiang and Youdin (2010) estimate that for typical parameters the dust density ρ_{d} must be over 1,000 times the gas density ρ_{g} or equivalently, the dust-to-gas ratio must be increased by a factor of 60,000. Although this task seems hopeless, having the barriers for the coagulation scenario (section 2.3.1) in mind, Youdin and Shu (2002) proposed some mechanisms which could enhance the dust-to-gas ratio globally and above all locally. As global mechanisms they propose *removal of gas* from the relatively gas-rich (because of dust settling to the midplane) upper layers of a protoplanetary disc. This could be done by photo-evaporation, layered accretion, and stripping by stellar winds. As a local mechanism, they propose that *particles pile up* while they drift radially inwards in the disc. This is a consequence of the drift speed v_{drift} (Eq. 2.24) depending on the Stokes number St, which in turn depends on the gas density (Eq. 2.18), i.e. on the location in the disc. This is, essentially, based on the same physics as trapping of particles in pressure maxima (see section 2.3.1).

one-phase fluid

two-phase fluid

Since the revival of the GI scenario, however, many counterarguments have also been collected (see, e.g. Cuzzi and Weidenschilling 2006, and references therein). Firstly, the model assumption of a *one-phase fluid* used by Sekiya (1998), Youdin and Shu (2002), Youdin (2004), and others is criticised. For this assumption to be valid, $\mathrm{St} < 10^{-2}$ has to be fulfilled. From Eq. 2.18 we see that this puts a constraint on the turbulence parameter of the disc. As a consequence, for enhanced dust-to-gas ratio a global turbulence of $\alpha < 10^{-8}$ and for nominal solar abundance even $\alpha < 10^{-10}$. In Sec. 2.1.1 and 2.1.4 we have seen that the disc has to be more viscous to explain the observed accretion rates and MRI generated turbulence is estimated to yield $\alpha \sim 10^{-3}$. Hence, the assumption of fully non-turbulent discs is not applicable. Secondly, it is very hard to find dust-to-gas ratio enhancing mechanisms for those particles which are tightly coupled to the gas. Thirdly, the most serious obstacle for a one-phase fluid GI was brought forward by Sekiya (1983): incipient collapse by the dust aggregates also compresses the entrained gas. This leads to an outward pressure which inhibits further collapse of gas and also dust particles. To overcome this hurdle, a dust-to-gas ratio of 10^7 is required at 2.5 AU, which is illusory. Also in *two-phase models* (Weidenschilling 1980, 1984, 1995, Cuzzi et al. 1993, Dobrovolskis et al. 1999, etc.) a quiescent disc must be assumed to prepare the ground for GI. There, another obstacle is brought forward by Weidenschilling (1995, 2003) targeting the radial pile up proposed by Youdin and Shu (2002). There exists not only a velocity dispersion between midplane and adjacent layers. Also in later stages, when particles drift towards the star, they have different drift velocities given by their size (Eq. 2.18). Consequently, the size distribution of the dust aggregates generates a velocity dispersion in radial drift. This, however, results in an increase of the Toomre parameter (Eq. 2.26) and the criterion for GI is not met.

As a reply to these critics, Chiang and Youdin (2010) more and more draw the focus of GI promoting dust enhancements to locally acting mechanisms. In an admirable way, they turn mechanisms that formerly prevented GI into supporters. In principle, they argue that instabilities that have been discovered in the past decade work together to make GI assisted planetesimal growth possible. Firstly, Goodman and Pindor (2000) have proposed a *secular instability* based on the formation of over-dense annuli of the disc using a single-fluid approximation. In an unperturbed state, dust drifts inwards at a constant rate. If this state is perturbed and a ring of width dr is over-dense, it exerts a gravitational pull inwards at its outer edge. Consequently, dust has to rotate faster there because the Keplerian velocity is increased locally. The gas velocity remains unaltered. This causes an inflow of dust into the annulus due to an increased headwind. The reverse is happening at the inner edge: the Keplerian velocity is locally lowered, dust experiences a tailwind and flows in the annulus. By this mechanism the instability grows and increases the dust-to-gas ratio in the annulus. Secondly, the *streaming instability* was discovered by Youdin and Goodman (2005) and further explored by Johansen et al. (2006a,b, 2007, 2009). This instability is a consequence of the sub-Keplerian velocity of the gas and the back-reaction of dust on the gas. For some reason dust clumps form in the streaming environment of the disc. As high mass objects tend to orbit with Keplerian speed, clumps with a higher dust-to-gas ratio move faster than clumps with lower dust-to-gas ratio. The former start to overtake the latter and finally crash into them, forming an even larger clump. By this process the clumps gain more and more mass. At the same time, a rarefaction tail forms behind the clump along the sub-Keplerian gas stream and some mass is lost. The final mass of the clump is determined by the balance of both processes. Thirdly, Johansen et al. (2006a,b, 2007, 2009) were also able to show, that MRI generated turbulence does not necessarily obstruct GI. On the contrary, turbulence can generate long lived *pressure maxima*, which act as an efficient trap for particles. Also all other particle trapping mechanisms already presented in section 2.3.1 like pressure bumps (for example near the ice line, Kretke and Lin 2007, Brauer et al. 2008b), gaseous spiral arms (Rice et al. 2004), and vortices (Barge and Sommeria 1995, Klahr and Henning 1997, Klahr and Bodenheimer 2006) may act as particle concentration mechanisms, which, in turn, create seedlings for other instabilities, which can concentrate particles long enough for GI to work. Johansen et al. (2007) demonstrated impressively that with a compilation of most of these physics objects of Ceres size can form within a few orbital times.

secular instability

streaming instability

pressure maxima

To conclude this section, it has to be said that planetesimal formation by gravitational instability is an attractive alternative to the coagulation scenario. Focussing on local dust-to-gas ratio enhancements it presents a very fast way out of all barriers outlined in section 2.3.1. However, both scenarios do not exclude each other. As Weidenschilling (1980) already conjectured planetesimal formation might be a composite process of both. Weidenschilling (1980, 1995, 2000), and Johansen et al. (2007), to name only a few, point out that for GI to work it might require the assembly of boulders of metre size and larger to provide sufficient dust density in the midplane and to overcome the radial dispersion problem. This has to be done by coagulation, which again underlines the importance of investigating the metre size barrier, which is the focus of this thesis.

2.4. Gravity Takes Over - Growing Planets

In the previous section it has been shown that the process of planet formation is still enigmatic. On the one hand, it is unclear whether the conditions for a gravitational instability are met. On the other hand in the coagulation scenario the sticking mechanism is unknown. However, under the assumption that kilometre sized planetesimals have formed somehow, the last step of planet formation can be investigated starting from a population of planetesimals. Here, the velocities are in the order of the escape velocity of the planetesimal and the sticking mechanism in collisional growth is gravitational attraction. The process of planet formation from planetesimals is rather well understood and the results of this research are presented in this section, which is mainly based on the review articles by Lissauer and Stewart (1993), Chambers (2004), and Goldreich et al. (2004a,b).

2.4.1. Methods and characteristic quantities

Unlike metre sized pre-planetesimals, kilometre sized planetesimals can be detected via observational methods through the perturbations they create (Natta et al. 2007). The last stage of planet formation itself, however, cannot be observed. Therefore, semi-analytical and numerical methods have been developed to investigate this process.

N-Body simulations

The most obvious way is to integrate the equations of motion of a population of planetesimals orbiting around a host star with all gravitational interactions in an *N-Body simulation.* This approach is the most accurate one, but it has two main drawbacks. First of all, the computational costs are proportional to the square of the number of planetesimals. Simulating a population of planetesimals that are sufficient to assemble only one planet exceeds current computational resources by far. Secondly, there are fundamental uncertainties regarding initial sizes and velocities of the planetesimals as well as the question of whether they stick or fragment. However, this method has been proven extremely valuable in the late stages of planet formation, where the number of bodies decreases considerably (e.g. Kokubo and Ida 1996, 1998, 2000).

particle-in-a-box approach

For the early stages of the growth step from planetesimals to planets, the *particle-in-a-box approach* has widely been used (e.g. Greenberg et al. 1978, Wetherill and Stewart 1989, Weidenschilling 1997). This method is similar to the dust coagulation simulations (application in sections 2.2 and 2.3, method in section 3.3). All bodies with similar masses are grouped together in mass bins. These groups interact with each other using a coagulation equation and a collision probability. The velocity distribution is computed by means of kinetic theory. As a drawback, the positions of the bodies are not taken into account. Consequently, the method is only valid for a nearly uniform spatial distribution of planetesimals, which is only true for the early stages of the last growth step.

statistical method

The previous approach is simplified even further with the *statistical method.* Only two groups of bodies are considered: protoplanets and planetesimals and their velocity dispersions. This assumption is valid for the late stages of planet formation, where big protoplanets already have formed. Ormel et al. (2010b) even define the beginning of this late stage as the time when the two-component approximation becomes valid. With the statistical method (e.g. Wetherill and Stewart 1989, Ida and Makino 1993) analytical formulae for growth rates of protoplanets can be derived. Although it is valid only for late times, the statistical method allows a good categorisation of the growth modes in the last step of planet formation. I will rely on this approach throughout this section. Recently, Ormel et al. (2010b) have presented a hybrid model which preserves the individual particle nature of bodies (like the N-Body approach) and also has a statistical nature. Essentially, they confirm the results of ordinary N-Body codes.

For the following description of the growth from planetesimals to planets some characteristic quantities based on the statistical method have to be defined: protoplanets (sometimes also called planetary embryos) are of intermediate size between planetesimals and planets. They are specified by their surface density $\Sigma_{\rm pp}$, velocity dispersion $\bar{w}$, radius S, and mass $M_{\rm pp}$. The bulk of mass, however, is represented by planetesimals with surface density $\sigma_{\rm ps}$, velocity dispersion $\bar{u}$, radius s, and mass $m_{\rm ps}$. The respective *escape velocities* are defined as

escape velocity

$$w_{\rm esc} = \sqrt{\frac{{\rm G}M_{\rm pp}}{S}} \tag{2.28}$$

$$u_{\rm esc} = \sqrt{\frac{{\rm G}m_{\rm ps}}{s}}\,, \tag{2.29}$$

where G is the gravitational constant. As another important quantity, the *Hill radius*

Hill radius

$$S_{\rm H} \sim a\left(\frac{M_{\rm pp}}{3M_*}\right)^{1/3}\,, \tag{2.30}$$

where M_* is the mass of the host star, helps to distinguish between two areas of gravitational influence on a planetesimal. Inside $S_{\rm H}$ around a protoplanet, the gravitational field of the star is negligible and the planetesimal's motion is dominated by the protoplanet's gravitational attraction. Outside, the behaviour is vice versa. At a distance $S_{\rm H}$ the orbital frequency of a planetesimal around the protoplanet is comparable to the orbital frequency of the protoplanet around the star. Associated with the Hill radius is the *Hill velocity*

Hill velocity

$$w_{\rm H} \sim \Omega_{\rm K} S_{\rm H} \sim \frac{{\rm G}M_*}{a^3} S_{\rm H}\,, \tag{2.31}$$

where a is the semi-major axis around the star. Equivalent to the above distinction, for $\bar{u} > w_{\rm H}$ the protoplanet-planetesimal system is *dispersion dominated* and the situation is well approximated by two-body mechanics. Whereas for $w_{\rm H} > \bar{u}$ the tidal gravity of the sun must be taken into account and the system is *shear dominated.*

dispersion dominated

shear dominated

The velocity dispersions $\bar{w}$ and $\bar{u}$ evolve by three important processes: cooling by dynamical friction, heating by dynamical friction, and viscous stirring. These originate from gravitational stirring that converts energy of orbital motion of a swarm of planetesimals into random motions. *Dynamical friction* describes the equipartition of random kinetic energies, i.e. more massive bodies are damped to lower velocities while the velocities of smaller bodies are increased. In contrast, *viscous stirring* increases random kinetic energies. Planetesimals dominate the dynamical friction, whereas protoplanets provide most of the viscous stirring. Protoplanets heat the surrounding planetesimals faster than they accrete them. Therefore, planetesimals have to be cooled via dynamical friction in inelastic collisions. Otherwise planet formation would have taken far too long.

dynamical friction

viscous stirring

The most important mechanism in this epoch of planet formation is *gravitational focussing*, i.e. the enlargement of the effective scattering cross section by self-gravity of the protoplanet, which is equivalent to the condition $\bar{u} = w_{\rm esc}$. Without gravitational focussing the formation of Neptune

gravitational focussing

would have taken about 4×10^{11} yr which is about 85 times the age of the solar system (Goldreich et al. 2004a). Kokubo and Ida (2000) showed that the effect of gas can almost be neglected for the growth process. This is consistent with the fact that planetesimals almost fully decouple from the gas.

In the following the characteristics of the substages of the last step of planet formation will be described. These are orderly growth, runaway growth, and oligarchic growth.

2.4.2. Orderly growth

In orderly growth mode gravitational focussing is weak ($\bar{u} > w_{\mathrm{esc}}$) and the growth of the velocity dispersion in the disc is dominated by the protoplanet (Rafikov 2003), i.e. dynamical friction is neglected and there is no sufficient cooling mechanism for the planetesimals. This phase is characterised by very long time scales ($10^8 - 10^9$ yr in the terrestrial zone, Safronov 1969). Many small protoplanets compete for the same population of planetesimals. Imagine two neighbouring protoplanets: the larger one has the larger escape velocity, but at the same time, because the velocity dispersion is dominated by the protoplanet, it stirs its surrounding planetesimals to a bigger amount. As a consequence, the smaller one grows relatively faster, but never overtakes the bigger one, since in both cases the accretion rate decreases with increasing size. It is given by

$$\frac{1}{M_{\mathrm{pp}}} \frac{\mathrm{d}M_{\mathrm{pp}}}{\mathrm{d}t} \propto \frac{1}{S} \frac{\mathrm{d}S}{\mathrm{d}t} \propto \frac{1}{S} \,. \tag{2.32}$$

However, Rafikov (2003) has pointed out that the conditions for orderly growth might be never met. He proposes that the protoplanet's accretion cross section is always strongly increased over its gravitational cross section and that cooling by dynamical friction is effective. Hence, gravitational focussing is always strong and the protoplanet never grows in an orderly way, but starts off in the runaway mode. It was shown in multi-zone simulations that different growth modes apply for different regions of a planetary system. Cooling by dynamical friction depends on the surface density of the planetesimals, which drops with increasing distance from the star. Additionally, the velocity dispersion is influenced by non-linear effects, such as fluctuating spiral features in the disc (Weidenschilling 2008, Clarke and Lodato 2009). As a consequence, the velocity dispersion might prevent runaway growth in the outer parts. Orderly growth might dominate there.

2.4.3. Runaway growth

In a classic view (Wetherill and Stewart 1989, also Ida and Makino 1993 and Weidenschilling 2000, 2008), the situation changes when cooling by dynamical friction is considered. Firstly, because of the equipartition of energy between bigger bodies and smaller bodies the velocity dispersion of the protoplanets $\bar{w}$ is decreased and $\bar{u}$ is increased. Consequently, relative velocities between protoplanet and planetesimals are decreased, which in turn enhances the gravitational focussing of protoplanets. And at the same time, gravitational focussing of planetesimals is decreased owing to the increasing velocity dispersion $\bar{u}$. Hence, big protoplanets grow even more rapidly and small planetesimals grow slowly. The evolution results in runaway growth. This phase can, therefore, be characterised by a growth of velocity dispersion, which is dominated by the planetesimals, and a strong gravitational focussing (Rafikov 2003). Additionally, velocities of planetesimals are cooled by mutual inelastic collisions.

Goldreich et al. (2004a) and Ormel et al. (2010b) correct this view. Runaway growth does not take place, when the system is in the shear dominated regime. It is also prohibited in the dispersion dominated regime when the velocity dispersion of the protoplanets is chosen to be $\bar{w} > w_{\text{esc}}$. In this case dynamical friction reduces $\bar{w}$ relative to $\bar{u}$ and as a side effect $\bar{w}$ evolves such that $w_{\text{esc}} > \bar{w}$. Dynamical friction is not required to sustain runaway growth as long as the system is in the dispersion dominated regime and $w_{\text{esc}} > \bar{w}$.

The bigger a protoplanet grows, the more gravitational attraction is increased. Therefore, the mass accretion rate is often stated as

$$\frac{1}{M_{\text{pp}}} \frac{\mathrm{d}M_{\text{pp}}}{\mathrm{d}t} \propto \frac{1}{S} \frac{\mathrm{d}S}{\mathrm{d}t} \propto S\,, \tag{2.33}$$

for $w_{\text{esc}} > \bar{u} > w_{\text{H}}$. This is true for the very first phase of runaway growth (see, e.g. Kokubo and Ida 1996). However, the bigger the protoplanets grow the more they viscously stir their surrounding planetesimals. This effect increases the relative velocities between both populations and, as a consequence, gravitational focussing of the protoplanet is also reduced with increasing velocity dispersion of the planetesimals. Taking this into account Goldreich et al. (2004a) formulate

$$\frac{1}{M_{\text{pp}}} \frac{\mathrm{d}M_{\text{pp}}}{\mathrm{d}t} \propto \frac{1}{S} \frac{\mathrm{d}S}{\mathrm{d}t} \sim \frac{S}{\bar{u}^2}\,, \tag{2.34}$$

for $w_{\text{esc}} > \bar{u} > w_{\text{H}}$. Often the time when protoplanets dominate their surrounding by viscous stirring is proclaimed as the end of runaway growth (e.g. Ida and Makino 1993, Rafikov 2003, Thommes et al. 2003). However, according to Eq. 2.34 the growth is still runaway, but it increasingly turns from a global to a local one.

Runaway growth can end in several ways (Goldreich et al. 2004a). As a first possibility, protoplanets grow large enough that $w_{\text{H}} > \bar{u}$. Subsequent growth then no longer depends on the size of the protoplanet. This is called *neutral growth.* Secondly, planetesimals are stirred sufficiently such that $\bar{u} > w_{\text{esc}}$. Then growth proceeds in an orderly way. Thirdly, the system enters the oligarchic growth phase.

neutral growth

The *transition* from runaway growth to the next step is still under debate. Goldreich et al. (2004a) suggest that a protoplanet must *solely* dominate viscous stirring in its surrounding. Ormel et al. (2010b) define that runaway growth must be local and the local system must be isolated. This is quantified by Ormel et al. (2010a): the transition takes place at transition radii of 300 km, 600 km, and 1,000 km at 1 AU, 6 AU, and 35 AU, respectively.

transition runaway – oligarchy

2.4.4. Oligarchic growth

The growth phase presented in this section was investigated by Kokubo and Ida (1998, 2000), who coined the term *oligarchic growth.* No matter when the transition point from runaway growth is set, this mode is characterised by its self-limiting nature. The reason for this is similar to the processes in orderly growth: the more massive a protoplanet is, the more it viscously stirs the planetesimals in its area of influence, which in turn reduces its gravitational focussing. The accretion rate drops from runaway ($\propto S$) to orderly ($\propto S^{-1}$). In oligarchy, neighbouring protoplanets maintain approximately even orbital spacings of $\sim 5 - 10\,S_{\text{H}}$. This is because dynamical friction and occasional gravitational interactions generate some *orbital repulsion.* The area of influence of each oligarch is called *feeding zone*, from which the protoplanet accretes most of its mass. While

orbital repulsion

feeding zone

in oligarchy, the growth proceeds in locksteps with almost similar mass accretion rates. In this time, orbits of the accreting bodies rarely cross.

The more the oligarchs grow the more their feeding zones also grow. Eventually, two feeding zones overlap. Now the two competing protoplanets share the same population of planetesimals. As a consequence, the growth mode switches to runaway again and the larger of the oligarchs outgrows the smaller one and finally accretes it. Goldreich et al. (2004a) describe this situation as *battling oligarchs*, where protoplanets battle for local dominance in a winner-takes-all war.

battling oligarchs

At the end of oligarchy, the number of planetesimals in the feeding zones decreases and the oligarchs become more and more isolated from each other. Consequently, dynamical friction also decreases and viscous stirring cannot be balanced anymore. As a result, orbital repulsion breaks down and protoplanets no longer stay within their feeding zones. They start to interact strongly with neighbouring protoplanets and collisions take place. The oligarchic growth phase, which lasts a rather short time of about $0.1 - 1 \times 10^6$ yr, is terminated by chaos. Thommes et al. (2003) propose that oligarchic growth was not required to form the terrestrial planets of the solar system. Goldreich et al. (2004a) suppose that oligarchy is the final stage of planet formation in the outer solar system.

2.4.5. Final stages

merging

ejection

In the final stages of planet formation at about 10^8 yr the protoplanets are still embedded in a disc of gas and sparsely distributed debris. As already mentioned above, the protoplanets start to gravitationally interact with each other. In the inner solar system, where the ratio of the escape velocities from the surface of the protoplanets to the escape velocities from their orbits around the star is smaller than unity, the protoplanets collide and *merge*. For the protoplanets in the outer solar system, this ratio rises above unity and random velocities of the protoplanets rise until they are *ejected* and reside, e.g. in the Oort cloud (Goldreich et al. 2004b). Eventually, the protoplanetary system was populated by a few dozen protoplanets of the size of Moon or Mars (Chambers 2004), which were still scattered inwards and outwards, destroying the order established in the oligarchic phase and mixing material from the inner solar system outwards and vice versa.

orbit regularisation

The end of this chaotic behaviour is marked by the process of *orbit regularisation*. It is widely accepted that dynamical friction with the residual debris and gas drag circularise and flatten the orbits of the surviving protoplanets. However, in a recent study Leinhardt et al. (2009) have shown that catastrophic planetesimal collisions provide not enough background material to provide significant dynamical friction for this process.

gap clearing

clean up

At the same time, protoplanets open gaps in the gas-debris disc and accrete material by the process of *gap clearing*. Dynamical friction is still active in this phase. This planet disc interaction leads to various types of planet migration. The influence of this effect and the direction of migration under various conditions are subjects of ongoing research (e.g. Papaloizou et al. 2007, Kley et al. 2009). The *clean up* of the remaining debris and gas by the protoplanets terminates the process of planet formation.

2.5. The Focus of this Thesis: Planetesimal Formation

As a conclusion to this chapter, the thematic location of the thesis at hand has to be specified. It became clear from the preceding sections, that, despite some unresolved questions, the first and last epochs of planet formation are thoroughly investigated and well understood. In Sec. 2.2 the growth mechanism from dust grains to centimetre sized pre-planetesimals was lined out. The onset of dust growth is fractal: dust grains collide and stick due to dipole-dipole interactions forming fractal, chain-like structures. These get compacted as collision velocities increase. As a result porous dust balls of centimetre size are generated. Skipping the problematic intermediate step, Sec. 2.4 describes the epoch from kilometre sized planetesimals to planets: typical velocities in a planetesimal swarm no longer exceed the escape velocity of the planetesimal. Gravity assisted growth is the consequence. The onset may be slow in orderly growth mode, then proceeds (or even starts) in a runaway fashion until protoplanets dominate their surroundings. Then, growth proceeds in a self-limiting way, where protoplanets are more and more isolated from each other. The growth has become oligarchic. After a short phase of chaos, where the oligarchs scatter each other inwards and outwards, the orbit of the remaining almost-planets become regularised, gaps open in the disc and remaining material is cleaned up by accretion onto the planets.

from grains to pre-planetesimals

from planetesimals to planets

The intermediate growth step from centimetre sized pre-planetesimals to kilometre sized planetesimals is still full of mysteries. With the core accretion and gravitational instability hypotheses (Sec. 2.3) two possibly competing theories have been developed extensively to overcome this problem. Maybe in the end the efforts of both have been joined to successfully explain this enigmatic epoch. The core accretion theory assumes that collisions between pre-planetesimals lead to a net growth, which finally generates a sufficient population of planetesimals. This theory is mainly endangered by increasing collision velocities which increasingly lead to catastrophic disruption of the pre-planetesimals. Furthermore, the sticking mechanism is unclear and a considerable amount of collisions could result in restitution with the collision partners bouncing off each other without net growth. Things become more complicated if observational constraints are considered. It seems inevitable that some fragmentation occurs if the dust emission features in SEDs are to be explained successfully (grain retention problem). These and other problems were discussed in Sec. 2.3.1. On the other hand, the gravitational instability theory assumes that parts of the disc become dense enough to collapse under their own gravity. Planetesimals or even larger objects could be generated by this process. However, it is unclear how the required enhancement of the dust-to-gas ratio can be achieved. For this it could be necessary that boulders of a few metres in size have to exist in the midplane of the protoplanetary disc. The size step from centimetre sized pebbles to metre sized boulders has to be bridged by collision and sticking.

from pre-planetesimals to planetesimals

Consequently, for both theories collisions of centimetre to at least metre sized dust aggregates have to be investigated more thoroughly. A gap opens between the need that metre sized boulders have to grow somehow by collisions and the need that, at the same time, a sufficient portion of dust has to be generated in these collisions. For a long time, the question for a sticking mechanism for these collisions was in the spotlight. The new problems brought up in recent years require a modification of this question: what is the right balance between sticking and fragmentation in the collisions? Therefore, this thesis is dedicated to the investigation of two-body collisions between porous dust aggregates. Thresholds for sticking, bouncing and fragmentation have to be quantified as thoroughly as possible. The amount of dust produced in sticking,

right amount of growth and fragmentation bouncing and fragmenting collisions has to be estimated. The outcome of these collisions has to be explored depending on parameters such as collision velocities, collision parameter, object porosity, object size, etc. For methodological reasons these data cannot, or only insufficiently, be provided by laboratory experiments or molecular dynamics simulations (see Sec. 3).

applicability of data from this thesis

The brought description of planet formation in this chapter is justified by the equally brought possible applications of the data produced for and presented in this thesis. The dust size distribution produced in pre-planetesimal collisions has considerable influence on the predictions of SEDs for model discs (Sec. 2.1.2). The amount of dust generated by these collisions has an influence on generating shear instabilities, on the size of dead zones where MRI is inhibited, and on the thermal structure of the disc. All together these effects have influences on the dynamics inside the disc and its accretion rate (Sec. 2.1.4). Energy dissipation in pre-planetesimal collisions through compaction or fragmentation influence might lower collision velocities and therefore promote growth (Sec. 2.2.4 and 2.3.1). Detailed data from collisions help to improve dust coagulation models, which follow the planetesimal formation process by core accretion in detail. Detailed fragmentation statistics could help to resolve the grain retention and late pebble problems (Sec. 2.3.1). Sticking, bouncing, and fragmentation data is probably also required to understand the collision processes in particle trapping mechanisms, which are important for both the core accretion and the gravitational instability hypotheses (Sec. 2.3.1 and 2.3.2). Additionally, data presented in this thesis could help to lay out the ground for a gravitational instability (Sec. 2.3.2). Above all, these data may provide the answer to the key question, whether gravitational instability is needed or whether planetesimal formation can be achieved with coagulation alone (Sec. 2.3). Based on this data, planetesimal formation simulations of either hypothesis could provide information on the initial population of planetesimals, which then proceeds in orderly, runaway, and/or oligarchic growth (Sec. 2.4).

Finally it can be said, that this thesis is not bound to any special hypothesis. It tries to provide data on a very basic, but essential process which takes place in nearly every location in the protoplanetary disc: the collision of two porous dust aggregates from centimetre sizes onwards in a wide parameter space. Because of this fundamental setup, the application of the data obtained is applicable to many aspects of the planet formation process.

3. Investigating Planetesimal Formation - A Selection of Methods

In this chapter I briefly review some important methods, which have been used to investigate planet formation. The insights presented in the previous chapter originate from these branches. Each of the following sections describes basic concepts, results, and limitations of the specific method. At the end of this chapter the methodological choice of this thesis will be justified considering the aims presented in Sec. 2.5 and the given methodological limitations.

3.1. Dust Growth in the Laboratory

Dust growth in the laboratory has been reviewed and categorised by Blum and Wurm (2008) and Güttler et al. (2010). Results from this approach were already presented in Sec. 2.2.3, 2.2.4, and 2.3.1 in the relevant contexts of dust coagulation and planetesimal growth by coagulation. In this section the focus lies on the experimental method and its limitations.

3.1.1. Basic concepts

dust analogues

protoplanetary disc conditions

Since realistic protoplanetary material is difficult or expensive to produce, laboratory experiments mostly work with protoplanetary *dust analogues* (e.g. Poppe et al. 2000, Blum and Wurm 2008). The broadest systematic studies were carried out with silica (SiO_2). To simulate *protoplanetary disc conditions* most of the experiments were performed in microgravity and many in a vacuum environment.

µm *regime*

Hereby, laboratory experiments tried to cover both, a broad size and collision velocity range. The onset of dust aggregation takes place in the *micrometre regime*. Coagulation from individual grains was studied by Blum et al. (1998, 2000, 2002), Wurm and Blum (1998), Poppe et al. (2000), and Krause and Blum (2004). Collision velocities ranged from $10^{-3} - 100\,\mathrm{m/s}$. Aggregates in this regime grow by a hit-and-stick mechanism. At low velocities ($v_0 < 0.2\,\mathrm{m/s}$) aggregates grow as chain-like fractal structures. At higher velocites ($0.2 < v_0 < 0.7\,\mathrm{m/s}$) they get compacted. At $0.7\,\mathrm{m/s}$ partial fragmentation occurs until for $v_0 > 2\,\mathrm{m/s}$ catastrophic disruption takes place. In these experiments, dust growth could be observed directly. The vacuum chamber served as representative piece of a protoplanetary disc.

mm – cm *regime*

impact type

In contrast, collisions in the *millimetre* to *centimetre regime* are investigated as single events. For this regime, the experiments can be subdivided into two types. I call the first one the *impact type*. There, a (often millimetre sized) projectile impacts a larger (centimetre to decimetre sized) target. The second type is the *collision type*, where two nearly equally sized (mostly centimetre sized) objects collide. Impact type experiments have been carried out in a quite large number. This category can be subdivided into low velocity impacts ($v_0 < 5\,\mathrm{m/s}$) investigated by Langkowski et al. (2008), where sticking and bouncing was observed. More frequently this type was used for high velocity impacts ($v_0 > 5\,\mathrm{m/s}$) by Wurm et al. (2005a,b), Paraskov et al. (2007) and Teiser and

Wurm (2009b). These experiments resulted in parts of the target and projectile being ejected in the impacts, but mostly net growth was observed. Real *collision type* experiments are very rare. They have been performed by Blum and Münch (1993) and Heißelmann et al. (2007).

collision type

analogous type

Particularly collisions with low velocity, a third type of experiment was frequently used in recent times. This is the *analogous type* of experiments, where collisional outcome for dust aggregates is derived not directly from dust aggregate collisions but from collisions with a hard surface or impacts of other material into dust. Weidling et al. (2009) investigated low velocity collisions ($\sim 0.2\,\mathrm{m/s}$) with a vibrating plate (no microgravity, no vacuum). They found bouncing and compaction. Güttler et al. (2010) shot micrometre and millimetre sized dust aggregates bottom-up onto a solid glass plate with velocities of some $\mathrm{m/s}$ (no microgravity, no vacuum). They found sticking, bouncing, and fragmentation. In another experiment, Güttler et al. (2010) collided a millimetre sized dust aggregate with a free falling glass bead of the same size. They found fragmentation and partial sticking on the glass bead.

sweeping type

As a last experimental type, the *sweeping type* setup has to be mentioned. There, the direct assembly of centimetre to decimetre sized dust aggregates from micrometre sized grains or aggregates is investigated. This situation is analogous to large aggregates sweeping up very small ones in the protoplanetary disc. This process is essential for the grinding growth model (see Sec. 2.3.1 and Fig. 2.5). Recently, Teiser and Wurm (2009b) studied the aggregation of decimetre sized dust agglomerates from $100\,\mu\mathrm{m}$ small dust agglomerates at impact speeds of $v_0 \sim 8\,\mathrm{m/s}$. They found, that objects of intermediate porosity ($\phi \sim 0.3$) form. With random ballistic deposition (RBD) experiments, Blum and Schräpler (2004) and Blum et al. (2006b) ($v_0 < 2.2\,\mathrm{m/s}$) generated highly porous dust aggregates ("dust cakes") of some centimetres in size.

material parameters

As an essential ingredient for this thesis, Blum and Schräpler (2004), Blum et al. (2006b) and Güttler et al. (2009) measured the *material parameters* of macroscopic SiO_2 aggregates such as the bulk modulus and the compressive and tensile strengths. This topic will be discussed in more detail in Sec. 5.3. As an input for molecular dynamics (MD) simulations (see Sec. 3.2), microscopic material parameters were also measured: the pull-off force and rolling friction between two spherical grains were determined by Heim et al. (1999) with the aid of atomic force and optical microscopy.

3.1.2. Results

Without a doubt, laboratory dust experiments provide the key to understanding pre-planetesimal and planetesimal formation. All numerical simulations have to be put onto this empirical basis. The main results can be summarised as follows:

1. Dust growth starts from micrometre sized dust grains. Under protoplanetary disc conditions growth in the beginning is very efficient. Initially, it proceeds in a fractal way. With higher collision energies the aggregates get compacted (see also Sec. 2.2.3 and 2.2.4).

2. Fractal growth and compaction produces fluffy, highly porous dust aggregates. Pre-planetesimals, therefore, are presumably more similar to dust balls than to brittle rocks (see also Sec. 2.3.1).

3. In the centimetre size regime, collisions can result in (partial) sticking, bouncing, and fragmentation. Collisional outcome types were suggested by Güttler et al. (2010). Velocity-size maps (Güttler et al. 2010) and maps which corelate collision partner size (Blum and Wurm

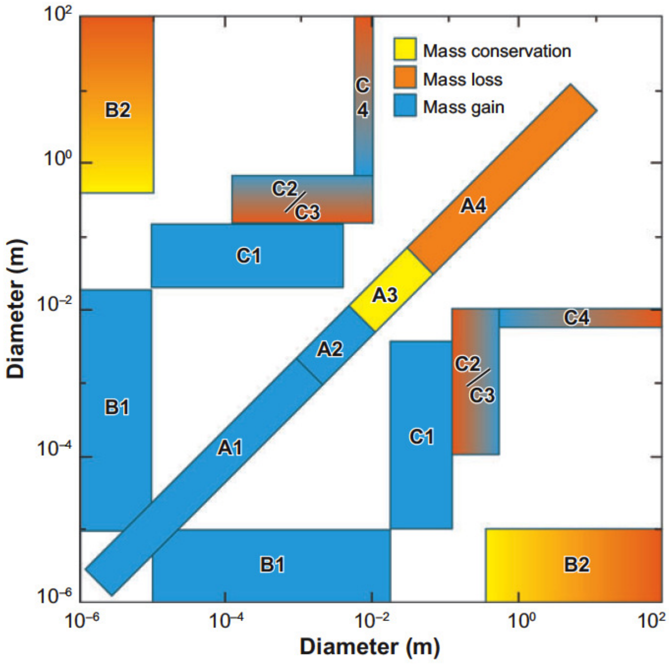

Figure 3.1. *Laboratory dust experiments.* Overview of laboratory dust experiments (alphanumeric labelling) with mass conservation, loss, and gain (colour coded) for collisions of dust agglomerates of different sizes (axes). Group A are collision type experiments from millimetre to centimetre size, group B are sweeping type and group C impact type experiments. Mass gain is ensured for hit-and-stick growth and the grinding growth model up to centimetre size. In larger size regimes, particularly for collision type experiments, mass loss or fragmentation dominates (figure from Blum and Wurm 2008).

2008, and Fig. 3.1) with mass gain, conservation, and loss were produced. For disruptive collisions fragment statistics were derived.

4. Decimetre sized dust agglomerates can form by the aggregation of showers of micrometre sized dust particles. Depending on the impact speed, they gain high or intermediate porosity.

5. Macroscopic and microscopic material parameters of dust aggregates and grains, respectively, were measured. These parameters serve as input for Molecular Dynamics Simulations (see Sec. 3.2) and simulations based on continuum methods (see Sec. 3.4).

3.1.3. Limitations

Despite their importance for pre-planetesimal and planetesimal formation, laboratory experiments struggle with some drawbacks. These mostly deal with the difficult treatment of dust material under realistic protoplanetary disc conditions. The main critics and limitations are:

1. Experiments have been carried out with different materials and different grain sizes and shapes. Poppe et al. (2000) showed that grain sizes and shapes have considerable influence on stickiness and other mechanical properties such as compressive and tensile strength (see also Blum et al. 2006b). Despite these findings, results from experiments with differing grain properties in different size regimes have been compiled as if it was the same material (Güttler et al. 2010). A systematic study with *one* material covering the broad pre-planetesimal size regime is still missing. This thesis enables a numerical treatment of this issue.

2. To investigate dust coagulation in realistic protoplanetary disc conditions, microgravity and vacuum are necessary. Size limitations of the experimental apparatus make it unfeasible to examine dust growth by coagulation beyond decimetre size.

3. Collisions of macroscopic dust aggregates are investigated as single events. Because of inhomogeneities in these dust aggregates, a large number of individual collisions for each aggregate size and collision velocity is needed to obtain statistically significant results for sticking, bouncing, and fragmentation thresholds and fragment distributions. Compared with these uncertainties the number of investigated events for each velocity-size combination was very low. Sometimes only a single collision was carried out. The same criticism was brought forward by Teiser and Wurm (2009a).

4. Single event collisions are not unique in their prediction (Blum and Münch 1993, Wurm et al. 2005a,b, Langkowski et al. 2008). Instead, adding mass, bouncing, or mass loss was observed in experiments with individual projectiles (see also Teiser and Wurm 2009a)

5. Particularly for highly porous aggregates, pre-processing, which alters the aggregate properties, cannot be excluded when preparing the experiments (C. Güttler, personal communication).

6. It is questionable whether a realistic outcome of collisions of two dust aggregates can be derived from analogous type experiments without any correction. Because of differing

surface properties and other mechanical quantities such as the bulk modulus and compressive, tensile, and shear strengths, colliding a dust aggregate with a glass surface might be essentially different from colliding two highly porous dust aggregates. This problem will be addressed in the thesis at hand.

3.2. Molecular Dynamics Simulations

3.2.1. Basic concepts

Molecular dynamics (MD) codes numerically simulate the behaviour of dust aggregates based on the microscopic forces between individual dust grains. Under the influence of external forces, the particles have six degrees of freedom to move around this contact (see Fig. 3.2): vertical (pull-off, Chokshi et al. 1993), tangential (rolling, sliding, Dominik and Tielens 1995), and torsional (twisting, Dominik and Tielens 1996). Chokshi et al. (1993) showed that stresses between grains are transported on sound speed time scales. Thus, for the external forces (e.g. by collision) changing on time scales shorter than the sound travel time, adjustments of the contact can be treated as quasi-static. Additionally, as long as external forces stay below some limit, the deformation of the contact area is reversible, i.e. elastic. If the force exceeds this limit, irreversible deformation takes place and energy is dissipated. For example, pulling forces in the vertical direction first diminish the contact area and finally, irreversibly, break the contact. Each degree of freedom shows this kind of resistance and consequential energy dissipation. Hence, there is resistance to pull-off, rolling, sliding, and twisting. The exact amount of resistance depends on grain size and morphology (Dominik et al. 2007), e.g. small grains break rather than allow rolling (Dominik and Tielens 1996). These findings from the microscopic physics of dust grains underline that dust analogues for protoplanetary dust have to be chosen carefully.
MD simulations have been performed, e.g. by Dominik and Tielens (1995, 1996, 1997), Paszun and Dominik (2006, 2008, 2009), Suyama et al. (2008), and Wada et al. (2007, 2008, 2009) for ice and silica grains. In order to simulate large particle numbers and approach the continuum limit, recent works (Seizinger 2010, in prep.) develop parallel MD codes which are also able to run on graphic cards. With this technique it will be possible to simulate millions of particles.

3.2.2. Results

With MD simulations some important results, particularly for the onset of dust growth, have been attained (see Sec. 2.2.4). These and other insights can be summarised as follows:

1. MD simulations augmented the understanding of the first growth step from dust grains to macroscopic dust aggregates. The essential mechanisms, already proposed by laboratory experiments, are fractal hit-and-stick growth, restructuring, and aggregate compaction.
2. Using the breaking (E_{break}), rolling (E_{roll}), and collision energies (E_{eff}), thresholds for sticking without restructuring, for restructuring, maximum compression, erosion, and catastrophic disruption of aggregates with some hundred monomers have been derived (see also Sec. 2.2.3 and Tab. 3.1).
3. The importance of the impact parameter and aggregate rotation for the collisional outcome became evident in MD simulations (e.g. Paszun and Dominik 2009, Wada et al. 2009).

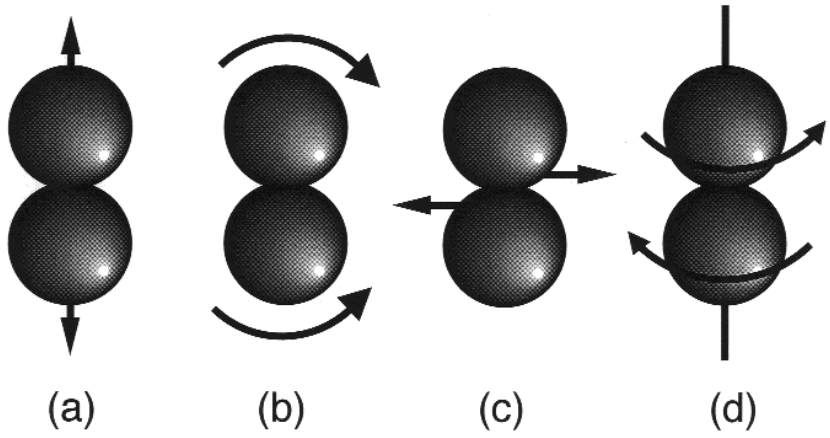

Figure 3.2. *Degrees of freedom in MD simulations.* Two dust grains have six degrees of freedom (and respective motions) around their contact (a) vertical (pull-off, 1 degree), (b) tangential (rolling, 2 degrees), (c) tangential (sliding, 2 degrees), and (d) torsional (spinning, 1 degree). Each degree of freedom has its own resistance and associated friction (figure from Dominik and Tielens 1997).

4. Taking into account the masses, porosities, collision energy, and impact parameter, elaborate recipes were developed for the collisional outcome. Tabulated values for fragment distribution and change in porosity after a collision served as input for coagulation simulations such as Ormel et al. (2007, 2009).

5. Mainly because of rolling (but also sliding) friction and breaking contacts, energy is dissipated in the restructuring process. Hence, restructuring in compressing collisions may provide an important energy sink for reducing collision velocities in the disc (Dominik and Tielens 1997). Energy dissipation in collisions will also be addressed in this thesis.

6. Even at maximum compression the dust aggregates remain rather fluffy (Wada et al. 2008, Suyama et al. 2008). This emphasises that dust aggregates behave more like porous fluffy material rather than brittle rock-like material (if sintering processes are neglected).

7. Comparisons between ice and silica revealed that ice features a 25 times larger velocity threshold for catastrophic disruption (50 m/s, Wada et al. 2009) than silica. This stresses the importance of water ice and dust-ice mixtures for planet formation in disc regions beyond the snowline.

8. Coming from the microscopic properties of individual dust grains, MD simulations with particle numbers close to the continuum limit can provide macroscopic material parameters such as the compressive strength and the sound speed (Paszun and Dominik 2008, Seizinger 2010, in prep.). These and other material parameters are the key ingredient of continuum solid body and porosity models such as the one used in this thesis.

impact energy	impact velocity [m/s]	collisional outcome
$E_{\mathrm{eff}} < 5E_{\mathrm{roll}}$	0.2	sticking without restructuring (fractal growth)
$E_{\mathrm{eff}} \sim 5E_{\mathrm{roll}}$	0.7	onset of local restructuring
$E_{\mathrm{eff}} \sim 3n_{\mathrm{c}}E_{\mathrm{break}}$	1.2	onset of erosion
$E_{\mathrm{eff}} \sim 10n_{\mathrm{c}}E_{\mathrm{break}}$	1.9	catastrophic disruption

Table 3.1. *Submillimetre aggregate collision thresholds.* Impact energy and velocity thresholds for sticking, restructuring, and disruption of submillimetre SiO_2 dust aggregates, derived in MD simulations by Dominik and Tielens (1997). Velocities are taken from Blum and Wurm (2000). E_{break} and E_{roll} denote the energy to break a grain-grain contact and to roll a contact a quarter of a grain's circumference, respectively.

3.2.3. Limitations

As promising as it seems to simulate dust coagulation on the basis of microscopic grain properties, this bottom-up approach has some drawbacks. Some of them have already been collected by Paszun and Dominik (2009):

1. Contemporary MD codes simulate collisions of aggregates with a few thousand particles in reasonable time. This is still far from the continuum limit. Aggregates of about 100 µm in size already consist of a billion of particles.
2. Current MD models are based on the interactions between spherical grains. The simulation of irregularly shaped grains is theoretically possible, but in fact computationally unfeasible. However, irregular grains show different material strengths (Blum et al. 2006b) and might be relevant for the planetesimal formation process.
3. Like all numerical models, MD simulations depend on microscopic material parameters such as surface energy, displacement potentials and critical displacements. These have to be determined in laboratory experiments as accurately as possible. Small changes in these quantities might alter the behaviour of aggregates significantly.

3.3. Dust Coagulation Models

3.3.1. Basic concepts

For the complete picture of planetesimal formation from dust grains to kilometre sized boulders, the dynamics of gas flows in the disc, which drive dust coagulation, and the physics of aggregate collisions (see Sec. 2.2.3, 3.1, 3.2 and 3.4) have to be combined via particle gas interaction (see Sec. 2.2.2). This is the task of *dust coagulation models*. With their aid, dust motions such as Brownian motion, differential settling, turbulent mixing, and radial drift (see Sec. 2.2.4) and their influence regarding dust coagulation can be studied (e.g. Dullemond and Dominik 2005, Brauer et al. 2008a).

Essentially, these models follow the evolution of the number density N_i of dust particles with mass m_i, where particle masses are divided into mass bins. Depending on the complexity of the coagulation model, N_i is computed for a range of vertical and/or radial locations in the protoplanetary disc. At the heart of each coagulation model lies the Smoluchowski *coagulation equation* (Smoluchowski 1916, as stated in Brauer et al. 2008a)

coagulation equation

$$\dot{N}_i = \sum_{m_i=m_k+m_j} \Delta v_{kj} \sigma_{kj} p_c N_k N_j - \sum_j \Delta v_{ij} \sigma_{ij} p_c N_i N_j \tag{3.1}$$

where Δv_{ij} is the relative velocity between particles with mass m_i and m_j, σ_{kj} their collisional cross section and p_c the sticking probability. The first term of Eq. 3.1 is the gain rate of particles with mass m_i due to the coagulation of smaller particles with m_j and m_k. The second term is the loss rate of particles with m_i. $\dot{N}_i$ is the change rate of the number density of particles with mass m_i.

collision kernel

The quantity $\Delta v_{ij} \sigma_{ij} p_c$ is often called the *collision kernel* which includes all the collisional physics is hidden, particularly in the collision/fragmentation probability p_c. Since the collision kernel is essentially based on the interaction between two particles, all collisional physics can be reduced to a *two-body collision*. However, this simplicity is misleading. In contrast, a realistic collision kernel may become very complex if it is to contain all parameters which influence the outcome of a dust aggregate collision. These include the collision velocity, the impact parameter, the porosities of the bodies, their sizes, their spin, and probably even their collisional history. For understandable reasons, computing the complex collisional physics cannot be included in the coagulation simulations. Therefore, these are based on velocity thresholds, simple recipes, and analytical formulae for fragment distributions (such as Eq. 2.25). In the literature, assumptions for collision kernels range from the perfect sticking assumption ($p_c = 1$) to very elaborated versions with several sticking, bouncing, and fragmentation types (Güttler et al. 2010, Zsom et al. 2010).

two-body collision

Global dust coagulation simulations, which consider the vertical and radial dimensions of a protoplanetary disc, are numerically very challenging (Dominik et al. 2007). Therefore, in the past decades important results on the dust aggregation process have been gained with *local coagulation models*. An overview of the most important work is shown in Tab. 3.2. The effect of dust settling in the inner and outer region were investigated with vertical slices of disc models. In contrast, radial drift motions were studied with vertically averaged radial models. Also the effect of global turbulence was considered in both. Particularly Weidenschilling stressed the importance of collective motions of dust in the midplane, which may dominate over individual particle motions.

local coagulation models

global coagulation models

Mainly in the last decade, computational power and numerical techniques allowed *global coagulation simulations* to be performed. These were carried out, e.g. by Mizuno (1989), Kornet et al. (2001), Dullemond and Dominik (2004, 2005), Barrière-Fouchet et al. (2005), Ciesla and Cuzzi (2006), Ormel et al. (2007), Brauer et al. (2008a), Laibe et al. (2008), Zsom and Dullemond (2008) and Zsom et al. (2010). In most of them the effects of Brownian motion, global turbulence, differential settling, and radial drift were included.

3.3.2. Results

The insight gained by coagulation models, both global and local, into the planetesimal formation process are too numerous to be stated completely. Therefore, I will restrain to the most important ones:

publication	disc region		model type		global	collective
	inner	outer	vertical	radial	turbulence	effects
Weidenschilling (1980)	✓		✓			✓
Nakagawa et al. (1981)	✓		✓			
Weidenschilling (1984)	✓	✓	✓		✓	
Mizuno et al. (1988)		✓		✓	✓	
Schmitt et al. (1997)	✓	✓		✓	✓	
Weidenschilling (1997)		✓	✓		✓	✓
Weidenschilling (2000)	✓		✓			✓
Weidenschilling (2003)	✓	✓		✓		✓
Weidenschilling (2006)	✓		✓			✓
Weidenschilling (2010)	✓		✓			✓

Table 3.2. *Local dust coagulation models.* Exemplary overview of local dust coagulation models. Items are classified according to the following categories: Coagulation processes are investigated in the inner (around 1 - 3 AU) or outer (several tens of AU) disc regions. The model type can either average over the vertical structure (radial model) or focus on a vertical slice at a certain radial distance (vertical model). The protoplanetary disc is considered to be laminar or with global turbulence. Some models consider collective effects of the dust population in the midplane, which can lead to shear induced local turbulence.

1. Collective effects induce shear turbulence due to faster rotation of a dust-rich midplane layer and a resulting Kelvin-Helmholtz-instability. This is one of the main obstacles of a gravitational instability (see also Sec. 2.1.4 and 2.3.2) but also problematic for the grinding growth model (see Sec. 2.3.1).
2. Studies with different disc models resulted in a strong dependence of relative collision velocities between aggregates in the respective disc (see Sec. 2.1.3). With certain assumptions about fragmentation, growth is halted at different aggregate sizes.
3. Coagulation models allowed the investigation of the influence of Brownian motion, turbulent mixing, differential settling, and radial drift both separately and in concert. The details are presented in Sec. 2.2.4.
4. Joining data from coagulation models with radiative transfer methods permitted direct comparisons of observed discs with their model analogues. This revealed the grain retention and late pebble problems and consequently the necessity of fragmentation (see Sec. 2.3.1).
5. With coagulation models it became possible to investigate the different aspects of the metre-size barrier, namely the fragmentation, drift, and bouncing barriers (see Sec. 2.3.1).
6. Certain regions have been identified to promote planetesimal formation, e.g. the snow line.

3.3.3. Limitations

Limitations of coagulation models arise mostly from an inadequate treatment of the collisional physics by means of the collision kernel:

1. Via the collision kernel, coagulation simulations crucially depend on velocity thresholds for sticking, bouncing, and fragmentation. Simplifying assumptions such as velocity independent perfect sticking or catastrophic disruption leads to unphysical results, which are not in agreement with observations.

2. The fragmentation barrier and grain retention problems show that simple threshold velocities, which separate perfect sticking from catastrophic disruption, do not suffice to model aggregate collision behaviour with the necessary accuracy. Elaborate fragmentation statistics, which depend on impact velocity, object sizes and porosities and other parameters, may provide the right amount of fragmentation.

3. Porous objects are able to dissipate a considerable amount of energy by compaction in sticking as well as in bouncing and disruptive collisions. The reduction in kinetic energy comes from collisional physics and has to be fed back into the coagulation simulation as an altered velocity distribution.

4. The complex collisional physics has to be mapped to fit formulae for fragment distributions and other simplifications to make it numerically treatable for coagulation models.

5. Coagulation simulations might have to trace different materials which possibly dominate the planetesimal formation process in different regions. For example, dust might be the dominant material in inner regions of the disc while ice and ice-dust mixtures might be more important beyond the snow line.

6. Important physical processes such as re-accretion of grains due to gas flow or photophoresis are mostly neglected.

7. Kempf et al. (1999) find that the Smoluchowski theory is not suitable for describing the kinetics of dust growth at densities typical for the cold part of a protoplanetary disc.

3.4. The method used in this thesis: Collisions with solid body mechanics

3.4.1. Methodological motivation

collisional physics in coagulation simulations

The methodological motivation of this thesis arrises as a consequence from the limitations of the methods presented in Sec. 3.1, 3.2, and 3.3. I begin with the latter. An adequate implementation of the *collisional physics* of dust aggregates is *essential for dust coagulation models.* Zsom et al. (2010) have shown this in an impressive way: until their works fragmentation was the most serious obstacle to planetesimal formation. By considering the effect of bouncing they found that hardly any dust aggregates fragment. Instead, these simply bounce off each other and growth is halted at pebble sizes, which no longer stick due to insufficiently strong surface forces. The important point is not wether this is a realistic scenario, but that by introducing novel collision physics the whole picture of planetesimal formation changed. Because of the form of the collision kernel, studying dust aggregate collisions can be reduced to studying two-body collisions.

task of this thesis

Therefore, the *task of this thesis* is to investigate the outcome of two-body collisions of porous dust aggregates in full depth. Velocity thresholds for sticking, bouncing, and fragmentation are to be derived. In all cases the reduction in kinetic energy is to be determined. With the grain retention problem in mind, the possible production of dust has to be considered for the three collisional types. Since porosity is a key parameter in aggregate collisions, the change in this quantity also must be studied for sticking, bouncing, and disruptive collisions. For the latter, velocity dependent fragment distributions are to be derived. The dependence of the collisional outcome on parameters such as object size, porosity, and homogeneity as well as collision velocity and impact parameter must be verified and, where applicable, quantified.

size limit for MD and experiment

Since microscopic dust growth is very well understood thanks to laboratory experiments and MD simulations, the collisional physics is unclear roughly from centimetre to kilometre sizes – still five orders of magnitude. Because of size restrictions of the experimental apparatus (see Sec. 3.1.3), these *sizes are inaccessible* to laboratory experiments. As a consequence one has to switch on numerical simulations of larger dust aggregates. MD simulations are the physically most accurate way to fill in the gap because they rely on well known microscopic physics. However, not every material can be simulated and due to limitations in computational resources a 100 micron aggregate is nearly impossible to simulate. The study of metre sized boulders with MD simulations is illusory.

smoothed particle hydrodynamics (SPH)

Therefore, for this thesis a different numerical method was chosen. Based on the theory of continua it works with continuous quantities such as the density. In principle, mesh based as well as particle based methods come into consideration for the given task. Because of its advantages in treating collisions the Lagrangian particle method smoothed particle hydrodynamics (SPH) was chosen to simulate the collisions in this thesis.

method between experiment and disc model

By adopting measured (laboratory) or simulated (MD simulations) material parameters and by supplying attained data to coagulation simulations, this thesis not only closes the size gap from the smallest pre-planetesimals to planetesimals, it also bridges the *abyss between simulations and experiments*. With the concept of close collaboration between experimentalists and disc modellers this thesis has its place between laboratory experiments and disc simulations.

3.4.2. Drawbacks and solutions

Of course the methodological choice of this thesis comes with some drawbacks. In the following, these are listed together with the solutions that are used and proposed by this work. At the same time, the below enumeration also contains a short overview of Ch. 4 and 5.

1. SPH at first sight is designed for pure hydrodynamics (see Sec. 4.2), but it was extended to simulate solid bodies as discussed in Sec. 4.3.

2. The essential effect of porosity has to be modelled. This is accomplished by the choice of a suitable porosity model (see Sec. 4.3.4).

3. Any numerical model depends on the right choice of material parameters such as bulk and shear moduli as well as compressive, shear, and tensile strengths. In principle, laboratory experiments are able to provide values or relations for these. In fact, in this thesis some could be adopted without any problem, but others had to be found in an iterative process between experiments and simulations, which was a main task of this thesis (see Sec. 5.3). Also contemporary MD simulations are more and more able to provide macroscopic material properties (Paszun and Dominik 2008).

4. Even if realistic material parameters from laboratory experiments are adopted, the correct functionality of the numerical model has to be demonstrated. This has been done by reproducing three benchmark experiments, which were carried out in the laboratory and reproduced by simulations (see Sec. 5.1).
5. In continuum models the choice of resolution and purely numerical parameters could significantly alter the results. For this reason these dependences have been checked in Sec. 5.2.
6. For addressing the grain retention problem, high resolutions are desirable to resolve the small size of dust fragments as well as possible. Therefore, this thesis relies on a parallel SPH code with trusted and profound scaling properties.
7. It is impossible for SPH to simulate dust aggregates in the size regime where the continuum limit does not apply. However, simulations in this regime are not necessary because dust growth from individual grains has been studied extensively by laboratory experiments and MD simulations.

3.4.3. Advantages over other methods

The following listing directly answers the limitations of the other methods presented in this chapter. It is shown how this thesis' methodological choice tries to fill the data gap, which exists because of the given limitations of other methods:

1. Different materials can easily be simulated by implementing the respective material parameters. Unlike MD simulations, aggregate simulations with SPH are not bound to material with spherical monomers.
2. Collisions can be studied in realistic protoplanetary environments without expensive experimental setups.
3. The initial conditions for the dust aggregates can be controlled easily. Object inhomogeneities can be excluded or generated and quantified, if desired. Therefore, many collisions for a reliable statistical basis are not necessary. Unintentional pre-processing is also excluded and there are negligible errors in all relevant quantities.
4. The collisional outcome can be quantified in many aspects without loss of information through the choice of a particular experimental technique. This makes sticking, bouncing, and fragmentation statistics more accurate and reliable.
5. Because of the continuum ansatz, there is in principal no upper size limitation for the dust aggregates.
6. Dust aggregate collisions can be simulated directly without circumventive analogous experiments (see Sec. 3.1).
7. All quantities used in the solid body SPH approach can be traced spatially and in time. This provides valuable insight into the physical processes taking place inside the aggregates during the collision. Therefore, simulations enhance our understanding of the behaviour of highly porous dust aggregates.

4. Smoothed Particle Hydrodynamics and Solid Bodies

4.1. Basics

The numerical method *smoothed particle hydrodynamics (SPH)* was developed by Lucy (1977) and afterwards, but independently, by Gingold and Monaghan (1977). Originally designed for the simulation of compressible flows in astrophysical contexts, it was enhanced in the past decades and is nowadays applicable for a variety of physical problems. The research contexts where SPH is used are too numerous to be listed here. To the interested reader, I recommend the works by Benz (1990), Monaghan (1992), Speith (1998), Monaghan (2005) and Speith (2007), which offer a broad overview of research fields and method improvements. Particularly, Rosswog (2009) reviews the application of SPH in astrophysics. In this section I will restrain to the topics which are related to the context of this thesis.

astrophysical context

Since external and self-gravity can be implemented easily into the SPH scheme, it became a popular method to investigate the collapse of a molecular cloud as sketched in Sec. 2.1.1 (e.g. Whitehouse and Bate 2006, Stamatellos et al. 2007, Forgan et al. 2009). Besides dust coagulation models (see Sec. 3.3), grain growth by coagulation (see Sec. 2.2.4 and 2.3.1) was also simulated with two-phase SPH codes (e.g. Barrière-Fouchet et al. 2005, Laibe et al. 2008). Concerning the final stages of planet formation (see Sec. 2.4.5), the interaction between a gaseous disc and a planet was studied with SPH, e.g. by Lufkin et al. (2004), Schäfer et al. (2004) and Schäfer (2005).

solid body simulations

In the above examples, SPH was used because of its advantages in pure hydrodynamics. However, by including stress-strain relations this scheme can be expanded for the simulation of solid bodies instead of flows and fluids. This was carried out by Libersky and Petschek (1991) and later pursued, e.g. by Libersky et al. (1993), Benz and Asphaug (1994), Randles and Libersky (1996), and Libersky et al. (1997). Since the simulation of porous pre-planetesimals belongs to the realm of solid body mechanics, the numerics of this thesis is based on these works. Firstly, solid body SPH was applied in hyper-velocity collisions and explosions for military and industrial purposes (e.g. Libersky et al. 1993, Stellingwerf and Wingate 1994). Later its suitability for impact simulations also became valuable in astrophysical contexts: Benz and Asphaug (1994, 1995) implemented a model for brittle fracture which made it possible to simulate collisions between rocky asteroids. This model was applied to study the formation of asteroid families in high-velocity impacts (Benz and Asphaug 1999, Michel et al. 2002, 2003, 2004). Under the assumption that planetesimals consist of rock-like material, also planetesimal collisions were simulated (Benz 2000).

porous objects

All these works did not involve the treatment of porosity. Sirono (2004) proposed a model with porosity-dependent strength quantities which he applied to the collision of ice aggregates. This thesis extends his model. A different approach was developed by Jutzi et al. (2008, 2009b). Based on a different porosity model by Herrmann (1969), they expanded the works by Benz and Asphaug (1994, 1995) for the simulation of porous rock-like brittle material. Again, asteroid collisions and the influence of porosity were studied (Jutzi et al. 2009a, 2010).

mesh-free Lagrangian particle method

As a short characterisation it can be noted, that SPH is a *mesh-free Lagrangian particle method.* The SPH particles are the sampling points of the scheme. Particularly with fragmentation in mind, they must not be confused with real particles. Instead, the continuum of a solid body is discretised into small mass packages, which interact with each other. For example, the density at a certain point x_0 is given by the contribution of all surrounding SPH particles and not only by the SPH particle at x_0. The contribution of each SPH particle is weighted by the smoothing kernel.

The method is Lagrangian, because it is based on the Lagrangian form of the continuity, momentum, and energy equation. Therefore, the SPH particles follow the flow, concentrate at high densities and rarefy at low densities. Each SPH particle represents a fluid element and carries its mass, momentum, energy, velocity, and so forth. As time evolves, the SPH particles interact with each other and exchange momentum.

advantages of SPH

In Sec. 3.4.3 I described the advantages of continuum based computer simulations over other methods of investigating pre-planetesimal collisions. Several *benefits of SPH* over other (mainly mesh-based) numerical methods are listed. Again, I will restrain to those relevant for this thesis. Some of them were also pointed out, e.g. by Monaghan (2005) and Speith (2007) to name only the most recent reviews:

1. The SPH formalism allows an easy implementation of *different materials* by assigning material properties to different sets of SPH particles. In this work this feature will be used to distinguish a glass sphere impacting into porous dust or a dust ball hitting a glass surface.

2. In pre-planetesimal collisions *fragmentation* plays an essential role. The SPH scheme models fragmentation very naturally by the separation of particle clusters. Singularities caused by the absence of particles are consequently avoided.

3. Because SPH is a mesh-free method and SPH particles are understood as sampling points of the scheme, this allows *large deformations* of solid bodies to be simulated. Since the method is Lagrangian, the SPH particles follow the deformation of the material. Computation only takes place where there is material. This avoids large computational domains with overhead evaluation at grid points where no interesting physical processes take place. In simulations with fragmentation, all fragments carry their computational domain with them. In grid-based simulations, these fragments can leave the domain.

4. The SPH scheme is potentially *adaptive.* Because SPH particles follow the flow, they concentrate at regions with high density and they are sparse in low density regions.

5. By simple SPH particle placement, deliberately complex geometries can be generated. In this thesis, spheres, half-spheres, boxes and cylinders will be simulated.

disadvantages of SPH

Unfortunately, the SPH numerical method also comes with some *disadvantages*, which also affect the results of this thesis:

1. The most important disadvantage of SPH is given by its *high level of noise* which originates from the stochastic nature of the method. The noise level is higher than in grid-based method.

2. *Local accuracy* and *spatial resolution* are lower than in grid-based simulations with a corresponding number of grid points.

3. The treatment of *fixed boundaries* can cause problems in SPH. High density contrasts between two adjacent sets of particles can induce spurious particle oscillations and particle separation.

4. To model shocks accurately, artificial viscosity has to be introduced in the scheme. As a consequence, *spurious dissipation* and viscous shear may occur.

5. Because of the special form of the particle kernel, it is difficult to use other than cartesian coordinates with SPH (see e.g. Omang et al. 2006, 2007). Consequently, *geometrical symmetries* (e.g spherical and cylinder) cannot be utilised to reduce the computational costs.

6. In solid body and magnetohydrodynamics simulations SPH is prone to a *tensile instability* due to the low order of consistency of standard SPH.

Despite these disadvantages, the benefits of SPH outweigh the drawbacks for the topic of this thesis (see also Sec. 3.4).

4.1.1. Kernel interpolation and discretisation

In this section I will give a short overview of the basic numerical principle of SPH. The kernel interpolation, the interpolation of the spatial derivatives, and their discretisation will be introduced.

For the subsequent description I will follow the works of Schäfer (2005) and Speith (2007). The latter particularly offers a profound insight into the numerical properties of SPH. I will restrain to the relations which are directly relevant for this thesis. Throughout this section latin superscripts index SPH particles and particle dependencies. Greek subscripts denote vector components. The Einstein sum convention is applied to Greek indices, unless otherwise stated.

Kernel interpolation

In the SPH scheme, the continuous numerical quantities (e.g. density) appearing in the continuity, Euler, and energy equation have to be interpolated and discretised. For this an arbitrary function $f(\mathbf{x})$ can be expressed by the delta distribution function $\delta(\mathbf{x})$:

$$f(\mathbf{x}) = \int_V f(\mathbf{x}')\delta(\mathbf{x}-\mathbf{x}')\mathrm{d}^3x'. \tag{4.1}$$

The $\delta(\mathbf{x}-\mathbf{x}')$ is smoothed out over a distance h, the *smoothing length.* The latter controls the width of the function $W(\mathbf{x},\mathbf{x}';h)$, which determines the range of interactions with other SPH particles. The kernel function is required to converge for vanishing smoothing length

smoothing length

$$\lim_{h\to 0} W(\mathbf{x},\mathbf{x}';h) = \delta(\mathbf{x}-\mathbf{x}') \,. \tag{4.2}$$

$W(\mathbf{x},\mathbf{x}';h)$ is the *kernel function.* Hence, the approximation of $f(\mathbf{x})$ is given by

kernel function

$$\langle f(\mathbf{x})\rangle = \int_V f(\mathbf{x}')W(\mathbf{x},\mathbf{x}';h)\mathrm{d}^3x' \,. \tag{4.3}$$

normalisation It can be shown that this approximation is first order if Eq. 4.2 holds and the following *normalisation* condition is met:

$$\int_V W(\mathbf{x},\mathbf{x}';h)\mathrm{d}^3x' = 1\,. \tag{4.4}$$

spherical symmetry It proves to be convenient to choose $W(\mathbf{x},\mathbf{x}';h)$ such that it is *spherically symmetric*

$$W(\mathbf{x},\mathbf{x}';h) = W(|\mathbf{x}-\mathbf{x}'|;h) = W(\tilde{r};h)\,, \tag{4.5}$$

differentiability where $\tilde{r} = |\mathbf{x}-\mathbf{x}'|$, and with compact support, i.e. $W(\tilde{r};h) = 0$ for $\tilde{r} > h$. As a last condition $W(\tilde{r};h)$ has to be *differentiable* at least to first order.

Kernel interpolation and spatial derivatives

It can be shown that for compact, first order differentiable kernels, which fulfil the conditions of Eq. 4.2, 4.4 and 4.5, the following relations hold

$$\frac{\partial W(\tilde{r};h)}{\partial x_\alpha} = -\frac{\partial W(\tilde{r};h)}{\partial x'_\alpha}\,, \tag{4.6}$$

$$\int_V \frac{\partial W(\tilde{r};h)}{\partial x'_\alpha}\mathrm{d}^3x' = 0\,. \tag{4.7}$$

spatial derivative By partial integration and exploiting the antisymmetry of the kernel derivative in Eq. 4.6, the approximation of a *spatial derivative* is obtained

$$\left\langle \left.\frac{\partial f}{\partial x_\alpha}\right|_{\mathbf{x}} \right\rangle = \int_V f(\mathbf{x})\frac{\partial W(\tilde{r};h)}{\partial x_\alpha}\mathrm{d}^3x'\,, \tag{4.8}$$

where the surface term of the partial integration has been neglected. This is only valid if the computational domain is unlimited. If a fixed boundary problem is simulated with the standard algorithm anyway, this may cause severe numerical problems. Within this thesis boundary particles are used, which interact directly with the remaining set of particles. By this approach the boundary problem is avoided.

A more general version of Eq. 4.8 can be obtained by introducing a constant of integration $\hat{f}(\mathbf{x})$

$$\left\langle \left.\frac{\partial f}{\partial x_\alpha}\right|_{\mathbf{x}} \right\rangle = \int_V \left(f(\mathbf{x}') - \hat{f}(\mathbf{x})\right)\frac{\partial W(\tilde{r};h)}{\partial x_\alpha}\mathrm{d}^3x'\,, \tag{4.9}$$

which will prove to be useful for the following discretisation of the derivatives. It has to be underlined, that in Eq. 4.8 and 4.9 the interpolations of the derivatives were expressed by the derivative of an analytically known kernel function. This is one of the most important advantages of the SPH approach.

Discretisation

For the discretisation of Eq. 4.3 and 4.8 or 4.9, respectively, into a particle distribution some other quantities have to be introduced. The particle density $n(\mathbf{x})$ of N particles is given by

$$n(\mathbf{x}) = \sum_{a=1}^{N} \delta(\mathbf{x} - \mathbf{x}^a), \tag{4.10}$$

where $\mathbf{x}^a$ are the coordinates of the particles and $a = 1, \dots, N$. Using the convergence property of the kernel function (Eq. 4.2), the interpolation of the particle density can be expressed as

$$\lim_{h\to 0} \langle n(\mathbf{x}')\rangle = \lim_{h\to 0} \sum_{a=1}^{N} W(\mathbf{x}', \mathbf{x}^a; h) = n(\mathbf{x}')\,. \tag{4.11}$$

By multiplying Eq. 4.3 by $n(\mathbf{x}') / \langle n(\mathbf{x}')\rangle$ one finds

$$\langle\langle f(\mathbf{x}^a)\rangle\rangle = \sum_{b=1}^{N} \frac{f(\mathbf{x}^b)}{\langle n(\mathbf{x}^b)\rangle} W(\mathbf{x}^a, \mathbf{x}^b; h). \tag{4.12}$$

For the subsequent discussion the following abbreviations apply

$$f^a \equiv f(\mathbf{x}^a) \quad \text{and} \quad W^{ab} \equiv W(\mathbf{x}^a, \mathbf{x}^b; h)\,. \tag{4.13}$$

Eq. 4.12 can now be related to the interpolated density ρ^a and the mass m^a associated with the SPH particle at $\mathbf{x}^a$. Together with the definition

$$m^a \equiv \frac{\rho^a}{\langle n^a\rangle}, \tag{4.14}$$

the discretised version of Eq. 4.3 reads

SPH sum

$$\langle f^a\rangle = \sum_b \frac{m^b}{\rho^b} f^b W^{ab}\,, \tag{4.15}$$

where it is summed over the interaction partners of SPH particle b, i.e. all particles within a radius h around $\mathbf{x}^b$. This relation is commonly known as the *SPH sum*. Remarks on the approximation and the consistency of the SPH scheme can be found in Speith (2007).

The interpolation of the spatial derivative (Eq. 4.8) can be obtained in a similar way

spatial derivation interpolation

$$\left\langle \frac{\partial f^a}{\partial x^a_\alpha} \right\rangle = \sum_b \frac{m^b}{\rho^b} f^b \frac{\partial W^{ab}}{\partial x^a_\alpha}\,. \tag{4.16}$$

The discretisation obtained from Eq. 4.9 is used more frequently. It ensures that derivatives of constant functions always vanish, and hence leads to zeroth order consistency. It reads

$$\left\langle \frac{\partial f^a}{\partial x^a_\alpha} \right\rangle = \sum_b \frac{m^b}{\rho^b} (f^b - f^a) \frac{\partial W^{ab}}{\partial x^a_\alpha}\,, \tag{4.17}$$

where in the further discussion the approximation brackets will be omitted. This representation of the SPH derivative will be used in this thesis. The relations obtained for the discretisation of the kernel interpolation and its spatial derivatives can now be applied to the equations of hydrodynamics, which will be presented in the next section. The angle brackets, indicating the approximate character of $\langle f^a \rangle$, will be omitted from now on.

4.2. Hydrodynamics

The Euler and Navier-Stokes equations will be stated in the subsequent description without explicitly deriving them. This section closely follows an earlier work (Geretshauser 2006, and references therein). A more comprehensive treatment of the physics is given, e.g. by Landau and Lifshitz (1966). The interested reader is referred to this reference and other standard textbooks.

The theory of hydrodynamics is a macroscopic theory. Hence, it describes fluids and flows not in terms of moving molecules, but in terms of continua. That is, the physical behaviour of fluids and flows is completely determined by their spatially and temporally continuous velocity distribution $\mathbf{v}(\mathbf{x},t)$ and two arbitrary thermodynamic quantities. Commonly the pressure $p(\mathbf{x},t)$ and density $\rho(\mathbf{x},t)$ are chosen for this purpose. The theory of continua also assumes that an infinitesimally small fluid element is small compared to the whole of the fluid. However, it is large enough to contain a sufficient number of molecules for the continuum approximation to be satisfied. This is the important difference between the approach utilised in this thesis and MD simulations (see Sec. 3.2), which reach the continuum limit only for very large particle numbers. Therefore, an SPH particle is more similar to a fluid element, than to a molecule.

4.2.1. Equation of Continuity

The equation of continuity originates from the fundamental idea of the conservation of mass inside a finite volume element. The relation ensures that any change in density inside this volume element is caused only by flux of mass inwards or outwards. The equation of continuity reads in its (stationary) Eulerian form

$$\frac{\partial \rho}{\partial t} = -\frac{\partial(\rho v_\alpha)}{\partial x_\alpha} . \tag{4.18}$$

The Einstein notation is applied for spatial (Greek) indices throughout the section. Since SPH is a Lagrangian method, the sampling points (SPH particles) are co-moving with the flow. Therefore, the Eulerian time derivative $\partial/\partial t$ has to be replaced by the Lagrangian (substantial) time derivative $\mathrm{d}/\mathrm{d}t$. Both are related by

$$\frac{\mathrm{d}}{\mathrm{d}t} = \frac{\mathrm{d}x_\alpha}{\mathrm{d}t}\frac{\partial}{\partial x_\alpha} + \frac{\partial}{\partial t} = v_\alpha \frac{\partial}{\partial x_\alpha} + \frac{\partial}{\partial t} . \tag{4.19}$$

Consequently, the total derivative of the density is given by

$$\frac{\mathrm{d}\rho}{\mathrm{d}t} = \frac{\partial \rho}{\partial t} + v_\alpha \frac{\partial \rho}{\partial x_\alpha} , \tag{4.20}$$

and using this relation the *continuity equation* in Lagrangian form reads

Lagrangian continuity equation

$$\frac{\mathrm{d}\rho}{\mathrm{d}t} = -\rho \frac{\partial v_\alpha}{\partial x_\alpha} \,. \tag{4.21}$$

With the aid of Eq. 4.15, the density ρ can be directly converted into SPH representation for $f^a = \rho^a$, which yields

$$\rho^a = \sum_b m^b W^{ab} \,. \tag{4.22}$$

This representation works fine for purely hydrodynamical simulations. Therefore, it is widely used in astrophysical applications. By construction, the density is always positive and an additional time integration can be avoided. However, this representation is not suitable for solid body mechanics (see, e.g. Schäfer 2005, Geretshauser 2006, Speith 2007). This is because solid bodies usually have sharp boundaries. Particles at these edges have fewer interaction partners than particles in the centre of the body. As a consequence, the density associated with particles at an edge is lower, which can be seen from

$$\rho_{\mathrm{edge}} = \rho^a = \sum_b^N m^b W^{ab} < \sum_b^M m^b W^{cb} = \rho^c = \rho_{\mathrm{middle}} \,, \tag{4.23}$$

where $N < M$. Because the pressure is computed from the density distribution, the pressure for particles at the edge is negative, while particles in the centre have zero pressure. This effect can lead to unphysical particle motions and an unstable solid body.

For this reason, Randles and Libersky (1996) derive the SPH representation of the continuity equation from the alternative expression of the spatial derivative (Eq. 4.17). They find

SPH continuity equation (this thesis)

$$\frac{\mathrm{d}\rho}{\mathrm{d}t} = -\rho^a \sum_b \frac{m^b}{\rho^b} (v_\alpha^b - v_\alpha^a) \frac{\partial W^{ab}}{\partial x_\alpha} \,. \tag{4.24}$$

This representation is used for all simulations in this thesis. Other possibilities are listed by Speith (2007).

4.2.2. Euler and Navier-Stokes Equations

While the continuity equation takes care of the conservation of mass, the Euler equation is derived from the conservation of momentum. In general fluid elements can exchange momentum in motions tangential and perpendicular to each other. Therefore, the rate of change of momentum depends on a tensor

$$\rho \frac{\mathrm{d}v_\alpha}{\mathrm{d}t} = \frac{\partial \sigma_{\alpha\beta}}{\partial x_\beta} \,, \tag{4.25}$$

where $\sigma_{\alpha\beta}$ is the *stress tensor*. For an ideal fluid, tangential interactions of fluid elements is neglected and the stress tensor only depends on the pressure p

stress tensor

$$\sigma_{\alpha\beta} = -p\delta_{\alpha\beta} \,. \tag{4.26}$$

Lagrangian Euler equation

Hence, the *Euler equation* for ideal fluids reads

$$\rho \frac{\mathrm{d}v_\alpha}{\mathrm{d}t} = -\frac{\partial p}{\partial x_\alpha} \tag{4.27}$$

where p is the pressure. For the conservation of linear and angular momentum (Monaghan 1992), the pressure gradient term is symmetrised by

$$\frac{1}{\rho}\frac{\partial p}{\partial x_\alpha} = \frac{\partial}{\partial x_\alpha}\left(\frac{p}{\rho}\right) + \left(\frac{p}{\rho^2}\right)\frac{\partial p}{\partial x_\alpha}\,, \tag{4.28}$$

SPH Euler equation

inserted in Eq. 4.27 and discretised with Eq. 4.16 the SPH representation of the Euler equation is

$$\frac{\mathrm{d}v_\alpha^a}{\mathrm{d}t} = -\sum_b m^b \left(\frac{p^a}{(\rho^a)^2} + \frac{p^b}{(\rho^b)^2}\right)\frac{\partial W^{ab}}{\partial x_\alpha}\,. \tag{4.29}$$

A different representation (Schäfer 2005, Speith 2007)

$$\frac{\mathrm{d}v_\alpha^a}{\mathrm{d}t} = -\sum_b m^b \,\frac{p^b + p^a}{\rho^b \rho^a}\,\frac{\partial W^{ab}}{\partial x_\alpha} \tag{4.30}$$

is proposed to be more suitable and stable for solid body simulations. However, this was not tested within this work.

For the treatment of viscous fluids, the stress tensor (Eq. 4.26) has to be expanded by the *viscous stress tensor* $\tilde{\sigma}_{\alpha\beta}$. So far, only the translation of the fluid elements was considered. Viscosity, however, goes along with an irreversible momentum transfer (internal friction). Friction only appears, when moving fluid elements have different velocities with respect to each other. Therefore, the viscous stress tensor $\tilde{\sigma}_{\alpha\beta}$ depends on the spatial derivatives of the velocity field. As a consequence, the stress tensor is given by

$$\sigma_{\alpha\beta} = -p\delta_{\alpha\beta} + \tilde{\sigma}_{\alpha\beta}\,. \tag{4.31}$$

Lagrangian Navier-Stokes equation

Thus, the Lagrangian formulation of the obtained *Navier-Stokes equation* reads

$$\rho \frac{\mathrm{d}v_\alpha}{\mathrm{d}t} = -\frac{\partial p}{\partial x_\alpha} + \frac{\partial \tilde{\sigma}_{\alpha\beta}}{\partial x_\beta}\,, \tag{4.32}$$

viscous stress tensor

where the viscous stress tensor is defined as

$$\tilde{\sigma}_{\alpha\beta} \equiv \eta\left[\frac{\partial v_\alpha}{\partial x_\beta} + \frac{\partial v_\beta}{\partial x_\alpha} - \frac{2}{3}\delta_{\alpha\beta}\frac{\partial v_\gamma}{\partial x_\gamma}\right] + \zeta\delta_{\alpha\beta}\frac{\partial v_\gamma}{\partial x_\gamma}\,. \tag{4.33}$$

viscous shear

The term in brackets is symmetric and traceless. It is called *viscous shear tensor*. The quantity η is the corresponding *shear viscosity coefficient*[1] and describes the strength of energy dissipation by pure shearing of fluid elements. Pure shearing is characteristic for viscous incompressible fluids.

---

[1] The shear viscosity coefficient η is also known as *dynamic viscosity*

kinematic viscosity

The ratio between the shear viscosity coefficient and density is the *kinematic viscosity*

$$\nu = \frac{\eta}{\rho} . \tag{4.34}$$

In protoplanetary accretion discs, the effective kinematic viscosity is used to model the angular momentum transport in the accretion process (see Eq. 2.4, Sec. 2.1.1, and Sec. 2.1.4).

bulk viscosity

The last term in Eq. 4.33 is a diagonal tensor named *bulk viscosity*[2] and ζ is the *bulk viscosity coefficient*. The expression describes the energy dissipation by pure compression in compressible viscous fluids, for example by shocks. The according coefficient represents the dissipative strength. For incompressible fluids the bulk viscosity term vanishes.

In general, the viscosity coefficients depend on pressure and temperature which are not constant throughout the fluid. Consequently, ζ and η depend on the location in the fluid. For most fluids, this dependence can be neglected and the coefficients are treated as scalar constants. However, for the following discussion it is assumed that η^a and ζ^a depend on $\mathbf{x}^a$. Thus, they are attached to an SPH particle a and can assume different values for different SPH particles.

With the alternative representation of the spatial derivative (Eq. 4.17) the components of the velocity fields in Eq. 4.33 can be discretised to

$$v^a_{\alpha\beta} \equiv \frac{\partial v^a_\alpha}{\partial x_\beta} = \sum_b \frac{m^b}{\rho^b}(v^b_\alpha - v^a_\alpha)\frac{\partial W^{ab}}{\partial x^a_\beta} . \tag{4.35}$$

With this expression the viscous stress tensor (Eq. 4.33) can be written as

$$\tilde{\sigma}^a_{\alpha\beta} = \eta^a \left(v^a_{\alpha\beta} + v^a_{\beta\alpha} - \frac{2}{3}\delta_{\alpha\beta} v^a_{\gamma\gamma} \right) + \zeta^a \delta_{\alpha\beta} v^a_{\gamma\gamma} . \tag{4.36}$$

In analogy to Eq. 4.29, the SPH representation of the viscous part (e.g. Speith 1998) of the Navier-Stokes equation is given by

$$\left.\frac{\mathrm{d}v^a_\alpha}{\mathrm{d}t}\right|_{\mathrm{visc}} = \sum_b m^b \left(\frac{\tilde{\sigma}^a_{\alpha\beta}}{(\rho^a)^2} + \frac{\tilde{\sigma}^b_{\alpha\beta}}{(\rho^b)^2} \right) \frac{\partial W^{ab}}{\partial x^a_\beta} , \tag{4.37}$$

SPH Navier-Stokes equation

and with 4.29 and Eq. 4.31 the full equation can be written as

$$\begin{aligned} \frac{\mathrm{d}v^a_\alpha}{\mathrm{d}t} &= \sum_b m^b \left(\frac{(-p^a\delta_{\alpha\beta} + \tilde{\sigma}^a_{\alpha\beta})}{(\rho^a)^2} + \frac{(-p^b\delta_{\alpha\beta} + \tilde{\sigma}^b_{\alpha\beta})}{(\rho^b)^2} \right) \frac{\partial W^{ab}}{\partial x^a_\beta} \\ &= \sum_b mb \left(\frac{\sigma^a_{\alpha\beta}}{(\rho^a)^2} + \frac{\sigma^b_{\alpha\beta}}{(\rho^b)^2} \right) \frac{\partial W^{ab}}{\partial x^a_\beta} . \end{aligned} \tag{4.38}$$

A closer analysis (Speith 1998) reveals that this approach conserves linear momentum, but angular momentum is not conserved. Other possibilities of modelling this physical viscosity are listed, e.g. by Speith (1998, 2007) and Schäfer (2005). The ability of SPH to model viscous fluids was used to model protoplanetary accretion discs in various situations. Here, the SPH repre-

---

[2] Bulk viscosity is sometimes synonymously called *volume viscosity*.

sentation of the Navier-Stokes equations is only stated for the sake of completeness. However, the presented relations are related to the those of solid body SPH, which is described in Sec. 4.3. Physical viscosity can also be modelled by means of artificial viscosity by adding an extra pressure term Π^{ab} inside the square brackets. This will be discussed in Sec. 4.4.2.

4.2.3. Energy equation

Lagrangian energy equation

Using the mass (Eq. 4.21) and momentum (Eq. 4.32) conservation equations, the conservation of internal energy u can be formulated. It reads in Lagrangian form

$$\rho \frac{\mathrm{d}u}{\mathrm{d}t} = -p \frac{\partial v_\alpha}{\partial x_\alpha} + \tilde{\sigma}_{\alpha\beta} \frac{\partial v_\alpha}{\partial x_\beta} \,. \tag{4.39}$$

ideal fluid

The derivation of the SPH representation of the energy equation for *ideal fluids* consistent with Eq. 4.35 and 4.38 is given by

SPH energy equation ideal fluid

$$\frac{\mathrm{d}u^a}{\mathrm{d}t} = \frac{1}{2} \sum_b m^b \left(\frac{p^a}{(\rho^a)^2} + \frac{p^b}{(\rho^b)^2} \right) \left(v_\alpha^a - v_\alpha^b \right) \frac{\partial W^{ab}}{\partial x_\alpha} \,. \tag{4.40}$$

For viscous fluids the viscous stress tensor $\tilde{\sigma}_{\alpha\beta}$ (Eq. 4.33) has to be taken into account again and the SPH representation reads

SPH energy equation viscous fluid

$$\frac{\mathrm{d}u^a}{\mathrm{d}t} = \frac{1}{2} \sum_b m^b \left(\frac{\sigma_{\alpha\beta}^a}{(\rho^a)^2} + \frac{\sigma_{\alpha\beta}^b}{(\rho^b)^2} \right) \left(v_\alpha^a - v_\alpha^b \right) \frac{\partial W^{ab}}{\partial x_\beta} \,. \tag{4.41}$$

EOS

The set of continuity (Eq. 4.21), Euler (or Navier-Stokes) (Eq. 4.27 and 4.32), and energy (Eq. 4.39) equations has to be closed by the equation of motion of the SPH particles and a suitable *equation of state (EOS)*. For the simulations in this thesis the EOS is energy independent, and therefore the energy equation will not be used.

4.2.4. Equation of motion

With the equations presented so far the system of partial differential equations is underdetermined. To close this set, the equation of motion of the SPH particles has to be specified. Generally it is assumed that the particles move according to the velocity field at their respective location

$$\frac{\mathrm{d}x_\alpha^a}{\mathrm{d}t} = v_\alpha^a \,. \tag{4.42}$$

After sketching the application of SPH to pure hydrodynamical problems, I now turn to the second numerical basis of this thesis: the equations of solid body mechanics and their SPH interpolation and discretisation.

4.3. Solid Body Mechanics

Because the continuum theory of solid bodies is rarely used in astrophysical contexts, I will profoundly review its derivation and its most important quantities such as stress and strain tensors, bulk and shear moduli. In this description, I will stress the differences between fluids and solid bodies, which lead to additional material equations. This section closely follows an earlier introduction (Geretshauser 2006, and references therein). Firstly, the relations for the elastic behaviour of solid bodies are derived. As a second step, a theory for plasticity is described. In the third section, the relations obtained will be closed by a suitable porosity model, which appears as an equation of state. The SPH representations used in this thesis are presented at the appropriate locations.

4.3.1. Elastic behaviour of solid bodies

Both, the equations of hydrodynamics (presented in Sec. 4.2) and solid body mechanics belong to the theory of continua. Thus, molecules are again described as a collective by means of thermodynamical quantities such as density, pressure, and temperature. Therefore, the continuity equation can be transferred directly. The conservation laws for momentum and energy, however, have to be reformulated using different relations for the stress tensor $\sigma_{\alpha\beta}$. The reason for this lies in the fundamental difference between a fluid and a solid body: While in a fluid molecules can move around freely, in a solid body the intermolecular bonds are strong. As a consequence, elastic and plastic deformation of a solid body become possible. This constraint leads to new relations, which are derived in the following.

Deformation and the strain tensor

Let x_α be a (continuous) position inside a solid body. For some external force, acting on the solid body, each of its points is displaced to a new position $\tilde{x}_\alpha$. Then the *displacement vector* is given by

displacement vector

$$r_\alpha = \tilde{x}_\alpha - x_\alpha \,. \tag{4.43}$$

The displacement vector, as a function of the old coordinates, contains all information about the deformation of a solid body. The displacement vector can also be written as

$$\mathrm{d}\tilde{s}^2 = \mathrm{d}(\tilde{x}_\alpha)^2 = (\mathrm{d}x_\alpha + \mathrm{d}r_\alpha)^2 \;, \tag{4.44}$$

where $\mathrm{d}s = \sqrt{\mathrm{d}(x_\alpha)^2}$ and $\mathrm{d}\tilde{s} = \sqrt{\mathrm{d}(\tilde{x}_\alpha)^2}$ are infinitesimal distances between two points before and after the deformation, respectively. By means of the total differential

$$\mathrm{d}r = \frac{\partial r_\alpha}{\partial x_\alpha}\mathrm{d}x_\beta \,, \tag{4.45}$$

the infinitesimal displacement can be written as

$$\mathrm{d}\tilde{s}^2 = \mathrm{d}s^2 + \left(\frac{\partial r_\alpha}{\partial x_\beta} + \frac{\partial r_\beta}{\partial x_\alpha} + \frac{\partial r_\gamma}{\partial x_\alpha}\frac{\partial r_\gamma}{\partial x_\beta}\right)\mathrm{d}x_\alpha \mathrm{d}x_\beta \tag{4.46}$$

$$= \mathrm{d}s^2 + 2\epsilon_{\alpha\beta}\mathrm{d}x_\alpha \mathrm{d}x_\beta\,. \tag{4.47}$$

Green's strain tensor

By this construction the information of the deformation is transferred to the *Green's strain tensor* $\epsilon_{\alpha\beta}$, which can be derived from Eq. 4.47 in its exact form as

$$\epsilon_{\alpha\beta} = \frac{1}{2}\left(\frac{\partial r_\alpha}{\partial x_\beta} + \frac{\partial r_\beta}{\partial x_\alpha} + \frac{\partial r_\gamma}{\partial x_\alpha}\frac{\partial r_\gamma}{\partial x_\beta}\right)\,. \tag{4.48}$$

A quick look shows that $\epsilon_{\alpha\beta}$ is symmetric. Therefore, it can be diagonalised using principle axis transformation (PAT). However, the specific diagonal form of $\epsilon_{\alpha\beta}$ is only valid for (an infinitesimal region around) a chosen location. In general, the diagonal form does not apply for the whole solid body.

With the diagonal form of $\epsilon_{\alpha\beta}$, any deformation can be understood as the superposition of three independent deformations. Hence, Eq. 4.47 can be rewritten

$$\mathrm{d}\tilde{s}^2 = (1+2\epsilon_{11})\mathrm{d}x_1^2 + (1+2\epsilon_{22})\mathrm{d}x_2^2 + (1+2\epsilon_{33})\mathrm{d}x_3^2 \tag{4.49}$$

$$= \mathrm{d}\tilde{x}_1^2 + \mathrm{d}\tilde{x}_2^2 + \mathrm{d}\tilde{x}_3^2\,. \tag{4.50}$$

For the elastic case, it can be assumed that in a solid body molecules do not fully detach from each other. Otherwise the body fractures or becomes a fluid. Hence, homogeneous deformations are assumed, where neighbouring points have similar displacements, i.e. displacements do not vary largely with location and $|\partial r/\partial x_\alpha| \ll 1$. As a consequence, second order terms can be omitted. This leads to the definition of the (infinitesimal) strain tensor

strain tensor

$$\epsilon_{\alpha\beta} = \frac{1}{2}\left(\frac{\partial r_\alpha}{\partial x_\beta} + \frac{\partial r_\beta}{\partial x_\alpha}\right)\,. \tag{4.51}$$

While Green's strain tensor (Eq. 4.48) vanishes for rigid body motion in the case of finite strains, the infinitesimal strain tensor does not. Therefore, it has to be made sure that the latter is small for each timestep (Wegner and Haddow 2009). With Eq. 4.50 the deformation of an infinitesimal volume $\mathrm{d}V_1$ to $\mathrm{d}V_2$ can be expressed by means of the strain tensor $\epsilon_{\alpha\beta}$ in the following way

$$\begin{aligned}\mathrm{d}V_2 &= \mathrm{d}V_1(1+\epsilon_{11})(1+\epsilon_{22})(1+\epsilon_{33})\\ &= \mathrm{d}V_1(1+\epsilon_{11}+\epsilon_{22}+\epsilon_{33})\\ &= \mathrm{d}V_1(1+\epsilon_{\alpha\alpha})\,,\end{aligned} \tag{4.52}$$

where, again, higher order terms are neglected. The trace $\epsilon_{\alpha\alpha}$ is invariant under coordinate transformation and Eq. 4.52 holds for any coordinate system.

Forces and the stress tensor

From the deformation of a solid body the focus now turns to the resulting inner stresses. These are described by the *stress tensor.* With no external forces, the inner forces between adjacent volume elements vanish and the body is in *thermal equilibrium.* From the microscopic point of view, the Brownian motion of all molecules is balanced, such that there is no macroscopic motion.

thermal equilibrium

When external forces are applied, *inner stresses* arise and try to restore the original shape of the body, bringing it back to thermal equilibrium. The microscopic reasons for this are short range forces by molecular bonds. Transferring this to the macroscopic picture, this means that in continuum theory the inner stresses have to be formulated as forces acting on volume elements. Thus, the microscopic forces have to be expressed in terms of surface forces.

The resulting force F_α on a finite volume element V is given by

$$F_\alpha = \int_V \mathscr{F}_\alpha \mathrm{d}V\,, \tag{4.53}$$

where $\mathscr{F}_\alpha$ is the force density. Because the resulting force can be expressed in terms of the surface forces, the Gaussian Divergence Theorem can be applied. This reformulates the surface force as divergence of a vector. The force density can therefore be expressed as a tensor

$$F_\alpha = \int_V \mathscr{F}_\alpha \mathrm{d}V = \int_V \frac{\partial \sigma_{\alpha\beta}}{\partial x_\beta} \mathrm{d}V = \oint_{\delta V} \sigma_{\alpha\beta} \mathrm{d}f_\beta\,, \tag{4.54}$$

where $\mathrm{d}f_\beta$ is an infinitesimal surface element with the normal vector pointing outwards. In a Cartesian coordinate system with $\mathbf{z} || \mathbf{df}$, σ_{zz} is a surface density acting perpendicular to the surface, while σ_{zx} and σ_{zy} are tangential. Thus, $\sigma_{\alpha\beta}$ is symmetric.

hydrostatic compression

For the case of hydrostatic compression, there are no shear forces. Thus, $\sigma_{\alpha\beta} = 0$ for $\alpha \neq \beta$ and for the diagonal elements it holds that $\sigma_{\alpha\alpha} = -p$, where the direction of the pressure is antiparallel to $\mathbf{df}$. Consequently, the stress tensor can be written as

$$\sigma_{\alpha\beta} = -p\delta_{\alpha\beta}. \tag{4.55}$$

Stress strain relations

constitutive equations

Relations connecting the deformation (strain) of a material with its response (stress) are called (mechanical) *constitutive equations.* However, the term is used ambiguously throughout the literature. I regard constitutive equations to be the subset of the equations of state (discussed in Sec. 4.3.3), which relate thermodynamic state variables with each other. In this sense, constitutive equations connect the specific thermodynamic variables stress $\sigma_{\alpha\beta}$ and strain $\epsilon_{\alpha\beta}$ and their time derivatives with each other. For the derivation of such constitutive relations, $\epsilon_{\alpha\beta}$ and $\sigma_{\alpha\beta}$ have to be related to thermodynamic quantities such as the internal energy and free enthalpy. For this, the deformation work W carried out by internal forces F_α has to be defined. With small displacements δr_α, the change in work density is given by $\delta\mathscr{W} = \mathscr{F}_\alpha \delta r_\alpha$ and the total work reads

$$\begin{aligned} W &= \int_V \delta\mathscr{W} \mathrm{d}V' \\ &= \int_V \frac{\partial \sigma_{\alpha\beta}}{\partial x_\beta} \delta r_\alpha \mathrm{d}V' \\ &= -\int_V \sigma_{\alpha\beta} \frac{\partial}{\partial x_\beta} \delta r_\alpha \mathrm{d}V' \\ &= -\frac{1}{2}\int_V \sigma_{\alpha\beta}\delta\left(\frac{\partial r_\alpha}{\partial x_\beta} + \frac{\partial r_\beta}{\partial x_\alpha}\right)\mathrm{d}V' \\ &= -\int_V \sigma_{\alpha\beta}\delta\epsilon_{\alpha\beta}\mathrm{d}V' , \end{aligned} \tag{4.56}$$

where from the second to the third line, partial integration with a vanishing surface term is used. In the fourth line, the symmetry of $\sigma_{\alpha\beta}$ is exploited. As a result, the work density for small displacements is given by

$$\delta\mathscr{W} = -\sigma_{\alpha\beta}\delta\epsilon_{\alpha\beta} \tag{4.57}$$

reversible deformations

In this section only elastic deformations will be considered. In other words, the deformations are *reversible* and inner stresses restore the original shape of a body, once external forces vanish. As a second assumption, deformations shall take place slowly enough that for any point in time, the body is in thermal equilibrium. Plastic deformations are treated in Sec. 4.3.2.

internal energy

The infinitesimal change of *internal energy* is given by the sum of deformation work and heat produced in this process

$$\begin{aligned} \mathrm{d}U &= T\mathrm{d}S + \mathrm{d}W \\ &= T\mathrm{d}S + \sigma_{\alpha\beta}\mathrm{d}\epsilon_{\alpha\beta} , \end{aligned} \tag{4.58}$$

where $\mathrm{d}S$ is the infinitesimal change of entropy and T is the temperature. With Eq. 4.57 $\mathrm{d}U$ is related to $\sigma_{\alpha\beta}$ and $\epsilon_{\alpha\beta}$. For hydrostatic compressions $\sigma_{\alpha\beta} = -\delta_{\alpha\beta}p$ (Eq. 4.55) and

$$\begin{aligned} \mathrm{d}U &= T\mathrm{d}S - p\delta_{\alpha\beta}\mathrm{d}\epsilon_{\alpha\beta} \\ &= T\mathrm{d}S - p\mathrm{d}\epsilon_{\alpha\alpha} \\ &= T\mathrm{d}S - p\mathrm{d}V , \end{aligned} \tag{4.59}$$

free and Gibbs energies

where for the last line Eq. 4.52 is used[3]. By means of Laplace transformations of the thermodynamic variables, two other forms of energy can be derived from Eq. 4.58

$$F = U - TS \qquad \text{free energy} \tag{4.60}$$

$$G = F - \sigma_{\alpha\beta}\epsilon_{\alpha\beta} \qquad \text{Gibbs energy} , \tag{4.61}$$

---

[3] Please note that in Eq. 4.52 $\mathrm{d}V$ denotes a infinitesimal volume, whereas in Eq. 4.59 $\mathrm{d}\epsilon_{\alpha\alpha} = \mathrm{d}V$ denotes an infinitesimal change in volume.

and their respective infinitesimal changes are given by

$$\mathrm{d}F = -S\mathrm{d}T + \sigma_{\alpha\beta}\mathrm{d}\epsilon_{\alpha\beta} \tag{4.62}$$

$$\mathrm{d}G = -S\mathrm{d}T - \epsilon_{\alpha\beta}\mathrm{d}\sigma_{\alpha\beta}\,. \tag{4.63}$$

At the same time, the total differentials for $U(S,\epsilon_{\alpha\beta})$, $F(T,\epsilon_{\alpha\beta})$, and $G(T,\sigma_{\alpha\beta})$ read

$$\mathrm{d}U = \left(\frac{\partial U}{\partial S}\right)_{\epsilon_{\alpha\beta}} \mathrm{d}S + \left(\frac{\partial U}{\partial \epsilon_{\alpha\beta}}\right)_S \mathrm{d}\epsilon_{\alpha\beta}, \tag{4.64}$$

$$\mathrm{d}F = \left(\frac{\partial F}{\partial T}\right)_{\epsilon_{\alpha\beta}} \mathrm{d}T + \left(\frac{\partial F}{\partial \epsilon_{\alpha\beta}}\right)_T \mathrm{d}\epsilon_{\alpha\beta}, \tag{4.65}$$

$$\mathrm{d}G = \left(\frac{\partial G}{\partial T}\right)_{\sigma_{\alpha\beta}} \mathrm{d}T + \left(\frac{\partial G}{\partial \sigma_{\alpha\beta}}\right)_T \mathrm{d}\sigma_{\alpha\beta}\,. \tag{4.66}$$

For $S = const.$ in Eq. 4.64 and for $T = const.$ in Eq. 4.65 the total differentials can be compared with Eq. 4.58 and 4.62, respectively, which yields the following relations for the stress tensor

$$\sigma_{\alpha\beta} = \left(\frac{\partial U}{\partial \epsilon_{\alpha\beta}}\right)_S = \left(\frac{\partial F}{\partial \epsilon_{\alpha\beta}}\right)_T\,. \tag{4.67}$$

In analogy, the strain tensor can be expressed with Eq. 4.63 and 4.66 under the condition $T = const.$

$$\epsilon_{\alpha\beta} = -\left(\frac{\partial G}{\partial \sigma_{\alpha\beta}}\right)_T\,. \tag{4.68}$$

In order to derive a stress-strain relation, the isothermal condition in Eq. 4.67 is used. For small deformations F can be expanded into a Taylor series

$$F(\epsilon_{\alpha\beta}) = F(0) + \left.\frac{\partial F}{\partial \epsilon_{\alpha\beta}}\right|_{\epsilon_{\alpha\beta}=0} \epsilon_{\alpha\beta} + \frac{1}{2}\left.\frac{\partial^2 F}{\partial \epsilon^2_{\alpha\beta}}\right|_{\epsilon_{\alpha\beta}=0} \epsilon^2_{\alpha\beta} + \ldots\,, \tag{4.69}$$

where $\epsilon^2_{\alpha\beta}$ represents a scalar constructed from the strain tensor $\epsilon_{\alpha\beta}$. At constant temperature[4] and in an undeformed state ($\epsilon_{\alpha\beta} = 0$) all internal stresses are expected to vanish. Therefore, according to Eq. 4.67, the linear term of the expansion also has to vanish

$$\left.\sigma_{\alpha\beta}\right|_{\epsilon_{\alpha\beta}=0} = \left.\frac{\partial F}{\partial \epsilon_{\alpha\beta}}\right|_{\epsilon_{\alpha\beta}=0} = 0 \tag{4.70}$$

Neglecting terms of third and higher order, Eq. 4.69 can be expressed as

Lamé coefficients

$$F = F_0 + \frac{\lambda}{2}(\epsilon_{\alpha\alpha})^2 + \mu\epsilon_{\alpha\beta}\epsilon_{\alpha\beta}\,, \tag{4.71}$$

where λ and μ are the *Lamé coefficients*, which are scalars for isotropic media. For this equation, the second order term $\epsilon^2_{\alpha\beta}$ is decomposed into two independent scalar quantities: the square of

---

[4] The isothermal condition excludes deformation by change of temperature such as thermal expansion.

the trace $(\epsilon_{\alpha\alpha})^2$ and the sum over the squares of all components $\epsilon_{\alpha\beta}\epsilon_{\alpha\beta}$.

Since $\epsilon_{\alpha\beta}$ is a symmetric tensor, it can be decomposed into a symmetric traceless and a diagonal tensor

$$\epsilon_{\alpha\beta} = \left(\epsilon_{\alpha\beta} - \frac{1}{3}\delta_{\alpha\beta}\epsilon_{\gamma\gamma}\right) + \frac{1}{3}\delta_{\alpha\beta}\epsilon_{\gamma\gamma} \,. \tag{4.72}$$

The first part accounts for pure shear whereas the physical meaning of the second part is hydrostatic compression. For hydrostatic compression the volume of the body changes (see also Eq. 4.52), whereas for pure shear only the shape changes while the volume remains constant.

Inserting the decomposition of $\epsilon_{\alpha\beta}$ into Eq. 4.71 and omitting the constant F_0 yields

$$F = \mu\left(\epsilon_{\alpha\beta} - \frac{1}{3}\delta_{\alpha\beta}\epsilon_{\gamma\gamma}\right)^2 + \frac{K}{2}(\epsilon_{\gamma\gamma})^2 \tag{4.73}$$

with the *bulk modulus K* and the *shear modulus μ*, where the former is defined as

$$K = \lambda + \frac{2}{3}\mu \,. \tag{4.74}$$

Because the free energy F is always positive, it holds $K > 0$ and $\mu > 0$. Finally, for the stress-strain relation Eq. 4.73 is differentiated. This yields

$$\begin{aligned} \mathrm{d}F &= K\epsilon_{\gamma\gamma}\mathrm{d}\epsilon_{\alpha\alpha} + 2\mu\left(\epsilon_{\alpha\beta} - \frac{1}{3}\delta_{\alpha\beta}\epsilon_{\gamma\gamma}\right)\mathrm{d}\left(\epsilon_{\alpha\beta} - \frac{1}{3}\delta_{\alpha\beta}\epsilon_{\gamma\gamma}\right) \\ &= K\epsilon_{\gamma\gamma}\mathrm{d}\epsilon_{\alpha\alpha} + 2\mu\left(\epsilon_{\alpha\beta} - \frac{1}{3}\delta_{\alpha\beta}\epsilon_{\gamma\gamma}\right)\mathrm{d}\epsilon_{\alpha\beta} \\ &= \left(K\epsilon_{\alpha\alpha}\delta_{\alpha\beta} + 2\mu\left(\epsilon_{\alpha\beta} - \frac{1}{3}\delta_{\alpha\beta}\epsilon_{\gamma\gamma}\right)\right)\mathrm{d}\epsilon_{\alpha\beta} \\ &= \sigma_{\alpha\beta}\mathrm{d}\epsilon_{\alpha\beta} \,. \end{aligned} \tag{4.75}$$

From the first to the second line the term in brackets vanishes by multiplication with $\delta_{\alpha\beta}$, because this term is a traceless tensor. In the third line $\mathrm{d}\epsilon_{\alpha\alpha} = \delta_{\alpha\beta}\mathrm{d}\epsilon_{\alpha\beta}$ is used. The last line is given by Eq. 4.62 under the condition of constant temperature, where $-S\mathrm{d}T$ vanishes. Finally, this yields the desired stress-strain relation

stress-strain relation

$$\sigma_{\alpha\beta} = K\epsilon_{\gamma\gamma}\delta_{\alpha\beta} + 2\mu\left(\epsilon_{\alpha\beta} - \frac{1}{3}\delta_{\alpha\beta}\epsilon_{\gamma\gamma}\right) \,. \tag{4.76}$$

Hooke's law

strain-stress relation

This is a more general form of *Hooke's law*, which states that the force is proportional to the elongation of, e.g. a spring. Conversely, the strain tensor can be expressed as

$$\epsilon_{\alpha\beta} = \frac{1}{9K}\delta_{\alpha\beta}\sigma_{\gamma\gamma} + \frac{1}{2\mu}\left(\sigma_{\alpha\beta} - \frac{1}{3}\delta_{\alpha\beta}\sigma_{\gamma\gamma}\right) \,, \tag{4.77}$$

where $\sigma_{\alpha\alpha} = 3K\epsilon_{\alpha\alpha}$ is used, which follows directly from Eq. 4.76. For the case of hydrostatic compression the shear term in Eq. 4.76 vanishes and with Eq. 4.55 the change in volume solely *compressibility*

depends on the bulk modulus and the pressure p

$$\epsilon_{\alpha\alpha} = -\frac{p}{K} = -p\kappa \,, \tag{4.78}$$

where $\kappa = K^{-1}$ is the *compressibility*. Consequently, the stress tensor can be expressed as

$$\sigma_{\alpha\beta} = -p\delta_{\alpha\beta} + S_{\alpha\beta} \,, \tag{4.79}$$

deviatoric stress tensor

with the *deviatoric stress tensor* $S_{\alpha\beta}$ defined as

$$S_{\alpha\beta} = 2\mu\left(\epsilon_{\alpha\beta} - \frac{1}{3}\delta_{\alpha\beta}\epsilon_{\gamma\gamma}\right) . \tag{4.80}$$

Lagrangian momentum equation for solid body mechanics

The general equation for the conservation of momentum in solid body mechanics is identical to the pure hydrodynamics case (Eq. 4.25). The essential difference is in the form of the stress tensor. For the Euler and Navier-Stokes equations the stress tensor depends on the velocity field of the fluid. In contrast, for a solid body the stress tensor depends on the strain, i.e. on the deformation of a body. The *Lagrangian momentum equation for solid body mechanics* is given by

$$\rho\frac{\mathrm{d}v_\alpha}{\mathrm{d}t} = \frac{\partial\sigma_{\alpha\beta}}{\partial x_\beta} = -\frac{\partial p}{\partial x_\alpha} + \frac{\partial S_{\alpha\beta}}{\partial x_\beta} . \tag{4.81}$$

SPH momentum equation (this thesis)

The SPH representation of this equation used throughout this thesis reads

$$\frac{\mathrm{d}v^a_\alpha}{\mathrm{d}t} = \sum_b m^b\left(\frac{\sigma^a_{\alpha\beta}}{(\rho^a)^2} + \frac{\sigma^b_{\alpha\beta}}{(\rho^b)^2}\right)\frac{\partial W^{ab}}{\partial x^a_\beta} \tag{4.82}$$

with $\sigma_{\alpha\beta}$ as defined in Eq. 4.79. However, while p is given by a suitable EOS for every point in time, the time evolution of the deviatoric stress tensor and hence the time evolution of the strain tensor has to be specified.

Stress and strain rates

strain rate

For the time evolution of the strain, one has to define the velocity field $v_\alpha(\mathbf{x}, t)$ of the points constituting the solid body. In general, this velocity field depends on time and location. Infinitesimal displacements are given by $\mathrm{d}r_\alpha = v_\alpha \mathrm{d}t$. With the definition of the strain tensor (Eq. 4.51) for homogenous deformations ($|\partial r_\alpha / x_\beta| \ll 1$) the *strain rate tensor* is given by

$$\begin{aligned}
\dot{\epsilon}_{\alpha\beta} =& \frac{\mathrm{d}\epsilon_{\alpha\beta}}{\mathrm{d}t} && (4.83)\\
=& \frac{1}{2}\left(\frac{\mathrm{d}}{\mathrm{d}t}\frac{\partial r_\alpha}{\partial x_\beta} + \frac{\mathrm{d}}{\mathrm{d}t}\frac{\partial r_\beta}{\partial x_\alpha}\right) \\
=& \frac{1}{2}\left(\frac{\partial}{\partial x_\beta}\frac{\mathrm{d}r_\alpha}{\mathrm{d}t} + \frac{\partial}{\partial x_\alpha}\frac{\mathrm{d}r_\beta}{\mathrm{d}t}\right) \\
=& \frac{1}{2}\left(\frac{\partial v_\alpha}{\partial x_\beta} + \frac{\partial v_\beta}{\partial x_\alpha}\right) . && (4.84)
\end{aligned}$$

Its SPH representation is given by

$$\dot{\epsilon}^a_{\alpha\beta} = \frac{1}{2}\sum_b \frac{m^b}{\rho^b}\left((v^b_\alpha - v^a_\alpha)\frac{\partial W^{ab}}{\partial x^a_\beta} + (v^b_\beta - v^a_\beta)\frac{\partial W^{ab}}{\partial x^b_\alpha}\right) . \tag{4.85}$$

frame invariance

Eringen (1962) introduced the *axiom of objectivity*, which states that the constitutive equation must be invariant under changes of reference frame. Based on this work, Truesdell and Noll (1965) investigated the concept of *frame invariance* and its significance for mechanics. A quantity or equation is *frame invariant* if it transforms in a defined way with the frame of reference. The transformation between two frames of reference can be written as

$$\bar{\mathbf{x}}(t) = \mathbf{Q}\mathbf{x}(t) + \mathbf{c}(t) , \tag{4.86}$$

where $\mathbf{Q}$ is an orthogonal rotation tensor of second order, and $\mathbf{c}$ is a vector. The time dependence will not be stated explicitly for the following discussion. For $Q_{\alpha\beta} = \delta_{\alpha\beta}$ and $\mathbf{c}(t) = const.$ the transformation is Galilean.

Any vector $\mathbf{w}$ and tensor $\mathbf{T}$ is called objective or frame invariant if they fulfil the conditions

$$\bar{\mathbf{w}} = \mathbf{Q}\mathbf{w} \tag{4.87}$$

$$\bar{\mathbf{T}} = \mathbf{Q}^{\mathrm{T}}\mathbf{T}\mathbf{Q} , \tag{4.88}$$

where $\mathbf{Q}^{\mathrm{T}}$ denotes the transpose of $\mathbf{Q}$. With Eq. 4.86 the transformation of the spatial partial derivative is given by

$$\frac{\partial}{\partial\bar{\mathbf{x}}} = \frac{\partial}{\partial\mathbf{x}}\frac{\mathrm{d}\mathbf{x}}{\mathrm{d}\bar{\mathbf{x}}} = \frac{\partial}{\partial\mathbf{x}}\frac{\partial}{\partial\bar{\mathbf{x}}}\left(\mathbf{Q}^{\mathrm{T}}\mathbf{x} - \mathbf{c}\right) = \frac{\partial}{\partial\mathbf{x}}\mathbf{Q}^{\mathrm{T}} , \tag{4.89}$$

and, consequently, the partial derivative is not objective. The displacement vector $\mathbf{r} = \mathbf{x}_2 - \mathbf{x}_1$ (Eq. 4.43) is objective, which follows directly from Eq. 4.86. However, the velocity field given by differentiating Eq. 4.86, denoted by the common dot-abbreviation,

$$\begin{aligned}\bar{\mathbf{v}} = \frac{\mathrm{d}\bar{\mathbf{x}}}{\mathrm{d}t} &= \dot{\mathbf{Q}}\mathbf{x} + \mathbf{Q}\dot{\mathbf{x}} + \dot{\mathbf{c}} \\ &= \mathbf{Q}\mathbf{v} + \dot{\mathbf{c}} + \dot{\mathbf{Q}}(\bar{\mathbf{x}} - \mathbf{c}) , \end{aligned} \tag{4.90}$$

is not objective. In this relation the common abbreviation $\dot{\mathbf{x}} = \frac{\mathrm{d}}{\mathrm{d}t}\mathbf{x}$ is used. From this one can define two useful quantities

$$\bar{\mathbf{G}} = \frac{\partial\bar{\mathbf{r}}}{\partial\bar{\mathbf{x}}} = \mathbf{Q}\frac{\partial\mathbf{r}}{\partial\mathbf{x}}\mathbf{Q}^{\mathrm{T}} = \mathbf{Q}\mathbf{G}\mathbf{Q}^{\mathrm{T}} \tag{4.91}$$

$$\bar{\mathbf{L}} = \frac{\partial\bar{\mathbf{v}}}{\partial\bar{\mathbf{x}}} = \mathbf{Q}\frac{\partial\mathbf{v}}{\partial\mathbf{x}}\mathbf{Q}^{\mathrm{T}} + \dot{\mathbf{Q}}\mathbf{Q}^{\mathrm{T}} = \mathbf{Q}\mathbf{L}\mathbf{Q}^{\mathrm{T}} + \dot{\mathbf{Q}}\mathbf{Q}^{\mathrm{T}} . \tag{4.92}$$

It follows that the strain tensor

$$\begin{aligned}\bar{\epsilon} &= \frac{1}{2}\left(\bar{\mathbf{L}} + \bar{\mathbf{L}}^{\mathrm{T}}\right)\\ &= \frac{1}{2}\left(\mathbf{QGQ}^{\mathrm{T}} + \left(\mathbf{QGQ}^{\mathrm{T}}\right)^{\mathrm{T}}\right)\\ &= \frac{1}{2}\left(\mathbf{QGQ}^{\mathrm{T}} + \mathbf{QG}^{\mathrm{T}}\mathbf{Q}^{\mathrm{T}}\right)\\ &= \mathbf{Q}\epsilon\mathbf{Q}^{\mathrm{T}}\,, \end{aligned} \tag{4.93}$$

is objective. However, for an arbitrary objective tensor **T** the time derivative is not frame invariant since

$$\dot{\bar{\mathbf{T}}} = \mathbf{Q}\dot{\mathbf{T}}\mathbf{Q}^{\mathrm{T}} + \dot{\mathbf{Q}}\mathbf{T}\mathbf{Q}^{\mathrm{T}} + \mathbf{Q}\mathbf{T}\dot{\mathbf{Q}}^{\mathrm{T}}\,. \tag{4.94}$$

For the construction of arbitrary frame invariant tensors, a *rotation rate tensor* is defined as

rotation rate

$$\begin{aligned}\bar{\mathbf{R}} &\equiv \frac{1}{2}\left(\frac{\partial \mathbf{v}}{\partial \bar{\mathbf{x}}} - \left(\frac{\partial \mathbf{v}}{\partial \bar{\mathbf{x}}}\right)^{\mathrm{T}}\right)\\ &= \frac{1}{2}\left(\bar{\mathbf{L}} - \bar{\mathbf{L}}^{\mathrm{T}}\right)\\ &= \frac{1}{2}\left(\mathbf{QLQ}^{\mathrm{T}} - \mathbf{QL}^{\mathrm{T}}\mathbf{Q}^{\mathrm{T}} + 2\dot{\mathbf{Q}}\mathbf{Q}^{\mathrm{T}}\right)\\ &= \mathbf{QRQ}^{\mathrm{T}} + \dot{\mathbf{Q}}\mathbf{Q}^{\mathrm{T}}\,, \end{aligned} \tag{4.95}$$

where the identity $\mathrm{d}/\mathrm{d}t\,(\mathbf{QQ}^{\mathrm{T}}) = \dot{\mathbf{Q}}\mathbf{Q}^{\mathrm{T}} + \mathbf{Q}\dot{\mathbf{Q}}^{\mathrm{T}} = 0$ is used. In SPH formalism the rotation rate tensor is formulated as

SPH rotation rate (this thesis)

$$R^a_{\alpha\beta} = \frac{1}{2}\sum_b \frac{m^b}{\rho^b}\left((v^b_\alpha - v^a_\alpha)\frac{\partial W^{ab}}{\partial x^a_\beta} - (v^b_\beta - v^a_\beta)\frac{\partial W^{ab}}{\partial x^a_\alpha}\right). \tag{4.96}$$

From this quantity one obtains

$$\dot{\mathbf{Q}} = \bar{\mathbf{R}}\mathbf{Q} - \mathbf{QR} \tag{4.97}$$

$$\dot{\mathbf{Q}}^{\mathrm{T}} = -\mathbf{Q}^{\mathrm{T}}\bar{\mathbf{R}} + \mathbf{RQ}^{\mathrm{T}}\,, \tag{4.98}$$

which can be inserted into Eq. 4.94. Together with the definition for an objective tensor (Eq. 4.88) this yields the relation

$$\dot{\bar{\mathbf{T}}} - \bar{\mathbf{R}}\bar{\mathbf{T}} + \bar{\mathbf{R}}\bar{\mathbf{T}} = \mathbf{Q}(\dot{\mathbf{T}} - \mathbf{RT} + \mathbf{RT})\mathbf{Q}^{\mathrm{T}}\,, \tag{4.99}$$

which states that the quantity in brackets on the right is an objective tensor rate. This is the *co-rotational or Jaumann rate* proposed by Jaumann (1911).

Jaumann rate

With Eq. 4.99 the constitutive equation for the *deviatoric stress* rate can be formulated from Eq. 4.80 in a frame invariant form as

deviatoric stress rate

$$\frac{\mathrm{d}S_{\alpha\beta}}{\mathrm{d}t} = 2\mu\left(\dot{\epsilon}_{\alpha\beta} - \frac{1}{3}\delta_{\alpha\beta}\dot{\epsilon}_{\gamma\gamma}\right) + S_{\alpha\gamma}R_{\gamma\beta} - R_{\alpha\gamma}S_{\gamma\beta}\,. \tag{4.100}$$

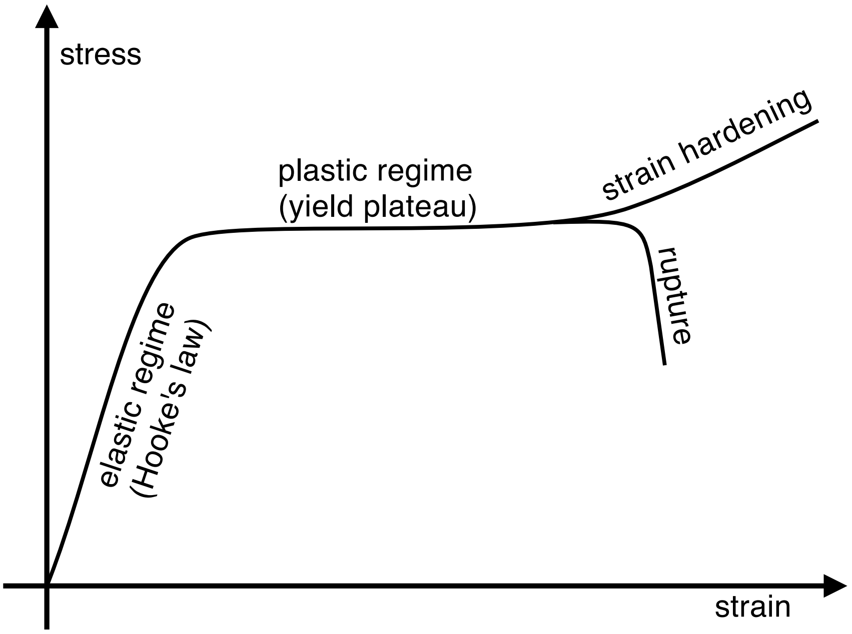

Figure 4.1. *Schematic stress-strain relation.* With increasing strain, the material develops a stress, which is proportional to the strain. This is synonymous with Hooke's law. In this regime the deformation is elastic and reversible. Once the strain reaches the yield limit, the stress remains constant with increasing strain. This behaviour is referred to as yield plateau. Various behaviours are possible after this regime. Either the material ruptures or the stress increases again with higher strain. The latter behaviour is called strain hardening.

Its SPH representation is given by substituting Eq. 4.85 and Eq. 4.96 into this expression. Before the set of equations is closed with a suitable EOS by the applied porosity model, a short introduction on the theory of plasticity has to be given.

4.3.2. Plastic behaviour of solid bodies

As a motivation for the theory of plasticity used in this thesis, I present a short example: A small steel spherule is dropped not too far from the surface of a wooden desk. After hitting the solid surface, the ball will bounce off before it falls down again. A closer look reveals that neither the ball nor the desk show any kind of damage. During the impact both materials are deformed elastically and thus returned to their previous states. This experiment can be repeated with increasing height and at a certain height a little dint in the desk appears. Because of the higher impact speed, which yields higher dynamic pressure onto the surface, the material of the desk leaves the elastic regime and is deformed plastically. Therefore, it is reasonable to assume that there is some kind of pressure threshold which marks the transition from the elastic to the plastic regime. A schematic stress-strain relation for the elastic and plastic regimes is shown in Fig. 4.1. Initially, the material shows elastic behaviour with stress responding proportionally to increasing strain (Hooke's law). Then it reaches the *yield plateau*, where stress remains constant while the strain is increased. It can easily be seen why this condition leads to irreversible plastic deformation. Increasing strain is equivalent to increasing deformation. If stress in the elastic regime is understood as the ability of a material to restore its original shape for vanishing external forces, then constant stress for increasing deformation means that internal stress only partially restores the original shape once external stresses cease. The consequence is plastic deformation. The behaviour after the yield plateau depends on the material type. For some materials stress increases with strain again. This phenomenon is called *strain hardening*. Other materials rupture in plastic flow or simply fracture.

yield plateau

strain hardening

Since the stress tensor $\sigma_{\alpha\beta}$ is symmetric, it can be diagonalised by means of principle axis transformation (PAT). As a result, any stress can be represented by the principle stresses σ_1, σ_2, and σ_3 with $\sigma_1 \geq \sigma_2 \geq \sigma_3$ (see Kachanov 1971, for a comprehensive introduction). For most materials the change in shape is caused by shear deformations. Therefore, at first a criterion for the plastic deformation by shear is formulated. Such criteria are often referred to as yield criteria, which cause the yield plateau in Fig. 4.1. The principle is simple: once the shear exceeds a certain limit, the deformation is plastic and the shear is reduced in a suitable way. By the reduction of the shear stress, the material deviates from Hooke's law and follows the yield plateau path. Because yielding by shear is the most prominent plasticity criterion, the threshold value is often simply called *yield strength*. Since in Sec. 4.3.4 two other yield criteria for pure hydrostatic pressure will be introduced, I will use the more appropriate term *shear strength* for the shear threshold.

shear strength

For isotropic media, the shear strength has to be a symmetric function of the principal stresses

$$f(\sigma_1, \sigma_2, \sigma_3) = const. = K\,. \tag{4.101}$$

Because the influence of the mean pressure p on plastic deformations by shear can be neglected, the plasticity criterion for shear can be formulated by means of the deviatoric stress tensor $S_{\alpha\beta}$ and its principal deviatoric stresses s_1, s_2, and s_3, which are parallel to the respective principal stresses. Thus, it is

$$f(s_1, s_2, s_3) = const. = K\,. \tag{4.102}$$

From the deviatoric stress tensor three invariants can be constructed. These are

$$I_1(S_{\alpha\beta}) = S_{\alpha\alpha} = 0\,, \tag{4.103}$$

$$I_2(S_{\alpha\beta}) = \frac{1}{2} S_{\alpha\beta} S_{\alpha\beta} = \frac{1}{6}\left((\sigma_1 - \sigma_2)^2 + (\sigma_2 - \sigma_3)^2 + (\sigma_3 - \sigma_1)^2\right)\,, \tag{4.104}$$

$$I_3(S_{\alpha\beta}) = \frac{1}{3} S_{\alpha\beta} S_{\beta\gamma} S_{\gamma\alpha} = s_1 s_2 s_3\,. \tag{4.105}$$

The first invariant I_1 vanishes because $S_{\alpha\beta}$ is constructed to be traceless. The second invariant is expressed by the principal axes of $\sigma_{\alpha\beta}$ and the third invariant by the principal axes of $S_{\alpha\beta}$. Now, the plasticity criterion can be reformulated

$$f\left(I_1(S_{\alpha\beta}), I_2(S_{\alpha\beta}), I_3(S_{\alpha\beta})\right) = f\left(I_2(S_{\alpha\beta}), I_3(S_{\alpha\beta})\right) = K\,. \tag{4.106}$$

From experiments, the French engineer Tresca conjectured that for a material in a yield state (on the yield plateau) the maximum tangential stress $1/2\,\sigma_s$ is the same at all points of the medium.

Tresca-Saint Vernant criterion

From that he formulated the *Tresca-Saint Vernant criterion*

$$\begin{aligned}|\sigma_1-\sigma_2| &\leq \sigma_\mathrm{s}\\ |\sigma_2-\sigma_3| &\leq \sigma_\mathrm{s}\\ |\sigma_3-\sigma_1| &\leq \sigma_\mathrm{s}\end{aligned} \tag{4.107}$$

von Mises criterion

Because of mathematical difficulties in three-dimensional problems, von Mises approximated this by what became known as the *von Mises criterion*

$$(\sigma_1-\sigma_2)^2+(\sigma_2-\sigma_3)^2+(\sigma_3-\sigma_1)^2=2\sigma_s^2\,. \tag{4.108}$$

Both criteria are clearly constructed from the second invariant I_2 of the deviatoric stress tensor. In this thesis the more commonly used van Mises criterion is applied.

stress space

This criterion can be interpreted geometrically (Fig. 4.2) in *stress space* (see Kachanov 1971, for an approach to the geometrical interpretation). In this space every possible stress is represented by a point given as a linear combination of the principle stresses σ_1, σ_2, and σ_3, which represent the axes of stress space. In there, the van Mises criterion takes the form of a cylinder[5] with radius $Y=\sqrt{2/3}\,\sigma_\mathrm{s}$ and infinite extensions in the z-direction. The cylinder is centred around the *hydrostatic axis* given by $\sigma_1=\sigma_2=\sigma_3$, which represents the set of stresses with pure hydrostatic compression ($p>0$) or tension ($p<0$) and vanishing shear. Any parallel line to the hydrostatic axis not intersecting the origin represents a set of stresses with hydrostatic compression or tension at constant shear. Conversely, the plane perpendicular to the hydrostatic axis intersecting the origin is called *deviatoric plane*, which is identical to a set of stresses with pure shear and vanishing mean pressure. Any parallel plane represents shear stress at constant mean pressure.The points inside this cylinder represent stresses in the elastic regime; those outside represent stresses in the plastic regime. The points on the surface are stresses, where the transition takes place.

In Fig. 4.2 the cylinder has finite length[6] given by $\Sigma+T$, where the *compressive strength* Σ, is given by the distance from the deviatoric plane to the bottom plane, limits hydrostatic compression and the *tensile strength* T limits hydrostatic tension. These quantities are introduced by the porosity model (see Sec. 4.3.4). From this point of view entering the plastic regime can happen in two ways: leaving the cylinder at its top or base and leaving it at its lateral surface. Exiting at the bottom corresponds to compressing the material until it reaches the critical transition point for plastic compression. Leaving the cylinder at the top is equivalent to the material rupturing during expansion. Exiting through the lateral surface corresponds to exceeding the shear strength Y.

4.3.3. Equations of state

EOS

In general, *equations of state (EOS)* relate thermodynamic state variables such as pressure, temperature, density, etc. with each other. They are essential for the description of the behaviour of solids and fluids, since they close the system of partial differential equations given by the continuity equation (Eq. 4.21), the momentum equation (Eq. 4.81), and the energy equation (Eq. 4.39). While these equations are derived from fundamental conservation principles, the EOS contain all the material-dependent physics. In this section I will shortly introduce some important EOS.

---

[5] The Tresca-Saint Vernant criterion has the shape of a hexagon.

[6] Distances in stress space are measured in pressure units, i.e. Pa.

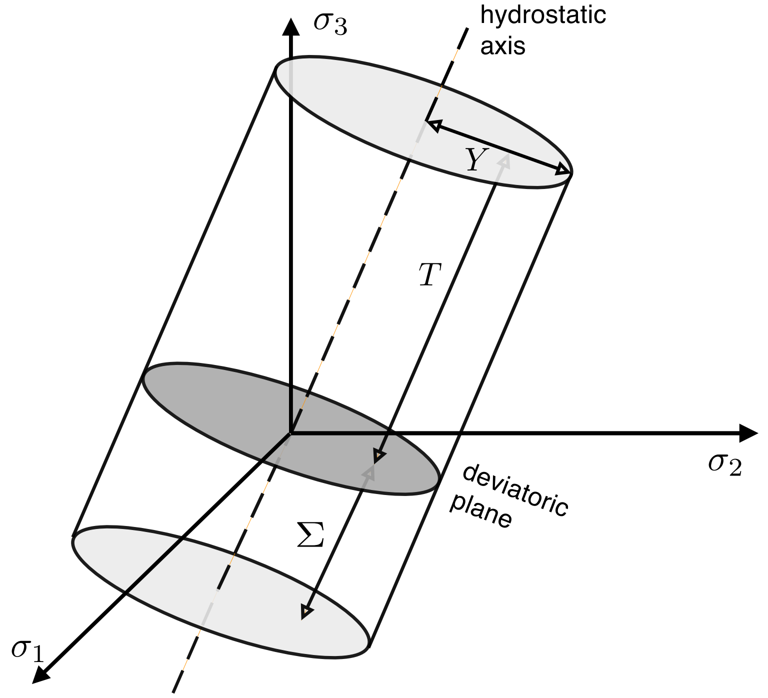

Figure 4.2. *Porosity model yield conditions.* In stress space given by the principal stresses σ_1, σ_2, and σ_3 the yield conditions can be interpreted geometrically. The von Mises yield criterion is represented as a cylinder around the hydrostatic axis, which is perpendicular to the deviatoric plane. Pure shear stresses at a given mean pressure p are represented as points on a surface parallel to the deviatoric plane intersecting the point $\sigma_1 = \sigma_2 = \sigma_3 = p$ of the hydrostatic axis. Pure pressure increase and decrease at constant shear is represented by lines parallel to the hydrostatic axis. The elastic regime is given by the set of points inside the cylinder. Outside applied stresses lead to plastic deformations. Pure shear is delimited by the shear strength Y, while the hydrostatic pressure thresholds are the compressive (Σ) and tensile (T) strengths, respectively.

Liquid equation of state

For liquids, the pressure p depends linearly on the density ρ of the liquid, if the compressions and expansions remain small, then the continuity equation and momentum equation are connected by

$$p = c_s^2(\rho - \rho_0)\,, \tag{4.109}$$

where c_s is the sound speed and ρ_0 is the density for an uncompressed liquid. This EOS is independent of the specific internal energy u. Therefore, the energy equation does not need to be solved for liquids governed by Eq. 4.109. The sound speed is related to the bulk modulus

$$c_s^2 = \frac{K_0}{\rho_0}. \tag{4.110}$$

The liquid equation of state looses its validity once ρ becomes significantly smaller than ρ_0. For values of 80-95% of the ratio ρ/ρ_0 Melosh (1989) recommends setting the pressure to zero in simulations.

Perfect gas equation

The equation for a perfect gas is given by

$$p = (\gamma - 1)\rho u\,, \tag{4.111}$$

where u is the specific internal energy and the adiabatic coefficient $\gamma = C_p/C_V$. C_p and C_V are the specific heat at constant pressure and volume, respectively. The quantity γ is related to the number of degrees of freedom of the gas. For example for a monoatomic gas $\gamma = 5/3$. For the perfect gas equation all three conservation equations have to be solved.

Murnaghan equation of state

This equation of state is an expansion of the liquid equation of state. In contrast to the latter the dependency of the pressure on the density here is nonlinear

$$p = \left(\frac{K_0}{n}\right)\left(\left(\frac{\rho}{\rho_0}\right)^n - 1\right) \tag{4.112}$$

where K_0 is the bulk modulus at zero pressure. The constant n is one of the Murnaghan parameters of which a list can be found in Melosh (1989) for various materials. This equation of state has a wide range of applications.

Within this thesis, the Murnaghan EOS is used to simulate glass in the benchmark experiments presented in Ch. 5. Since it does not depend on the internal energy its use is limited to the condition of isothermal compression.

Tillotson equation of state

The Tillotson EOS was originally developed by Tillotson (1962) for high-velocity impacts of metals in military context. Two regimes are distinguished using the specific internal energy u

$$p = \begin{cases} \left(a + \frac{b}{u/(u_\mathrm{v}\eta^2)+1}\right)\rho u + A(\eta - 1) + B(\eta - 1)^2 & u < u_\mathrm{iv} \\ a\rho u + \left(\frac{b\rho u}{u/(u_\mathrm{v}\eta^2)+1} + A(\eta - 1)e^{-\beta(\rho_0/\rho - 1)}\right) e^{-\alpha(\rho_0/\rho - 1)} & u > u_\mathrm{cv} \end{cases}, \tag{4.113}$$

where u_iv and u_cv are the specific energies for incipient and complete vaporisation, respectively. The former characterises a compressed state, while the latter refers to an expanded state. The quantity u_v is a fit parameter close to the vaporisation energy. ρ denotes the material density and ρ_0 the density at zero external pressure and $\eta = \rho/\rho_0$. The quantities α, β, a, b, A, and B are material constants. For internal energies $u_\mathrm{iv} < u < u_\mathrm{cv}$ a linear interpolation between compressed and expanded states is applied.

The relatively simple analytical form of the Tillotson EOS has the advantage of low computational costs. The numerous free material parameters open a wide field of possible applications. In particular, the sophisticated treatment of the internal energy makes the equation applicable to processes where melting and (partial) vaporisation plays a role, e.g. in high-velocity collisions. However, the needed material parameters are difficult to determine, and thus known only for a few materials.

In astrophysics the Tillotson EOS was used for asteroid collisions in the km/s regime. Many simulations based on the code by Benz and Asphaug (1994, 1995) apply the Tillotson EOS. Michel et al. (2002, 2003, 2004) utilise material parameters for basalt and Jutzi et al. (2008, 2009b,a, 2010) implemented a simplified version of the Tillotson EOS with basalt parameters except for the density, which was set to the value of pumice.

For this thesis the Tillotson EOS is not applied for two reasons: Firstly, this work focuses on low velocity impacts where the processes of vaporisation and melting do not play a significant role. Secondly, the material parameters needed are not available for SiO_2 dust. For this reason, I utilise an approach which combines a suitable porosity model with the equation of state. This is presented in the next section.

4.3.4. The porosity model

Sub-resolution porosity

Colloquially, a porous material is a solid which is interspersed with small hollow spaces. In molecular dynamics simulations (see Sec. 3.2) voids are naturally simulated, where no monomers are present. In contrast, combining a continuum approach with a suitable porosity model reveals a subtle but striking difficulty. As long as the typical size of the voids is larger than the spatial resolution, then voids can simply be modelled as regions with vanishing density. As in this thesis, the continuum approach is usually chosen because it allows averages over microscopic structures to be carried out and to simulate objects of arbitrary sizes by adjusting the spatial resolution. However, this area of application conflicts with resolving the microscopic structures of porous aggregates. In other words, a way has to be found to implement the influence of porous structures below the spatial resolution of the macroscopic material properties.

filling factor, porosity

For this, the two continuous quantities

$$\Phi = \frac{V_\mathrm{h}}{V} \quad \text{and} \quad \phi = \frac{V_\mathrm{s}}{V} \tag{4.114}$$

are defined, where Φ is the *porosity* and ϕ denotes the *filling factor*. V, V_h, and V_s are the total, hollow, and solid volumes, respectively. Both quantities are related by

$$\phi = \frac{V_\mathrm{s}}{V} = \frac{V - V_\mathrm{h}}{V} = 1 - \frac{V_\mathrm{h}}{V} = 1 - \Phi. \tag{4.115}$$

The filling factor ϕ will be the primary quantity that describes the porous properties of dust aggregates in this thesis. To express ϕ in terms of the density of the solid matrix material ρ_s and the actual density ρ of the porous body, which is averaged over hollow and filled volumes, the relation

$$\rho = \frac{m}{V} = \frac{m_\mathrm{s} + m_\mathrm{h}}{V_\mathrm{s} + V_\mathrm{h}} = \frac{m_\mathrm{s}}{V_\mathrm{s} + V_\mathrm{h}} = \frac{\frac{m_\mathrm{s}}{V_\mathrm{s}}}{1 + \frac{V_\mathrm{h}}{V_\mathrm{s}}} = \frac{\rho_\mathrm{s}}{1 + \frac{V_\mathrm{h}}{V - V_\mathrm{h}}}, \tag{4.116}$$

is used, where the mass of the hollow space $m_\mathrm{h} = 0$. This yields the definition of ϕ

$$\frac{\rho}{\rho_\mathrm{s}} = \frac{V - V_\mathrm{h}}{V} = \frac{V_\mathrm{s}}{V} = \phi\,. \tag{4.117}$$

distention

A third quantity to describe the porosity of a body is the *distention* which is defined as

$$\alpha \equiv \frac{\rho_\mathrm{s}}{\rho} = \frac{1}{\phi} = \frac{1}{1 - \Phi} \tag{4.118}$$

where $\alpha = 1$ refers to a completely compressed state, where $\rho = \rho_\mathrm{s}$. In contrast to the distention, filling factor and porosity have the advantage of depicting the ratio between filled and hollow volume.

Porosity models

porosity models

Various porosity models for hydrodynamics codes were proposed in the past. They can be divided into two classes: *matrix-based models* and *plasticity-based models* (e.g. Arena and Speith 2011).

matrix-based porosity models

Matrix based porosity models originate from the $p - \alpha$ model developed by Herrmann (1969). Offsprings of this family are the $\rho - \alpha$ model by Benz and Jutzi (2007) and the $\epsilon - \alpha$ model by Wünnemann et al. (2006). A comparison between these kinds of models is given by Jutzi et al. (2008) and on a wider theoretical basis by Arena and Speith (2010, 2011).

The basic assumption behind all matrix-based models is that the pressure in the porous material p can be obtained by scaling the pressure of the solid material p_s with the inverse of the distention. Mostly, the surface energy of the pores is neglected and the internal energy of the porous

Hugoniot relation

material is $u = u_s$. The system of EOS closing the system of conservation laws is then given by

$$p = \frac{1}{\alpha} p_s(\rho_s, u_s) = \frac{1}{\alpha} p_s(\alpha\rho, u) \tag{4.119}$$

$$u = u(\rho, p)\,. \tag{4.120}$$

These equations are complemented by a suitable relation for the distention. As a whole, this system of equations is named *Hugoniot relation.*

$p - \alpha$ model

For the $p-\alpha$ model the distention relation is given as a function of the pressure $\alpha(p) = \alpha(p(\alpha\rho, u))$, which is split into an elastic and a plastic part. This yields an implicit relation for α. In the approach by Jutzi et al. (2008) the internal energy (Eq. 4.119) is considered implicitly through the EOS of the matrix $p(\alpha\rho, u)$.

$\epsilon - \alpha$ model

Wünnemann et al. (2006) introduced the $\epsilon - \alpha$ model, where the distention is related to the volumetric strain

$$\epsilon_V = \int_V V_0 \frac{V'}{\mathrm{d}V'} = \ln\left(\frac{V}{V_0}\right)\,. \tag{4.121}$$

Hence, the distention is given by $\alpha(\epsilon_V)$ and a relation for ϵ_V, which is also split into an elastic and a plastic part. α can therefore be computed directly and not via an implicit relation.

$\rho - \alpha$ model

The $\rho - \alpha$ model was introduced by Benz and Jutzi (2007) as a simplified porosity model, where the distention depends directly on the density via Eq. 4.118. An analysis by Jutzi et al. (2008) revealed that the $\rho - \alpha$ model has similarities with the $\epsilon - \alpha$ model with $\alpha = \alpha_0 \exp(\epsilon_V)$ with an initial distention of α_0.

In test simulations Jutzi et al. (2008) found that the $\rho-\alpha$ and $\epsilon-\alpha$ models are inappropriate for the treatment of highly porous material, which shows anomalous behaviour in the fully compressed state ($\alpha = 1$). There, the density happens to be below the initial density of the matrix. Later, Arena and Speith (2010, 2011) were able to demonstrate that the $\rho - \alpha$ and $\epsilon - \alpha$ models are subject to a singularity in their governing equations. Therefore, these models are incapable of reproducing this physical anomalous behaviour.

An essential disadvantage of the matrix-based models considered so far, is that only the deviatoric part $S_{\alpha\beta}$ of the stress tensor $\sigma_{\alpha\beta}$ is considered for plastic deformations of the porous body.

plasticity-based porosity models

In contrast, plasticity based porosity models (see, e.g. Gurson 1977, for an introduction) involve the whole stress tensor $\sigma_{\alpha\beta}$. Given the geometrical interpretation in stress space (Fig. 4.2), matrix-based models work with an infinite cylinder. Therefore, plastic deformation can only happen by exceeding the shear strength Y (crossing the side surface from inside out). Plasticity-based porosity models also allow plastic deformation via pure hydrostatic pressure by putting limiting surfaces at the top (compressive strength Σ) and the bottom of the cylinder (tensile strength T). For this thesis, I adopt the plasticity-based porosity model by Sirono (2004) with some modifications, as specified below.

The porosity model adopted in this thesis

As already briefly outlined in Sec. 4.3.2 plasticity can be modelled by deviating from the elastic path given by Hooke's law. This is done by reducing inner stress according to a given EOS. Inner stress is the response of a material to external deformation. In the elastic case, these stresses restore thermal equilibrium and hence the original shape of the body. Once stress is reduced in an ongoing deformation, the material partially loses the ability to return to its original shape. After external deformation ceases, the remaining stresses only partially restore the body's state before deformation begins. This behaviour can be illustrated by applying tension to a rubber band. In the elastic regime, inner stresses restore the original length. If the band is overstretched, i.e. the tension has exceeded the tensile strength, inner stresses are relieved and it becomes easier to tear the rubber band apart. If the applied tension is then taken away, the band still contracts, but in its final state it is longer than before. The porosity model used in this thesis was already described in Geretshauser et al. (2010). Following the approach by Sirono (2004) the plasticity of hydrostatic pressure p and the deviatoric stress tensor $S_{\alpha\beta}$ is treated separately. As an EOS for the elastic regime, I adopt Sirono's modification of the Murnaghan equation. That is

elastic EOS

$$p(\phi) = K(\phi_0')\left(\frac{\phi}{\phi_0'} - 1\right), \tag{4.122}$$

reference density

where $\phi_0' = \rho_0'/\rho_\mathrm{s}$. The quantity ρ_0' denotes the *reference density*, i.e. the density of the material at zero external stress, and $K(\phi)$ is the bulk modulus. Eq. 4.122 is represented by the elastic paths $E_j(\phi)$ in Fig. 4.3, which intersect the ϕ-axis at ϕ_j'. Their slope varies according to the bulk modulus.

bulk and shear moduli

Following Sirono furthermore, the filling factor dependence of the *bulk* $K(\phi)$ and *shear* $\mu(\phi)$ *moduli* is modelled by a power law

$$K(\phi) = 2\mu(\phi) = K_0\left(\phi/\phi_\mathrm{i}\right)^\gamma , \tag{4.123}$$

where $\phi_\mathrm{i} = \rho_\mathrm{i}/\rho_\mathrm{s}$. For the simulations in Ch. 6 the values for $K_0 = 5.0\,\mathrm{kPa}$ and $\gamma = 4$ are used. This choice is motivated in Sec. 5.3.5. According to Sirono (2004) ρ_i is the initial density of the material at the beginning of the simulation. In contrast, for this thesis it has to be ensured that the dust material possesses the same bulk modulus relation $K(\rho)$ even for simulations with different initial densities. In Sec. 5.3.5 this relation will be determined by numerical experiments, where the dust material has two different densities at the beginning of a bouncing and fragmentation benchmark setup. According to Sirono (2004), the materials should feature two different ρ_i. As a consequence, $K(\rho)$ and in particular K_0, depends on the initial setup. Because these two quantities are to be validated by using two different setups, a unique ρ_i has to be fixed for all simulations. We choose ρ_i such that $K(\rho_i) = K_0$ is the bulk modulus of the generic uncompressed dust material that is produced by the random ballistic deposition (RBD) method (Blum and Schräpler 2004).

sound speed (elastic)

Directly connected with the bulk modulus $K(\rho)$ is the *sound speed of the material* during elastic deformation, which reads

$$c_s(\rho_0') = \sqrt{K(\rho_0')/\rho_0'}. \tag{4.124}$$

Together with Eq. 4.123, this relation shows that the sound speed is a strong function of density. This behaviour was seen in molecular dynamics simulations by Paszun and Dominik (2008).

After the EOS for the elastic case, I now turn to the relations governing the plastic behaviour. For the deviatoric stress tensor, it is assumed that the dust material is isotropic, which makes the von Mises yield criterion applicable (see Sec. 4.3.2). For this criterion, the shear strength Y (see also

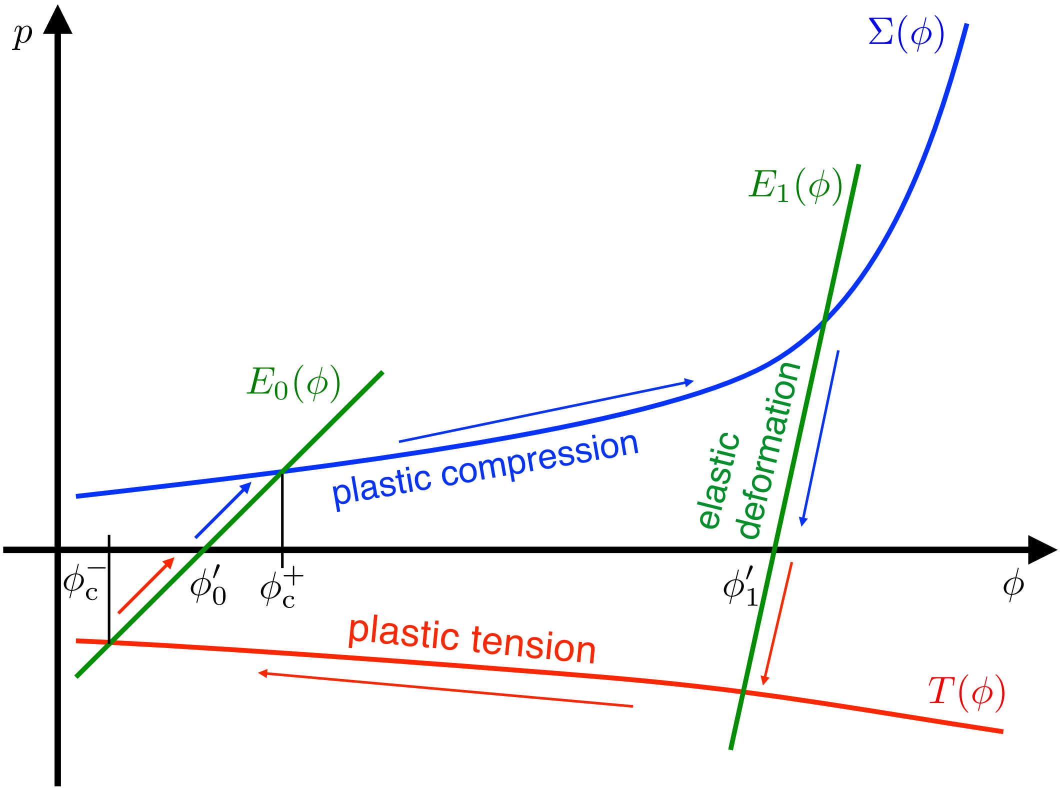

Figure 4.3. *Porosity model.* In the porosity model used in this thesis, the regime of elastic, purely hydrostatic deformation is limited by the compressive strength $\Sigma(\phi)$ and the tensile strength $T(\phi)$ relations. $\Sigma(\phi)$ represents the transition threshold to plastic compression for $p > \Sigma(\phi)$, while $T(\phi)$ marks the transition to plastic tension for $p < T(\phi)$. In between these regimes the material moves on elastic paths. Two examples are given by $E_0(\phi)$ and $E_1(\phi)$, which intersect the ϕ-axis at the reference filling factors ϕ_0' and ϕ_1', respectively. These represent the filling factors of the material at vanishing external pressure. Each pair of $E_j(\phi)$ and ϕ_j' has two critical filling factors ϕ_c^- and ϕ_c^+ with $E_j(\phi_c^-)$ and $E_j(\phi_c^+)$ intersecting the tensile and compressive strength curves, respectively. The elastic filling factor regime around, e.g. ϕ_0' is $\phi_c^- \leq \phi \leq \phi_c^+$. The blue arrows represent an example for the plastic compression path, where a solid body element is compressed from ϕ_0' to ϕ_1'. The red arrows exemplarily show a typical tension path, where the material is stretched from ϕ_1' to ϕ_0'. In general the reference densities can be arbitrary for both paths as long as compression and tension proceed in positive and negative ϕ direction, respectively. In this figure the compression and tension paths are closed to demonstrate the damage restoration capability of the approach of this thesis.

Sec. 5.3.2) is given as a composite of the compressive and tensile strengths

$$Y(\phi) = \sqrt{\Sigma(\phi)\left|T(\phi)\right|}. \tag{4.125}$$

Sirono (2004) uses a pre-factor of $\sqrt{2/3}$ for this relation, which I drop. The suitability of this choice is demonstrated in Sec. 5.3.2. Additionally, for the model of this thesis the power laws for the compressive strength $\Sigma(\phi)$ and tensile strength $T(\phi)$ (after toner particle measurements by Valverde et al. 1998) are replaced by more suitable relations for SiO_2 dust, which are worked out based on laboratory measurements as a part of this thesis. This procedure is presented in Ch. 5. The von Mises plasticity criterion is based on the second irreducible invariant of the deviatoric stress tensor (Eq. 4.104). The implementation of the deviatoric stress reduction also deviates from the approach by Sirono (2004) and follows Benz and Asphaug (1995) and Schäfer et al. (2007)

$$S^{\alpha\beta} \to f S^{\alpha\beta}, \tag{4.126}$$

where $f = \min\left[Y^2(\phi)/3J_2, 1\right]$. The hydrostatic pressure is limited by the tensile strength $T(\phi)$ for $p < 0$ and by the compressive strength $\Sigma(\phi)$ for $p > 0$:

$$p(\phi) \to \begin{cases} \Sigma(\phi) & \phi > \phi_c^+ \\ T(\phi) & \phi < \phi_c^- \end{cases}. \tag{4.127}$$

The compressive strength relation in this porosity model is given by

$$\Sigma(\phi) = p_m \left(\frac{\phi_2 - \phi_1}{\phi_2 - \phi} - 1\right)^{\Delta \ln 10} \tag{4.128}$$

for $\phi_1 + \varepsilon < \phi < \phi_2$ and $\varepsilon = 0.005$. The quantities $\phi_1 = 0.12$ and $\phi_2 = 0.58$ denote the minimum and maximum filling factors, respectively, in the compressive strength relation. However, the material can exceed both of these values. The power of the compressive strength relation is ln(10) times the parameter Δ with $\Delta = 0.58$. The mean pressure of the relation is given by $p_m = 0.26\,\mathrm{kPa}$.The choice of the parameters is motivated in Sec. 5.3.3. For $\phi \leq \phi_1 + \varepsilon$ the compressive strength relation is continuously extended by the constant function $\Sigma(\phi) = \Sigma(\phi_1 + \varepsilon)$ and for $\phi_2 \leq \phi$ I set $\Sigma(\phi) = \infty$. The tensile strength relation (see Sec. 5.3.1) is given by a power law

$$T(\phi) = -10^{a+b\phi}\mathrm{Pa} \tag{4.129}$$

where $a = 2.8$ and $b = 1.48$.

For $\phi_c^- \leq \phi \leq \phi_c^+$, the material is in the elastic regime and Eq. 4.122 is applied. The symbols ϕ_c^- and ϕ_c^+ denote the filling factors where the elastic path intersects the tensile strength and compressive strength, respectively (see Fig. 4.3).

compression path

For pure hydrostatic compression, the resulting *compression path* of an SPH-particle (blue arrows) in the EOS-diagram (Fig. 4.3) can be described as follows. Initially, the dust material possesses the filling factor ϕ_i, and therefore $\phi_0' = \phi_i$. With increasing pressure $0 < p < \Sigma(\phi_c^+)$, the filling factor is increased on the elastic path $E_0(\phi)$. After a purely elastic compression with $p < \Sigma(\phi_c^+)$, the filling factor returns to its original value ϕ_0' once external pressure vanishes. However, if the pressure increases such that $\Sigma(\phi_c^+) < p$, then the compression becomes plastic. Consequently, ϕ follows the plastic compression path given by the compressive strength relation $\Sigma(\phi)$.

If external pressure decreases again, the material follows a new elastic path $E_1(\phi)$ until it reaches the new filling factor $\phi = \phi_1'$ at vanishing external pressure. The latter elastic response describes a slight expansion of the material, which can be seen in the laboratory experiments as well as in the simulations in Ch. 5. At the end of a plastic compression, ϕ is increased from ϕ_0' to ϕ_1' at $p = 0$, i.e. the material is compressed irreversibly.

implementation of pressure reduction

The pressure reduction process is implemented such that at each time step, p is computed using Eq. 4.122. If for a given ϕ, $p(\phi) > \Sigma(\phi)$ and $\phi > \phi_c^+$, then the pressure $p(\phi)$ is reduced to $\Sigma(\phi)$. The deformation becomes irreversible once the new reference density ρ_0' is computed using Eq. 4.122 and the elastic path is shifted towards higher densities. Hereby the limiting filling factors ϕ_c^- and ϕ_c^+ are also set anew. In principal, there are two possible implementations of this: (1) Plasticity becomes effective immediately and ρ_0' is computed whenever $p > \Sigma$; and (2) plasticity becomes effective after pressure decrease, which is equivalent to $\phi < \phi_c^+$. The latter procedure was used by Schäfer (2005) and Schäfer et al. (2007). In this thesis I tested both implementations and find that possibility (1) is closer to the underlying physical process. In addition, it proves to be more stable. Therefore, option (1) is used throughout this thesis.

Sirono's damage (restoration) model

For the tensile regime, i.e. for $\phi < \phi_c^-$, I do not adopt the damage and damage-restoration model presented by Sirono (2004). This damage model for brittle material (see Sec. 4.3.5) such as rocks or pumice was developed for SPH by Benz and Asphaug (1994, 1995) and used by Jutzi et al. (2008, 2009b,a, 2010). It is assumed that a material contains flaws, which are activated and develop under tensile loading (Grady and Kipp 1980). Schäfer et al. (2007) found that the model is not applicable to their simulations of porous ice because it includes compressive damage effects. Brittle material such as pumice and rocks tend to disintegrate when compressed, i.e. they are crushed. In contrast, for highly porous SiO_2 dust, both the tensile and compressive strengths increase with compression. This is because the monomers are able to form new bonds when they come into contact.

tension path

Therefore, I mirror Sirono's prescription for the compression regime to the tensile regime. The result is displayed in Fig. 4.3. If tension is applied to a solid body element it follows the *tension path* (red arrows). At first, the response is elastic. Starting, e.g. from an initial filling factor ϕ_1', the material follows the elastic path $E_1(\phi)$ for $T(\phi) < p < 0$. Once the pressure exceeds the tensile strength, the deformation becomes plastic and the material follows $T(\phi)$ in the negative ϕ-direction until the external tension drops below the tensile strength limit. Then the material slightly contracts (from ϕ_c^- to ϕ_0') along the elastic path $E_0(\phi)$ and reaches the final filling factor ϕ_0' at $p = 0$. As a result of the tension path, the material is irreversibly expanded to a lower filling factor. Please note that this works for arbitrary $\phi_0' < \phi_1'$. In Fig. 4.3 they have been chosen to be identical to the reference densities of the compression path to demonstrate the damage restoration effect of the porosity model adopted in this thesis.

damage restoration

Damage restoration is implemented in a very natural way. Following the blue and red arrows in Fig. 4.3 illustrates this effect. The filling factor of the material can be increased from ϕ_0' to ϕ_1' via the compression path. This compression is, from the thermodynamical point of view, irreversible. This is because it needs an external force to stretch the material via the tension path from ϕ_1' to ϕ_0'. For this model I implicitly assume that the material possesses no memory of its deformation history. The model becomes unrealistic for fast compressions and tensions. In Sec. 5.3.1 I demonstrate how this model is applicable for porous SiO_2 dust.

rupture

In the SPH scheme with this porosity model, *rupture* takes place because of plastic flow as in ductile materials. The more two sets of SPH particles are torn apart, the more the density decreases in the middle region and inner tension is relieved according to the tensile strength relation $T(\phi)$.

Finally, the sets of SPH particles are torn apart such that their smoothing lengths no longer overlap and are completely separated. Separated sets of SPH particles are considered as fragments.

Energy considerations

Since the porosity model presented as EOS in the previous section does not include an energy dependence, the energy equation (Eq. 4.39) is not explicitly solved in my simulations. However, in this section I show that the construction of the used porosity and plasticity models are consistent with the assumption that kinetic energy is converted into heat by plastic deformations.

I consider an energetically closed system, where heat transfer is possible between the deformed object and its environment. The total energy U of this system is initially given by the kinetic energy of the collision partners. According to the first law of thermodynamics

$$\begin{aligned} \mathrm{d}U &= T\mathrm{d}S + \sigma_{\alpha\beta}\mathrm{d}\epsilon_{\alpha\beta} && (4.130)\\ &= T\mathrm{d}S - p\delta_{\alpha\beta}\mathrm{d}\epsilon_{\alpha\beta} + S_{\alpha\beta}\mathrm{d}\epsilon_{\alpha\beta} && (4.131)\\ &= T\mathrm{d}S - p\mathrm{d}V + S_{\alpha\beta}\mathrm{d}\epsilon_{\alpha\beta} && (4.132)\end{aligned}$$

where T is the temperature, S is the entropy, p is the pressure, $\epsilon_{\alpha\beta}$ is the strain tensor, $V = \epsilon_{\alpha\alpha}$ is the volume, $\sigma_{\alpha\beta} = -p\delta_{\alpha\beta} + S_{\alpha\beta}$ is the stress tensor and $S_{\alpha\beta}$ is the deviatoric stress tensor. $\delta Q = T\mathrm{d}S$ is the heat that is introduced into the system to perform work. With the relation

$$\epsilon_{\alpha\beta} = \frac{1}{2\mu}S_{\alpha\beta} + \frac{1}{3}\delta_{\alpha\beta}\epsilon_{\gamma\gamma}\,, \tag{4.133}$$

Eq. 4.132 can be rewritten as

$$\mathrm{d}U = T\mathrm{d}S - p\mathrm{d}V + \frac{1}{2\mu}\mathrm{d}(\frac{1}{2}S_{\alpha\beta}S_{\alpha\beta})\,, \tag{4.134}$$

where $\mathrm{d}(S_{\alpha\beta}S_{\alpha\beta}) = 2S_{\alpha\beta}\mathrm{d}S_{\alpha\beta}$ and $\delta_{\alpha\beta}S_{\alpha\beta} = S_{\alpha\alpha} = 0$ have been used and $I_2 = {}^1\!/_2 S_{\alpha\beta}S_{\alpha\beta}$ is the second irreducible invariant of the deviatoric stress tensor.

The volume V can be replaced by the filling factor via $V = m(\rho_\mathrm{s}\phi)^{-1}$ and the differential reads

$$\mathrm{d}V = -\frac{m}{\rho_\mathrm{s}}\frac{\mathrm{d}\phi}{\phi^2}\,, \tag{4.135}$$

and the first law of thermodynamics is given by

$$\mathrm{d}U = T\mathrm{d}S + \frac{m}{\rho_\mathrm{s}}\frac{p}{\phi^2}\mathrm{d}\phi + \frac{1}{4\mu}\mathrm{d}(S_{\alpha\beta}S_{\alpha\beta})\,. \tag{4.136}$$

elastic deformations

For *elastic deformations* the process is reversible, i.e., $\mathrm{d}S = 0$ and, hence

$$\mathrm{d}U = \frac{m}{\rho_\mathrm{s}}\frac{p}{\phi^2}\mathrm{d}\phi + \frac{1}{4\mu}\mathrm{d}(S_{\alpha\beta}S_{\alpha\beta})\,, \tag{4.137}$$

for the pure pressure term this corresponds to moving along the elastic paths in Fig. 4.3 or along the hydrostatic axis in Fig. 4.2 inside the von Mises cylinder with

$$p(\phi) = K(\phi_0')(\phi/\phi_0' - 1)\,. \tag{4.138}$$

For the pure shear term this means moving on the yield surface within the cylinder of Fig. 4.2. With increasing pressure and/or increasing shear, internal energy is stored in the body. Conversely, energy can be decreased by decreasing the pressure or filling factor.

plastic deformations

In *plastic deformations*, part of the energy will always be stored in the solid body by elastic deformation. This energy is released by an elastic swing back at the end of plastic deformations. When considering plastic deformations, I neglect the little portion of energy stored in the solid body and assume that energy is conserved, i.e., $\mathrm{d}U = 0$. For slow deformations (below the sound speed), where no shocks appear, the temperature of the body is nearly constant $T = \mathit{const.}$ and the entropy is increased $\mathrm{d}S > 0$. This yields the condition

$$-T\mathrm{d}S = \frac{m}{\rho_\mathrm{s}}\frac{p}{\phi^2}\mathrm{d}\phi + \frac{1}{4\mu}\mathrm{d}(S_{\alpha\beta}S_{\alpha\beta}) > 0\,. \tag{4.139}$$

Since $\delta Q_\mathrm{in} = T\mathrm{d}S$ is defined as the heat that is introduced into the system, $\delta Q_\mathrm{out} = -T\mathrm{d}S$ is the heat transported out of the system. Given the condition that heat energy leaves the system $\delta Q_\mathrm{out} > 0$, and with $\phi > 0$, $m > 0$, and $\rho_\mathrm{s} > 0$ this yields the conditions

$$\text{for} \quad \mathrm{d}\phi > 0 \quad \rightarrow \quad p(\phi) > 0 \tag{4.140}$$

$$\text{for} \quad \mathrm{d}\phi < 0 \quad \rightarrow \quad p(\phi) < 0\,. \tag{4.141}$$

These conditions are fulfilled by following the arrows in Fig. 4.3. For compressions ($p > 0$) the system evolves towards greater ϕ. In contrast, for tension ($p < 0$) the filling factor is reduced.

With the von Mises criterion for plastic deformation the pure shearing term can be written as

$$\mathrm{d}(S_{\alpha\beta}S_{\alpha\beta}) \approx \mathrm{d}Y^2(\phi)\,, \tag{4.142}$$

and with $Y(\phi) = \sqrt{\Sigma(\phi)|T(\phi)|}$ this expression can be differentiated (not explicitly stating the ϕ-dependence)

$$\mathrm{d}Y^2 = 2\frac{|T|\mathrm{d}\Sigma + \Sigma\mathrm{d}|T|}{\Sigma|T|} \tag{4.143}$$

$$= \frac{2}{\Sigma|T|}\left(|T|\frac{\partial\Sigma}{\partial\phi}\mathrm{d}\phi - \Sigma\frac{\partial T}{\partial\phi}\mathrm{d}\phi\right) \tag{4.144}$$

For the compressive strength $\Sigma(\phi)$ holds

$$\text{for} \quad \mathrm{d}\phi > 0 \quad \rightarrow \quad \frac{\partial\Sigma}{\partial\phi} > 0 \tag{4.145}$$

$$\text{for} \quad \mathrm{d}\phi < 0 \quad \rightarrow \quad \frac{\partial\Sigma}{\partial\phi} < 0\,, \tag{4.146}$$

and the derivative term of Σ is always positive. The tensile strength develops as follows

$$\text{for} \quad \mathrm{d}\phi > 0 \rightarrow \quad \frac{\partial T}{\partial \phi} < 0 \tag{4.147}$$

$$\text{for} \quad \mathrm{d}\phi < 0 \rightarrow \quad \frac{\partial T}{\partial \phi} > 0\,, \tag{4.148}$$

hence the derivative term of T is always negative. Consequently, the term in brackets in Eq. 4.144 is always positive as well as the fraction outside the brackets. As a result, $\delta Q_{\mathrm{out}} > 0$ for the assumed relations of $\Sigma(\phi)$, $T(\phi)$, and $Y(\phi)$.

As a conclusion, the porosity and plasticity models presented in this thesis are consistent with the assumption that kinetic energy in the plastic deformation process is converted into heat. This can also be seen from the microscopic picture, where energy is dissipated by breaking molecular bonds. In MD simulations this is modelled by exceeding the critical rolling, twisting, and displacement lengths. These thresholds can be seen as the microscopic reason for the macroscopic compression, tension, and shear thresholds.

4.3.5. Damage models

Brittle material

In contrast to ductile media, brittle materials, such as basalt, granite, or porous pumice, do not rupture by plastic flow. This is because the material is not completely homogeneous but contains little flaws. These are little defects in the medium. With increasing strain, cracks develop originating from these flaws and start to pervade the solid body. In brittle media, stress is relieved by developing cracks.

Benz and Asphaug (1994, 1995) developed an SPH implementation for dynamic fracture model by Grady and Kipp (1980). A description of the implementation can also be found, e.g. in Schäfer (2005) and Jutzi et al. (2008). Sirono (2004) used a modified version of this damage model and included the effect of damage restoration. However, Schäfer et al. (2007) found that Sirono's damage model was not applicable for their simulations of porous ice because it includes damage by compression. As already pointed out in Sec. 4.3.4, some materials such as porous ice and porous SiO_2 dust form new molecular bondings when they are compressed. Thus, their strengths increase and do not decrease as supposed by the Sirono damage model. Other materials however, such as porous pumice, crush when they are compacted and do not form new molecular bondings. This behaviour makes the damage model by Grady and Kipp (1980) applicable, which was carried out by Jutzi et al. (2009b,a, 2010).

To model damage, Grady and Kipp (1980) introduced a scalar parameter $0 \leq D \leq 1$, where $D = 0$ and $D = 1$ represent undamaged and fully disintegrated material, respectively. Please note that neither the von Mises yield criterion nor pressure limitation by compressive and tensile strength is applied here as for ductile materials. In general, the plasticity model presented in Sec. 4.3.2 and 4.3.4, which is compiled in Fig. 4.3, is not valid for brittle material (for a combination of von Mises plasticity with a damage model for porous materials (see Jutzi et al. 2008). Instead, stress reduction via flaws and cracks enters via the damage parameter

$$\sigma_{\mathrm{dam}} = (1 - D)\sigma\,. \tag{4.149}$$

This can be split into the pure hydrostatic and pure shear part

$$\sigma_{\mathrm{dam}} = \hat{p}\delta_{\alpha\beta} + (1-D)S_{\alpha\beta}\,, \tag{4.150}$$

$$\text{with } \hat{p} = \begin{cases} p & p \geq 0 \\ (1-D)p & p < 0 \end{cases}\,. \tag{4.151}$$

While for compressions ($p > 0$) the pressure is unlimited, tension and shear stresses are relieved via the dynamically evolving damage parameter D. Thus, damaged material can be interpreted to feel less stress than undamaged material. If the damage parameter is transferred to the bulk and shear moduli

$$K_{\mathrm{dam}} = (1-D)K\,, \tag{4.152}$$

$$\mu_{\mathrm{dam}} = (1-D)\mu\,, \tag{4.153}$$

one can see that for tension and shear, damaged material deviates from the elastic path in the stress-strain diagram (Fig. 4.1. This deviation represents a reduction in the strength of the material with respect to the elastic case. From this perspective, Eq. 4.152 and 4.153 are analogous to the tensile and shear strength relations. In the porosity model in Sec. 4.3.4, the strength quantities depend on the filling factor and hence evolve with the time evolution of the density. In contrast, the damage D has its own local time evolution, which can be derived from its definition: a crack of half length a relieves stress in a volume given by its circumscribing sphere. If a given sphere with radius R_s is filled out by a crack, all the stress is relieved and the sphere is totally damaged. Consequently, the local damage D is defined as the ratio between the volume defined by the growing crack and the volume V in which the crack is growing

$$D = \frac{\frac{3}{4}\pi a^3}{V} = \frac{a^3}{R_\mathrm{s}^3}\,. \tag{4.154}$$

The time evolution is then given by

$$\frac{\mathrm{d}D^{1/3}}{\mathrm{d}t} = n_{\mathrm{act}}\frac{c_\mathrm{g}}{R_\mathrm{s}} \tag{4.155}$$

where n_{act} accounts for crack accumulation and denotes the number of activated flaws. The quantity c_g is the crack growth velocity. The concept of flaw activation originates from the idea that cracks do not start to grow for any strain applied, but they get activated for some strain threshold ϵ_{act}. The number of flaws n per unit volume with ϵ_{act} is mostly given by a power law

$$n(\epsilon_{\mathrm{act}}) = k\epsilon_{\mathrm{act}}^m\,. \tag{4.156}$$

This distribution for flaws in a brittle material was proposed by Weibull (1939). It is based on two material parameters k and m, where k is the number of flaws per unit volume and typically $3 < m < 9$. Materials with a strong variation of ϵ_{act} normally feature small m, whereas homogeneous rock with uniform thresholds have large values of m. The flaw distribution according to Eq. 4.156 is set as an initial condition for the material before the simulation.

As a disadvantage, the material parameters k and m are rarely available, because they are hard to measure. Unfortunately, small variations of k and m lead to highly differing activation thresholds and simulation results (e.g. Schäfer 2005).

Because this damage model is only suitable for brittle material, it is not applicable to the material this thesis is dealing with: SiO_2 dust, which possesses properties between a ductile and a brittle material. Therefore it is desirable, to develop a simple damage model, which is consistent with the porosity model of Sec. 4.3.4 and its damage restoration properties. Based on the ideas presented up to here, I propose the following inhomogeneity damage model.

Inhomogeneity damage model

The starting point again is the inhomogeneous nature of the material. In case of brittle material, small defects in the crystal lattice are the seeds of cracks. Within the close collaboration between experimentalists and the author of this thesis, investigations of the macroscopic dust aggregates created by the random ballistic deposition (RBD) method reveal that the aggregates are not completely homogeneous (Güttler et al. 2009). Instead, the filling factor was found to follow a Gaussian distribution around a median of $\phi \sim 0.15$.

According to the porosity model of Sec. 4.3.4, regions of lower filling factor also represent regions of weaker compressive, tensile, and shear strengths, whereas regions of higher filling factor are stronger. Therefore, as an analogue to the Weibull distribution I propose an initial distribution of the filling factor given by the Gaussian function

$$n(\phi) = \frac{1}{\sqrt{2\pi}\phi_\sigma} \exp\left(-\frac{1}{2}\frac{\phi - \phi_\mu}{\phi_\sigma}\right) \tag{4.157}$$

where $n(\phi)$ is the number density for a filling factor ϕ, ϕ_σ the width of the distribution function, and ϕ_μ the median filling factor.

Associated with each filling factor ϕ are two critical filling factors ϕ_c^+ and ϕ_c^- (see also Fig. 4.3). These threshold values mark the transition from the elastic to the plastic hydrostatic regime, where stress is relieved. The pressure limits of compressive, tensile, and shear strengths $\Sigma(\phi)$, $T(\phi)$, and $Y(\phi)$, respectively, are analogues to the activation threshold ϵ_{act}. Hence, associated with each ϕ are analogues to the activation threshold.

Damaged areas in this simple inhomogeneity scheme are therefore represented by areas of low filling factor. Under constant tension, ϕ continues to decrease in these regions and due to the ϕ-dependence of the tensile $T(\phi)$ or shear strength $Y(\phi)$ the strength decreases with increasing D in these regions just as in Eq. 4.152 and 4.153.

This illustrates the twofold role of the filling factor ϕ. On the one hand, it represents a quantity which determines the activation thresholds for the plastic regime and on the other hand, it also represents the damage parameter D, which decreases the strength quantities. Therefore, in the inhomogeneity damage model, the time evolution of the damage is given by the time evolution of ϕ, or equivalently, the density. For increasing filling factor, the strength quantities also increase. This is the effect of damage restoration as already discussed in Sec. 4.3.4.

Test simulations of the proposed inhomogeneity damage model are presented in Sec. 6.2. A great advantage of this approach is that the material parameters ϕ_σ and ϕ_μ can be determined in laboratory measurements by X-ray tomography (Güttler et al. 2009).

4.4. Numerical Issues

4.4.1. The kernel function

In section 4.1.1 the replacement of the δ function by an integral kernel W (Eq. 4.3) is described as the first step in the SPH discretisation scheme. To achieve the convenient handling of spatial derivatives (Eq. 4.8), the kernel is required to have the following properties: convergence to the δ-function for small smoothing lengths h (Eq. 4.2), normalisation (Eq. 4.4), spherical symmetry (Eq. 4.5), compactness, and first order differentiability. A number of kernel choices fulfilling these criteria can be found, e.g. in Speith (1998, 2007) and Monaghan (2005). For the scheme used in this thesis I use the kernel introduced by Monaghan and Lattanzio (1985), which has become the standard choice in the past decades. The kernel is constructed as a B-spline cubic function and reads (having regard to a factor of two for the smoothing length, see Speith 1998 or Schäfer 2005 for details)

$$W(\tilde{r};h) = \frac{\chi}{h^d}\begin{cases} 6(\tilde{r}/h)^3 - 6(\tilde{r}/h)^2 + 1 & 0 \le \tilde{r}/h < 1/2 \\ 2\,(1-\tilde{r}/h)^3 & 1/2 \le \tilde{r}/h \le 1 \\ 0 & \tilde{r}/h > 1 \end{cases}, \tag{4.158}$$

with dimension d and the constant χ

$$\chi = \begin{cases} \frac{4}{3} & d=1 \\ \frac{40}{7\pi} & d=2 \\ \frac{8}{\pi} & d=3 \end{cases}. \tag{4.159}$$

Then, the first derivative of kernel reads

$$\frac{\partial W(\tilde{r};h)}{\partial \tilde{r}} = \frac{6\chi}{h^{d+1}}\begin{cases} 3(\tilde{r}/h)^2 - 2(\tilde{r}/h) & 0 \le \tilde{r}/h < 1/2 \\ -\,(1-\tilde{r}/h)^2 & 1/2 \le \tilde{r}/h \le 1 \\ 0 & \tilde{r}/h > 1 \end{cases}. \tag{4.160}$$

It can be shown that this choice of the kernel fulfils all conditions stated above.

4.4.2. Artificial viscosity

In impact simulations, particularly if shocks develop, particles move with high velocities. In this case the use of the SPH Lagrangian numerical scheme causes the problem of mutual particle interpenetration. To avoid this unphysical behaviour and to be able to resolve shocks an *artificial viscosity* is introduced. In this thesis, I follow the approach by Monaghan and Gingold (1983), who include an additional scalar pressure term Π^{ab} in the SPH equations. For ideal and viscous fluids, this term is added to the respective SPH representations of the momentum (Eq. 4.29 and 4.38) and energy equations (Eq. 4.40 and 4.41). In case of solid body SPH, Π^{ab} is added to Eq. 4.82 and to the corresponding energy equation. In any case, the hydrostatic pressure term in brackets is replaced in the following way

$$\left(\frac{p^a}{(\rho^a)^2}+\frac{p^b}{(\rho^b)^2}\right) \quad \rightarrow \quad \left(\frac{p^a}{(\rho^a)^2}+\frac{p^b}{(\rho^b)^2}+\Pi^{ab}\right). \tag{4.161}$$

The Monaghan artificial viscosity term Π^{ab} is defined as

$$\Pi^{ab}=\begin{cases}\frac{-\alpha_{\mathrm{av}}\bar{c}_{\mathrm{s}}^{ab}\mu^{ab}+\beta_{\mathrm{av}}(\mu^{ab})^2}{\bar{\rho}^{ab}} & (\mathbf{v}^a-\mathbf{v}^b)\cdot(\mathbf{x}^a-\mathbf{x}^b)<0\\ 0 & (\mathbf{v}^a-\mathbf{v}^b)\cdot(\mathbf{x}^a-\mathbf{x}^b)\geq 0\end{cases}, \tag{4.162}$$

which is now established as a standard implementation. The first term in the numerator corresponds to an artificial bulk viscosity, whose strength is regulated with $\alpha_{\mathrm{av}}>0$. Whereas the second term represents a von Neumann and Richtmyer (1950) viscosity scaled with $\beta_{\mathrm{av}}>0$. The term μ^{ab} approximates the divergence. It is given by

$$\mu^{ab}=\frac{\bar{h}^{ab}(\mathbf{v}^a-\mathbf{v}^b)\cdot(\mathbf{x}^a-\mathbf{x}^b)}{(\mathbf{x}^a-\mathbf{x}^b)^2+\epsilon_{\mathrm{av}}(\bar{h}^{ab})^2}, \tag{4.163}$$

where $\bar{h}^{ab}$ is the averaged smoothing length $\bar{h}^{ab}=(h^a+h^b)/2$. In case of very small particle separations, i.e. $\left|\mathbf{x}^a-\mathbf{x}^b\right|\sim 0$, the $\epsilon_{\mathrm{av}}(\bar{h}^{ab})^2$ prevents a singularity of the factor μ^{ab}. Π^{ab} only acts on particles approaching each other, it vanishes if they move apart. Usually the parameters are chosen to be of order one tenth to unity: e.g. $\alpha_{\mathrm{av}}=1$ and $\beta_{\mathrm{av}}=2$, or $\alpha_{\mathrm{av}}=0.1$ and $\beta_{\mathrm{av}}=0.2$. In contrast, ϵ_{av} is usually smaller. A typical value is 10^{-2}.

The quantities $\bar{\rho}^{ab}$ and $\bar{c}_{\mathrm{s}}^{ab}$ are the average density and sound speed, respectively, of the particles a and b. They read

$$\bar{\rho}^{ab}=\frac{\rho^a+\rho^b}{2} \quad \text{and} \quad \bar{c}_{\mathrm{s}}^{ab}=\frac{c_{\mathrm{s}}^a+c_{\mathrm{s}}^b}{2}. \tag{4.164}$$

For *porous materials*, Sirono (2004) restricted the application of artificial viscosity only to particles that approach each other faster than the sound speed. This is to avoid unnecessary energy dissipation which can promote spurious aggregate sticking.

In contrast to Sirono's simulations, I find it necessary to apply artificial viscosity for the simulations of dust and glass material. This is carried out for mainly two reasons: firstly, it increases the stability of the simulation and secondly, the dust material possesses dissipative features which can easily be simulated with artificial viscosity. This energy dissipation and its advantages for the simulation of pre-planetesimal collisions and the benchmark experiments are discussed in Sec. 5.2.4. As a result of this investigation, I will only make use of the bulk viscosity term with a small α_{av} value of 0.1. The effect of the von Neumann-Richtmyer term is negligible and I set $\beta_{\mathrm{av}}=0$.

For small gradients of density and sound speed and $\beta_{\mathrm{av}}=0$, the effect of artificial viscosity can be quantified in terms of the kinematic viscosity (Eq. 4.34) with the approximation by Meglicki et al. (1993)

$$\nu=\chi\alpha_{\mathrm{av}}c_{\mathrm{s}}h\,, \tag{4.165}$$

with

$$\chi = \begin{cases} -\frac{\pi}{8}\int\limits_0^\infty \tilde{r}^2 \frac{\partial W(\tilde{r};h)}{\partial \tilde{r}} \mathrm{d}\tilde{r} & \text{in 2D} \\ -\frac{2\pi}{15}\int\limits_0^\infty \tilde{r}^3 \frac{\partial W(\tilde{r};h}{\partial \tilde{r}} \mathrm{d}\tilde{r} & \text{in 3D} \end{cases} . \tag{4.166}$$

Other approaches for a artificial viscosity are discussed in Monaghan (2005), Speith (2007) and Rosswog (2009).

4.4.3. Tensile instability and artificial stress

In solid body and magnetohydrodynamics simulations with SPH a frequently arising problem is the tensile instability. This numerical instability phenomenon is caused by the inaccuracies of the function approximation, which is not even of zeroth order consistency (Speith 2007, and references therein). The stability of SPH was analysed by Morris (1996) and Swegle et al. (1995). The analysis of the latter revealed that SPH becomes unstable for compression if the second derivative of the kernel function $(W^{ab})'' < 0$ and for tension if $(W^{ab})'' > 0$. The tensile instability results in artificial particle clumping, which finally leads to unphysical results. For example in the collision of two rubber rings the tensile instability leads to spurious fracture (see, e.g. Schäfer 2005).

Many approaches have been proposed to cure the tensile instability by increasing the order of consistency. Besides his own suggestions iSPH and eSPH, Speith (2007) lists the following (and the according references): normalised SPH, corrected SPH (CSPH), moving least squares interpolation (MLSPH), additional stress points, conservative smoothing (CSA), regularised SPH (RSPH), and many more.

Within this thesis the approach by Monaghan (2000) is used. Following this approach a small artificial stress is added to the SPH equations. This stress acts as a repulsive force between the SPH particles and prevents the clumping caused by tensile instability. Similar to the procedure presented for the artificial viscosity (Sec. 4.4.2) an additional term is added to the hydrostatic pressure term in the momentum equations (Eq. 4.29, 4.38, or 4.82)

$$\left(\frac{p^a}{(\rho^a)^2} + \frac{p^b}{(\rho^b)^2}\right) \quad \rightarrow \quad \left(\frac{p^a}{(\rho^a)^2} + \frac{p^b}{(\rho^b)^2} + A^{ab}_{\alpha\beta}(f^{ab})^n\right) . \tag{4.167}$$

This can be combined with artificial viscosity by also adding Π^{ab} in the brackets. $A^{ab}_{\alpha\beta}$ is the artificial stress given by

$$A^{ab}_{\alpha\beta} = A^a_{\alpha\beta} + A^b_{\alpha\beta} , \tag{4.168}$$

with

$$A^a_{\alpha\beta} = \begin{cases} -\epsilon_{\text{as}} \frac{\sigma^a_{\alpha\beta}}{(\rho^a)^2} & \sigma^a_{\alpha\beta} > 0 \text{ (tension)} \\ 0 & \sigma^a_{\alpha\beta} \leq 0 \text{ (compression)} \end{cases} . \tag{4.169}$$

where ϵ_{as} determines the strength of the artificial stress. Typical values are $\epsilon \sim 0.01 - 0.2$. The artificial stress in Eq. 4.167 is scaled with the quantity f^{ab} and an exponent $n > 0$, typically $2 \leq n \leq 6$. Since the repulsive force has to decrease with increasing particle separation f^{ab} is chosen such that

$$f^{ab} = \frac{W^{ab}}{W(\Delta p)} \tag{4.170}$$

where Δp is the mean particle distance. The tensile instability fix by Monaghan has very low computational costs and usually removes the tensile instability. Within this thesis this approach is tried to settle some numerical difficulties in simulating the benchmark experiments. As described in Sec. 5.2, the application of Monaghan's fix has negligible influence on the results.

4.4.4. Rotational instability and correction factors

A phenomenon called rotational instability is another consequence of the low order consistency of the standard SPH scheme, which already was the reason for the tensile instability (see Sec. 4.4.3). Here, the conservation of angular momentum of a rigidly rotating solid body is significantly violated. Speith (2007) showed through simulations of a rotating plate, that at first the rotation speed decreases and finally the rotation changes direction. He found that this behaviour does not originate from an inaccuracy caused by the kernel interpolation. Instead, this unphysical effect is due to increasing particle disorder, and hence is a discretisation effect.

Similar to an earlier correction by Randles and Libersky (1996), Speith (2007) proposed a correction to the velocity derivatives such that the scheme is linearly consistent. In contrast to the former reference, Speith only corrects the velocity derivatives of the strain rate (Eq. 4.85) and rotation rate (Eq. 4.96) tensors. According to the standard SPH scheme the spatial derivative of the velocity components is given by

$$\frac{\partial v_\alpha^a}{\partial x_\beta^a} = \sum_b \frac{m^b}{\rho^b} (v_\alpha^b - v_\alpha^a) \frac{\partial W^{ab}}{\partial x_\beta^a} \,. \tag{4.171}$$

This expression is replaced by

$$\frac{\partial v_\alpha^a}{\partial x_\beta^a} = \sum_b \frac{m^b}{\rho^b} (v_\alpha^b - v_\alpha^a) \frac{\partial W^{ab}}{\partial x_\gamma^a} C_{\gamma\beta} \,. \tag{4.172}$$

where $C_{\gamma\beta}$ is the inverse of

$$\sum_b \frac{m^b}{\rho^b} (x_\alpha^b - x_\alpha^a) \frac{\partial W^{ab}}{\partial x_\gamma^a} \,, \tag{4.173}$$

which is

$$\sum_b \frac{m^b}{\rho^b} (x_\alpha^b - x_\alpha^a) \frac{\partial W^{ab}}{\partial x_\gamma^a} C_{\gamma\beta} = \delta_{\alpha\beta} \,. \tag{4.174}$$

By construction the errors caused by particle disorder cancel out, which allows correct simulations of rigid body rotation. I apply this correction to most of the simulations of Ch. 5 and to all simulations of Ch. 6.

5. Calibration

The key ingredients of the elasticity, plasticity, and porosity models described in Sec. 4.3 are the material parameters and relations. Only with a precise knowledge of these specific macroscopic properties a realistic simulation of the material is possible. At the same time, reliable measurements are sparse. As already pointed out in Sec. 3.1 and 3.2, the material which is studied best in the laboratory and in molecular dynamics simulations consists of mono-disperse SiO_2 spheres with a diameter of 1.5 µm. For this reason, I use this as the reference material for the whole calibration process. A detailed specification of this dust analogue can be found in Blum and Schräpler (2004) and Blum et al. (2006b). Despite the difficult handling of highly porous SiO_2 dust, laboratory experiments provided data for the compressive $\Sigma(\phi)$ and tensile strength $T(\phi)$ at the start of the calibration process described in this chapter. In contrast, relations for the shear strength $Y(\phi)$, bulk modulus $K(\phi)$ and, shear modulus $\mu(\phi)$ were missing and only possible relations were available.

dust material

input parameters

However, implementing realistic parameters alone is not sufficient for a *valid numerical model*. The applicability of the solid body and porosity models and also the correct functionality of the code need to be validated in suitable benchmark experiments, which are carried out numerically and in the laboratory. Alike comparisons were performed earlier, for example Jutzi et al. (2009b) validated their porosity model for brittle material with pumice impact experiments. In contrast to their calibration, the thesis at hand does not rely on one type of experiment (impact) only, but it uses three different setups to validate the elastic, compression, and fragmentation properties of SiO_2 dust.

model validation

In the course of the calibration process, it is found that the data provided by Blum and Schräpler (2004) and Blum et al. (2006b) are *not directly applicable* for the porosity model at hand. This is because their relations are quasi-static, whereas in pre-planetesimal collisions dynamic relations are needed. As a consequence, the correct material parameters have to be found by numerical parameter studies using the benchmark setups. This results in a profound calibration process in intensive and close collaboration with experimental physicists. In the end, all benchmark tests can be reproduced with a *consistent set of material parameters*. Finally, the calibration process not only yields a validated numerical model but also estimates for material parameters, which were unknown before. The results of this fruitful collaboration are published in Güttler et al. (2009) and Geretshauser et al. (2010).

inapplicable relations

calibration condition

In this chapter I describe the calibration process. As a basis the benchmark experiments are introduced in Sec. 5.1. The influence of numerical parameters on the outcome of the benchmark simulations are investigated in Sec. 5.2. The actual calibration process and the resulting material parameters are presented in Sec. 5.3. In Sec. 5.4, I summarise the results of this chapter.

5.1. Benchmark Experiments

5.1.1. Compaction setup

The following setup is chosen as an easy and well-defined calibration experiment: A glass sphere drops with known impact velocity v_0 into a dust sample ($\phi = 0.15$) generated by random ballistic deposition (RBD Blum and Schräpler 2004). The calibration parameters are quantities describing the dynamic behaviour of the sphere. These include the deceleration curve, stopping time, and intrusion depth for various velocities and projectile diameters. Additionally, the compaction of the dust under the glass bead for a 1.1 mm projectile with a velocity of 0.65 m/s is considered. Compaction of porous dust aggregates is an efficient way of dissipating kinetic energy in mutual collisions. Lower collision velocities decrease the probability and amount of fragmentation and increase the probability of sticking (see Sec. 2.3.1). Therefore, a correct reproduction of the compaction properties is highly important for the planetesimal formation process.

Laboratory setup

In this section, I give a short summary of the laboratory compaction calibration setup, which has been described by Güttler et al. (2009) in detail.

A glass sphere with a diameter of 1 to 3 mm impacts into the dust aggregate material with a velocity between 0.1 and 1 m/s under vacuum conditions (pressure 0.1 mbar). For the measurement of the dynamic behaviour (see Fig. 5.1, left), an elongated epoxy projectile is used instead of the glass sphere. The bottom shape and the mass resemble the glass bead while the lower density and the therefore longer extension makes it possible to observe the projectile during the intrusion. The projectile is observed by a high-speed camera (12,000 frames per second) and the position of the upper edge is followed with an accuracy of ~ 3 μm. With this setup three calibration quantities can be determined: the *maximum intrusion*, *stopping time*, and *(normalised) deceleration curve.*

maximum intrusion Firstly, the maximum intrusion is defined by the distance from the bottom of the spherule to the upper surface plane of the dust sample. The elongation is necessary because in most of the experiments the maximum intrusion is deeper than the diameter of the sphere.

stopping time Secondly, the stopping time is defined by the time difference between first contact of the spherule with the sample surface and the moment of maximum intrusion.

deceleration curve Thirdly, the deceleration curve $h(t)$ is given by tracing the intrusion depth for every point in time from first touch until maximum intrusion. To make several experiments with different impact velocities and maximum intrusions comparable, the deceleration curve is normalised by the maximum intrusion and stopping time. The normalised data can be fitted well by a sine curve (Fig. 5.17, also Güttler et al. 2009).

While the dynamic properties are measured for various sphere diameters and impact velocities, the compaction of dust underneath the impacted glass bead is only determined for a 1.1 mm projectile with $v_0 = 0.65$ m/s. The density structure is reconstructed by X-ray micro-tomography (see Fig. 5.1, right). The glass bead diameter and velocity in these experiments correspond to the compaction calibration setup described in Table 5.1. The dust is enclosed in a plastic tube with 7 mm diameter. After the impact, the sample with an embedded glass spherule is positioned onto a rotatable sample carrier between an X-ray source and the detector. During the rotation through 360°, 400 transmission images are taken, from which a 3D density reconstruction is computed with a spatial resolution of 21 μm. This setup yields the density structure underneath the

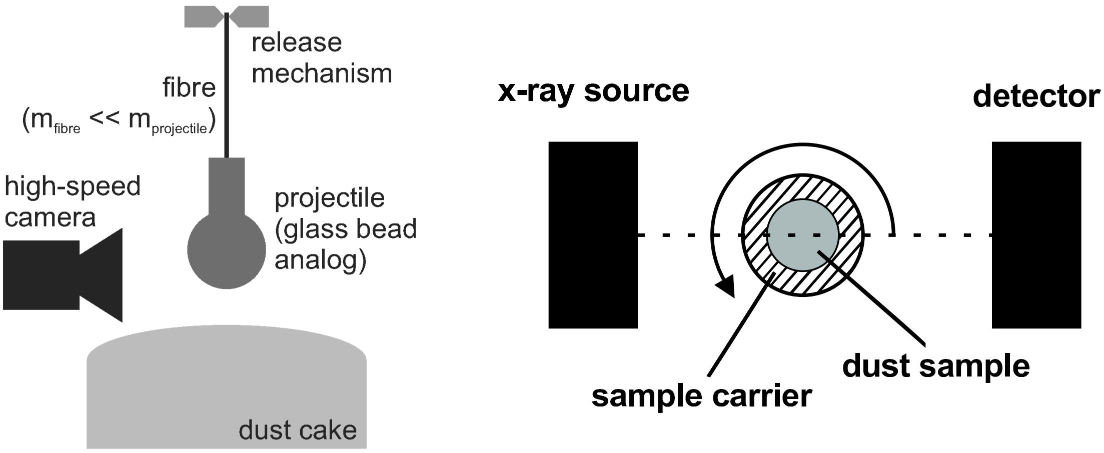

Figure 5.1. *Laboratory compaction setup.* Setup for deceleration and intrusion depth measurement (left): an elongated projectile as a glass bead analogue is dropped into the dust sample from a height of 1 to 40 mm. It is initially suspended on a fibre with negligible mass to avoid rotational motion. A high-speed camera observes the deceleration of the projectile. Setup for density profile measurement in an X-ray micro-CT device (left): The dust sample is rotated between an X-ray source and a detector. A 3D density reconstruction is computed from the transmission images (figures from Güttler et al. 2009).

glass bead generated by the impact. From these data another three calibration quantities can be derived: the *vertical density profile*, *vertical density cross-section*, and *density distribution of the cumulated volume*.

vertical density profile

Firstly, the vertical density profile or - because of Eq. 4.117 synonymously - vertical filling factor profile displays the filling factor along a straight line after the impact. The line intersects the centre of the impacted spherule and is perpendicular to the sample surface, which represents the origin of the profile (see Fig. 5.2 for an illustration). Vertical density profiles from laboratory data are exclusively produced in presence of the spherule, which is not removed when creating the X-ray tomography images (see the experimental data, e.g. in Fig. 5.12, 5.13, and 5.18). The vertical density profile represents a one-dimensional insight into the most important region of the density structure. In the calibration process it proves to be one of the most sensible instruments.

vertical density cross-section

Secondly, the *vertical density* (or filling factor) *cross-section* is a two-dimensional expansion of the vertical density profile. For this the density data from the X-ray tomography is radially averaged around the vertical density profile axis. The result is a two-dimensional image with the density structure colour coded (Fig. 5.19, left).

density distribution

Thirdly, the *density distribution* of the cumulated volume provides insight into the three-dimensional density structure of the dust sample after the impact. It is computed from the full data set of the X-ray tomography measurements and displays the volume (in sphere volumes) which is compacted to filling factors greater than a given ϕ. This calibration parameter is very sensitive to changes in the compressive strength relation $\Sigma(\phi)$ (Eq. 4.128). Examples are shown in Fig. 5.13 (middle), 5.14 (bottom), 5.16 (bottom), and 5.18 (bottom).

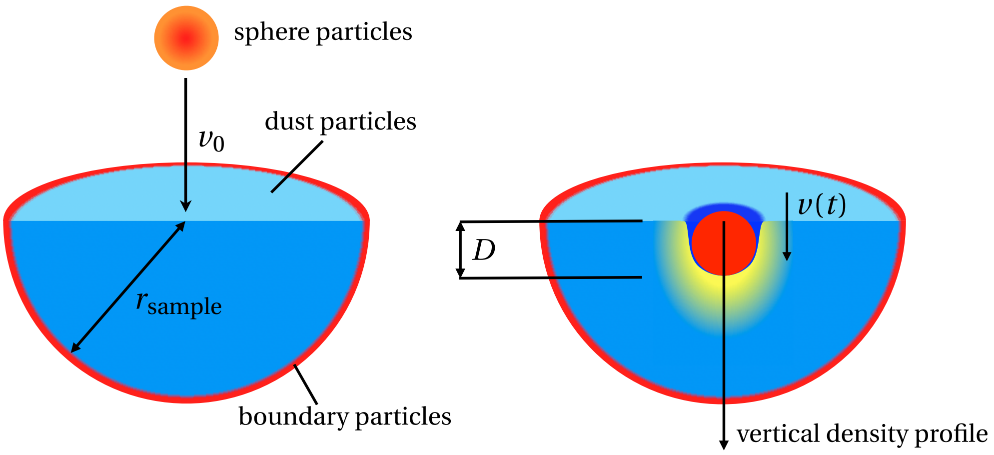

Figure 5.2. *Numerical compaction setup.* Both panels show a vertical cut through the midplane of the setting. As initial setup (left), a glass sphere impacts into the centre of an SiO_2 dust sample with initial velocity v_0. The sample with radius r_{sample} is bowl-shaped in 3D and hemicircle-shaped in 2D. In any case the dust is surrounded with boundary particles at its bottom. After the impact (right) the bottom of the sphere rests at intrusion depth D. Underneath, the dust material is compressed (indicated by the yellow area). This leads to a vertical density profile which is measured along an axis through the centre of the sphere and perpendicular to the sample surface. During the impact the bottom of the sphere is tracked for the deceleration curve. The parameters for the bouncing calibration setup are displayed in Tab. 5.1.

Numerical setup

numerical modelling The *numerical equivalent* (see Fig. 5.2) of the experimental setup described above is designed as follows: the glass spherule (diameter 1.1 mm) is modelled with the Murnaghan equation of state (Eq. 4.112) with the parameters specified in Tab. 5.1. The sphere hits a dust sample ($\phi = 0.15$) with impact velocity v_0. Gravity is taken into account. The influence of the shape of the sample is investigated in Sec. 5.2.3. A bowl shaped target consisting of a hemisphere with radius $r_{\mathrm{sample}} = 3.3\,\mathrm{mm}$ is found to be the most suitable setup with the lowest computational costs. The dust material is simulated with the plasticity and porosity models presented in Sec. 4.3.4. The sample is enclosed in a few layers of boundary SPH particles, which are treated as dust material but their acceleration is set to zero in every time step. This is equivalent to reflecting boundary conditions. Fixing the sample within a bowl reproduces the situation of the sample enclosed in the plastic tube. The diameter of the boundaries in the numerical setup is comparable to the laboratory setup. By this enclosure, dust material cannot evade to the side, which may alter the vertical density profile. This is an important improvement to earlier simulations (Geretshauser 2006).

numerical calibration parameters For the evaluation, the bottom of the sphere is traced during the simulation to determine stopping time, maximum intrusion, and deceleration curve. For the vertical density profile, the evaluation program described in Appx. A.1 determines the dust density along a line perpendicular to the sample surface going through the centre of the resting spherule (see Fig. 5.2, right). The density structure of the vertical density profile, vertical density cross-section, and density distribution is evaluated by means of the SPH sum (Eq. 4.15) and converted into the volume filling factor via Eq. 4.117. Vertical density profiles from the simulation data are produced in the presence (e.g. Fig. 5.6) and absence of the spherule (e.g. Fig. 5.8, and 5.10). Due to the perfect cylinder symmetry of the setup around the impact site the data for the vertical density cross-section is not averaged azimuthally as in the laboratory setup but a simple vertical 2D cross-section intersecting the vertical density profile line is produced from the simulation data. For the density distribution of the cumulated volume, the setup is divided into small volume cubes for which the density is averaged. The volume cubes are then cumulated with their respective densities.

setup dimension

In order to reduce computational costs, many simulations are carried out in 2D. In these cases the dust bowl reduces to a hemicircle and the glass sphere to a circle of the respective radius. The numerical setup uses cartesian coordinates although the symmetry of the problem would be more accurately described by cylindrical coordinates. However, the SPH scheme in cylindrical or polar coordinates battles with the problem of a singularity at the origin of the kernel function. There are only few attempts to resolve this issue (e.g. Omang et al. 2006), which are still under development and require high implementation efforts. Since 2D simulations provide only an indication of the calibration required and 3D simulations are aimed at, I stick to cartesian coordinates in this work.

artificial viscosity

In order to damp high frequency oscillations in the glass material, artificial viscosity ($\alpha_{\mathrm{av}} = 1$, $\beta_{\mathrm{av}} = 0$) is applied to the sphere particles. In order to prevent instabilities the dust particles are generally simulated with $\alpha_{\mathrm{av}} = 0.1$ and $\beta_{\mathrm{av}} = 0$. Those dust particles which are in contact with the sphere are an exception: They feature the same artificial viscosity parameter as the glass: $\alpha_{\mathrm{av}} = 1.0$ and $\beta_{\mathrm{av}} = 0$. In this way, glass and dust material are separated from each other by an artificial pressure (see Sec. 4.4.2 and in particular Eq. 4.162) and spurious energy dissipation among the dust particles is minimised. The actual choice of these values is motivated in Sec. 5.2.4 where the influence of artificial viscosity on the simulation outcome is also quantified and its curing effect on instabilities is discussed.

compaction setup usage

The compaction calibration setup is the most important and most elaborate benchmark experiment in this chapter. Therefore, the size and shape of the dust sample (Sec. 5.2.1) as well as the difference between 2D and 3D setup (Sec. 5.2.3) are studied carefully before the setting is used for calibration purposes. Subsequently, the compaction calibration setup is used to investigate the influence of the numerical parameters (1) spatial resolution, (2) numerical resolution, and (3) artificial viscosity. In detail, (1) the spatial resolution is given by the lattice constant l_{c}, which determines the distances between the SPH particles in the initial distribution. (2) The numerical resolution is governed by the smoothing length h. It regulates the number of interaction partners of each SPH particle. The resolution parameters are studied in Sec. 5.2.2. (3) The artificial viscosity is responsible for numerical stability and dissipative features of the dust material. It is investigated in Sec. 5.2.4. After establishing a profound numerical basis, the compaction calibration setup provides information on the shear strength (Sec. 5.3.2) and compressive strength (Sec. 5.3.3).

5.1.2. Bouncing setup

The bouncing calibration setup tests the porosity model for a combination of compaction and mainly restitution. To date, numerical simulations of porous dust aggregates (in particular MD simulations, see Sec. 3.2) were not able to reproduce the rebound at low impact velocities. In this work, this feature is simulated for the first time for porous SiO_2 dust. The setup is rather simple: A spherical dust aggregate of defined size hits a hard surface with a certain (low) velocity

Physical Quantity	Symbol	Value	Unit
Glass bead			
Bulk density$^{(*)}$	ρ_0	2,540	$\mathrm{kg\,m^{-3}}$
Bulk modulus$^{(*)}$	K_0	5×10^9	Pa
Murnaghan exponent$^{(*)}$	n	4	-
Radius	r	0.55×10^{-3}	m
Impact velocity	v_0	0.65	$\mathrm{m\,s^{-1}}$
Dust sample			
geometry (2D)$^{(b)}$		box/semicircle	-
geometry (3D)$^{(b)}$		hemisphere	-
sample size$^{(b)}$	$d_{\mathrm{sample}}, r_{\mathrm{sample}}$	3.3 mm	
Initial filling factor	ϕ	0.15	-
Bulk density	ρ_{s}	2,000	$\mathrm{kg\,m^{-3}}$
Reference density	ρ_0'	300	$\mathrm{kg\,m^{-3}}$
Filling factor RBD dust sample	ϕ_{RBD}	0.15	-
Bulk modulus	K_0	3×10^5	Pa
ODC mean pressure$^{(a)}$	p_{m}	260	Pa
ODC max. filling factor	$\phi_{\max}$	0.58	-
ODC min. filling factor	$\phi_{\min}$	0.12	-
ODC slope$^{(a)}$	Δ	0.58	-
Numerical parameters$^{(b)}$			
Lattice type (2D)		triangular	
Lattice constant (2D)	l_{c}	25×10^{-6}	m
Smoothing length (2D)	h	140×10^{-6}	m
Min. no. interaction partners (2D)	$I_{\min}$	~ 30	-
Av. no. interaction partners (2D)	I_{av}	~ 100	-
Max. no. interaction partners (2D)	$I_{\max}$	~ 180	-
Lattice type (3D)		cubic	
Lattice constant (3D)	l_{c}	50×10^{-6}	m
Smoothing length (3D)	h	187.5×10^{-6}	m
Min. no. interaction partners (3D)	$I_{\min}$	~ 70	-
Av. no. interaction partners (3D)	I_{av}	~ 240	-
Av. no. interaction partners (3D)	$I_{\max}$	~ 370	-
Artificial viscosity (bulk)	α_{av}	0.1	-
Artificial viscosity (von Neumann-Richtmyer)	β_{av}	0	-

Table 5.1. *Selected parameters for the compaction calibration setup.* ODC stands for omnidirectional compressive strength relation (Eq. 4.128). RBD denotes the random ballistic deposition method by Blum and Schräpler (2004). Quantities marked by (*) represent the parameters for sandstone in Melosh (1989) which I adopt for glass here. The material parameters calibrated by means of this setup in Sec. 5.3.3 are denoted by (a). The numerical and geometrical parameters marked by (b) are varied and tested in Sec. 5.2. The values shown in this table represent the final choices resulting from these studies.

v_0. The calibration parameter is the rebound velocity v_f or equivalently the dissipated energy. Since bouncing might be an obstacle to planetesimal formation (see Sec. 2.3.1), it is of particular importance to simulate the restitution behaviour of dust aggregates correctly to accurately determine the transitions between sticking, bouncing, and fragmentation. Inelastic restitution might also reduce the collision velocities of pre-planetesimals, which in particular affect the fragmentation barrier. Therefore, the dissipation of kinetic energy also has to be calibrated for in this benchmark setup.

Laboratory setups

aggregate - aggregate collision

Heißelmann et al. (2007) performed collisions between two cubic millimetre sized dust aggregates in an evacuated microgravity environment. From highly porous SiO_2 dust aggregates created by RBD (Blum and Schräpler 2004), they cut out cubes with $\phi \sim 0.15$. The collision velocity was $v_0 \sim 0.4\,\mathrm{m/s}$. In most of the collision experiments the aggregates became compacted and rebounded. From the velocities of the projectiles after the collision, it was estimated that only $\sim 5\,\%$ of the translational energy was preserved. The same result was obtained by shooting a highly porous cube onto a compact dust target with $v_0 \sim 0.2\,\mathrm{m/s}$.

aggregate - plate collisions

The numerical bouncing calibration setup described below (see also Fig. 5.3 and Tab. 5.2) is designed after the bouncing experiments by Weidling et al. (2009). Just like in the experiments by Heißelmann et al. (2007) highly porous SiO_2 dust cubes were obtained by cutting RBD aggregates ($\phi = 0.15$) into millimetre sized pieces. They were put onto a vibrating plate. In the subsequent collisions, the plate and dust aggregate hit each other with a mean velocity of $v_0 \sim 0.2\,\mathrm{m/s}$. In each collision the aggregate became slightly compacted and rebounded with a velocity, which is smaller than the collision velocity. The energy dissipation was consistent with the findings of Heißelmann et al. (2007).

Numerical setup

numerical modelling

In contrast to Weidling et al. (2009), a dust sphere is simulated instead of a dust cube. The latter was easier to cut from the RBD sample in the laboratory setup. For the simulations I choose the geometrically more regular object to circumvent uncertainties of the impact area and impact angle of a cube. As a second difference from the laboratory setup, I simulate only one impact and not hundreds of subsequent impacts with increasing compaction of the aggregate. This is because of limited computational resources.

The solid surface is a cylinder of radius $r_{\mathrm{plate}} = 0.8\,\mathrm{mm}$ and height $d_{\mathrm{plate}} = 0.1\,\mathrm{mm}$ (see Fig. 5.3), which is simulated with 115,677 SPH particles on a cubic lattice with lattice constant[1] $l_c = 12.5\,\mu\mathrm{m}$. This is motivated in Sec. 5.2.2. The plate consists of glass material for which the Murnaghan EOS (Eq. 4.112) is applied with the material parameters specified in Tab. 5.2.

Under the influence of gravity a dust sphere with radius $r = 0.5\,\mathrm{mm}$ hits the glass plate from above with a rather low velocity of $v_0 = 0.2\,\mathrm{m/s}$, which matches the setups by Weidling et al. (2009) and by Heißelmann et al. (2007) for collisions with a stationary target. The dust material is simulated with the plasticity and porosity models presented in Sec. 4.3.4 and the parameters in Tab. 5.2. In particular, the dust ball features an initial filling factor of $\phi = 0.15$ and it is composed of 267,737 SPH particles on a cubic lattice with $l_c = 12.5\,\mu\mathrm{m}$.

---

[1] The constant l_c of the cubic lattice is the edge length of one elementary cube of the lattice.

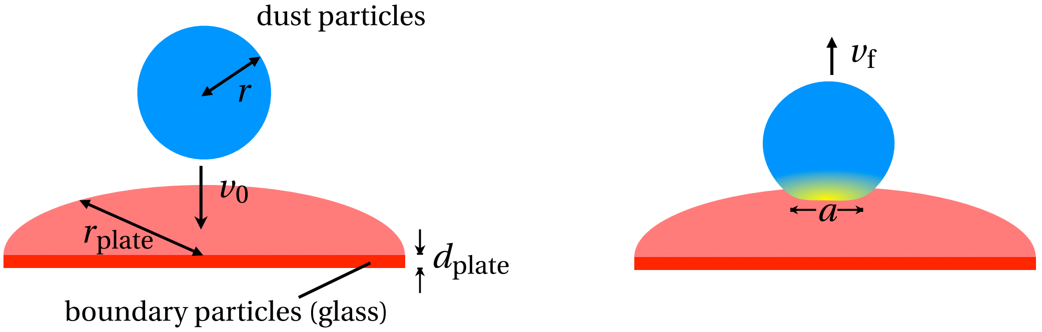

Figure 5.3. *Numerical bouncing setup.* Both panels show a vertical cut through the midplane of the setting. As a starting point (left), a dust sphere ($\phi = 0.15$) with radius $r = 0.5\,\mathrm{mm}$ hits a glass plate (radius $r_{\mathrm{plate}} = 0.8\,\mathrm{mm}$ and thickness $d_{\mathrm{plate}} = 0.1\,\mathrm{mm}$) with a low velocity $v_0 = 0.2\,\mathrm{m/s}$. During the impact the lower part of the dust sphere gets compacted (right, yellow area). The flattened area $A_{\mathrm{flat}} = (0.5a)^2\pi$ is estimated from the distance a of the outermost SPH particles enclosing the flattened bottom. The aggregate bounces off with a final velocity v_{f}. The SPH particles representing the glass plate are simulated as boundary particles with zero acceleration at each time step. The parameters for the bouncing calibration setup are compiled in Tab. 5.2.

artificial viscosity The parameters of the artificial viscosity are chosen as in the compaction calibration setup: The glass particles and all dust particles in contact with them have $\alpha_{\mathrm{av}} = 1$ and $\beta_{\mathrm{av}} = 0$ to prevent spurious mutual penetration of both materials. The dust particles are simulated with $\alpha_{\mathrm{av}} = 0.1$ and $\beta_{\mathrm{av}} = 0$ to minimise spurious energy dissipation. These choices are motivated in Sec. 5.2.4.

numerical resolution Regarding numerical resolution the smoothing length is set to $h = 3.75 \times l_{\mathrm{c}} \sim 46.9\,\mu\mathrm{m}$. This choice is justified in Sec. 5.2.2. This yields a minimum number of interaction partners of $I_{\mathrm{min}} \sim 65$. The average is $I_{\mathrm{av}} \sim 230$, and the maximum $I_{\mathrm{max}} = 340$. All interaction numbers are averaged over the total simulation time.

numerical calibration parameters At the low chosen speed the dust sphere bounces off the plate. The calibration parameter is the coefficient of restitution $\varepsilon_{\mathrm{rest}} = v_{\mathrm{f}} v_0^{-1}$, which is calculated from v_0 and v_{f}, which denote the initial and final velocity of the dust aggregate, respectively. For future comparison with experiments, which have not been carried out yet, I determine the contact time t_{cont}, which is defined as the time in which SPH particles of the sphere interact with plate particles[2]. Furthermore, I estimate the flattened area $A_{\mathrm{flat}} = (0.5a)^2\pi$ by determining the distance a between the outermost particles at the flattened bottom of the dust ball after the collision.

5.1.3. Fragmentation setup

The fragmentation calibration setup tests the porosity model for a complex interplay between tensile and compressive strength and in particular the bulk modulus. In the end the latter quantity proves to be most important for the final fragment mass distribution after a collision. The setup is similar to the bouncing setup: A dust ball hits a solid surface from below with a rather high impact speed v_0 such that the aggregate fragments. The fragment mass distribution is

---

[2] Interaction of SPH particles takes place when their smoothing lengths overlap.

Physical Quantity	Symbol	Value	Unit
Glass plate			
Bulk density$^{(*)}$	ρ_0	2,540	$\mathrm{kg\,m^{-3}}$
Bulk modulus$^{(*)}$	K_0	5×10^9	Pa
Murnaghan exponent$^{(*)}$	n	4	-
Radius	r_{plate}	0.8×10^{-3}	m
Thickness	d_{plate}	0.1×10^{-3}	m
Dust sample			
Initial filling factor	ϕ	0.15	-
Bulk density	ρ_{s}	2,000	$\mathrm{kg\,m^{-3}}$
Reference density	ρ_0'	300	$\mathrm{kg\,m^{-3}}$
Filling factor RBD dust sample	ϕ_{RBD}	0.15	-
Bulk modulus$^{(\mathrm{a})}$	K_0	5,000	Pa
ODC mean pressure$^{(\mathrm{a})}$	p_m	260	Pa
ODC max. filling factor	ϕ_2	0.58	-
ODC min. filling factor	ϕ_1	0.12	-
ODC slope	Δ	0.58	-
Impact velocity	v_0	0.2	$\mathrm{m\,s^{-1}}$
Radius	r	0.5×10^{-3}	m
Numerical parameters			
Lattice type (3D)		cubic	
Lattice constant (3D)	l_{c}	12.5×10^{-6}	m
Smoothing length (3D)	h	46.875×10^{-6}	m
Min. no. interaction partners (3D)	I_{min}	~ 65	-
Av. no. interaction partners (3D)	I_{av}	~ 230	-
Max. no. interaction partners (3D)	I_{max}	~ 340	-
Artificial viscosity (bulk)	α_{av}	0.1	-
Artificial viscosity (von Neumann-Richtmyer)	β_{av}	0	-

Table 5.2. *Numerical parameters for the bouncing calibration setup.* ODC stands for omni-directional compressive strength relation (Eq. 4.128). RBD represents the random ballistic deposition method by Blum and Schräpler (2004). Quantities marked by (*) represent the parameters for sandstone in Melosh (1989), which I adopt for glass here. The material parameters marked by (a) are varied and tested with this calibration setup (see Sec. 5.3.3 and 5.3.5). The values listed in this table are the final choices resulting from this study.

the calibration parameter. As it is pointed out in Sec. 2.5, not only fragmentation but the right amount of fragmentation might be essential to understand the planet formation process. Therefore, a quantitatively accurate reproduction of the fragmentation behaviour is particularly important for the intended field of application of the porosity model presented in this thesis.

Laboratory setup

This setup was described in Güttler et al. (2009, 2010) and Geretshauser et al. (2010). In an evacuated environment a device accelerates a nearly spherical dust aggregate with radius $r \sim 0.285\,\mathrm{mm}$ and filling factor $\phi = 0.35$ bottom up. This hits a polished solid surface from below with a collision speed of $v_0 = 8.4\,\mathrm{m/s}$. Only about 2 % of the projectile sticks to the target (Güttler et al. 2010). Most of the projectile shatters and the fragments fall down under the influence of gravity. The collision is observed by means of a high speed camera with a resolution of $16\,\mu\mathrm{m}$ per pixel. The measurement of the fragment masses is carried out by determining the projected surface area from the 2D images. With the assumptions of spherical shapes and unchanged filling factor of the fragments, the mass of the fragments can be calculated. Due to these assumptions, the filling factor is underestimated since compaction can be expected. The fragment distribution is then fitted by a power law (see also Eq. 5.9) whose parameters serve as calibration parameters.

Numerical setup

numerical modelling

The numerical fragmentation calibration setup (Fig. 5.4) is very similar to the bouncing calibration setup described above (see Sec. 5.1.2). A flat cylindrical object (radius $r_{\mathrm{plate}} = 0.8\,\mathrm{mm}$, thickness $d_{\mathrm{plate}} = 0.04\,\mathrm{mm}$) composed of 188,478 SPH particles and simulated by means of the Murnaghan EOS (Eq. 4.112) serves as an equivalent for the polished fixed target surface. The spherical dust aggregate consists of 189,296 SPH particles. Its filling factor is $\phi = 0.35$, which corresponds to a medium porosity aggregate in contrast to the high porosity aggregates of the compaction and bouncing calibration setups. For both objects the particles are placed on a cubic lattice with $l_{\mathrm{c}} = 8.0\,\mu\mathrm{m}$. With respect to the other setups, an increased spatial resolution is chosen such that a single SPH particle has less than 5×10^{-6} times the mass of the whole aggregate ($6.8 \times 10^{-8}\,\mathrm{kg}$).

numerical resolution

The smoothing length is $h = 30\,\mu\mathrm{m}$, which is $3.75 \times l_{\mathrm{c}}$ as motivated in Sec. 5.2.2. With this choice the minimum, average, and maximum number of interaction partners are $I_{\mathrm{min}} \sim 20$, $I_{\mathrm{av}} \sim 200$, and $I_{\mathrm{max}} \sim 350$, respectively. These values are averaged over the total simulation time.

artificial viscosity

As in the previous two setups the artificial viscosity parameters are set in the following way (details are explained in Sec. 5.2.4): The dust particles have $\alpha_{\mathrm{av}} = 0.1$ and $\beta_{\mathrm{av}} = 0$. This minimises dissipation by artificial viscosity. The glass particles and all dust particles in contact with them have $\alpha_{\mathrm{av}} = 1$ and $\beta_{\mathrm{av}} = 0$, which separates the two materials and prevents instabilities. The material separation leads to an important difference between the numerical and experimental fragmentation setups. In the laboratory some portion of dust is observed to stick on the target surface. This behaviour cannot be reproduced in the simulations because of the artificial separation by means of artificial viscosity. In the simulation results, the sticking portion of the laboratory is accounted for as a large fragment in the fragment distribution.

After the collision, the SPH particle distribution is evaluated by means of the fragment evaluation tool described in Appx. A.2. In the SPH scheme, fragmentation occurs when SPH particles within a solid body lose contact with their adjacent particles, i.e. when the SPH particles no longer in-

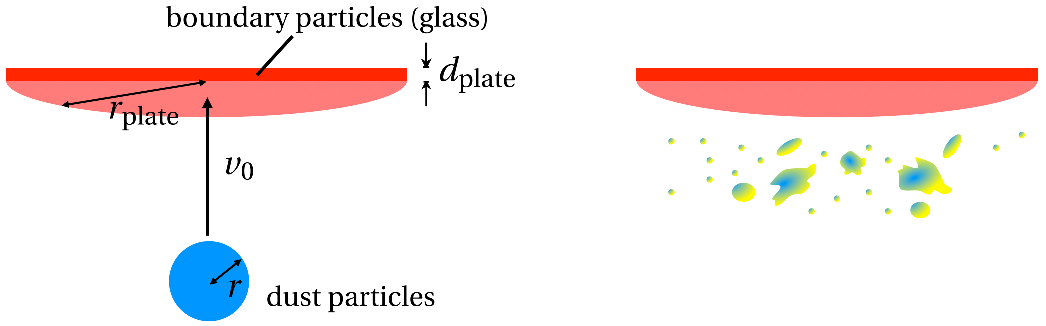

Figure 5.4. *Numerical fragmentation setup.* Both panels show a vertical cut through the midplane of the setting. As an initial condition (left), a dust ball ($\phi = 0.35$) with radius $r = 0.285\,\text{mm}$ hits a glass plate (radius $r_{\text{plate}} = 0.8\,\text{mm}$ and thickness $d_{\text{plate}} = 0.04\,\text{mm}$) from bottom up with a high velocity $v_0 = 8.4\,\text{m/s}$. During the impact the aggregate gets disrupted into a fragment distribution (right), which serves as a calibration parameter. The initial parameters for this setup are shown in Tab. 5.3.

numerical calibration parameters

teract. Two fragments are completely separated as soon as their respective subsets of particles reach a distance of more than $2h$ so that their kernels do not overlap onward. The fragment evaluation tool detects all separated sets of particles and calculates the centre of mass (CoM), the CoM velocity, and the mass of the fragment, amongst other quantities. In contrast to the method of determining the fragment masses in the laboratory setup, the change in filling factor and an inhomogeneous filling factor distribution of a fragment can be taken into account when the fragment mass is computed. Additionally, the simplifying assumption of a spherical shape is not necessary and the mass can be evaluated exactly for irregularly shaped fragments. While in the experimental setup the resolution of the smallest fragments is limited by the resolution of the camera, in the numerical setup the mass of an SPH particle is the smallest particle mass that can be resolved. For this numerical reason, I introduce the sub-resolution population in my suggestion for a new classification scheme for pre-planetesimal collision outcomes (see Sec. 6.1). As stated above, in the fragmentation calibration setup the resolution is chosen such that the numerical resolution is finer than the experimental resolution.

5.2. Numerical Setting

In this section, the influence of geometrical and numerical parameters on the outcome of simulations with the porosity model presented in Sec. 4.3.4 is tested. For this task I use the compaction calibration setup of Sec. 5.1.1. The basic parameters are specified in Tab. 5.1 and utilised where not stated otherwise. Since a relatively large dust sample with a considerable number of particles has to be simulated in the compaction calibration setup, the computational costs have to be minimised. As a first step (Sec. 5.2.1), a minimum size dust sample is chosen with a suitable shape, such that no artefacts due to size and shape are produced. This study is carried out in 2D. As a second step (Sec. 5.2.2), a suitable numerical and spatial resolution is determined in 2D and 3D simulations. After that, the effect of the dimension on the setup is quantified in Sec. 5.2.3. Finally in Sec. 5.2.4, the influence of artificial viscosity and other numerical parameters is discussed.

Physical Quantity	Symbol	Value	Unit
Glass plate			
Bulk density$^{(*)}$	ρ_0	2,540	$\mathrm{kg\,m^{-3}}$
Bulk modulus$^{(*)}$	K_0	5×10^9	Pa
Murnaghan exponent$^{(*)}$	n	4	-
Radius	r_{plate}	0.8×10^{-3}	m
Thickness	d_{plate}	0.04×10^{-3}	m
Dust sample			
Initial filling factor	ϕ	0.35	-
Bulk density	ρ_{s}	2,000	$\mathrm{kg\,m^{-3}}$
Reference density	ρ'_0	700	$\mathrm{kg\,m^{-3}}$
Filling factor RBD sample	ϕ_{RBD}	0.15	-
Bulk modulus$^{(\text{a})}$	K_0	4,500	Pa
ODC mean pressure	p_m	260	Pa
ODC max. filling factor	ϕ_2	0.58	-
ODC min. filling factor	ϕ_1	0.12	-
ODC slope	Δ	0.58	-
Impact velocity	v_0	8.4	$\mathrm{m\,s^{-1}}$
Radius	r	0.285×10^{-3}	m
Numerical parameters			
Lattice type (3D)		cubic	
Lattice constant (3D)	l_{c}	8×10^{-6}	m
Smoothing length (3D)	h	30×10^{-6}	m
Min. no. interaction partners (3D)	I_{min}	~ 20	-
Av. no. interaction partners (3D)	I_{av}	~ 200	-
Max. no. interaction partners (3D)	I_{max}	~ 350	-
Artificial viscosity (bulk)	α_{av}	0.1	-
Artificial viscosity (von Neumann-Richtmyer)	β_{av}	0	-

Table 5.3. *Numerical parameters for the fragmentation calibration setup.* ODC stands for omnidirectional compressive strength relation (Eq. 4.128). The random ballistic deposition method by Blum and Schräpler (2004) is abbreviated by RBD. Quantities marked by (*) represent the parameters for sandstone in Melosh (1989), which I adopt for glass here. The material parameters marked by (a) are varied and tested with this calibration setup (see Sec. 5.3.5). The values of this table are the final choices resulting from the fragmentation study.

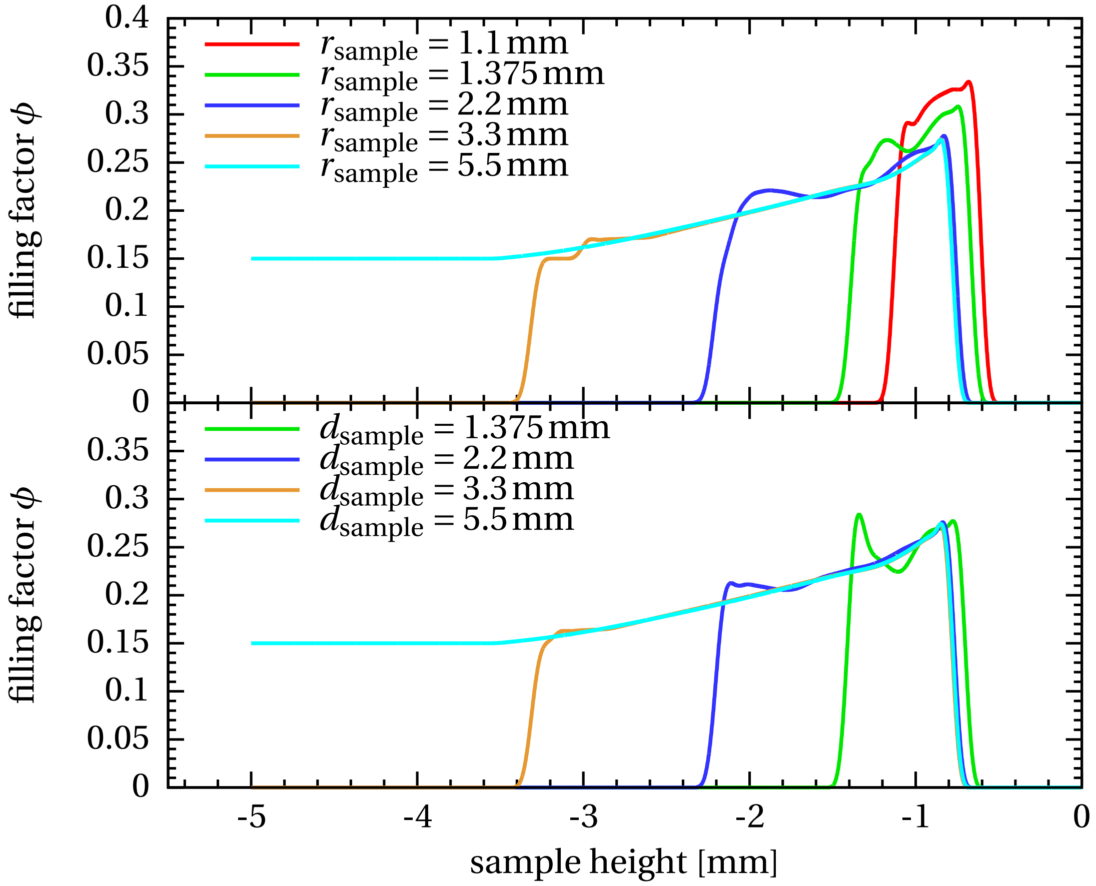

Figure 5.5. *Influence of dust sample size and shape on the compaction calibration setup.* Vertical density profile at maximum intrusion for different shapes of the 2D dust sample. For the semicircle (top) r_sample denotes the radius of the semicircle and for the 8 mm wide box (bottom) d_sample stands for the depth of the box. In both cases spurious boundary effects appear for $r_\mathrm{sample} < 3.3$ mm and $d_\mathrm{sample} < 3.3$ mm, respectively.

5.2.1. Computational domain and boundary conditions

In 2D simulations, the effect of changing the size and shape of the dust sample is tested. Initially the particles are placed on a triangular lattice with a lattice constant of 25 µm. The elementary structure of this lattice is an equilateral triangle. In this way, all SPH particles initially have the same distance. To be geometrically consistent with the cylindric experimental setup of a dust sample enclosed in a plastic tube, firstly a box with width 8 mm is chosen. Its depth is varied in the following range: 1.375 mm, 2.2 mm, 3.3 mm, and 5.5 mm. This is equivalent to $2.5\times, 4\times, 6\times$, and $10\times$ the radius of the sphere r. The impact velocity is $v_0 = 0.65\,\mathrm{m/s}$ and the vertical density profile (see Sec. 5.1.1 and Fig. 5.2) is used for result comparison. For this, the filling factor is evaluated along a line through the centre of the sphere perpendicular to the dust sample surface (see Fig. 5.2). Comparing the curves (Fig. 5.5, bottom), two features are remarkable: (1) The maximum filling factor at the top of the dust sample ($\phi \sim 0.27$ at $D \sim -0.8\,\mathrm{mm}$) and the intrusion depth D is nearly the same for all dust sample sizes. Because the filling factor ϕ and pressure p are connected by the compressive strength relation (Eq. 4.128), the maximum filling factor gives

2D box

h	h/l_c	I_{min}	I_{av}	I_{max}	T_{comp}	N_{steps}
0.050 mm	2	3	13	25	16.2 h	132401
0.075 mm	3	10	30	55	14.8 h	96912
0.100 mm	4	16	53	92	19.8 h	71175
0.125 mm	5	23	82	142	19.0 h	56347
0.150 mm	6	32	116	205	21.6 h	46782
0.175 mm	7	43	158	274	24.3 h	39980

Table 5.4. *Parameters for the convergence study regarding interaction numbers.* In this table, h is the smoothing length and l_{c} the lattice constant determining the distance of two SPH particles in the initial distribution. I_{min}, I_{av}, and I_{max} are the minimum, average, and maximum number of interaction partners, respectively. These quantities are averaged over the total simulation time. T_{comp} denotes the computation time of each simulation on a machine specified in the text and N_{steps} is the number of integration steps.

an indication for the maximum pressure that occurrs during the compaction phase. For $\phi \sim 0.27$ this gives $p_{\mathrm{max}} \sim 170\,\mathrm{Pa}$ for the finally calibrated relation. (2) For $d_{\mathrm{sample}} < 3.3\,\mathrm{mm}$, density peaks appear at the lower boundaries ($D \sim -1.4\,\mathrm{mm}$ and $D \sim -2.2\,\mathrm{mm}$). These peaks are generated by density waves that were reflected at the lower boundary.

2D semicircle

The box-shaped 2D sample resembles the laboratory setup more but for the purpose of reducing computation time, the geometrical shape of the dust sample is now changed: the dust sample is simulated as a semicircle using the same size variation as above for the box but with one additional step $r_{\mathrm{sample}} = 1.1\,\mathrm{mm}$. The resulting density profiles are shown in Fig. 5.5 (top). In contrast to the corresponding simulations with the box-shaped samples, for $r_{\mathrm{sample}} \leq 1.375\,\mathrm{mm}$ an increased maximum filling factor and a slightly reduced intrusion depth is found. Because of the greater volume lateral to the intrusion channel, material can be pushed aside more easily than inside the narrow boundaries of the semicircle. Therefore, a higher fraction of the material is compressed to higher filling factors. For $r_{\mathrm{sample}} > 3.3\,\mathrm{mm}$, the spurious boundary effects become negligible within the compaction calibration setup and the density structure shows no significant difference between box-shaped and semicircle-shaped dust samples.

resulting shape

As a result from this study, all further simulations with the compaction calibration setup are conducted on the basis of a semicircle in 2D or a hemisphere in 3D with a radius of $r = 3.3\,\mathrm{mm}$.

boundary conditions

In all cases, the dust sample is bordered by a few layers of boundary particles whose acceleration is set to zero at each integration step. This simulates reflecting boundary conditions. The equation of state is that of dust particles. I also tested damping boundary conditions by simulating two layers of boundaries. The outer layer was treated as described before, the inner (sufficiently large) layer was simulated with a high artificial α-viscosity. Since there was no significant difference in the outcome, all boundaries are fixed by zeroing their accelerations. Thus, they are considered to be reflecting.

5.2.2. Resolution and convergence

spatial resolution

Within the SPH scheme two kinds of resolution are of importance (Speith 2007, and references therein). Firstly, the *spatial resolution* accounts for the number of particles that resolve a spatial

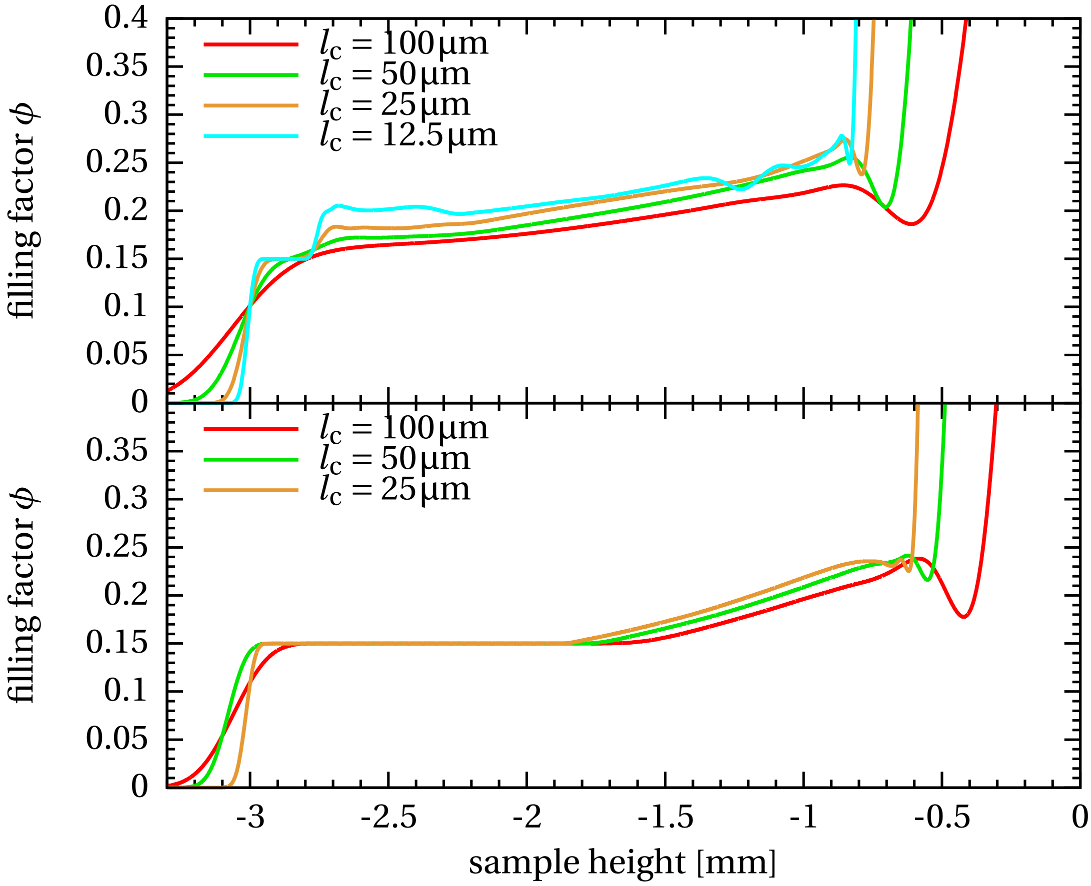

Figure 5.6. *Convergence study of spatial resolution I.* Convergence study of the vertical density profile for 2D (top) and 3D (bottom) compaction calibration setups with respect to the spatial resolution represented by the lattice constant l_c. The increase in filling factor towards the surface of the dust sample accounts for the glass bead, which is not removed in this plot. All curves show a characteristic density minimum between the sphere and dust sample and a characteristic density peak indicating the dust sample surface. The reason for these characteristic features is explained in the text.

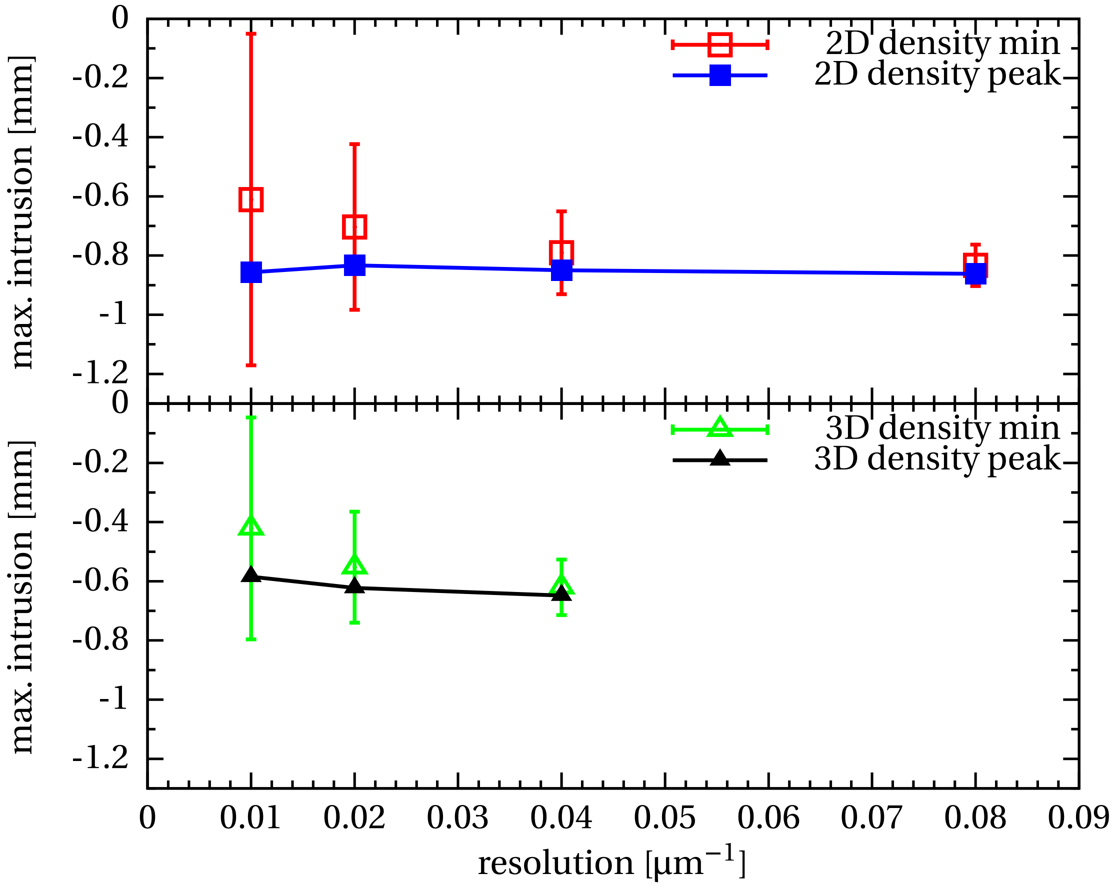

Figure 5.7. *Convergence study of spatial resolution II.* Convergence study of the maximum intrusion depth for the 2D (top) and 3D (bottom) compaction calibration setups. Filled symbols represent the position of the density peak of the dust material whereas empty symbols denote the position of the density minimum at the gap between the glass bead and dust material. The values are derived from the density profiles in Fig. 5.6. The smoothing length in the respective simulation is indicated by the error bars. While the density peak position remains almost constant at $D \sim -0.9\,\mathrm{mm}$ (2D) and $D \sim -0.65\,\mathrm{mm}$ (3D) with increasing spatial resolution, the position of the density minimum quickly converges to the same value. This is because of the artificial separation between dust and glass materials, which is of the order of a smoothing length. Further explanations are given in the text.

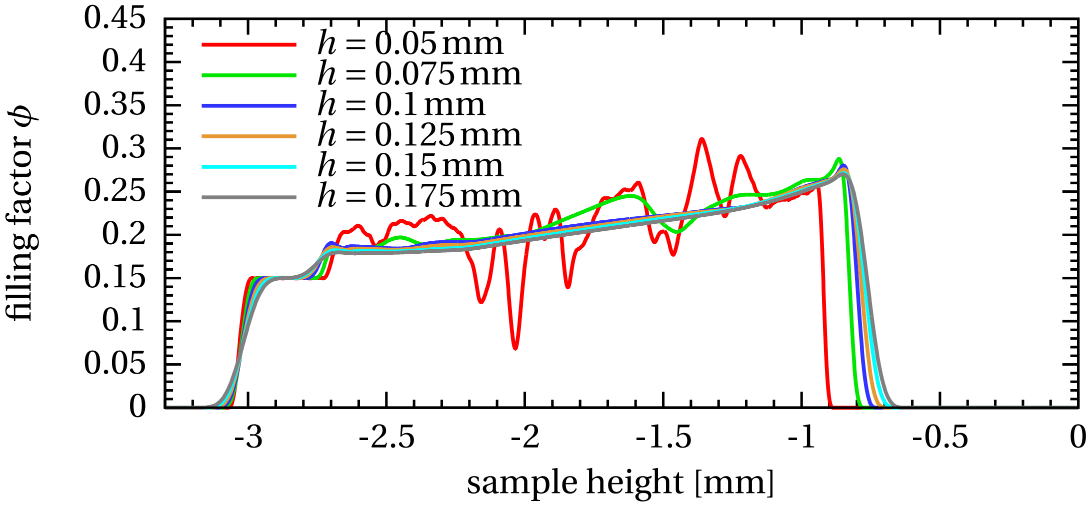

Figure 5.8. *Convergence study of numerical resolution.* Convergence study of the density profile using the 2D compaction calibration setup with varying smoothing length h. Through this variation, the number of interaction partners is varied according to Table 5.4 where a higher number of interaction partners denotes a higher numerical resolution. The glass bead is removed in this plot. For $h \le 0.075\,\mathrm{mm}$ clear signs of instabilities are visible. For $h \ge 0.1\,\mathrm{mm}$ the filling factor has the same value and its position remains constant. The smoothing of the dust sample surface is increased for increasing h.

element. In the context of this thesis, the spatial resolution corresponds to the smoothing length h and, if the numerical resolution is fixed, also to the lattice constant l_c, which is a measure for the distance between two SPH particles for the various lattice types. Secondly, the *numerical resolution* is given by the number of interaction partners of a single SPH particle. It was shown that within the SPH scheme an increase in spatial resolution may result in convergence problems if not at the same time the numerical resolution is increased (Speith 2007, and references therein). For this reason, in this section spatial resolution as well as numerical resolution are tested.

numerical resolution

previous studies

Geretshauser (2006) showed with a setting similar to the compaction calibration setup (Sec. 5.1.1) that the intrusion depth D may strongly depend on the spatial resolution of the dust sample. In particular, the intrusion depth of the glass bead can be doubled by doubling the spatial resolution. Since the benchmark experiments presented in this thesis are extremely sensitive even to minor changes in the setup, the convergence properties of the porosity model and the underlying SPH method are investigated carefully in this section.

spatial resolution study

The spatial resolution study utilises the compaction calibration setup (see Sec. 5.1.1, and Fig. 5.2) with the numerical and geometrical parameters presented in Tab. 5.1 except for a higher mean pressure $p_m = 1.3\,\mathrm{kPa}$. In addition, the lattice type and lattice constant are varied in this investigation. The smoothing length is varied such that the number of interaction partners (numerical resolution) is roughly constant.

For the 2D convergence study, particles are initially placed on a triangular lattice. The lattice constants l_c are 100, 50, 25, and 12.5 µm. The smoothing length h is kept constant relative to l_c at a ratio of $h = 5.6 \times l_c$. This leads to a constant number of interaction partners for each pair of h and l_c. Averaged over the total simulation time, the maximum, average, and minimum numbers of interaction partners are $I_{max} \sim 180$, $I_{av} \sim 100$, and $I_{min} \sim 30$, respectively.

In the 3D convergence study, a cubic lattice is used. The edge lengths of one elementary cube are $l_c = 100$, 50, and 25 µm. Consequently, the distances between single SPH particles are not exactly equal. The 25 µm resolution is simulated with 3.7 million SPH particles, which represents the current limit of the available computational resources. The ratio between smoothing length and lattice constant is fixed at $h = 3.75 \times l_c$, which yields $I_{max} \sim 370$, $I_{av} \sim 240$, and $I_{min} \sim 70$ as resulting interaction numbers, which are averaged over simulation time.

density minimum

The resulting vertical density profiles are presented in Fig. 5.6. In contrast to the plots in Fig. 5.5, the glass sphere is not removed here. Coming from the right side of the plot, the filling factor rapidly decreases from a high value beyond the edge of the plot describing the sphere. The filling factor reaches its minimum at an artificial gap between sphere and surface of the dust sample. This minimum is referred to as a *density minimum* in the further discussion. The width of this gap is about one smoothing length h. The existence of the gap has two reasons: (1) The sphere and dust material have to be separated by artificial viscosity for stability reasons. This issue is discussed in Sec. 5.2.4. (2) The volume of the sphere represents an area of extremely high density and pressure with respect to the dust sample. This area is smoothed out by the SPH method and the width of the smoothing is given by the smoothing length.

density peak

Although a clear convergence behaviour is evident in Fig. 5.6 for both the 2D and the 3D cases, a more unique convergence criterion has to be found. For this purpose, the maximum intrusion depth is more appropriate since it proved to be very sensitive to resolution changes (Geretshauser 2006). The shape of the filling-factor profile provides two ways in which the intrusion depth can be determined: (1) the density minimum, which is in between a sphere and a dust sample; and (2) the filling factor maximum of the dust material on the left of the gap between sphere and dust sample. The latter is referred to as *density peak* in the following discussion.

spatial convergence

Figure 5.7 shows the results for both cases in 2D (top) and 3D (bottom). The error bars around the minimum values represent the smoothing length in the respective simulation and provide an indication of the maximum error. The position of the density peak remains almost constant, converging to $D \sim -0.9$ mm (2D) and $D \sim -0.65$ mm (3D), respectively, at higher resolutions. The position of the density minimum at low resolutions differs significantly from the position of the density peak but converges quickly to the same intrusion depth at higher resolutions. However, the differences between the extrema remain well within one smoothing length. This is because of the separation of the sphere and dust sample discussed above. Comparing 2D and 3D convergence, the 3D case seems to converge more quickly.

spatial res. choice

Based on the findings of this study, I choose a spatial resolution of $l_c = 25$ µm for additional simulations in 2D. In the 3D case, $l_c = 50$ µm is sufficient but $l_c \leq 50$ µm is desirable if feasible.

numerical resolution study

After defining suitable values for the spatial resolution, the numerical resolution has to be investigated. To test this feature, the 2D compaction calibration setup is utilised with $l_c = 25$ µm. The ratio of smoothing length and lattice constant h/l_c is varied from 2 to 7 in unit steps. This determines the initial number of interaction partners that is smoothed over. The resulting maximum, average, and minimum interactions I_{max}, I_{av}, and I_{min}, respectively, and the corresponding smoothing lengths h can be found in Table 5.4.

Please note that in this test the spatial resolution h changes. Hence, a mixture of spatial and numerical convergence is investigated here. For a pure test of numerical resolution h must be fixed and l_c must be changed. However, for decreasing l_c this test is infeasible due to limited computational resources. Therefore, I choose this mixed test as an indication for sufficient numerical resolution.

Comparing the density profiles in Fig. 5.8, where the glass bead is removed, instabilities in the *numerical convergence*

form of filling factor fluctuations due to insufficient interaction numbers appear for smoothing lengths $h \leq 0.075\,\mathrm{mm}$, i.e. for $I_{\mathrm{av}} \leq 30$. For $h \geq 0.1\,\mathrm{mm}$, the density profile has essentially the same shape: the position and height of the filling factor peak remains nearly the same and ϕ drops smoothly to ~ 0.18 towards the bottom of the dust sample. Only the sharp edge at the top of the dust sample at $D \sim -0.7\,\mathrm{mm}$ is smoothed across a wider range due to the increased smoothing length.

computing time, integration steps

Additionally, I measure the time T_{comp} the computations take, simulated on 4 cores of a cluster with Intel Xenon Quad-Core processors (2.66 GHz) for a simulated time of 5 ms and the number of integration steps N_{step} of the adaptive Runge-Kutta Cash-Karp integrator.

Table 5.4 shows that the number of integration steps N_{step} decreases with increasing interaction numbers. This is because the elastic waves inside the dust sample are smoothed over a wider range causing the adaptive integrator to increase the duration of a time step. This is because density fluctuations do not have to be resolved as sharply as when a lower amount of smoothing is applied. As expected, the computation time T_{comp} generally increases with the increasing number of interactions. There are two exceptions: $h = 0.075\,\mathrm{mm}$ and $h = 0.125\,\mathrm{mm}$. Here, the decrease in N_{steps} overcompensates for the increase in the interactions leading to a decrease in T_{comp}. Hence, a ratio $h/l_c \sim 5$ yields the necessary accuracy and an acceptable amount of computation time. This study justifies the choice of $h/l_c = 5.6$, which is used for the 2D compaction calibration setup in the further course of this thesis.

numerical resolution choice

According to these findings, for 3D simulations an average interaction number of theoretically $I_{\mathrm{av}}^{3/2} \sim 750$ would be needed to achieve a numerical resolution comparable to the 2D setup. However, such simulations are infeasible and the choice of $I_{\mathrm{av}} \sim 240$ in 3D is equivalent to $I_{\mathrm{av}} \sim 40$ in 2D, which should provide sufficient and reliable accuracy.

The final choices for the numerical parameters of the compaction calibration setup are compiled in Tab. 5.1

5.2.3. Geometrical difference of 2D and 3D setups

As one can easily see in Fig. 5.7, 2D and 3D simulations have significantly different convergence values for the intrusion depth. This deviation is caused by the geometrical difference of the 2D and 3D setup. The 2D setup (glass circle impacts into dust semicircle) represents a slice through a glass cylinder and a semi-cylindrical dust sample, which implies an infinite expansion into the third spatial direction. In contrast, the 3D setup represents a real sphere dropping into a “bowl” of dust.

empirical intrusion relation

In the reference experiments for the compaction calibration setup, a linear dependence

$$D = \left(8.3 \times 10^{-4}\,\frac{\mathrm{m^2 s}}{\mathrm{kg}}\right)\frac{m v_0}{A}\,, \tag{5.1}$$

between intrusion depth D, cross section $A = \pi r^2$ and momentum $m v_0$ of the glass sphere is found for a series of impacts with 1 mm and 3 mm spherules at various impact velocities v_0 (Güttler et al. 2009). This linear relation contains the cross section A, and thus a geometrical dependence. Hence, Eq. 5.1 can be utilised to determine a rough correction factor between 2D and 3D simulation setups

geometrical correction factor

$$\frac{m_{3\mathrm{D}} v_0}{A_{3\mathrm{D}}} = \frac{\frac{4}{3}\pi r^3 \rho_0 v_0}{\pi r^2} = \frac{8}{3\pi}\,\frac{\pi r^2 \rho_0 v_0}{2r} = \frac{8}{3\pi}\,\frac{m_{2\mathrm{D}} v_0}{A_{2\mathrm{D}}}\,, \tag{5.2}$$

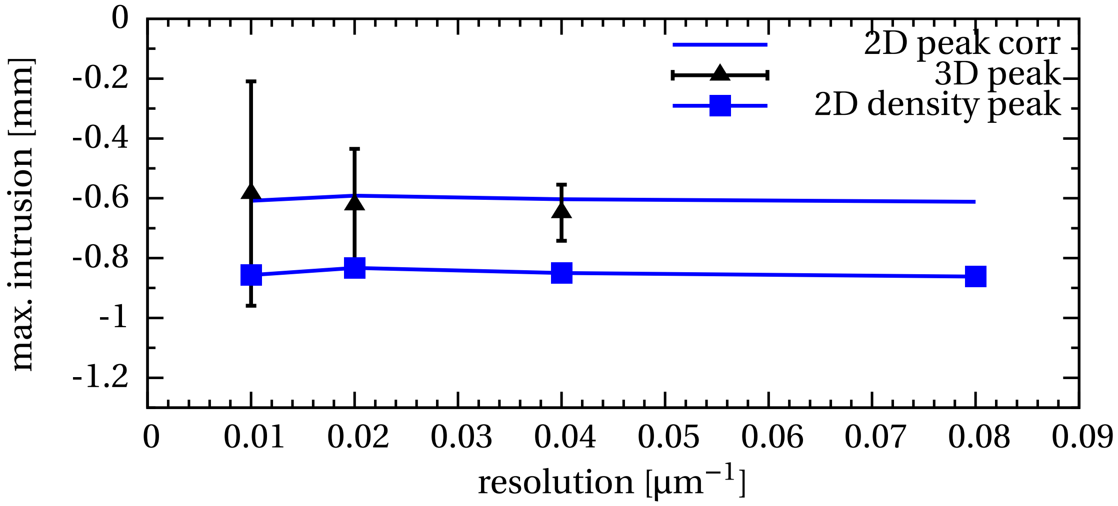

Figure 5.9. *Verification of the 2D-3D correction factor.* The filled symbols denote the position of the density peak of the dust material in Fig. 5.6. Triangles represent 3D and squares 2D values. The conversion from 2D to 3D intrusion depth utilising the correction factor from Eq. 5.1 and 5.2 due to the geometrical difference is indicated by the line without symbols. The 3D values are in very good agreement with the very rough theoretical prediction. They lie well within the errors.

where ρ_0 is the bulk density of the spherule, $m_{3\mathrm{D}}$ is the mass of a real 3D spherule and $m_{2\mathrm{D}}$ is the mass of the spherule per unit length. The 3D cross section $A_{3\mathrm{D}}$ is the area of a circle with radius r and the 2D equivalent $A_{2\mathrm{D}}$ is a line with length $2r$.

Hence, the 2D intrusion depth has to be corrected by a factor of $\sim 8/3\pi$ to determine the 3D intrusion depth. The comparison is shown in Fig. 5.9. For this figure I use the 2D and 3D data gained in the convergence study for the peak filling factor values shown in Fig. 5.7. Figure 5.9 shows the original 2D data, the corrected 2D data, and the corresponding 3D data (with error bars that indicate the smoothing length). The 3D values closely agree with the rough correction and remain well within the maximum error.

This comparison justifies the prediction of the mean pressure p_m of the compressive strength relation (Eq. 4.128) in Fig. 5.15 of Sec. 5.3.3. The higher peak filling factor visible in Fig. 5.6 resulting from 2D simulations compared to 3D is also taken into account in this prediction. As a consequence of Eq. 5.2, all calibration tests involving the intrusion depth can be carried out in 2D, saving a significant amount of computation time.

other 2D-3D differences

Comparing the vertical density profiles in Fig. 5.6 reveals another difference between the 2D and 3D setups. According to the experimental data (Fig. 5.12, Fig. 5.13, bottom, and Fig. 5.18, top, also Güttler et al. 2009), the filling factor drops to a value of $\phi \sim 0.16$ within a distance of $\sim 0.6\,\mathrm{mm}$ from the bottom point of the glass bead at maximum intrusion toward the bottom of the dust sample. For high-resolution 2D simulations (Fig. 5.6, top), the filling factor does not drop to this value for the entire dust sample. However, the 3D simulations (Fig. 5.6, bottom) show that this is because of the difference between the 2D and 3D geometry. Using the 3D setup, the filling factor drops to $\phi \sim 0.16$ within $\sim 0.9\,\mathrm{mm}$. All deviations from experimental findings in 2D numerical calibration experiments caused by this effect, in particular the large volume with $\phi \leq 0.2$ in the cumulated volume over filling factor diagrams (Fig. 5.14, bottom, Fig. 5.16, bottom, also Fig. 15

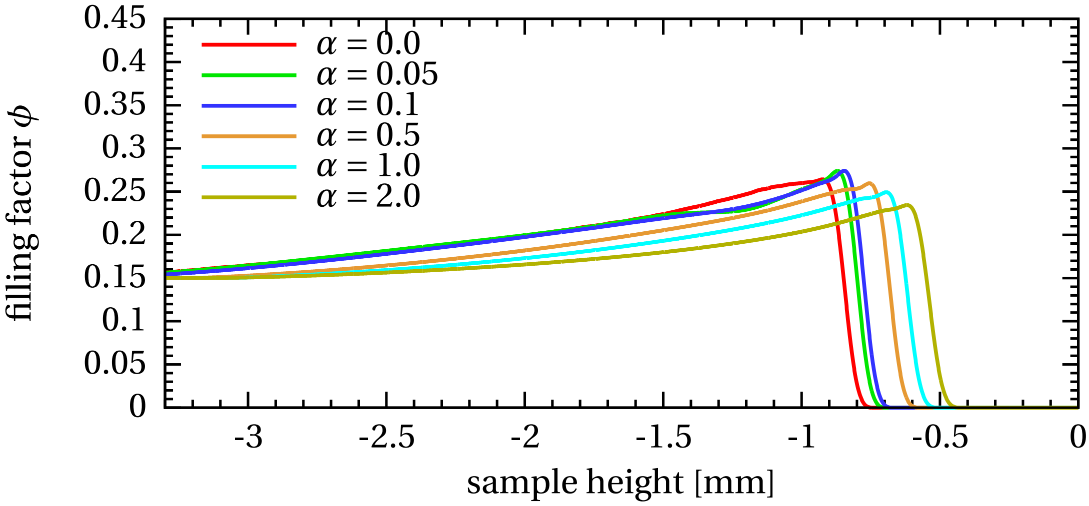

Figure 5.10. *Artificial viscosity study for the vertical density profile.* Density profile for different values of artificial α-viscosity in the frame of the compaction calibration setup. The shape of the density profile hardly changes, but increasing the α-viscosity decreases both the maximum filling factor and the maximum intrusion depth.

in Güttler et al. 2009), can be removed by switching to 3D simulations. They do not represent a fundamental error in the porosity model.

5.2.4. Artificial viscosity and other numerical parameters

numerical setting

Since artificial viscosity (AV, see Sec. 4.4.2) plays an eminent role in the stability of SPH simulations, its influence on the outcome of the compaction calibration setup (see Sec. 5.1.1 and Fig. 5.2) has to be investigated thoroughly to ensure a correct calibration. Deviating from the values in Tab. 5.1, the viscosity study is carried out with $p_{\mathrm{m}} = 1.3\,\mathrm{kPa}$. For all of the three cases below, the influence of β-viscosity on all benchmark parameters is tested but is found to be negligible. Hence, only artificial α-viscosity is applied for the compaction calibration setup. This has a threefold effect:

1. The α-viscosity dampens high oscillation modes of the glass bead caused by the stiff Murnaghan EOS (Eq. 4.112). Thereby it enlarges the time step of the adaptive integrator and saves computation time.
2. The α-viscosity is used to provide the dust material with a basic stability.
3. The α-viscosity separates the areas of Murnaghan EOS and dust EOS and prevents a so-called *cannonball instability.*

cannonball-instability

AV for glass bead

For case (1) the exact choice of the α-viscosity of the *glass bead* proves to be unimportant. Hence, I stick to the canonical value of $\alpha_{\mathrm{av}} = 1.0$. No influence on the physical benchmark parameters is detected for all α_{av} values, except for $\alpha_{\mathrm{av}} = 0$, which produces an instability. Values of $\alpha_{\mathrm{av}} > 1.0$ have no significant effect on the damping, and the influence for $0.1 < \alpha_{\mathrm{av}} < 1.0$ is not too high, but still observable.

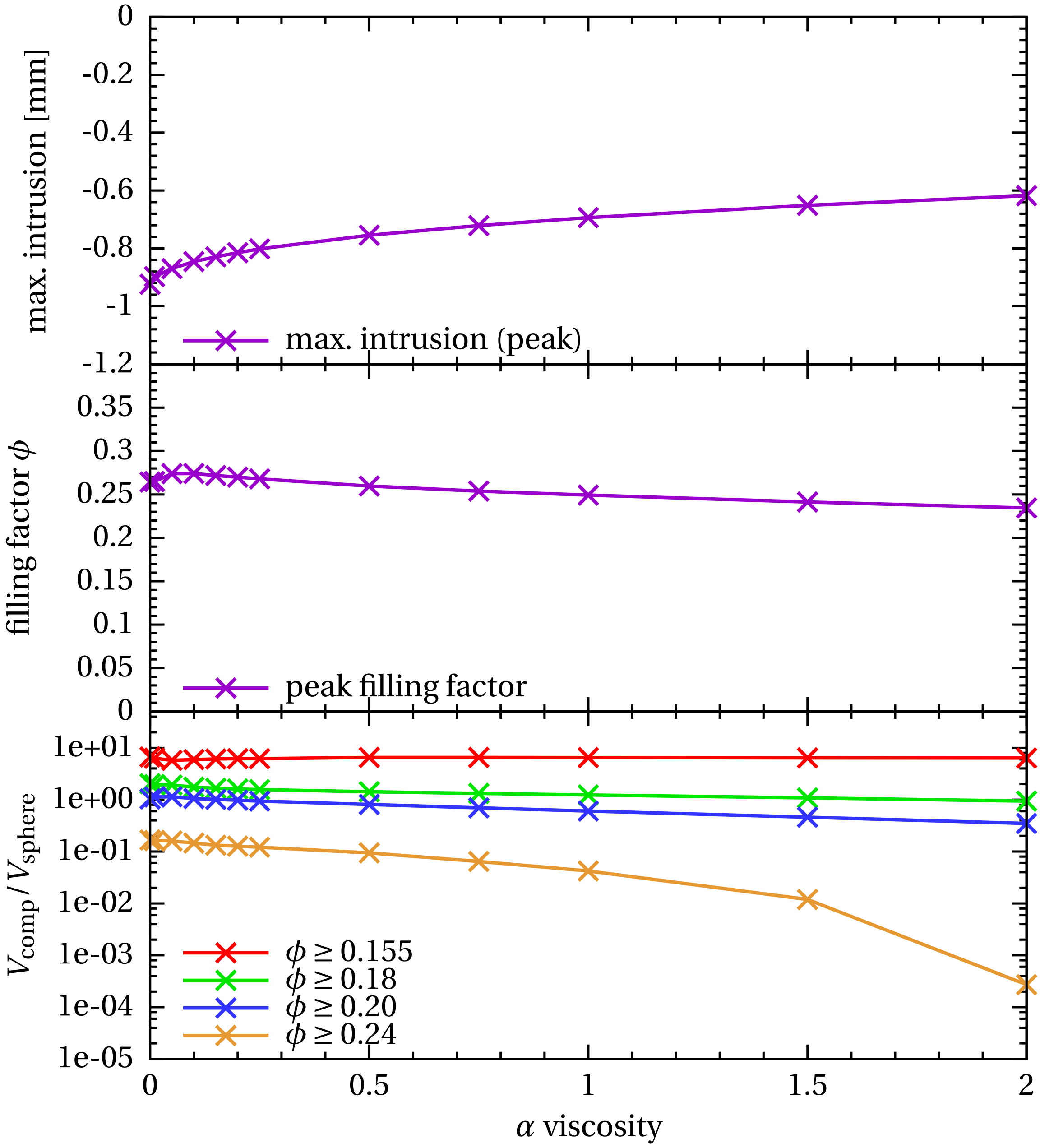

Figure 5.11. *Artificial viscosity study for various quantities.* Evolution of the maximum intrusion (top), the peak filling factor (middle), and the amount of compressed volume for filling factors greater than a given value (bottom) for different values of artificial α-viscosity. Intrusion depth and peak filling factor decrease with increasing values for α_{av}. This is an indication for the dissipative feature of the α-viscosity. The decrease of the peak filling factor and the amount of material which is compressed to $\phi \geq 0.24$, shows that the peak pressure during the impact drops with larger values of α_{av}.

AV for dust material

Regarding case (2), Sirono (2004) applied no artificial viscosity to his *porous ice* material to avoid dissipation. The results of my study are shown in Fig. 5.10 and 5.11 and confirm this choice in terms of the *dust material.* For the 2D compaction calibration setup (with the numerical parameters calibrated in Sec. 5.2.2, i.e. $l_c = 25\,\mu$m, $h/l_c = 5.6$), $\alpha_{\rm av}$ is varied from 0 to 2 and its influence on the vertical density profile (Fig. 5.10) is observed. Offering a different view, Fig. 5.11 shows the evolution of the maximum intrusion represented by the filling factor peak of the dust material (top), the peak filling factor itself (middle), and the amount of material which is compressed to filling factors greater than a certain value (bottom).

The essential effects of α-viscosity can be seen in the evolution of the vertical density profile (Fig. 5.10). While the profile maintains nearly the same shape, the maximum intrusion (given by the position of the density peak as in Sec. 5.2.2) and the height of the filling factor peak decrease with increasing $\alpha_{\rm av}$. The filling factor distribution of the compressed material also changes: more volume is compacted to lower filling factors and less material reaches high filling factors.

These features are broken down into the three panels in Fig. 5.11. The maximum intrusion ranges from $D \sim -0.92$ mm with $\alpha_{\rm av} = 0.0$ to $D \sim -0.62$ mm at $\alpha_{\rm av} = 2.0$ (Fig. 5.11, top). This clearly demonstrates the dissipative feature of the α-viscosity: a lower amount of kinetic energy of the glass bead is transformed into plastic deformation with higher $\alpha_{\rm av}$. As a consequence, the depth at which the spherule stops is not so deep. The residual energy must have been dissipated. However, the α-viscosity-intrusion curve seems to saturate at a value of $D \sim -0.6$ mm. Additionally, the peak filling factor itself decreases with increasing $\alpha_{\rm av}$ (Fig. 5.11, middle). The little increase for very small $\alpha_{\rm av}$ is caused by instabilities, which occur for these $\alpha_{\rm av}$ values. The peak filling factor reaches a maximum of $\phi \sim 0.274$ for $\alpha_{\rm av} = 0.1$ and decreases to $\phi \sim 0.234$ for $\alpha_{\rm av} = 2.0$. Since the filling factor is directly related to the peak pressure by the compressive strength relation $\Sigma(\phi)$ (Eq. 4.128) it can be concluded that an increasing artificial viscosity diminishes the peak pressure during compaction. According to $\Sigma(\phi)$, the peak pressures for the given setup are $p_{\rm peak} \sim 520$ Pa for $\alpha_{\rm av} = 0.1$ and $p_{\rm peak} \sim 295$ Pa for $\alpha_{\rm av} = 2.0$. The decrease in the peak pressure can also be seen in the filling factor distribution of the compressed material (Fig. 5.11, bottom). In units of the sphere volume, the figure shows the variation of the amount of compacted dust material, which is compressed to filling factors $\phi \geq 0.155$, 0.18, 0.20, and 0.24. The initial dust sample features a uniform filling factor of $\phi = 0.15$. The total amount of compressed material (represented by $\phi \geq 0.155$) hardly changes for higher values of $\alpha_{\rm av}$: it decreases by 4.80 % from ~ 6.66 ($\alpha_{\rm av} = 0$) to $\sim 6.34\,{\rm V}_{\rm sphere}$ ($\alpha_{\rm av} = 2.0$). In contrast, the material with $\phi \geq 0.18$ decreases by 54.1% (from 2.03 to $0.938\,{\rm V}_{\rm sphere}$) and for $\phi \geq 0.24$ the amount of compressed dust drops by 66.2 % (from 1.03 to $0.380\,{\rm V}_{\rm sphere}$). Material with $\phi \geq 0.24$ after the impact nearly disappears (decreases by 99.8 % from 0.167 to $2.71 \times 10^{-4}\,{\rm V}_{\rm sphere}$). The filling factor distribution can be regarded as a fingerprint of the peak pressure in the material. The altered filling factor distribution shows that with higher values of $\alpha_{\rm av}$, not only is the peak pressure in the contact area of the spherule and dust reduced, but the overall pressure is also decreased in large areas of the material.

In contrast to Sirono (2004), I find that it is necessary to apply a small amount of α-viscosity to the dust material. For $\alpha_{\rm av} < 0.1$, the results show evidences of an instability, which is also responsible for a rapid increase in the maximum intrusion (Fig. 5.11, top). Therefore, it is convenient to apply an artificial viscosity with $\alpha_{\rm av} = 0.1$ to the dust material, which holds for the previous simulations in this chapter as well as the following. The choice of a non-zero $\alpha_{\rm av}$ is also justified by experimental findings (Güttler et al. 2009): after impacting into the dust sample, the glass bead shortly oscillates because of the elastic properties of the dust. This oscillation is damped by internal friction, which can be modelled with artificial viscosity. Therefore, by choosing a non-zero

α_{av} the natural dissipative properties of the dust material are taken into account. A quantitative calibration of this parameter is not carried out within this thesis and is left to future work.

AV for material separation

Effect (3) of the use of artificial viscosity concerns the stability of the simulation: during the first simulations with the 2D compaction calibration setup, a so-called cannonball instability is observed. During the compaction process, when the glass bead intrudes into the dust material, single SPH particles at the sphere's surface begin to oscillate between the domains of the Murnaghan EOS (Eq. 4.112) and dust EOS (porosity model, Sec. 4.3.4). Because of the significant difference in the stiffness of these two equations of state, the particles acquire an enormous amount of unphysical kinetic energy until they move fast enough to generate a pressure on the dust material that exceeds the compressive strength $\Sigma(\phi)$ (Eq. 4.128). Eventually they disengage from the sphere's surface like a cannonball and dig themselves into the dust sample causing a huge amount of unphysical compaction. I tackle this problem for all dust SPH particles which interact with glass bead SPH particles by applying the same amount of α-viscosity to them as for the sphere, i.e. $\alpha_{\text{av}} = 1.0$. In the simulations for all three of the benchmark experiments, this is sufficient to prevent the cannonball instability. The spurious dissipation caused by this measure is negligible.

5.3. Adopting and Adapting Empirical Material Parameters

At the start of the collaboration between experimentalists carrying out the laboratory benchmark setups and the author of this thesis, the calibration process of code and porosity model was designed to be a one-way information flow: material parameters were to be measured empirically as well as benchmark parameters from the test experiments. The material parameters were supposed to be implemented directly into the porosity model and the three benchmark experiments presented in Sec. 5.1 were intended to be a test for the code and porosity model. However, in the course of the collaboration it turned out that some important material parameters were unfeasible to measure (shear strength $Y(\phi)$, see Sec. 5.3.2), not applicable to the dynamic case (compressive strength $\Sigma(\phi)$, see Sec. 5.3.3), or ambiguous (bulk modulus $K(\phi)$, see Sec. 5.3.5).

For this reason the benchmark experiments, originally intended to check the correct functionality of the code and the porosity model, are utilised to constrain the material parameters by numerical parameter studies. Thus, the cooperation, eventually yields new insights into the properties of the porous SiO_2 dust material, which are not easily accessible by laboratory experiments. With numerical simulations it becomes possible to investigate the effect of different material relations and their governing parameters on the simulated dust material. The result of this intensive study is presented in this section.

Due to the altered usage of the benchmark experiments in these parameter studies, their intended purpose as a strong check of the code and porosity model is weakened. However, the fact that unknown material parameters such as a dynamic compressive strength can be determined by computer simulations underlines the predictive power of the porosity model. Eventually, the calibration process is successful in the sense that the three test experiments can be simulated with one consistent set of material parameters. This fact is regarded as sufficient criterion for the successful calibration of the porosity model. The reproduction of all collision types found in a comprehensible collection of laboratory dust experiments (Güttler et al. 2010) with this code (see Sec. 6.1.1) supports this claim.

This section is composed as follows: the tensile strength $T(\phi)$, described in Sec. 5.3.1, is the only strength quantity which is not altered during the calibration process. The determination of the shear strength $Y(\phi)$, which was not at all available from laboratory measurements, is outlined in Sec. 5.3.2. The quantity which is investigated most thoroughly is the compressive strength $\Sigma(\phi)$. Therefore, in Sec. 5.3.3 a suitable functional expression is firstly constrained and subsequently the specific parameters of this expression are defined. After the successful investigation of the strength quantities which govern the plastic regime, the bulk modulus as an elasticity parameter is determined in Sec. 5.3.5. Finally, a short summary of the calibration process is given in Sec. 5.4.

5.3.1. Tensile Strength

The tensile strength of the mono-disperse SiO_2 dust material was measured for highly porous and compacted aggregates by Blum and Schräpler (2004): for packing densities of $\phi = 0.15$, $\phi = 0.41$, $\phi = 0.54$, and $\phi = 0.66$, tensile strengths of $|T| = 1{,}000\,\mathrm{Pa}$, $|T| = 2{,}400\,\mathrm{Pa}$, $|T| = 3{,}700\,\mathrm{Pa}$, and $|T| = 6{,}300\,\mathrm{Pa}$, respectively, were found. These measurements support a linear dependence between the tensile strength and the number of contacts per monomer (increasing with increasing ϕ), which yields the tensile strength as

$$T(\phi) = -10^{2.8+1.48\phi}\,\mathrm{Pa}\,. \tag{5.3}$$

As the tensile strength is a threshold for tension forces, the relation is denoted with a minus sign. The tensile strength was measured in an uniaxial, quasi-static setup (Blum and Schräpler 2004, Blum et al. 2006b). However, by definition pressure is homogeneous and omnidirectional. Consequently, for the compressive strength calibration (see Sec. 5.3.3) it turns out that a dynamic measurement in an omnidirectional setup is more appropriate to measure this quantity. It is very likely that the tensile strength relation is also altered for the dynamic, omnidirectional case. However, even static tensile strength measurements require a difficult experimental setup. Thus, the adequate empirical determination is unfeasible in the laboratory. Because of the excellent final results of the calibration, the influence of this strength quantity is not studied numerically within this thesis. The tensile strength relation $T(\phi)$ is plotted in Fig. 5.24.

5.3.2. Shear Strength

possible shear strength relations

Since no experimental data is available for the shear strength, $Y(\phi)$ is assumed to depend on the other strength quantities, i.e. the compressive strength $\Sigma(\phi)$ and the tensile strength $T(\phi)$. In parameter studies (see also Güttler et al. 2009), the following three different simple relations for $Y(|T|,\Sigma)$ are tested: $Y = |T|$, $Y = \Sigma$ and, following Sirono (2004), $Y = \sqrt{\Sigma|T|}$, which represents the geometric mean of both quantities. For all simulations, the 2D compaction calibration setup (see Sec. 5.1.1) is used. Deviating from the parameters in Tab. 5.1, the dust sample is a box and the ODC mean pressure is varied. The reason for the latter is discussed below and in Sec. 5.3.3. Particularly the vertical density profile (see Fig. 5.2 for an illustration) proves to be a suitable calibration parameter to constrain the shear strength relation. The results of this study are depicted in Fig. 5.12.

numerical setting

static relation

Using the statically measured compressive strength relation (Eq. 4.128) with $p_\mathrm{m} = 13.0\,\mathrm{kPa}$, each of the shear strength models the simulation results in a much too shallow intrusion depth and an insufficiently high maximum filling factor underneath the sphere (Fig. 5.12). The experimental reference, denoted by crosses in this figure, is derived from the X-ray tomography measurements presented in Sec. 5.1.1 (see also Fig. 5.1) and for practical reasons, the sphere is not removed for

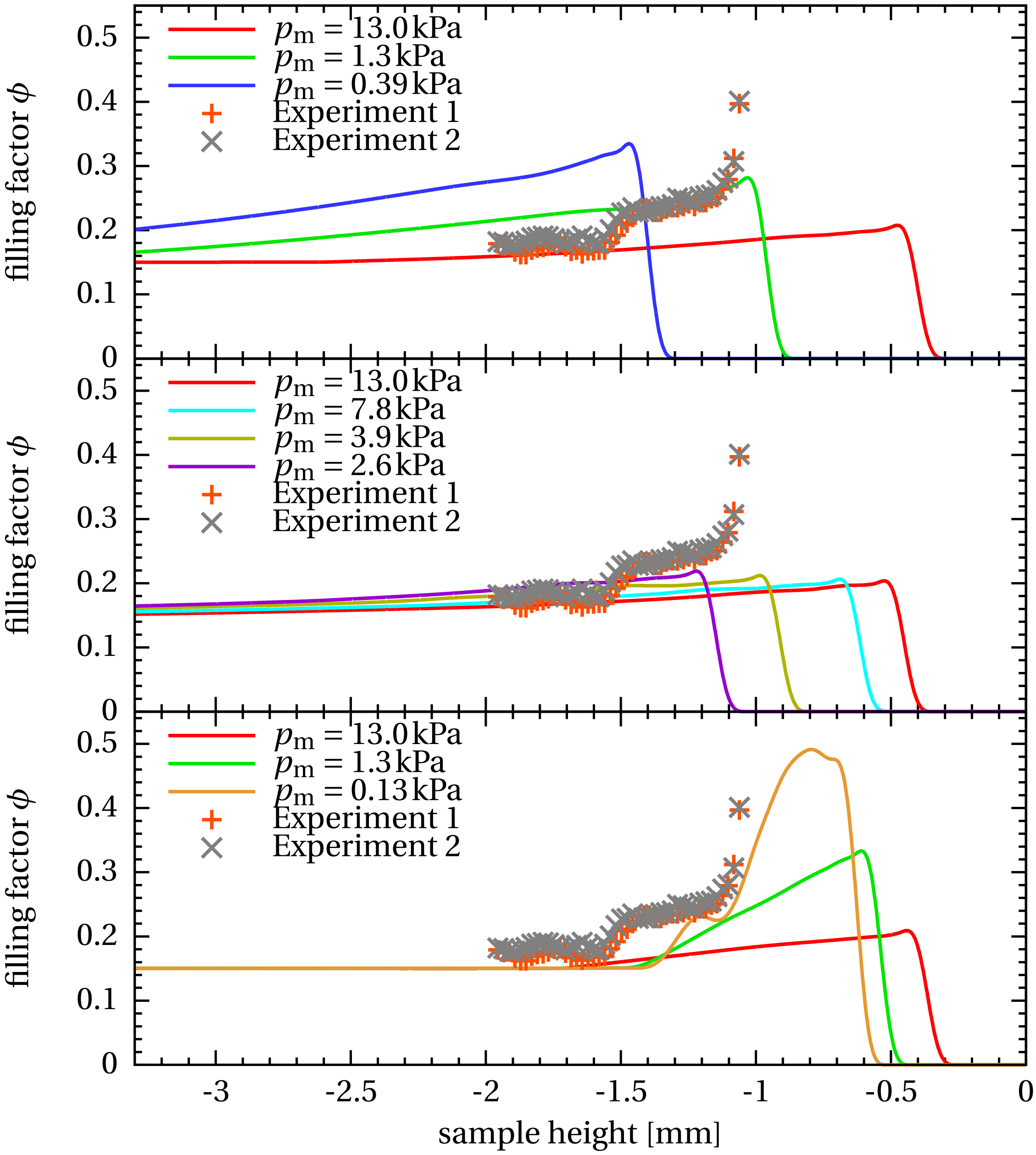

Figure 5.12. *Shear strength models.* Study of the three different shear strength models $Y = \sqrt{\Sigma|T|}$ (top), $Y = \Sigma$ (middle), and $Y = |T|$ (bottom) by means of the compaction calibration setup. The mean pressure p_m of the compressive strength relation is varied for each model. The figure shows the vertical density profile, which is measured after the impact along a line through the centre of the spherule and perpendicular to the surface of the dust sample, which is represented by a sample height of 0 mm. The laboratory reference, where the sphere was not removed for the measurement, is presented by crosses. The model $Y = \Sigma$ (middle) yields filling factors that are too small and the $Y = |T|$ model produces intrusions that are too shallow and filling factors that are too high. Hence, the $Y = \sqrt{\Sigma|T|}$ model is the best suitable choice.

these measurements. This results in a rapid filling factor increase at $D \sim -1\,\mathrm{mm}$. However, for the simulation results the sphere is removed to focus on the density structure of the dust only. The initial surface of the dust sample is at 0 mm.

dynamic relation

The shallow intrusion in the simulations using the static compressive strength relation are a first indication that this relation has to be modified in order to reproduce the experimental data. This is because $\Sigma(\phi)$ determines the threshold pressure which is necessary to compress a dust aggregate of a given filling factor ϕ. Lowering the mean pressure p_m results in lower threshold pressures and a deeper intrusion can be achieved. Therefore, I perform a parameter study varying the parameter p_m, i.e. I shift the compressive strength curve to lower pressures (see Fig. 5.14, top) for the different shear strength models, which depend on Σ. The effect of lowering p_m is studied in detail in Sec. 5.3.3.

A significant increase in the intrusion depth is only observed in the cases where $Y = \Sigma$ and $Y = \sqrt{\Sigma|T|}$ (Fig. 5.12, top and middle). In case of $Y = |T|$, the intrusion depth hardly changes with decreasing p_m (Fig. 5.12, bottom). Since the shear strength is unaltered and varying $\Sigma(\phi)$ via p_m does not have a significant effect on the intrusion depth, it can be concluded that shearing plays an important role during the intrusion.

Compared to the other cases, the shear strength reaches its highest values in the $Y = |T|$ case. Hence, the material can hardly be pushed away due to shear and has to be compressed. Lowering p_m lowers the pressure necessary to compress the material to a certain filling factor ϕ. Together with the fact that the material cannot escape to the side by shearing, this results in the highest filling factors for the $Y = |T|$ model compared to the other models (Fig. 5.12, bottom). The $Y = \Sigma$ model yields the lowest shear strength values. Hence, material is mostly sheared aside, less material is compressed and therefore this model leads to filling factors below the reference data (Fig. 5.12, middle).

excluding relations

As a result from this study two models can be excluded: the $Y = \Sigma$ model cannot reproduce the high values in the vertical filling factor profile (Fig. 5.12, middle) and the $Y = |T|$ model produces intrusion depths that are too shallow and peak filling factors that are too high (Fig. 5.12, bottom). In contrast, the $Y = \sqrt{\Sigma|T|}$ model yields an almost perfect match (Fig. 5.12, top) of the vertical density profile for a lowered p_m. Therefore, the shear strength model after Sirono (2004) is used for further simulations.

geometrical differences

Looking at Fig. 5.12 (top), it has to be kept in mind that this study is carried out in 2D. The geometrical differences between the 2D and 3D compaction calibration setup were already discussed in Sec. 5.2.3. The filling factor for the best fit ($p_\mathrm{m} = 1.3\,\mathrm{kPa}$) only slowly drops to the filling factor of the unaltered dust sample ($\phi \sim 0.15$) compared to the experimental reference. This is a 2D effect. For the 3D simulation (Fig. 5.18, top) the behaviour follows the laboratory measurements more closely.

Secondly, the intrusion depth for the mean pressure $p_\mathrm{m} = 1.3\,\mathrm{kPa}$ producing the best fit for the $Y = \sqrt{\Sigma|T|}$ model cannot be the final calibration value. This is because of the geometrical difference between 2D and 3D. As discussed in Sec. 5.2.3, a correction factor has to be applied to the intrusion depth (Eq. 5.2). The 2D intrusion depth is expected to be deeper than the respective 3D value.

shear strength choice

Therefore, I conclude this section with the summary that $Y = \sqrt{\Sigma|T|}$ is a suitable model for the shear strength, but the compressive strength relation has to be modified. The amount and effects of this modification are discussed in the next section.

5.3.3. Compressive Strength

BS relation

ODC relation

Besides the tensile strength relation $T(\phi)$, the compressive strength relation $\Sigma(\phi)$ is one of the few relations that are available from laboratory experiments. Blum and Schräpler (2004) measured this quantity in an uniaxial quasi-static setup. Their relation is labelled "BS" in the further course. They put an SiO_2 dust sample between two glass plates and consecutively applied defined pressures on the sample. In between the pressure increases they measured the filling factor of the dust sample. However, the uniaxial setup does not reproduce the homogeneous omnidirectional nature of pressure. For this reason, Güttler et al. (2009) measured the compressive strength relation in an omnidirectional setup within the calibration project. This relation is labelled by "ODC". The measurements by Blum and Schräpler (2004) as well as Güttler et al. (2009) can be interpolated by different functional expressions. At first, the effects of these expressions are studied. After a suitable function is found, the effect of the free parameters of this expression are studied and fixed.

Functional expression

functional expression vs. lookup table

The laboratory data for the compressive strength relation can be implemented into the porosity model in two ways: using a lookup-table and interpolating between the data points or as a functional expression. For this thesis both approaches were tried with respect to the relation provided by Blum and Schräpler (2004). However, with discontinuities in the interpolated curves the simulations are highly prone to instabilities. Therefore, it is more suitable to approximate the measured data by functional expressions. In the experimental context, the inverses of the tested functions are more common. They are plotted in Fig. 5.13 (top).

Fermi-Dirac function

Güttler et al. (2009) found that their ODC data as well as the BS data can be approximated by a Fermi-Dirac distribution function with the maximum filling factor ϕ_{max}, minimum filling factor ϕ_{min}, mean pressure p_{m}, and slope Δ. The result is the compressive strength relation $\Sigma(\phi)$ which was already introduced in Sec. 4.3.4 (Eq. 4.128)

$$\Sigma_{\mathrm{BS/ODC}}(\phi) = p_{\mathrm{m}} \left(\frac{\phi_{\mathrm{max}} - \phi_{\mathrm{min}}}{\phi_{\mathrm{max}} - \phi} - 1 \right)^{\Delta \ln 10} , \tag{5.4}$$

for $\phi_{\mathrm{min}} < \phi$. The function is continuously extended by a constant function for $\phi \le \phi_{\mathrm{min}}$. The minimum filling factor is nearly the same for both relations: $\phi_{\mathrm{min}} = 0.15$ (BS) and $\phi_{\mathrm{min}} = 0.12$ (ODC). Due to the uniaxial setup of BS, material can escape to the sides and the maximum filling factor is lower than for the ODC case where the dust sample is enclosed from all sides: $\phi_{\mathrm{max}} = 0.33$ (BS) and $\phi_{\mathrm{max}} = 0.58$ (ODC). The experimental setup is also the reason why in the BS case, higher pressures are necessary to achieve the same filling factor (see Fig. 5.13, top, for a comparison). This slightly changes the shape of the curve and consequently the mean pressure and the slope of the distribution: the BS-relation features $p_{\mathrm{m}} = 5.6\,\mathrm{kPa}$ and $\Delta = 0.33$, whereas for the ODC-relation $p_{\mathrm{m}} = 13.0\,\mathrm{kPa}$ and $\Delta = 0.58$.

However, in Sec. 5.3.2 it turned out that the static compressive strength relation is not applicable for the dynamic case, which is given when simulating pre-planetesimal collisions. Therefore, the compressive strength relation has to be shifted toward lower pressures to explain the experimental results. Further below I therefore study the BS-relation with lower values of p_{m}.

Although the Fermi-Dirac shaped function has already proven to be a suitable choice for the compressive strength, it is worthwhile to study other possible fits for two reasons: firstly, this

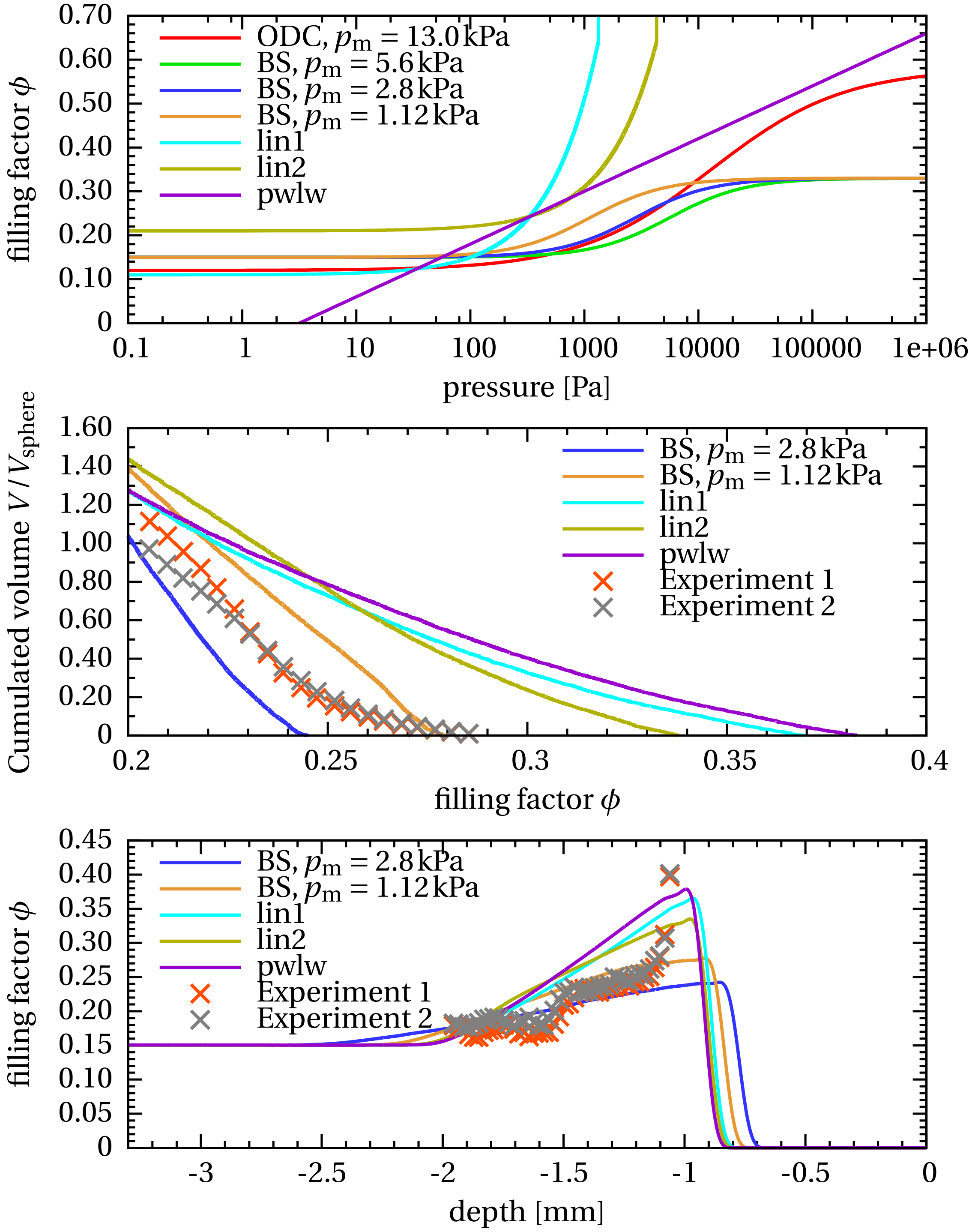

Figure 5.13. *Dynamic compressive strength models.* Study of two linear (lin1, lin2), a power-law (pwlw), and two shifted Blum-Schräpler (BS) relations as dynamic compressive strength models. The inverse of these relations, which is more common in experimental contexts, is depicted (top) for all possible dynamic relations together with the static ODC-curve (p_m = 13.0 kPa) and the static BS-curve (p_m = 5.6 kPa) as references. The effects are studied by means of the density distribution (middle) and vertical density profile (bottom). While the power-law and linear models produce an excess of compressed volume, the BS-curve yields good but not sufficient, approximations in both cases.

choice can be strengthened by excluding other models. Secondly, the influence of the shape of the compressive strength curve on the density structure produced in the compaction can be studied and certain features of the curve can be identified with density structure features.

linear function

The following possibilities for fits to compressive strength data were provided by C. Güttler without being published. These already take into account the shift of the compressive strength relation. The available models include two linear fits

$$\Sigma_{\mathrm{lin1}}(\phi) = \begin{cases} 2.5\times 10^{-3}\,\mathrm{Pa} & \text{for } 0 \le \phi \le 0.11 \\ 2{,}500.0\,\phi - 275.0\,\mathrm{Pa} & \text{for } 0.11 < \phi \le 0.64 \\ 1{,}325.0\,\phi\,\mathrm{Pa} & \text{for } 0.64 < \phi \end{cases}, \tag{5.5}$$

and

$$\Sigma_{\mathrm{lin2}}(\phi) = \begin{cases} 0.01\,\mathrm{Pa} & \text{for } 0 \le \phi \le 0.21 \\ 10^{4}\phi - 2{,}100.0\,\mathrm{Pa} & \text{for } 0.21 < \phi \le 0.64 \\ 4{,}300.0\,\phi\,\mathrm{Pa} & \text{for } 0.64 < \phi \end{cases}. \tag{5.6}$$

In both cases the respective middle line is based on the measurements and the lower and upper filling factor is set by the author of this thesis to fill the data gap.

power-law function

Another possibility is the following power-law

$$\Sigma_{\mathrm{pwlw}}(\phi) = 10^{(\phi-0.06)/0.12}\,\mathrm{Pa}\,. \tag{5.7}$$

numerical setting

The effect of the different compressive strength models is studied by means of the 2D compaction calibration setup as presented in Sec. 5.1.1 and Fig. 5.2. The parameters are the same as in Tab. 5.1, but the ODC-relations are replaced by the respective $\Sigma(\phi)$. The tensile strength and shear strength relations are the same as presented in Sec. 5.3.1 and Sec. 5.3.2, respectively.

Since the ODC-relation already proved to be a suitable choice in Sec. 5.3.2 and is studied further below in more detail, I do not consider it in the study of this section for reasons of clarity. A comparison of the ODC relation with the experimental reference data can be found in Fig. 5.18 of Sec. 5.3.4. Since the original, static BS-relation with $p_\mathrm{m} = 5.6\,\mathrm{kPa}$ yields unrealistic results and has to be shifted towards lower filling factors, I include only the BS-relation with three different values of p_m, the two linear models, and the power-law model for comparison. Looking at Fig. 5.13 (top), the BS-curves are similar to the static ODC-curve in the range of 0.1 to 10 kPa. Since the shapes of the curves remain the same but only a shift towards lower pressures takes place, similar density structures should be produced but with higher filling factors. The linear and power-law models are shifted toward lower pressures and higher filling factors. Consequently, these models should result in density structures with higher densities but different in shape.

density distribution

The effect of the different compressive strength models is studied by means of the vertical density profile (Fig. 5.13, bottom) and density distribution of the cumulated volume (Fig. 5.13, middle). These calibration properties are described in Sec. 5.1.1 in detail. Starting with the density distribution, one can see that the the two linear models and the power-law model produce too much volume at high filling factors. The power-law model and the lin1-model yield similar density distributions but the latter leads to slightly less volume at high filling factors and more volume at low filling factors. This is because for both linear models very high pressures (some hundreds of Pa) are necessary to achieve high filling factors ($\phi \sim 0.3$). Within the lin2-model it is easier to compress to low filling factors ($\phi \sim 0.2$) than to high filling factors ($\phi \sim 0.3$) compared to the lin1-model. Consequently, for the lin2-model more material features $\phi \geq 0.2$. Conversely, less material is compacted to $\phi \geq 0.3$. Finally, the two linear models and the power-law model produce filling factors much larger than in the experimental reference. In contrast, the BS-relations resemble the laboratory data. Both relations result in a similar density profile shape. This reflects the fact that the compressive strength relations feature the same shape. However, the BS-relation with $p_{\mathrm{m}} = 2.8\,\mathrm{kPa}$ results in filling factors that are too low. The BS-relation with $p_{\mathrm{m}} = 1.12\,\mathrm{kPa}$ produces too much volume compacted to $\phi \sim 0.25$ to 0.27 and insufficient volume with $\phi \geq 0.26$.

vertical density profile

This assessment is confirmed by looking at the vertical density profile (Fig. 5.13, bottom). The power-law and linear models produce peak filling factors that are too high and too much compacted material at high filling factors. The high mean pressure BS-relation produces a peak filling factor that is too low. The shape of the low mean pressure relation fits the experimental data quite well, although below $D \sim -1.5\,\mathrm{mm}$ the filling factor is too high. All relations yield an intrusion depth that is too shallow.

compressive strength choice

In this section, it is demonstrated how some features of the compressive strength relation can be identified with features in the calibration parameters. Concluding the comparison, the BS-relations, which are similar to the ODC-relation, yield the best reproduction of the experimental data. However, none of the presented relations is satisfactory. Therefore, the ODC-relation is studied in more detail below.

Mean pressure p_{m}

In Sec. 5.3.2 it was already found that by lowering the mean pressure p_{m} of the compressive strength relation, most of the features of the vertical density profile within the compaction calibration setup can be reproduced in a very satisfactory manner. This is confirmed by the preceding study using the shifted curves of the relation by Blum and Schräpler (2004). However, their uniaxial setup is not appropriate for the omnidirectional nature of the compressive strength relation. Therefore, in the following I return to the more appropriate ODC data by Güttler et al. (2009), which I shift towards lower pressures by reducing p_{m}. As a result, the yield pressure for compression is lowered, which is illustrated in Fig. 5.14 (top), where the curve with $p_{\mathrm{m}} = 13.0\,\mathrm{kPa}$ represents the static ODC relation, which is depicted as a reference.

numerical setting

Since no empirical data are available for p_{m} of the dynamical compressive strength curve, a parameter study is performed to determine a suitable choice for this important quantity. For this study, the 2D compaction calibration setup (see Sec. 5.1.1 and Fig. 5.2) and the parameters of Tab. 5.1 are utilised, except for p_{m} which is varied from 0.13 to 13.0 kPa. The effect of the mean pressure is studied by means of the vertical density profile (Fig. 5.14, middle), the density distribution (Fig. 5.14, bottom), and a maximum intrusion over stopping time diagram (Fig. 5.15). For a detailed description of these calibration parameters see Sec. 5.1.1.

intrusion depth, stopping time

The effect of lowering p_{m} can most clearly be seen in the vertical density profile (Fig. 5.14, middle). More material can be and is compressed to higher filling factors. The peak filling factor is increased from ~ 0.2 to 0.34. As a consequence, the glass bead intrudes more deeply (from $D \sim -0.4$ to $-1.4\,\mathrm{mm}$ into the dust sample. From experimental results, an intrusion depth of about one sphere diameter ($\sim 1\,\mathrm{mm}$) is expected. With the aid of the empirical relation between the ratio of momentum to impactor cross-section $m v_0 A^{-1}$ and intrusion depth D (Eq. 5.1) as well as the correction factor between 2D and 3D intrusion depth (Eq. 5.2), it can be estimated that $D_{\mathrm{3D}} \sim 1\,\mathrm{mm}$ corresponds to $D_{\mathrm{2D}} \sim 1.42\,\mathrm{mm}$. Fig. 5.15 shows the maximum intrusion over

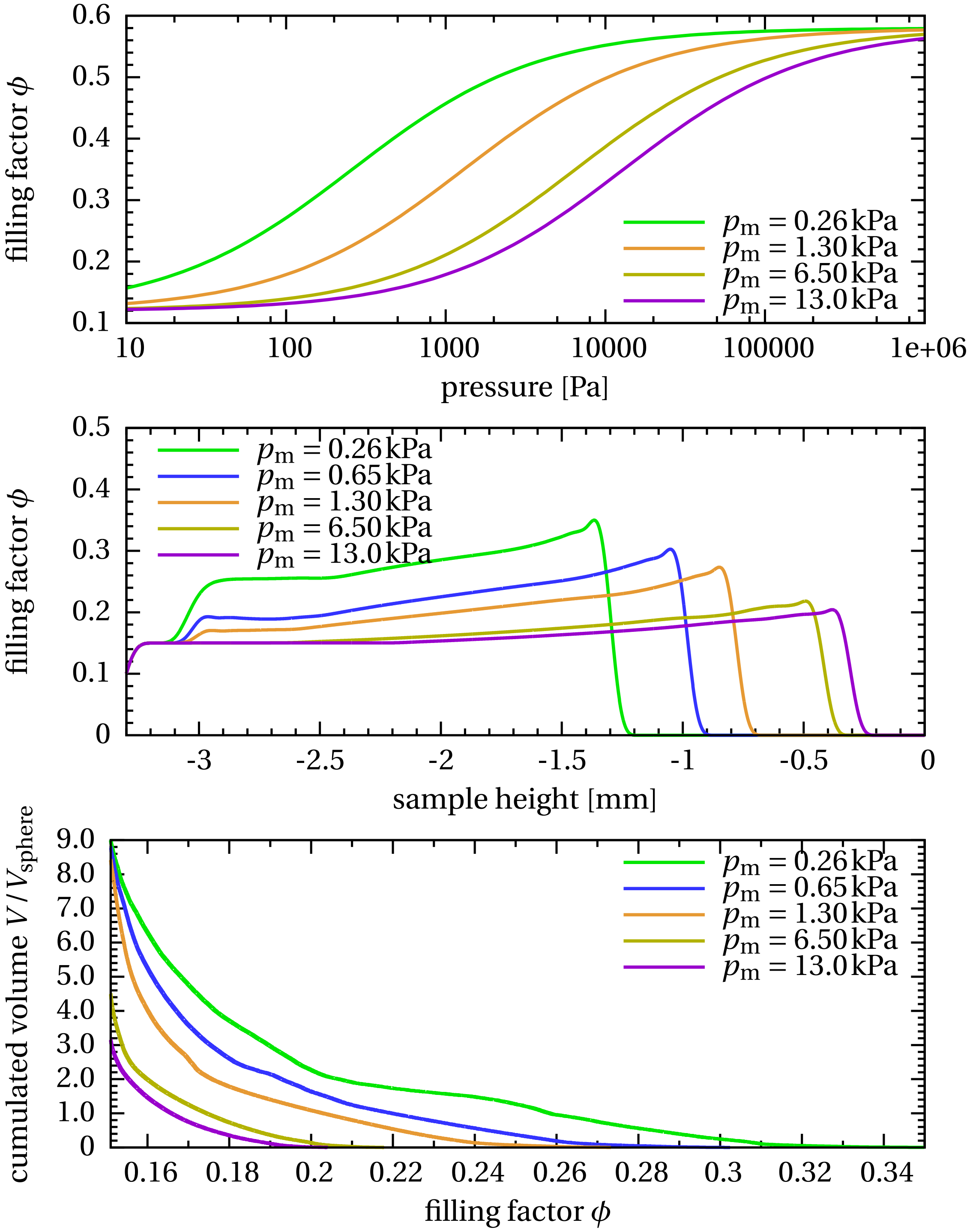

Figure 5.14. *Mean pressure study of the ODC compressive strength I.* Lowering the mean pressure p_m for the static omnidirectional compressive strength relation (Eq. 5.4, $p_\mathrm{m} = 13.0\,\mathrm{kPa}$) by Güttler et al. (2009) yields possible relations for the dynamic compressive strength (top). The effects of lowering p_m are studied by means of the vertical density profile (middle) and the density distribution (bottom) within the 2D compaction calibration setup. By decreasing p_m, the amount of compressed material is increased as well as the filling factors it is compacted to.

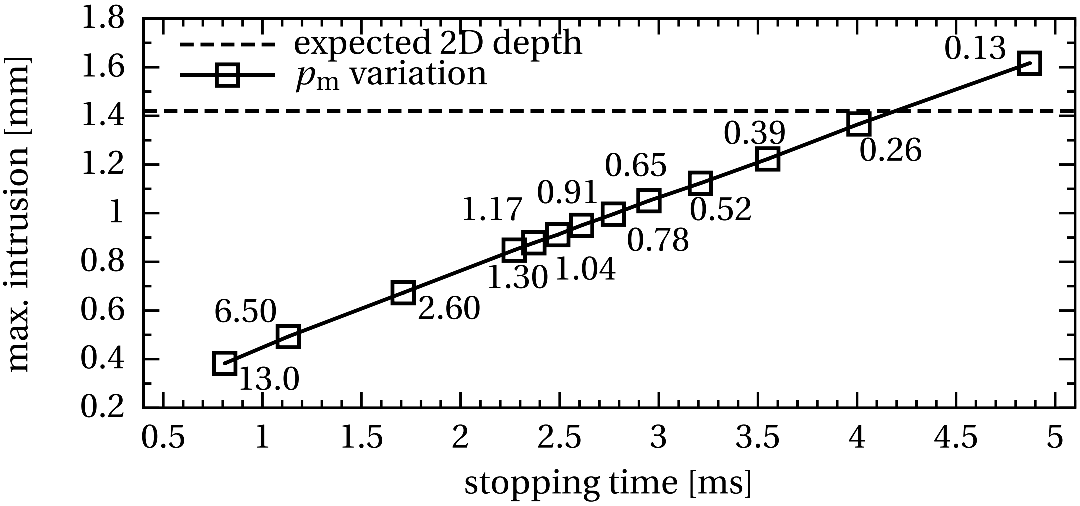

Figure 5.15. *Mean pressure study of the ODC compressive strength II.* Maximum intrusion over stopping time for different values of the mean pressure p_m (labels, in kPa) of the compressive strength relation (Eq. 5.4) using the 2D compaction calibration setup. The dashed line indicates the 2D intrusion depth that is equivalent to a 3D intrusion depth of ~ 1 mm according to Eq. 5.1 and the 2D-3D correction factor from Eq. 5.2. This supports the choice of the mean pressure $p_m = 0.26\,\mathrm{kPa}$ for further 3D simulations.

the stopping time for various values of p_m (labels). The estimated D_{2D} is indicated by a dashed line. In terms of intrusion depth, it follows that a dynamic mean pressure $p_m = 0.26\,\mathrm{kPa}$ is a suitable choice.

vertical density profile

This is supported by looking at the peak filling factor of the vertical density profile (Fig. 5.14, middle). For the compaction calibration setup, empirical data indicate that a peak filling factor of ~ 0.3 can be expected. The comparison between 2D and 3D results (Sec. 5.2.3, Fig. 5.6) has shown that the peak filling factor in the vertical density profile in the 2D case is generally higher than for the same situation in 3D. The equivalent of $\phi_{3D} \sim 0.3$ is a maximum filling factor of $\phi_{2D} \sim 0.34$ in 2D. This points to a choice of $p_m \sim 0.3\,\mathrm{kPa}$, which is consistent with the findings for the intrusion depth.

density distribution

The density distribution (Fig. 5.14, bottom) reveals the effect of changing p_m on the total compressed volume. The total amount of compacted material is increased from ~ 3 to ~ 9 sphere volumes. The maximum filling factor is also increased from ~ 0.19 to ~ 0.34. However, the slope of the material remains roughly the same. While the BS-curves in Fig. 5.13 (middle) approximately describe a straight line in the density distribution diagram, the ODC curves better describe the shape of the experimental data. This is evident when finally comparing the 3D simulations with the laboratory reference (Fig. 5.18, bottom).

mean pressure choice

As a result from this study the mean pressure can be fixed to $p_m = 0.26\,\mathrm{kPa}$, which will be used in the further studies. Using a completely different setting, this choice is also confirmed by means of the bouncing calibration setup, which is discussed in Sec. 5.3.5.

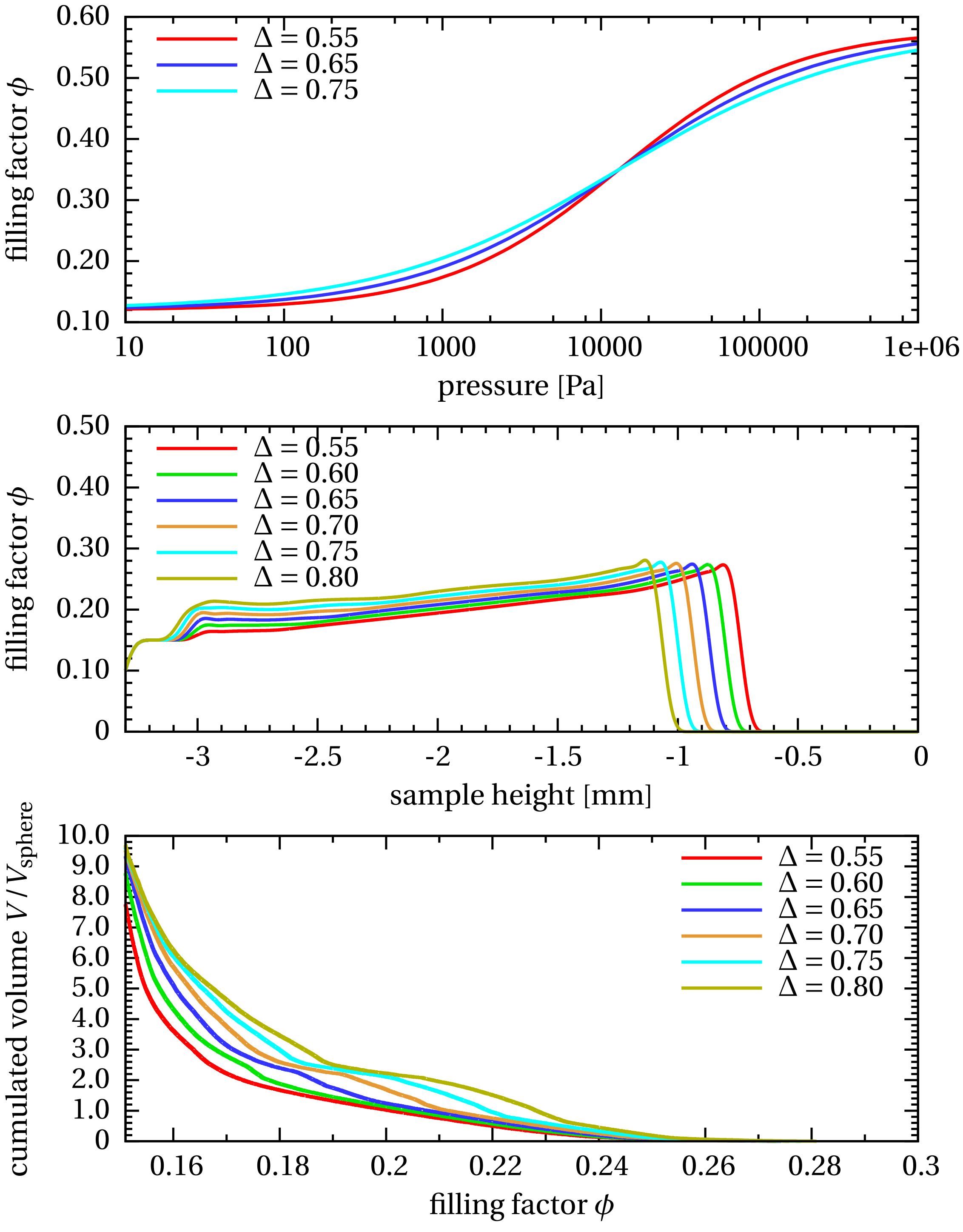

Figure 5.16. *Slope study of the ODC compressive strength.* For this study an ODC relation with $p_{\mathrm{m}} = 0.26\,\mathrm{kPa}$ is used. Changing the slope Δ of the compressive strength results in tilting the respective inverse relation (top). As a consequence, the threshold for plastic compression is lowered in the low pressure regime. This produces vertical density profiles (middle) of nearly the same shape but with deeper intrusions for higher values of Δ. The total amount of compressed volume in the density distribution (bottom) hardly changes but a shift towards higher filling factors occurs.

Slope Δ

numerical setting

Besides the mean pressure p_m, the ODC relation $\Sigma(\phi)$ (Eq. 5.4) contains a second free parameter Δ, which accounts for the slope of the Fermi-shaped curve. In the previous studies, this parameter was chosen to be identical to that of the static omni-directional compressive strength curve and a more careful investigation was not carried out. To understand the effect of Δ on the compaction properties of the dust sample, the *2D compaction calibration setup* (Sec. 5.1.1 and Fig. 5.2) is utilised again. Besides the variation of Δ from 0.55 to 0.80, the parameters of Tab. 5.1 are applied, in particular the previously calibrated mean pressure $p_\mathrm{m} = 0.26\,\mathrm{kPa}$. The effect of Δ on the inverse compressive strength is shown in Fig. 5.16 (top): with increasing Δ the slope of the curves becomes shallower. This means that for dynamic pressures below the mean pressure, higher filling factors are achieved. Conversely, for dynamic pressures above the mean pressure the filling factors are lower. Since for the compaction calibration setup the dynamic pressures are below the mean pressure, more compacted material with higher filling factors can be expected.

vertical density profile

density distribution

The resulting density structure is again studied by means of the *vertical density profile* (Fig. 5.16, middle) and the density distribution (Fig. 5.16, bottom). Both calibration parameters are described in detail in Sec. 5.1.1. From the vertical density profile, it can be seen that increasing Δ increases the intrusion depth but not as effectively as lowering the mean pressure p_m (Fig. 5.14, middle). This is because the curve is only slightly tilted towards lower pressures. Increasing Δ hardly increases the peak filling factor in the vertical density profile (Fig. 5.16, middle). Looking at the *density distribution* (Fig. 5.16, bottom) the intersection of the curves with the y-axis represents the total compressed volume, which is increased from ~ 7 to ~ 9.5 sphere volumes. The corresponding experimental measurements infer a value of roughly one sphere volume for this quantity. The total amount of compressed volume and the maximum filling factor only slightly increase with Δ but the distribution is shifted towards higher filling factors. In contrast, by lowering p_m the total amount of compressed volume and the maximum filling factor increase, maintaining nearly the same distribution. Comparing the distribution variation for Δ and p_m, the compacted volume fraction is increased in particular for $0.18 < \phi < 0.23$ in the former case.

geometrical difference

Δ choice

By comparing the 2D and 3D calibration setups (see Sec. 5.2.3), it can be deduced that a significant amount of this compaction (especially in the lower filling factor regime) is caused by the *geometrical difference*, which is resolved by using the 3D setup (Fig. 5.18). The experimental data do not indicate a particularly high amount of compaction to lower filling factors (rather the contrary). This suggests the choice of $\Delta = 0.58$.

Summary

In this section, a dynamic relation for the compressive strength $\Sigma(\phi)$ has had to be found. In Sec. 5.3.2 it was already shown that the physically more appropriate omnidirectional compressive strength relation measured by Güttler et al. (2009) provides satisfactory results. Nevertheless, other possible fits for dynamic relations (linear and power-law) have been studied at the beginning of this section. In this investigation, it has been possible to relate certain features of the model equations to respective features in the density structure. This has provided a valuable insight into the importance of the exact shape of the compressive strength relation and the sensitivity of the benchmark setup. After choosing the static ODC as a basis, the insight has been broadened further by studying the effect of the mean pressure p_m, which has turned out to be the essential quantity to convert the static ODC into a dynamic ODC for which $p_\mathrm{m} = 0.26\,\mathrm{kPa}$ has

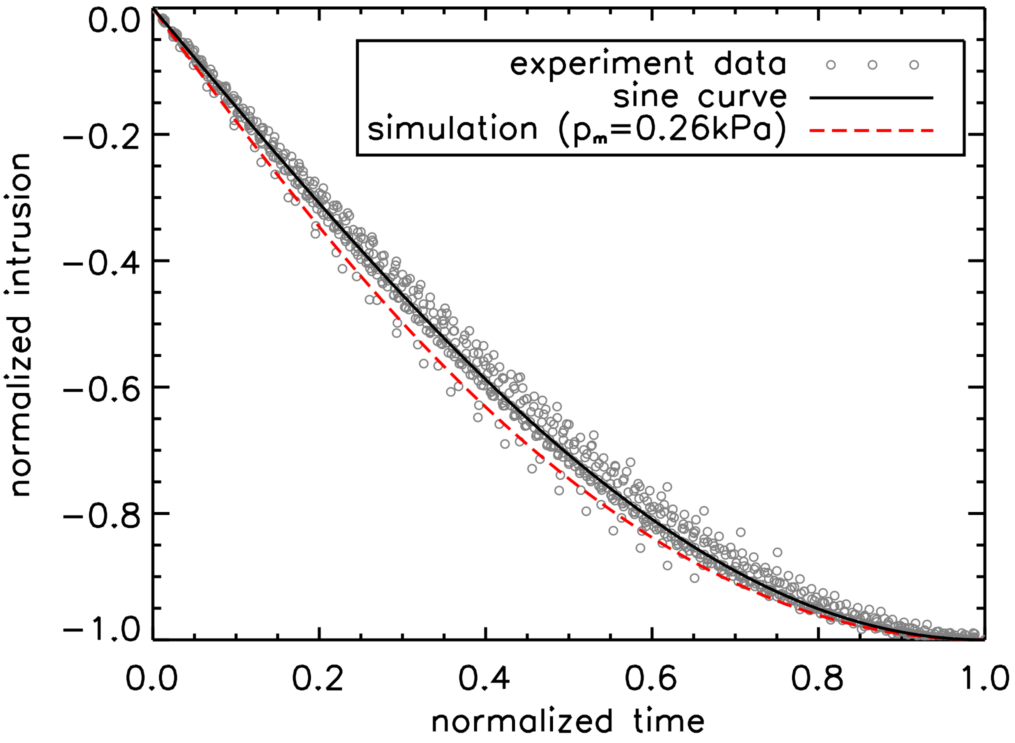

Figure 5.17. *Comparison with benchmark experiments I – deceleration curve.* Comparison between deceleration curves from drop experiments using 1 and 3 mm spheres and a 3D simulation using the compaction calibration setup (ODC relation, p_m = 0.26 kPa). The curves are normalised such that the origin represents the first touch of sphere and dust sample and (1,-1) denotes stopping time at maximum intrusion.The simulated curve lies slightly underneath the fit to the experimental data but well within the errors. The deviation is due to a shorter stopping time than in the experiments (figure from Geretshauser et al. 2010).

been suggested. As remaining parameter the ODC slope has been studied and fixed to $\Delta = 0.58$. All these studies have been carried out in 2D and inferences have been drawn for the 3D setup by means of the findings of the 2D-3D comparison (see Sec. 5.2.3). In the next section, the laboratory experiments are finally compared to 3D simulations of the compaction calibration setup.

5.3.4. Comparing the plastic properties with benchmark experiments

numerical setting

Finally, after the tensile, shear, and compressive strengths governing the plastic behaviour of the dust aggregates have been defined, the final comparison with the laboratory experiments is carried out by means of the *3D compaction calibration setup* (see Sec. 5.1.1 and Fig. 5.2). The numerical, geometrical, and material parameters are chosen as calibrated in the previous sections and presented in Tab. 5.1. The only exception is the bulk modulus of the dust material, which is set to $K_0 = 2\,\mathrm{kPa}$ (instead of $K_0 = 300\,\mathrm{kPa}$) since findings presented in Sec. 5.3.5 indicated a much lower bulk modulus. However, the choice of K_0 has little influence on the plastic compaction properties calibrated for in the compaction calibration setup. It governs the elastic properties,

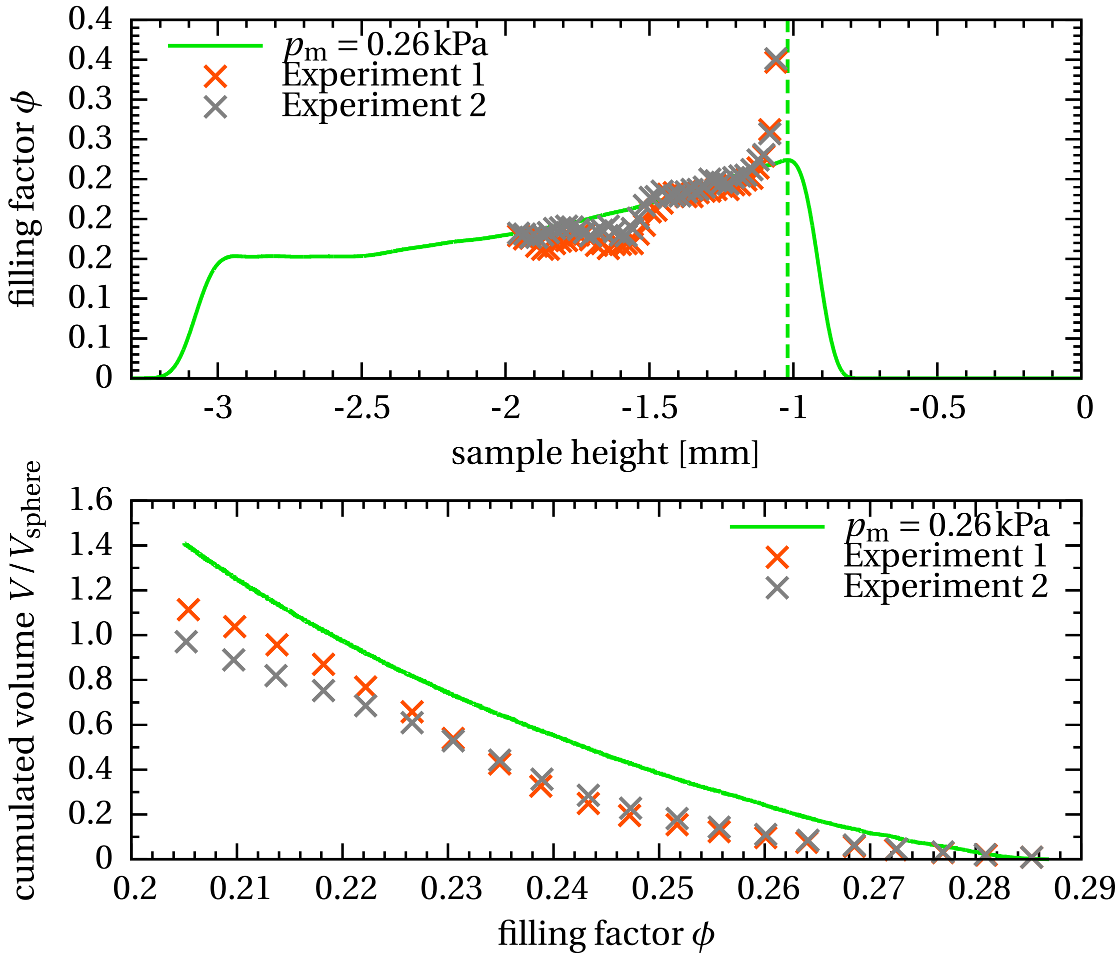

Figure 5.18. *Comparison with benchmark experiments II – vertical density profile and density distribution.* Experimentally measured (crosses, sphere not removed) and simulated (solid line, sphere removed) density profiles (top) at maximum intrusion for the compaction calibration setup. The dashed line indicates the position of the simulated maximum intrusion depth given by the density peak at $D_{\text{max}} \sim -1.02\,$mm. The simulation is carried out in 3D using an ODC mean pressure $p_m = 0.26\,$kPa. Both profiles are in excellent agreement. That the step-like structure of the experimental data cannot be seen in the simulation is a minor drawback since it is clearly interpolated. The bottom panel shows the density distribution for drop experiments (crosses and triangles) and the 3D simulation with the same setup (solid line). The plot displays the cumulated volume with a filling factor $> \phi$ over ϕ. The cumulated volume is normalised by the sphere volume. The simulation is in good agreement with the experimental findings. However, a greater amount of volume being compressed to high filling factors leads to an almost constant deviation for $\phi < 0.26$. The slope is reproduced very well.

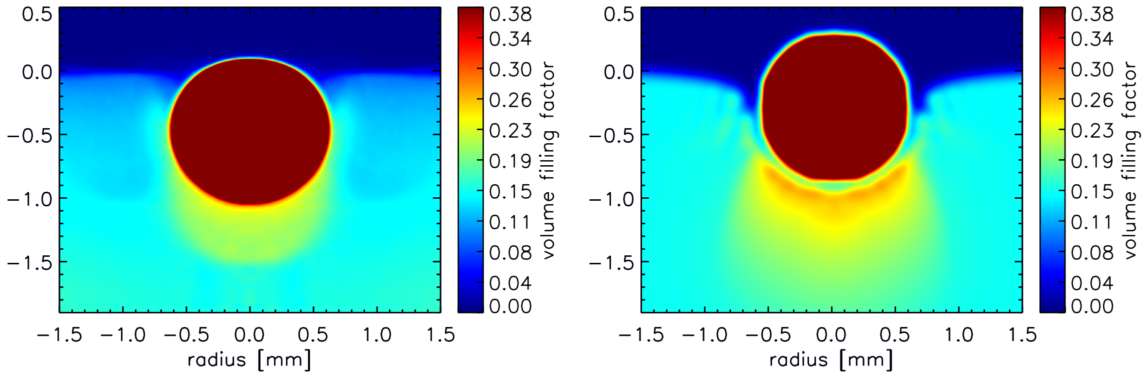

Figure 5.19. *Comparison with benchmark experiments III – vertical density cross-section.* Cross-section through the glass bead (red) and dust sample (light blue) at maximum intrusion for the drop experiment (left) and a 3D simulation (ODC, $p_\mathrm{m} = 0.26\,\mathrm{kPa}$, right). The colour indicates the spatially averaged filling factor. The density structures beneath the glass bead match very well. Even the slight compression along the tight intrusion channel can be reproduced. In the simulated plot, a gap between glass bead and the most dense area is clearly visible. This is caused by the smoothing of the sphere and is discussed in Sect. 5.2.2. The gap has roughly the size of one smoothing length h (figure from Geretshauser et al. 2010).

which are more important for bouncing and fragmentation as shown below.
The following features of the compaction calibration setup, described in full depth in Sec. 5.1.1, are measured in the laboratory and are used here for comparison:

1. stopping time T_s
2. deceleration curve of the projectile
3. vertical density profile
4. vertical density cross-section through both the sphere and the dust sample
5. density distribution of the cumulated volume

stopping time Starting with (1), the experiments show that the *stopping time* T_s of the glass bead is nearly constant at $T_s^\mathrm{exp} = 3.0 \pm 0.1$ ms for 1 mm projectiles over different impact velocities (see Güttler et al. 2009). The corresponding simulation yields $T_s^\mathrm{sim} = 2.42 \pm 0.05\,\mathrm{ms}$ which is not in excellent agreement but also not too far off the experimental results.

deceleration curve Continuing with (2), the *intrusion curve* $h(t)$ was cleared from gravity effects and normalised by evaluating $h'(t') = h(t)/D_\mathrm{max}$ and $t' = t/T_\mathrm{s}$, where $h(t)$ is the position of the bottom of the glass bead as a function of time, D_max the maximum intrusion depth, and T_s the stopping time. At first contact, t is given by $h'(t' = 0) = 0$ and at deepest intrusion $h'(t' = 1) = -1$ (see also Güttler et al. 2009, Sect. 3.2.2). The comparison is shown in Fig. 5.17: the intrusion curve generated by our simulation lies well within the data from the experiments with 1 and 3 mm spheres and only slightly below the fitted sine curve

$$h(t) = -D_{\mathrm{max}} \sin\left(\frac{\pi}{2} \frac{t}{T_{\mathrm{s}}}\right) \tag{5.8}$$

for which $D_{\mathrm{max}} = T_{\mathrm{s}} = 1$ in its normalised form $h'(t')$.

vertical density profile

Turning to the density structure (3), the experimentally measured *vertical density profile* and the results of the corresponding simulation are compared as shown in Fig. 5.18 (top). The crosses represent the data from the two experiments in which the sphere is not removed during measurement. For this reason, the filling factor reaches extremely high values at $D \sim -1\,\mathrm{mm}$, which corresponds to the bottom of the glass bead. The vertical density profile of the simulation is given by the solid line and the vertical dashed line is placed at its filling factor peak at $D \sim -1.02\,\mathrm{mm}$ representing the maximum intrusion depth. Compared with the experimentally measured maximum intrusion depth of $D_{\mathrm{max}} \sim -1.07\,\mathrm{mm}$, this is an excellent result. Since a depth of $D \sim -1\,\mathrm{mm}$ was required using Eq. 5.1 and 5.2 and the 2D intrusion depth study of Sec. 5.3.3, this result also supports the validity of these relations. In addition to the exact value of the intrusion depth, the simulation also reproduces the shape of the given experimental vertical density profile very well. The step-like structure at $D \sim -1.5\,\mathrm{mm}$ is not exactly mapped by the simulation but is instead interpolated.

density cross-section

A two-dimensional representation of the density structure is investigated (4) by comparing the *cross-sections* through both the sphere and dust sample along the z-axis (Fig. 5.19). This reveals where there is an excess of compressed volume. Firstly, the cross-section of the sphere is artificially enhanced by the smoothing of its boundaries, which is inherent to the SPH method. One effect of the smoothing is the existence of a gap between the sphere and dust sample, as already discussed in Sec. 5.2.2, and clearly visible in Fig. 5.19 (right). Hence, it is assumed that the dust sample actually begins where it possesses its maximum compression. The sphere pokes out of the dust sample a bit more than in the experiment because of the artificial enlargement of the cross-section. Secondly, it can be seen that in the experimental reference (Fig. 5.19, left) the compressed region is much narrower and more concentrated beneath the sphere. In the simulated result, the compacted region is a bit broader. This indicates that the shear strength seems to be slightly lower than assumed. Thirdly, the compression extends to high filling factors that are too high, which was already visible in the cumulated volume diagram. Nevertheless, both cross-sections match very well, especially with respect to the mediocre resolution. Remarkably, even the slight intrusion channel on the left and right side of the sphere, which features a slight compression, can be reproduced.

density distribution

Since the vertical density profile shows only a cut through the compressed volume. It contains information about the exact structure of the compression. (5) The *density distribution* (Fig. 5.18, bottom) has the advantage of representing the total compressed volume and its filling factors. Hence, these features are not fully independent but focus on different aspects of the compression. The cumulated volume is normalised by the sphere volume. In general, the experimental reference and our simulation show close agreement. Slightly too much volume is compressed to high filling factors in the simulation, which leads to an almost constant deviation for $\phi < 0.26$. This excess was already seen in the vertical density cross-section (Fig. 5.19). However, the slope is reproduced very well.

conclusion

To conclude, all of the calibration features of the compaction calibration setup can be reproduced with good or even very good accuracy with the tensile strength relation of Sec. 5.3.1,

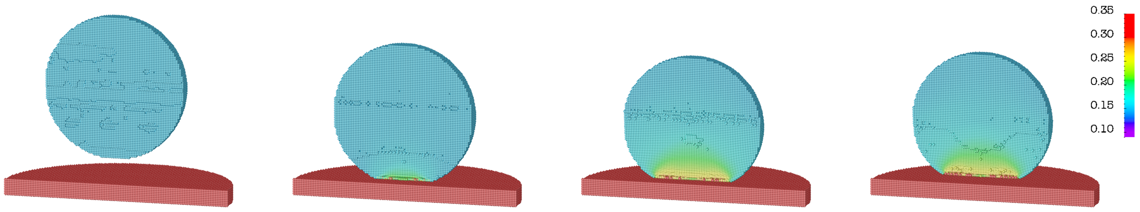

(a) (b) (c) (d)

Figure 5.20. *Bouncing sequence.* Bouncing sequence for $t = 0\,\mathrm{ms}$ (a), $t = 10\,\mathrm{ms}$ (b), $t = 18\,\mathrm{ms}$ (c), and $t = 25\,\mathrm{ms}$ (d). The colour code indicates the filling factor. An aggregate consisting of dust particles (Sirono EOS, see Sec. 4.3.4, diameter 1.0 mm) hits a solid surface simulated by boundary glass particles (Murnaghan EOS, Eq. 4.112, diameter 1.6 mm, thickness 0.1 mm) with a velocity of $v_0 = 0.2\,\mathrm{m/s}$. For this simulation a bulk modulus and mean pressure of $K_0 = 5.0\,\mathrm{kPa}$ and $p_\mathrm{m} = 0.26\,\mathrm{kPa}$, respectively, are used. The aggregate hits the surface and starts to be compacted at its bottom (b). While the plastic deformation at the bottom increases, the aggregate is also deformed elastically: it becomes broader (c). Eventually it leaves the surface with a final velocity v_f (d). It features a permanent compaction while the elastic deformation vanishes.

the shear strength relation calibrated in Sec. 5.3.2, and the compressive strength calibrated in Sec. 5.3.3 and the material parameters in Tab. 5.1. As a result, the plastic properties of the SiO_2 dust material are described very well by the aforementioned relations and the compaction calibration setup has proven to be a sensitive and powerful instrument in the calibration and testing process.

5.3.5. Bulk Modulus

empirical reference

From *laboratory measurements* there are two estimates of the bulk modulus K_0 for the uncompressed material with $\phi \sim 0.15$. It can be determined from sound speed measurements (Blum and Wurm 2008, Paszun and Dominik 2008) which provide $c_\mathrm{s} = 30\,\mathrm{m/s}$. With Eq. 4.124 this yields $K_0 = 300\,\mathrm{kPa}$. Other plausible derivations from bouncing experiments by Weidling et al. (2009) indicate a value which is two orders of magnitude smaller: $K_0 = 1\,\mathrm{kPa}$. The exact knowledge of this value is essential for the porosity model of this thesis (see Sec. 4.3.4) because K_0 is the pre-factor for computing the bulk modulus of higher filling factors with the aid of a power law (Eq. 4.123). As it turns out, the bulk modulus governs the bouncing and fragmentation properties of the dust aggregates. For this reason, I use the bouncing calibration setup and the respective laboratory experiment to determine this quantity on the basis of the previously calibrated plastic material properties. The final choice of K_0 is counterchecked by means of the fragmentation calibration setup and its empirical reference data.

Bouncing

numerical setting

Simulating the *bouncing calibration setup* of Sec. 5.1.2 (see also Fig. 5.3), a 3D dust sphere drops onto a solid surface with initial velocity $v_0 = 0.2\,\mathrm{m/s}$ (see Fig. 5.20). The material parameters are shown in Tab. 5.2. Since the bouncing dust sphere is also plastically deformed during the impact, the bulk modulus K_0 is varied with respect to two values of the mean pressure $p_\mathrm{m} = 0.26\,\mathrm{kPa}$ and

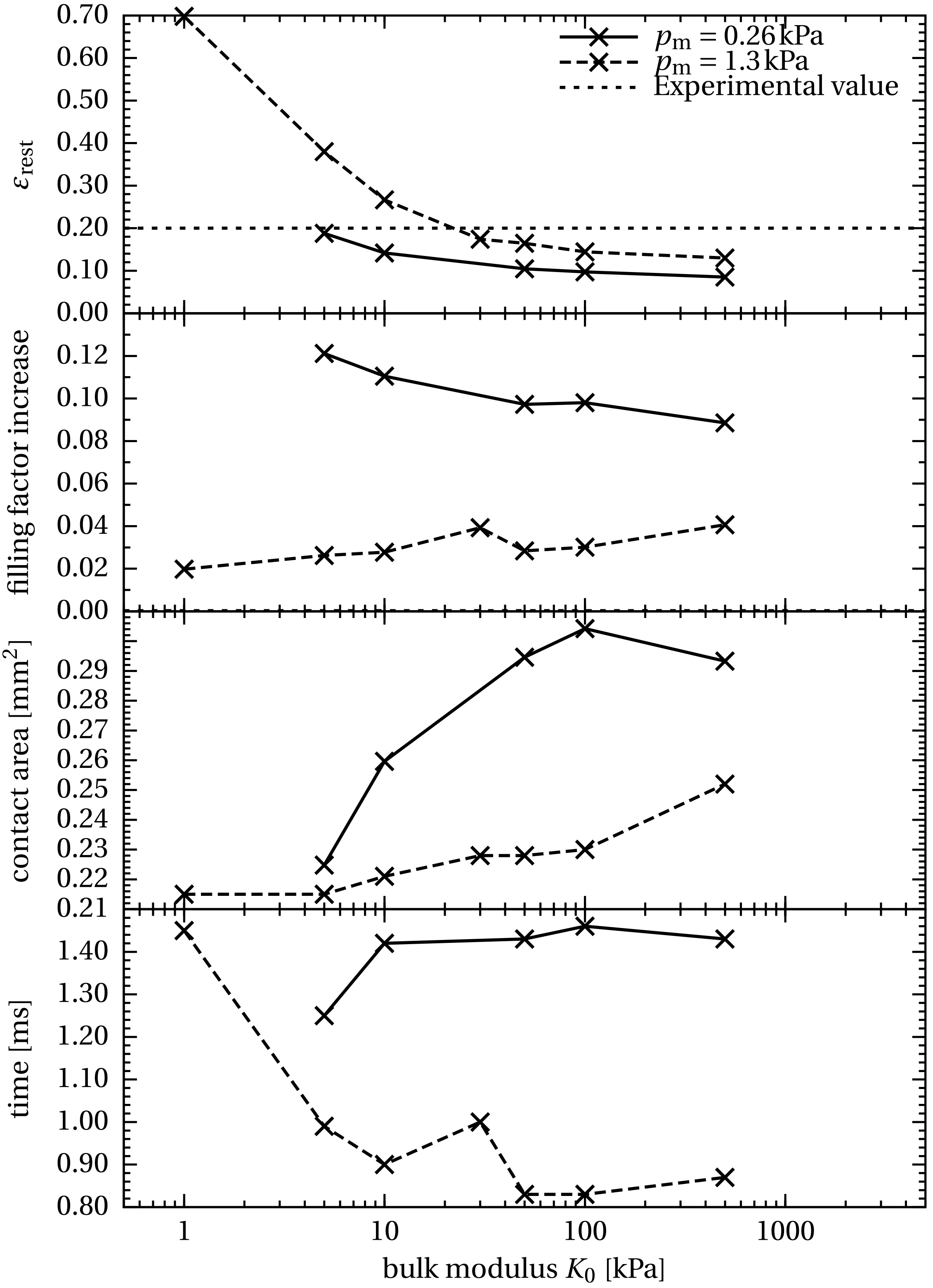

Figure 5.21. *Bouncing for different bulk moduli.* Coefficient of restitution $\varepsilon_{\mathrm{rest}}$ (top), filling factor increase in units of the initial filling factor $\phi = 0.15$ (second panel), flattened area A_{cont}, and contact time t_{cont} for different bulk moduli K_0 and a high ($p_{\mathrm{m}} = 1.3$ kPa) and a low ($p_{\mathrm{m}} = 1.3$ kPa) of the mean pressure of the compressive strength (Eq. 5.4). The determination of these quantities is described in Sec. 5.1.2.

K_0 [kPa]	ϕ increase	$\varepsilon_{\text{rest}}$	A_{flat} [mm^2]	t_{cont} [ms]
1	0.020	0.70	0.215	1.45
5	0.026	0.38	0.215	0.99
10	0.028	0.27	0.221	0.90
30	0.039	0.17	0.228	1.00
50	0.028	0.16	0.228	0.83
100	0.030	0.14	0.230	0.83
500	0.040	0.13	0.252	0.87

Table 5.5. *Results of the bulk modulus study for* $p_{\text{m}} = 1.3\,\text{kPa}$. Coefficient of restitution $\varepsilon_{\text{rest}}$, filling factor increase in units of the initial filling factor $\phi = 0.15$, flattened area A_{cont}, and contact time t_{cont} for different values of the bulk modulus K_0. The determination of these quantities is described in Sec. 5.1.2.

K_0 [kPa]	ϕ increase	$\varepsilon_{\text{rest}}$	A_{flat} [mm^2]	t_{cont} [ms]
5	0.12	0.19	0.2248	1.25
10	0.11	0.14	0.2596	1.42
50	0.097	0.10	0.2946	1.43
100	0.098	0.097	0.3042	1.46
500	0.089	0.085	0.2933	1.43

Table 5.6. *Results of the bulk modulus study for* $p_{\text{m}} = 0.26\,\text{kPa}$. Coefficient of restitution $\varepsilon_{\text{rest}}$, filling factor increase in units of the initial filling factor $\phi = 0.15$, flattened area A_{cont}, and contact time t_{cont} for different values of the bulk modulus K_0. The determination of these quantities is described in Sec. 5.1.2.

$p_{\mathrm{m}} = 1.3\,\mathrm{kPa}$ in the ODC relation for the compressive strength (Eq. 5.4). This is a further check for the correct mean pressure p_{m}, which was calibrated in Sec. 5.3.3 with a different setup. The main calibration parameter for this study is the coefficient of restitution $\varepsilon_{\mathrm{rest}} = v_{\mathrm{f}} v_0^{-1}$, for which an experimental reference value is available. The quantities v_0 and v_{f} denote the impact and final velocities of the aggregate, respectively. Additionally, the average filling factor increase is computed for the initially highly porous ($\phi = 0.15$) aggregate and compared with the experimentally based considerations by Weidling et al. (2009). For experiments which may be carried out in the future, the flattened surface A_{flat} and the contact time t_{cont} are determined as described in Sec. 5.1.2. The results are depicted in Fig. 5.21 and listed in Tab. 5.5 for the high p_{m} and in Tab. 5.6 for the low p_{m}.

Describing the bouncing process, during the impact (see Fig. 5.20) a small region of the bottom of the dust sphere is compressed. The deformed sphere then bounces off the target with reduced velocity v_{f}. The latter effect was already observed by Güttler et al. (2009) and demonstrates the ability of the code and the implemented porosity model to simulate the elastic properties of the dust correctly. This is the first time that bouncing of highly porous macroscopic dust aggregates can be reproduced in numerical simulations. From the laboratory experiments $\varepsilon_{\mathrm{rest}} \sim 0.2$ and $\sim 95\,\%$ energy dissipation are expected.

For both values of p_{m} the coefficient of restitution decreases with increasing K_0 (Fig. 5.21, top). For $p_{\mathrm{m}} = 0.26\,\mathrm{kPa}$ more energy is dissipated and $\varepsilon_{\mathrm{rest}}$ is generally lower. This is because the lower mean pressure causes the pressure threshold for plastic deformation to be lowered. Both curves intersect the experimental value represented by the dashed line. Based on the results of Sec. 5.3.3, where $p_{\mathrm{m}} = 0.26\,\mathrm{kPa}$ turned out to be a good choice for the mean pressure, the results for this experiment favour a bulk modulus $K_0 \sim 5\,\mathrm{kPa}$. This value is close to the value $K_0 = 1\,\mathrm{kPa}$ computed by Weidling et al. (2009) with a simplified model. The simulations yield a coefficient of restitution $\varepsilon_{\mathrm{rest}} = 0.19$ ($\sim 96\,\%$ energy dissipation) for $K_0 = 5.0\,\mathrm{kPa}$, which is in excellent agreement with the experimental results. On the other hand, for $K_0 = 500\,\mathrm{kPa}$ I find $\varepsilon_{\mathrm{rest}} = 0.085$ ($\sim 99\,\%$ energy dissipation), which is too far away from the reference value. A high value for the bulk modulus K_0 as given by the sound speed measurements is therefore excluded.

coefficient of restitution

Given the higher value $p_{\mathrm{m}} = 1.3\,\mathrm{kPa}$ for the compressive strength curve, $\varepsilon_{\mathrm{rest}}$ increases for all choices of K_0. For $K_0 = 1.0\,\mathrm{kPa}$ it becomes $\varepsilon_{\mathrm{rest}} \sim 0.7$ and only $\sim 50\,\%$ of the energy are dissipated. On the other hand, for $K_0 = 300\,\mathrm{kPa}$ I find that $\varepsilon_{\mathrm{rest}} \sim 0.13$, which is equivalent to $\sim 98\,\%$ energy dissipation. From these findings, a bulk modulus of $K_0 \sim 20\,\mathrm{kPa}$ is theoretically also possible but the higher value for the mean pressure is excluded by the results presented in Sec. 5.3.3 and $K_0 \sim 20\,\mathrm{kPa}$ is not supported by experiments.

filling factor increase

According to Weidling et al. (2009) the *filling factor increase* after one collision is $\sim 2 \times 10^{-3}$ times the initial filling factor. However, because of their model assumptions their relation (Eq. 4) for the filling factor variation is only valid for more than 150 subsequent collisions of the same aggregate. In the simulations presented in the thesis at hand (Fig. 5.21, second panel), the resulting filling factor in units of the initial filling factor exceeds the experimentally based value by about one ($p_{\mathrm{m}} = 1.3\,\mathrm{kPa}$, Tab. 5.5) and even two orders of magnitude ($p_{\mathrm{m}} = 0.26\,\mathrm{kPa}$, Tab. 5.6). The increase in filling factor remains almost constant with increasing K_0: ~ 0.03 and ~ 0.1 times the initial filling factor for the higher and the lower mean pressure, respectively. The reason for this difference is again the lower threshold for plastic deformation for the $p_{\mathrm{m}} = 0.26\,\mathrm{kPa}$ case. Interestingly, the variation for higher bulk moduli is not uniform: in the low mean pressure case the filling factor increase slightly decreases for larger K_0, while for the high mean pressure it increases.

flattened area

The area, which is flattened during the collision (Fig. 5.21, third panel), A_{flat} increases in both

K_0 [kPa]	Slope κ	Norm. largest fragment μ_{pw}
3.00	0.361 ± 0.004	0.200 ± 0.008
3.50	0.429 ± 0.002	0.172 ± 0.002
4.00	0.518 ± 0.011	0.230 ± 0.009
4.25	0.523 ± 0.006	0.194 ± 0.004
4.50	0.673 ± 0.017	0.234 ± 0.007
4.75	0.834 ± 0.025	0.196 ± 0.005
5.00	0.832 ± 0.063	0.198 ± 0.011
5.50	0.836 ± 0.052	0.220 ± 0.010
6.00	2.027 ± 0.121	0.171 ± 0.002
6.50	0.910 ± 0.053	0.390 ± 0.013

Table 5.7. *Results of the fragmentation calibration setup.* Results from the fragmentation calibration setup. The slope κ of the power law increases with increasing bulk modulus K_0. Remarkably, the size of the normalised largest fragment remains nearly constant around $\mu_{\mathrm{pw}} \sim 0.2$ for $K_0 \leq 6.0\,\mathrm{kPa}$.

mean pressure cases with increasing bulk modulus K_0. It increases more rapidly for the low mean pressure (see Tab. 5.6) case: from $0.225\,\mathrm{mm}^2$ (28.6 % of the sphere's cross section) to $0.293\,\mathrm{mm}^2$ (37.3 %). The values for the high mean pressure case (see Tab. 5.5) are: from $0.215\,\mathrm{mm}^2$ (27.4 %) to $0.252\,\mathrm{mm}^2$ (32.1 %). In general, the flattened area is larger for the low pressure case. The reason for this is again due to the fact that the material can be plastically deformed more easily because of the lowered compressive strength.

contact time The *contact time* t_{cont} (Fig. 5.21, bottom) is nearly constant for $p_{\mathrm{m}} = 0.26\,\mathrm{kPa}$: the aggregate touches the glass plate for ~ 1.4 ms (see also Tab. 5.6). For the higher mean pressure t_{cont} decreases from ~ 1.45 ms to ~ 0.85 ms and then remains constant (see Tab. 5.5). The reason for this behaviour is unclear. Contact times are in general longer for the case with higher plasticity. This is because a larger amount of the aggregate gets plastically deformed which takes more time.

bulk modulus choice In summary, this bouncing experiment fixes the choice of the bulk modulus to $K_0 \sim 5\,\mathrm{kPa}$ while $p_{\mathrm{m}} = 0.26\,\mathrm{kPa}$ is confirmed to be derived from the compaction calibration setup in Sec. 5.3.3. The bouncing calibration setup, just like the compaction calibration setup, is very sensitive to changes in the compressive strength curve. The effects between higher and lower plasticity can be clearly seen: the former case results in generally larger values for the filling factor increase, flattened area, and contact time. The lower coefficient of restitution $\varepsilon_{\mathrm{rest}}$ indicates a larger degree of energy dissipation, which is again caused by the lower plastic deformation threshold. In the following, it is shown that $K_0 \sim 5\,\mathrm{kPa}$ is also consistent with the fragmentation behaviour of the dust aggregates.

Fragmentation

numerical setting Since the intended field of application of the calibrated SPH code and porosity model is the simulation of pre-planetesimal collisions, it is of major importance to calibrate and test the fragmentation behaviour of the simulated material. For this reason, the *fragmentation calibration setup* described in Sec. 5.1.3 (see also Fig. 5.4) is utilised. The numerical, geometrical, and material

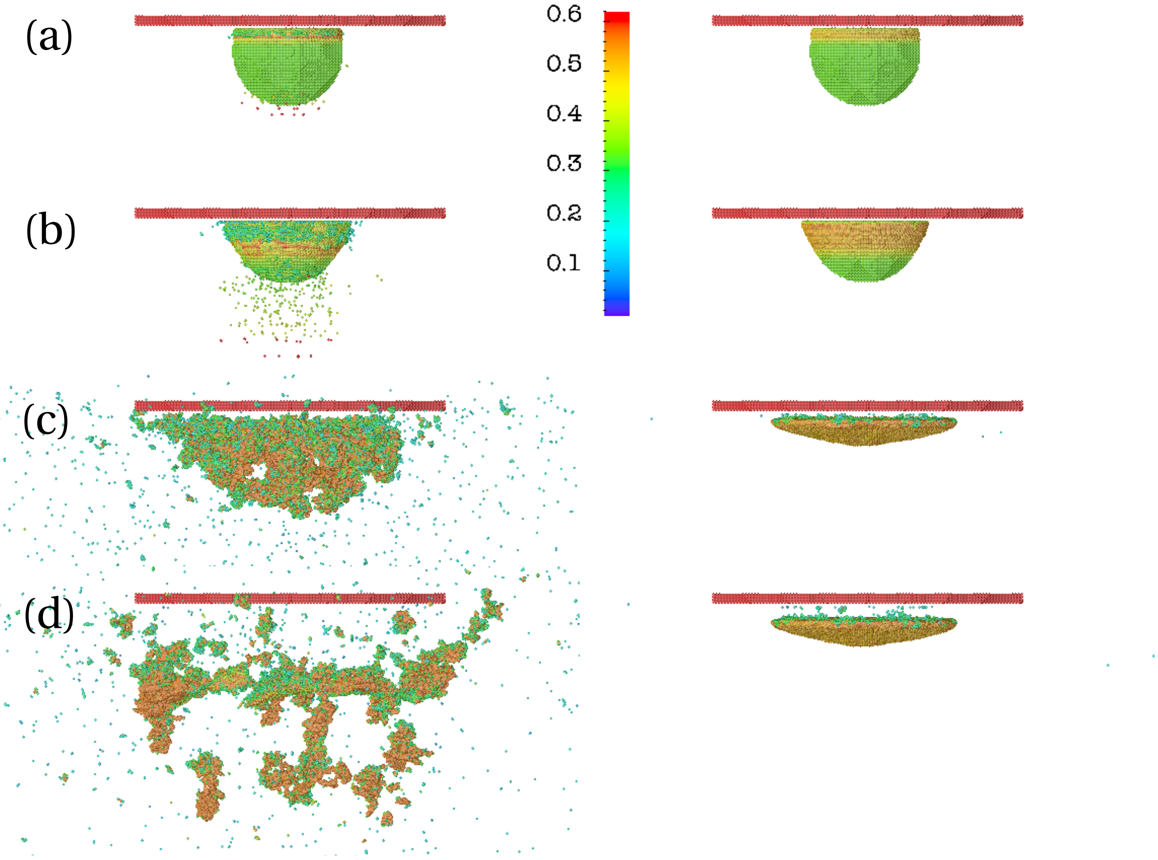

Figure 5.22. *Fragmentation sequence.* The snapshots are taken at the following times: (a) $t = 0.02\,\mathrm{ms}$ (b) $t = 0.03\,\mathrm{ms}$ (c) $t = 0.275\,\mathrm{ms}$ (d) $t = 0.7\,\mathrm{ms}$. The initial aggregates have an intermediate porosity of $\phi = 0.35$. For the left sequence the calibrated bulk modulus $K_0 = 4.5\,\mathrm{kPa}$ is used. The collision on the right is simulated with $K_0 = 50.0\,\mathrm{kPa}$. Both collisions illustrate the importance of the bulk modulus for fragmentation. Fragmentation occurs for the low bulk modulus while for high K_0 the aggregate gets compacted to a flat disc of nearly maximum filling factor. In the latter case only a few small fragments are chipped off.

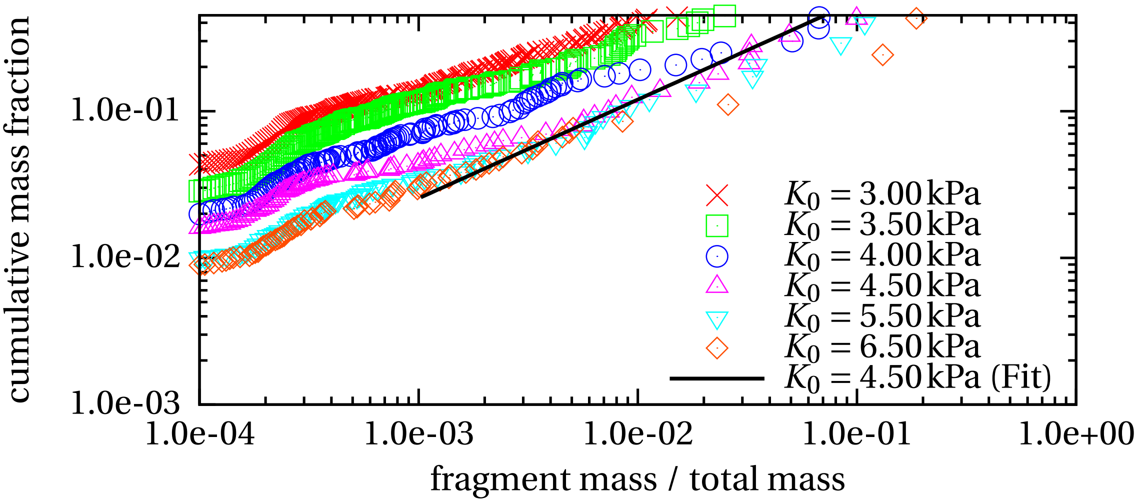

Figure 5.23. *Fragmentation for different bulk moduli.* Cumulative mass distribution of the fragments of a dust aggregate impacting on a glass plate for different values of K_0. The distribution is evaluated 0.8 ms after the collision. For low fragment masses the shape of all simulated curves differs from the experimental curve due to the limited resolution of the experimental setup. An increase in K_0 leads to an increase in the slope κ of the power-law fit. The best agreement with the experimentally measured slope 0.67 is found for the simulation with $K_0 = 4.5\,\text{kPa}$.

parameters are as listed in Tab. 5.3 except for K_0 which is varied in this study.

In this setup, a medium porosity ($\phi = 0.35$) dust aggregate hits a glass plate from below with an impact velocity of $v_0 = 8.4\,\text{m/s}$. The spatial resolution is chosen such that a single SPH particle has less than 5×10^{-6} times the mass of the whole aggregate ($6.8 \times 10^{-8}\,\text{kg}$) to be able to resolve the same fragment masses as the experimental reference. Gravity is taken into account.

As it can be seen from Fig. 5.22, the bulk modulus has a significant influence on the fragmentation behaviour. The illustration shows a fragmentation sequence for $K_0 = 4.5\,\text{kPa}$ (left) and $K_0 = 50\,\text{kPa}$ (right). In the first case, the aggregate shatters completely and the fragments bounce off at all angles. In the second case, the aggregate hardly produces any fragments but is compressed into a flat disc of nearly maximum filling factor. As the following study reveals, the fragment distribution is very sensitive to changes in the bulk modulus K_0.

cumulative mass distribution

For this reason, the value K_0 is varied in the order of the bulk modulus which was calibrated by means of the bouncing calibration setup, i.e. from 3.0 kPa to 6.5 kPa. For comparison with the reference experiment, the fragmentation data is plotted in a *cumulative way* (Fig. 5.23) and can be fitted in good agreement with a power-law

$$m_{\text{cum}}(m_{\text{f}}) = \int_0^{m_{\text{f}}} n(m)\, m\, \mathrm{d}m = \left(\frac{m_{\text{f}}}{\mu_{\text{pw}}}\right)^{\kappa} \tag{5.9}$$

where m_{f} is the fragment mass, $n(m)\,\mathrm{d}m$ is the number of fragments in the mass interval $[m, m + \mathrm{d}m]$, and μ_{pw} is the mass of the most massive member of the distribution. All of these quantities are normalised by the total mass of the distribution. The quantity μ_{pw} can be regarded as a measure for the strength of the fragmentation. Finally, κ is the power-law index and accounts for the slope of the power-law distribution. The *reference experiment* provides $\mu_{\mathrm{pw}} = 0.22$ and $\kappa = 0.67$. The simulation is evaluated 0.8 ms after the impact. The mass of a fragment is given by the sum of the mass of the SPH particles belonging to it. Two fragments are considered as being separated when they are not linked by SPH particles that interact with each other, i.e. when the closest SPH particles of two fragments are separated by a distance greater than $2h$.

empirical reference

The results of the simulation are presented in Fig. 5.23 and Tab. 5.7. In general, it can be said that an increase in the bulk modulus leads to an increase in the slope κ of the fragment distribution indicating a larger fraction of more massive fragments. In contrast, the size of the largest fragment (normalised through the total mass of the distribution) μ_{pw} remains roughly constant at $\sim 20\,\%$ up to $K_0 = 6.0\,\mathrm{kPa}$. For higher K_0, small chunks and single SPH particles mainly originate in the aggregate, which is only compressed but does not fragment (similar to the high bulk modulus simulation presented in Fig. 5.22).

bulk modulus choice

I now calibrate κ, which is more sensitive to changes in K_0 (see Table 5.7). Given the measured value of $\kappa = 0.67$, I find excellent agreement with the simulation results using $K_0 = 4.5\,\mathrm{kPa}$, which yields $\kappa = 0.673 \pm 0.017$. This simulation also reproduces the experimentally measured normalised mass of the largest fragment $\mu_{\mathrm{pw}} = 0.22$ to a very high accuracy ($\mu_{\mathrm{pw}} = 0.234 \pm 0.007$). The slight difference may be caused by the increase in the filling factor not being taken into account in the analysis of the experimental data, whereas in the simulation it is. The fragment distributions for different K_0 and the best fit for the power-law are shown in Fig. 5.23. The setup and outcome of the simulation are displayed in Fig. 5.22 (left). The choice of $p_{\mathrm{m}} = 0.26\,\mathrm{kPa}$ and $K_0 = 4.5\,\mathrm{kPa}$ is consistent with the results of the compaction and bouncing experiments. The fragmentation experiment proves the validity of these choices and the consistency of the underlying porosity model.

shear modulus

bulk modulus exponent

Since no empirical data is available for the *shear modulus*, I maintain the choice of the original Sirono porosity model and set $\mu(\phi) = 0.5\,K(\phi)$. Hence, the shear modulus is also fixed with the calibration of K_0. I do not investigate the influence of the free parameter γ of Eq. 4.123, which regulates the variation of the bulk modulus with the filling factor. This is because the bouncing benchmark test has been carried out with a highly porous aggregate ($\phi = 0.15$) and the fragmentation calibration with an aggregate of intermediate porosity ($\phi = 0.35$). Both experiments are very sensitive to changes in the bulk modulus and can be reproduced with $K_0 \sim 4.5\,\mathrm{kPa}$ and $\gamma = 4$. This serves as a good indication for an adequate value of γ although a more accurate study on this parameter could be carried out in future works.

In contrast to the experiments, no material sticks to the glass plate because of the simulation setup. As in Sec. 5.2.4, the artificial viscosity is used to separate the glass and dust materials. This leads to an additional pressure on the dust material which prevents sticking.

5.4. Summary

In this chapter, I have successfully calibrated the porosity model presented in Sec. 4.3.4 for the simulation of highly porous SiO_2 dust aggregates. These serve as pre-planetesimal analogues in the astrophysical context. Jointly with experimentalists, I designed three benchmark experiments to calibrate and test the correct functionality of this model: (1) compaction of dust by a dropped glass bead (compaction setup, Sec. 5.1.1), (2) rebound of a dust aggregate from a solid plate (bouncing setup, Sec. 5.1.2), and (3) shattering of a dust aggregate at a solid wall (fragmentation setup, Sec. 5.1.3).

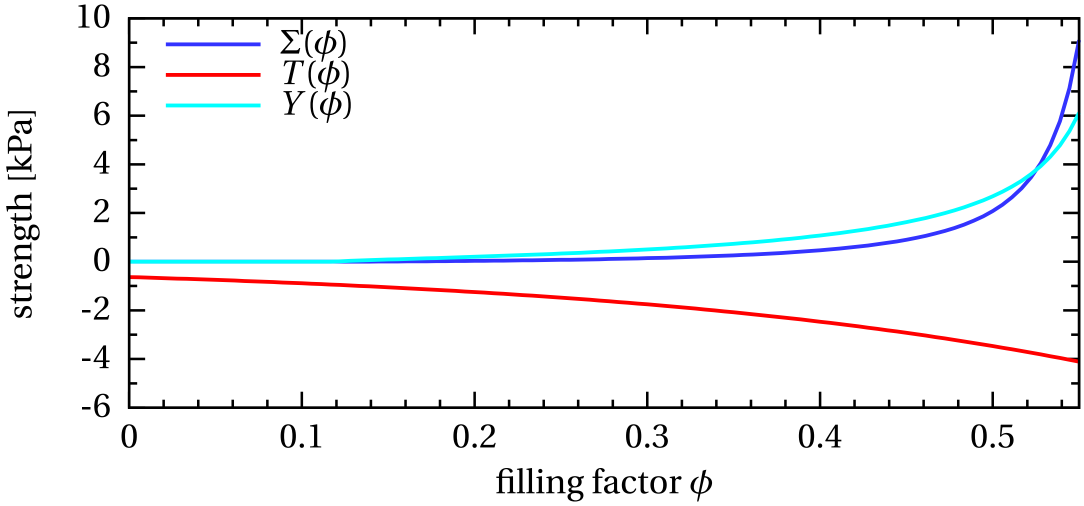

Figure 5.24. *Calibrated strength curves.* The compressive $\Sigma(\phi)$, tensile $T(\phi)$, and shear strength $Y(\phi)$ as a result of the calibration in this chapter.

Physical Quantity	Symbol	Value	Unit
Bulk density	ρ_s	2,000	$\mathrm{kg\,m^{-3}}$
Filling factor RBD sample	ϕ_{RBD}	0.15	-
Bulk modulus RBD sample	K_0	4.5×10^3	Pa
ODC mean pressure	p_{m}	260	Pa
ODC max. filling factor	ϕ_2	0.58	-
ODC min. filling factor	ϕ_1	0.12	-
ODC slope	Δ	0.58	-
Numerical parameters$^{(b)}$			
Lattice type (2D)		triangular	
Av. no. interaction partners (2D)	I_{av}	~ 100	-
Lattice type (3D)		cubic	
Av. no. interaction partners (3D)	I_{av}	~ 240	-
Artificial viscosity (bulk)	α_{av}	0.1	-
Artificial viscosity (von Neumann-Richtmyer)	β_{av}	0	-

Table 5.8. *Selection of numerical and material parameters after the calibration.* ODC stands for omnidirectional compressive strength relation (Eq. 5.4). The values presented in this table represent the final choices resulting from the completed calibration process.

Before the actual calibration process, the compaction setup has been used to profoundly investigate the numerical properties of the model and code (Sec. 5.2). As the first step (Sec. 5.2.1), I have determined the adequate size of the computational domain to exclude spurious boundary effects. As a second step (Sec. 5.2.2), I have tested to ensure adequate numerical and spatial resolutions, to exclude resolution effects on the calibration process. An average number of ~ 100 SPH particles in 2D and of ~ 240 SPH particles in 3D provides a sufficient numerical resolution. I have also shown that the results for this setup converge at higher spatial resolutions. For the purpose of saving computing time, many parameter studies have been carried out in 2D. Therefore, as a third step in Sec. 5.2.3, fundamental differences between these two setups have been found and qualified. In particular, a conversion relation for the intrusion depth (Eq. 5.2) between the dimensions has been derived and verified. As a fourth step (Sec. 5.2.4), the dissipative properties of the artificial viscosity and its role in the stability of the simulation have been investigated. It has been necessary to apply $\alpha_{\mathrm{av}} = 0.1$ and $\beta_{\mathrm{av}} = 0$ to the dust material to provide numerical stability and to account for its physical dissipative features caused by internal friction. To damp internal oscillations of the glass, this material has been simulated with $\alpha_{\mathrm{av}} = 1.0$ and $\beta_{\mathrm{av}} = 0$. Artificial viscosity has also been used to separate dust and glass material, which differ highly in the “stiffness” of their equations of state, therefore dust particles in contact with glass have been simulated with glass artificial viscosity. The numerical parameters derived from this study are collected in Tab. 5.8.

At the beginning of the calibration process, a static uniaxial compressive strength relation, a tensile strength relation and two possible values for the bulk modulus have been available from laboratory measurements. These data have been insufficient to apply the porosity model at hand. Therefore, the benchmark experiments - originally designed to test the model - have been used to determine the missing quantities (Sec. 5.3). However, the number of calibration features has still been larger than the number of missing quantities. Finally, the calibration has been regarded to be successful once all features could be simulated with a consistent set of material parameters. The tensile strength relation $T(\phi)$ has been adopted without modification (Sec. 5.3.1). The compaction calibration setup, in particular the vertical density profile has been used to constrain a shear strength relation $Y(\phi) = \sqrt{\Sigma(\phi)|T(\phi)|}$ as a function of the other plasticity thresholds (Sec. 5.3.2). Since the static compressive strength relation has proven to be unrealistic with respect to simulations and experiments, in Sec. 5.3.3 at first some possible functional expressions for a dynamic compressive strength relations have been excluded. Finally, a static omnidirectional (ODC) relation, measured by Güttler et al. (2009) (Eq. 5.4) specifically for this calibration process, has been turned into a dynamic relation by lowering the mean pressure p_{m} of its Fermi-Dirac fit function. The latter has been constrained to $p_{\mathrm{m}} = 0.26\,\mathrm{kPa}$ by a numerical study utilising the compaction calibration setup. In addition, the effects of the slope of the Fermi-Dirac function have been studied and fixed to $\Delta = 0.58$ by means of the same setup. To conclude the calibration process of the plastic properties, the result of the compaction simulation have been compared to laboratory data of the stopping time, deceleration curve, filling factor distribution, and vertical density cross-section. The results of the experimental references have been reproduced with good to excellent accuracy. The final material parameters are listed in Tab. 5.8. A graphical illustration of the final strength curves is shown in Fig. 5.24.

After calibrating the plastic properties of the SiO_2 dust, the bulk modulus K_0 governing the elastic properties has had to be fixed (Sec. 5.3.5). With the bouncing calibration setup it has been possible to simulate bouncing of highly porous macroscopic dust aggregates for the first time. As a result, it has been constrained that $K_0 = 5\,\mathrm{kPa}$, similar to the value proposed by Weidling et al. (2009), is more realistic than $K_0 = 300\,\mathrm{kPa}$ as suggested by sound speed measurements. The results have proven to be consistent with the calibrated $p_\mathrm{m} = 0.26\,\mathrm{kPa}$ for the ODC relation. Since an important application of this code is pre-planetesimal collisions, the ability to correctly simulate the fragmentation of dust aggregates quantitatively is highly important. To test this, I have used the fragmentation calibration setup, which has proven to be very sensitive to changes in the bulk modulus. For $p_\mathrm{m} = 0.26\,\mathrm{kPa}$, the closest agreement with the empirical reference has been achieved with $K_0 = 4.5\,\mathrm{kPa}$. Remarkably, this is consistent with the findings of the bouncing calibration setup, which represents a test for a totally different behaviour of the dust aggregates. The value for K_0 can also be found in Tab. 5.8. Since no empirical data was available for the shear modulus, this quantity is set to $\mu(\phi) = 0.5\,K(\phi)$.

As a final result from this calibration process, the presented porosity model and code are fully calibrated for the simulation of SiO_2 dust. The procedure presented in this chapter represents the most extensive code calibration for protoplanetary material which is currently available. Furthermore, the testing has been carried out for many aspects: compaction, bouncing, and fragmentation. Additionally, up to date unknown and hardly measurable material parameters have been constrained and determined. Consequently, the procedure described in this chapter can be used as a paradigm to calibrate and determine unknown material of other highly porous material.

6. Pre-Planetesimal Collisions

This section is dedicated to the investigation of pre-planetesimal collisions. In Sec. 6.1 I develop a new classification scheme for the outcome of pre-planetesimal collisions. This scheme categorises according to the mass of the resulting fragments. It provides sufficient accuracy to investigate possible obstacles of planetesimal formation such as the fragmentation and bouncing barriers as well as the dust emission features of late T Tauri discs. In Sec. 6.2 I present the first test simulations using the inhomogeneity damage model (Sec. 4.3.5), which is developed for a more realistic simulation of pre-planetesimals. The results provide valuable insight into the functionality of the model as well as the influence of inhomogeneity on the outcome of pre-planetesimal collisions. Bouncing of homogeneous aggregates and aggregates with hard shells is investigated in Sec. 6.3. This directly addresses the probability of a bouncing barrier. To conclude this chapter, I present the results of a broad head-on collision study of pre-planetesimals in the centimetre to decimetre regime in Sec. 6.4. In this section I focus on the influence of porosity on the velocity thresholds for transitions between positive, neutral, and negative growth of the aggregates. Hereby, I utilise the four-population classification scheme.

6.1. The four-population model: a new classification scheme for pre-planetesimal collision outcome[1]

As already pointed out in Sec. 2.3.1 and 2.5, the formation of planetesimals by core accretion requires the right amount of sticking, bouncing, and fragmentation to be consistent with observations. Therefore, collisions of pre-planetesimals have to be investigated as thoroughly as possible and their outcome has to be mapped as precisely as possible taking into account all the relevant parameters such as initial porosity, collision partner size, impact velocity, mass ratio, and rotation. To classify collision outcomes, Güttler et al. (2010) compiled 19 experiments and mapped them according to their sticking, bouncing, and fragmentation classification (Fig. 6.1). However, due to experimental restrictions they covered only small parts of the relevant parameter space. Many of their findings were not deduced from collisions between porous dust aggregates but from dust collisions with a solid object. Collisions between aggregates larger than decimetre size were not possible due to restrictions of their experimental apparatus. In addition, not all experiments could be carried out in protoplanetary disc conditions, i.e. in a vacuum and microgravity (see also Sec. 3.1).

After the successful code calibration with benchmark experiments in Ch. 5, it is shown in Sec. 6.1.1 that the code furthermore can reproduce all sticking, bouncing, and fragmentation types proposed by Güttler et al. (2010). However, I find that this categorisation can also introduce unnecessary complexity and on some occasions may lack the required accuracy. It is possible that in a collision more than one process of sticking, bouncing and fragmentation could take place and qualitative models do not make it clear whether the overall growth is positive, negative, or

---

[1] This section was previously published in Geretshauser et al. (2011) in a slightly altered version.

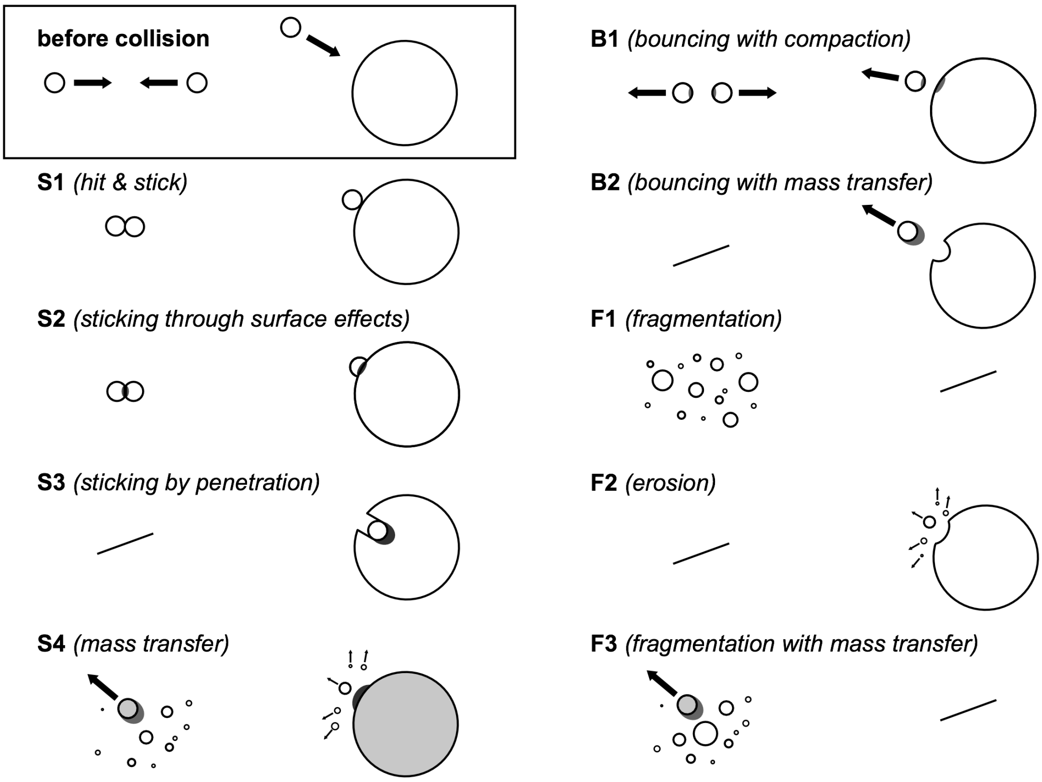

Figure 6.1. *Four-population model I – sticking, bouncing, and fragmentation classification.* Güttler et al. (2010) classify the outcomes of 19 experimental collision setups with dust aggregates into four types of sticking (S), two types of bouncing (B), and three types of fragmentation (F). The initial situation is distinguished according to collisions between objects of similar size and collisions with a projectile much smaller than the target. The experimental setups involved aggregate-aggregate collisions or collisions between a dust aggregate and a solid object. The classification is only qualitative and not always consistent in the choice of the categories (figure from Güttler et al. 2010).

neutral. Therefore, I find it necessary to improve the suggestion of qualitatively categorising into sticking, bouncing, and fragmentation events and propose a new, simpler but at the same time more quantitative model for mapping collisional data. This model is presented in Sec. 6.1.2 as the four-population model. To show its applicability, I present the first results of simulations of collisions between macroscopic objects consisting of realistic pre-planetesimal material in Sec. 6.1.3. Finally, the findings are summarised in Sec. 6.1.4.

6.1.1. Reproducing sticking, bouncing, and fragmentation collision types

sticking, bouncing, and fragmentation classification

The classification of laboratory experiments by Güttler et al. (2010) suggested categorising into four types of sticking, two types of bouncing, and three types of fragmentation (Fig. 6.1). The sticking events (S) were subdivided according to sticking mechanisms (hit-and-stick for micron sized monomers, surface effects, or deep penetration) and a quantitative criterion (mass transfer). With respect to rebound (B), growth neutral bouncing with compaction and bouncing with mass transfer were distinguished. Fragmentation (F) was split up according to its degree (complete fragmentation or erosion) and whether some sticking was involved (fragmentation with mass transfer).

In this section it is shown that the code and its underlying calibrated porosity model can reproduce these empirical outcome types in numerical simulations. Images of the final result of each example simulation are presented in Fig. 6.2 according to this categorisation. The end times of the simulations are chosen by visual control of the fragment evolution and particle velocities close to the thermal equilibrium for each fragment. For each category an exterior view (left) and a cut through the centre of the resulting aggregate(s) (right) is shown (except for type F1). The initial particle distribution is setup by the program `initgrid` (Appx. A.3). The target is always a dust aggregate with radius $r_t = 10\,\mathrm{cm}$ modelled using 238,238 SPH particles. The projectiles are modelled using 1,905 and 51,477 SPH particles for projectile radii $r_p = 2\,\mathrm{cm}$ and $r_p = 6\,\mathrm{cm}$, respectively, and placed on a cubic lattice with edge length 2.6 mm. The collision partners were aligned head-on with a shift of half a lattice constant into each direction perpendicular to the collision axis to avoid particle interpenetration. In all simulations (except F2), both objects are set up with $\phi = 0.35$ and the masses of the target, the 6 cm-, and 2 cm-projectiles were 2.93 kg, 0.63 kg, and 0.023 kg, respectively. An overview of the initial conditions of the simulations is given in Tab. 6.1. The colour in Fig. 6.2 indicates the filling factor ϕ. In the following the simulation outcomes are discussed in detail. I adopt the notation by Güttler et al. (2010).

numerical setting

S1 (hit & stick) is not represented in Fig. 6.2 as it is not applicable within the continuous SPH scheme. This category describes the outcome of collisions in which microscopic fractal dust aggregates are involved. In this regime, the continuum limit, which is a fundamental assumption of the model, is not valid. I focus on collisions of macroscopic dust since for the fractal regime the numerical and empirical basis is profound.

S1: hit & stick

S2 (sticking through surface effects) The example is the result of the impact of an aggregate with radius $r_p = 6\,\mathrm{cm}$ with collision velocity $v_0 = 2.0\,\mathrm{m/s}$. The image shows the situation 250 ms after the impact. The filling factor of the outer shell of the aggregates remains nearly unchanged as indicated by the exterior view. In contrast, large parts of the interior are compressed to $\phi \sim 0.45$. The target and the projectile merge into one object. The initial setup matches that used for the B2 case but with higher impact velocity. As a consequence, the contact area is larger and compressed to higher filling factors. This leads to a higher tensile strength in this region, which prevents the objects from rebounding each other. This situation is referred to as sticking through surface effects. A single aggregate remains and no fragments are ejected.

S2: surface effects

S3 (sticking by deep penetration) is found in the simulations if the projectile is sufficiently smaller than the target. In the example case the projectile features $r_p = 2\,\mathrm{cm}$ and hits the target with $v_0 = 10.0\,\mathrm{m/s}$. The image is taken 388 ms after the impact. A small crater is formed on the target and a small number of single SPH particles are ejected. This characterises deep penetration. The crater is visible in the cross section. Material is compressed to a maximum of $\phi \sim 0.52$ down to a depth of about one target radius.

S3: deep penetration

S4 (mass transfer) happens if the projectile is large and moves fast enough to stick but still slow enough to not fully disrupt the target. As an example an impact of a 6 cm aggregate onto a target with the same filling factor is chosen. The impact velocity is $v_0 = 10.0\,\mathrm{m/s}$ and the image shows the result after 50 ms. During the collision the target is highly deformed and compressed to filling factors of $\phi \sim 0.45$ to 0.52. Single SPH particles are ejected. Most of the projectile merges, which accounts for the mass transfer. The final mass of the largest fragment is 3.56 kg.

S4: mass transfer

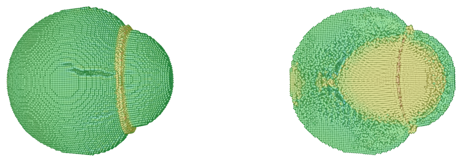

S2 (sticking through surface effects)

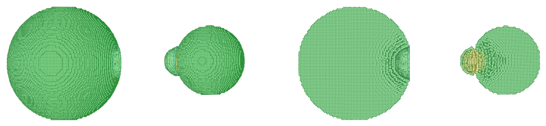

B2 (bouncing with mass transfer)

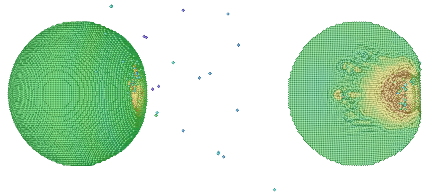

S3 (sticking by penetration)

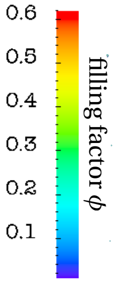

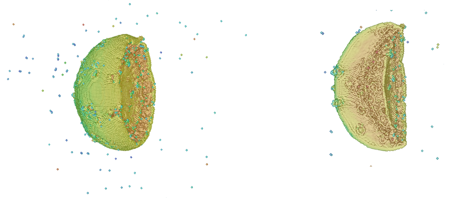

S4 (mass transfer)

F1 (fragmentation)

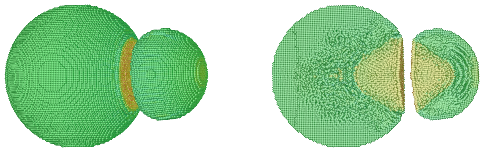

B1 (bouncing with compaction)

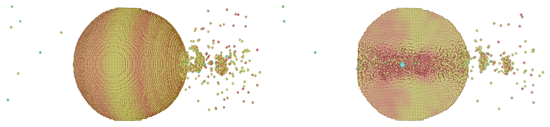

F2 (erosion)

Figure 6.2. *Four-population model II – reproducing sticking, bouncing, and fragmentation types.* The outcome of the simulations of pre-planetesimal collisions encompasses all sticking (S), bouncing (B), and fragmentation (F) types proposed by Güttler et al. (2010). The initial configurations for each simulation are summarised in Tab. 6.1, in particular a sphere with radius $r_t = 10\,\text{cm}$ is chosen as resting target and a sphere with $r_p = 6\,\text{cm}$ as projectile except for S3 and F2, where $r_p = 2\,\text{cm}$. The colour code indicates the filling factor ϕ. Both objects are initially set up with $\phi = 0.35$ except for the F2 case, where $\phi = 0.55$. The simulations are carried out with different impact velocities and the snap shots are taken at different times. The details are given in the text.

B1: compaction

B1 (bouncing with compaction) is only seen with objects of medium and low porosity at low collision speeds. Highly porous objects feature an extremely low compressive strength. As a consequence, low pressures suffice to plastically deform the target and the highly porous aggregates do not gain enough elastic loading for bouncing. In the example, the projectile is 6 cm in radius. It impacts at $v_0 = 1.0\,\mathrm{m/s}$. In Fig. 6.2, the final state at 500 ms is shown. In the collision, both objects are flattened at the impact site and the elastic loading is sufficient to make them rebound after the impact. A part of the interior of the target and projectile is compressed to $\phi \sim 0.45$. Note that this is exactly the same setup as in the S2 case but with a lower impact velocity. The bouncing event is a result of a smaller contact area and a lower tensile strength in this region, which is indicated by the lower filling factor. As a consequence, the two objects rebound. A close investigation reveals that in nearly every simulation with bouncing a small amount of material is transferred between the projectile and target. Thus, it is very unlikely that pure growth neutral bouncing without any mass transfer exists. In this particular simulation $\sim 0.54\,\mathrm{g}$ are transferred from the projectile to the target. Hence, the result could also be classified into the next category.

B2: mass transfer

B2 (bouncing with mass transfer) occurs in simulations where the compressive strength is sufficiently large to allow for elastic loading and consequential bouncing, and where the tensile strength is small enough such that the impactor can rip out a small fraction of mass from the target. This happens at very low impact speeds. The final state at 1.7 s after the collision is a result from a collision with $v_0 = 0.2\,\mathrm{m/s}$. The projectile has $r_\mathrm{p} = 6\,\mathrm{cm}$. During the impact a small region of target and projectile is compressed to $\phi \sim 0.45$. In the consequential rebound this region sticks to the projectile and is ripped out of the target. The remaining crater on the target can be seen in the cross section. In this collision 29.5 g are transferred from the target to the projectile.

F1:fragmentation

F1 (fragmentation) is generally the outcome of collisions with high impact velocities. Highly porous objects effectively dissipate energy by deformation because of their low compressive strength but they are also easy to disrupt because of their low tensile strength. In contrast, objects with low porosity feature high tensile strengths but lack the ability to dissipate large amounts of kinetic energy. The degree of fragmentation is therefore strongly porosity dependent. The example shows the result of a collision between objects, where the projectile features $r_\mathrm{p} = 6\,\mathrm{cm}$. The impact speed is $v_0 = 17.5\,\mathrm{m/s}$. During the collision both the target and the projectile completely shatter and the result of this collision (shown only in exterior view 800 ms after the impact) is a continuous fragment distribution, whose masses range from 285 g down to single SPH particles with 12 mg. The fragments consist of target and projectile material which are combined together. The filling factors of the fragment distribution are $\phi \sim 0.54$, which is close to the maximum filling factor of 0.58 (see Tab. 5.8).

F2 (erosion) is observed particularly for high filling factors and small projectile radii. The initial setup for the example case involves two objects with $\phi = 0.55$. The target and projectile masses are 4.60 kg and 0.037 kg, respectively. The projectile radius is $r_\mathrm{p} = 2\,\mathrm{cm}$ and the impact velocity $v_0 = 20.0\,\mathrm{m/s}$. During the intrusion of the projectile, fragments consisting of a small number of SPH particles are ejected opposite to the impact site. The figure shows the situation 438 ms after the collision, where small fragments and SPH particles are ejected from the crater. In this collision 63.2 g are eroded from the target. The projectile intrudes to the centre of the target and the intrusion channel is clearly visible in the cross section. Because of the high compressive strength elastic deformation also takes place on the target. The figure shows a snap shot of a decompression wave of lower filling factor, which appears as vertical ring on the target.

F3:mass transfer

F3 (fragmentation with mass transfer) contains conceptual difficulties. The first reason for this is that in simulation outcome of category F1 and F2 always some mass is transferred to the tar-

Type	v_0 [m/s]	r_t [cm]	m_t [kg]	r_p [cm]	m_p [kg]	$\phi_{\mathrm{t/p}}$
S2	2.0	10	2.93	6	0.63	0.35
S3	10.0	10	2.93	2	0.023	0.35
S4	10.0	10	2.93	6	0.63	0.35
B1	1.0	10	2.93	6	0.63	0.35
B2	0.2	10	2.93	6	0.63	0.35
F1	17.5	10	2.93	6	0.63	0.35
F2	20.0	10	4.60	2	0.037	0.55

Table 6.1. *Parameters for reproduction of collision types.* Initial parameters of the simulations shown in Fig. 6.2. The quantities are: collision velocity v_0, target radius r_t and mass m_t, projectile radius r_p and mass m_p, and the filling factor of the collision partners $\phi_{\mathrm{t/p}}$.

get. Secondly, the demarcation between sticking with mass transfer (S4) and F3 is unclear and a continuous transition between these categories can be expected. This issue is solved by the new model proposed below. The simulations include category F3 by reproducing the S4 and F1 types. In conclusion, the code is not only capable of quantitatively reproducing sticking, bouncing, and fragmentation in general, as shown in Ch. 5, but can also correctly simulate the sub-types for each macroscopic collision outcome. However, I also experienced difficulties classifying the results of our simulations according to the model by Güttler et al. (2010). This motivates a new approach.

6.1.2. A new model for mapping collision outcome

In this section a new model is introduced to classify the outcome of pre-planetesimal collisions. At first I describe and motivate its structure. Then I show that all sticking, bouncing, and fragmentation events of the previous section are encompassed by the new model.

Motivating a new classification scheme

The model by Güttler et al. (2010) was clearly developed with the respective laboratory setups in mind. In several of these, one of the collision partners was not a dust aggregate but a solid surface or a glass bead, which itself cannot fragment. Therefore, applying this categorisation to pre-planetesimal dust collisions, which here are solely carried out as simulations between dust aggregates, leads to some difficulties.

S-type difficulties

In the simulations, collision outcomes of the S3 (sticking by penetration) are always accompanied by the production of ejected dust. Therefore, it is unclear whether they should be sorted into S3 or rather S4 (mass transfer). On the other hand, S2 (sticking through surface effects) is also a mass transfer but without the production of fragments. It can also be expected that there is a continuous transition from S2 to S3 with increasing impact velocity. The demarcation between the sticking types is also conceptually difficult. The types S1 to S3 are distinguished according to the sticking mechanism, whereas for S4 the criterion is an increase in target mass and the generation of some fragments. In the context of pre-planetesimal growth the exact sticking mechanism is of minor importance. The distinction between growing and disruptive events is simply given by comparing the *largest fragment* before and after the collision.

largest fragment

B-type difficulties

Also applying the bouncing categories to collision data contains some difficulties. Pure bouncing with compaction (B1) events are never seen in the simulations. Analysing the final mass of both collision partners after the impact reveals that some mass is always transferred either from the projectile to the target or vice versa. In the first case growth is taking place and the result should be categorised under S4 with a growing target, but with one remaining fragment instead of a fragment distribution. If mass is transferred to the projectile, then the event belongs to B2 (bouncing with mass transfer). However, since the largest object is losing mass, B2 is also a type of erosion (F2), where instead of a fragment distribution only one big fragment (the enlarged projectile) is present. Since bouncing may be an obstacle to planetesimal growth (see Sec. 2.3.1), the effect of bouncing has to be included into any collision map. But instead of distinguishing between two types of bouncing, I find it sufficient to distinguish between the mass of the *largest* and the *second largest fragment*.

second largest fragment

F-type difficulties

Analysing the numerical results for disruptive events, it is also hard to distinguish between the types F1 (fragmentation) and F3 (fragmentation with mass transfer). As already mentioned above, in any fragmenting collision mass is transferred from the projectile to the target and the fragments consist of both projectile and target material. In eroding events (F2) mass is also transferred to the target and a fragment distribution is produced. Once again the continuous transition between the three fragmentation types and between sticking and fragmentation events cannot adequately be mapped with the given model. In my view it is sufficient to characterise the outcome of disruptive events by the size of the largest fragment (which for F2 is much larger than the other fragments) and a power-law distribution of the remaining fragments. Thus, for correct mapping of any combination of sticking, bouncing, and fragmentation the following objects have to be considered: *largest* and *second largest fragment* and a *power-law fragment distribution.*

power-law population

This discussion shows that the classification of different sticking, bouncing, and fragmentation events is not sufficient. This is because there exist many intermediate events. For example, a bouncing event can involve some sticking and some fragmentation, whereas a sticking event can also involve some fragmentation. The model by Güttler et al. (2010) tries to capture these intermediate events. However, it is based on physical mechanisms rather than collision outcome. Due to this discrete approach, this model generates some unnecessary complexity and cannot easily describe transitions between categories. To improve this, I propose a model which is solely oriented on quantitative aspects. It distinguishes between four types of fragment populations, which are characterised by continuous quantities such as their mass, filling factors, velocities, and size. This enables mapping of all types of sticking, bouncing, and fragmentation events but also modelling continuous transitions between these types.

Fragment populations

input parameters

The fundamental idea of the new classification is that any outcome of a collision can adequately be modelled by distinguishing four kinds of fragment “populations”. This is illustrated in Fig. 6.3. Example input parameters for the collision include the masses of the target (label “t”) m_t and projectile (label “p”) m_p, their filling factors ϕ_t and ϕ_p, their rotational energies $E_\mathrm{rot,t}$ and $E_\mathrm{rot,p}$, their impact parameter b and, most importantly, their collision velocity v_0 (see Fig. 6.3, left). Depending on these parameters, the collision between two bodies produces a well defined outcome of populations. To be able to map sticking, bouncing, and fragmentation events it is suitable to sort this distribution according to the mass of the fragments into the respective population. For these, output parameters such as mass, filling factor, rotational energy, and velocity are determined as

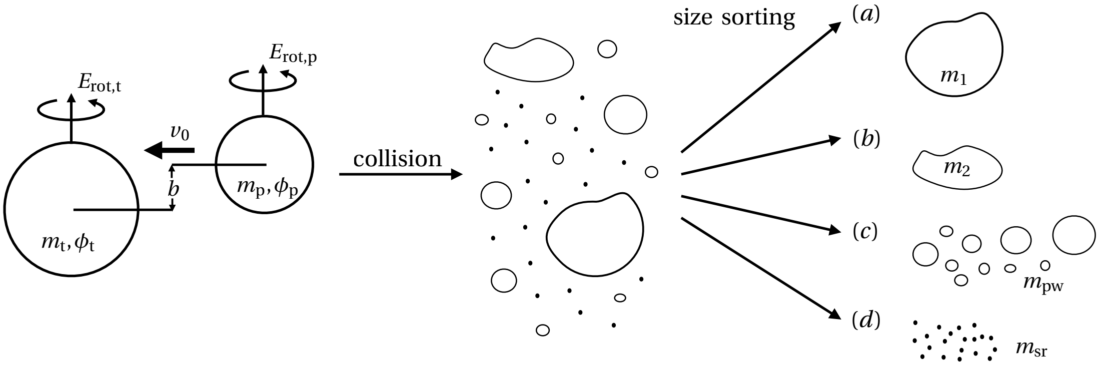

Figure 6.3. *Four-population model III - illustration.* The left side displays the situation before the collision: Two pre-planetesimals collide with impact velocity v_0 and impact parameter b. The target and projectile are characterised by their defining quantities, e.g. mass m, filling factor ϕ, and rotational energy E_{rot}. Depending on these parameters an outcome population is generated in the collision (middle). The four-population model distinguishes the fragments according to their mass. The population classes are: (a) the largest fragment, (b) the second largest fragment, (c) the power-law population, and (d) the sub-resolution population. This categorisation is sufficient to describe the outcome types of Fig. 6.2 as well as intermediate outcomes.

exact or averaged values, or as distributions depending on the population. Specifically, the new scheme consists of the following four types: (1) largest fragment, (2) second largest fragment, (3) power-law population, and (4) sub-resolution population.

largest fragment

(a) Largest fragment: Comparing the mass of the largest fragment before and after a collision distinguishes between positive and negative growth. The characteristic output quantities are supplied.

second largest fragment

(b) Second largest fragment: This enables bouncing events to be mapped. In pure bouncing events the largest and the second largest fragment will be the only members of the fragment population. The quantities describing this fragment are supplied. The second largest fragment only exists if it consists of more than a single SPH particle.

power-law population

(c) Power-law population: Particularly in disruptive collision events, the mass distribution of the fragments can be modelled by a power-law to describe the fragment distribution. Instead of describing each fragment of the power-law population with quantities as done so for the largest and second largest fragment, the number of parameters is significantly reduced by utilising distribution functions.

sub-resolution population

(d) Sub-resolution population: This population is introduced for numerical reasons. Fragments of the sub-resolution population consist only of a single SPH particle. The existence of this population represents the resolution limit of the simulations and therefore gives only an upper limit for the smallest dust fragments, which are produced in a collision. This population is also convenient to control sufficient resolution. The SPH numerical scheme is capable of simulating objects of metre size and more. However, because of limited computational resources, single SPH particles then represent objects of centimetre size and larger. The sub-resolution population keeps track of these objects. It is convenient to describe this population with averaged characteristic

quantities. Note that also in laboratory experiments a sub-resolution population exists when the fragment distribution is determined by high speed cameras.

complexity reduction

With this approach I considerably *reduce the complexity* of the sticking, bouncing, and fragmentation classification from nine types of collision outcomes to four fragment populations. Moreover, the model presented is solely based on continuous quantities characterising the collision outcome and not on physical mechanisms. This allows for modelling of any mixed types of collisions and transitions between growth and disruption with the necessary accuracy.

accuracy increase

Compared to fragmentation data which are mapped to a power-law distribution alone (e.g. Mathis et al. 1977, Davis and Ryan 1990, Blum and Münch 1993, Güttler et al. 2010) the new model is also *more accurate*. In some of the simulations a fragment distribution contains one large fragment and many small ones. The small ones can be accurately modelled with a power-law mass distribution. However, the mass of the largest fragment often does not match the power-law. This is particularly the case for grazing collisions between highly porous aggregates, where the filling factor of the largest remnant significantly differs from those of the other fragments. Since this has a major impact on subsequent collisions, the largest fragment together with its filling factor is treated separately. Furthermore, power-law distributions cannot map bouncing collisions. For these reasons, I separate out the largest *and* second largest fragment from the rest of the fragment distribution.

With the four given fragment populations and their defining properties I present a closed model which is capable of modelling any collision outcome of pre-planetesimals with minimum complexity but with the accuracy necessary to model the dust aggregation in global coagulation models. In the next section it is shown how the model by Güttler et al. (2010) can be represented in the new model.

Mapping sticking, bouncing, and fragmentation to the new model

mapping principle

The key idea behind mapping the sticking, bouncing, and fragmentation sub-types to the four-population model is to describe the collision outcome by the characteristic quantities of each of the four populations. If one of the populations does not exist, its characteristic quantity is simply set to zero. In principle, a number of quantities can be used to determine the population. To illustrate the use of this model, I select the characteristic quantities mass m and filling factor ϕ as examples. Tab. 6.2 demonstrates the successful mapping of the Güttler et al. (2010) types into the quantitative four-population model. The indices “t”, “p”, “1”, “2”, “pw”, and “sr” denote target, projectile, largest, second largest, power-law, and sub-resolution quantities, respectively. For the illustration it is assumed that the mass of the target m_t is greater than or equal to the projectile mass m_p, i.e. $m_\mathrm{t} \geq m_\mathrm{p}$. In contrast to many results presented by Güttler et al. (2010), who cannot always determine the change in the filling factor, I find a filling factor increase in all collisions if the initial filling factor is smaller than the maximum compaction at $\phi_\mathrm{max} = 0.58$ (see Fig. 6.8 for the largest fragment).

S-types

For pure sticking (S1 to S3 types) only one fragment in the final population exists, which is identified as the largest fragment. Consequently, this fragment contains the mass of the total system, i.e. $m_1 = m_\mathrm{t} + m_\mathrm{p}$. Within the four-population approach, the S1 to S3 sub-types can be combined with respect to the mass and filling factor. In general, the filling factor of the target ϕ_t was increased during the impact such that the filling factor of the largest fragment $\phi_1 > \phi_\mathrm{t}$. For sticking with mass transfer (S4) a range of fragments exists. Since sticking is identified with growth of the largest fragment it is $m_1 > m_\mathrm{t}$. If there are only fragments below the resolution limit, then the mass of the second largest fragment m_2 and the mass of the power-law population m_{pw} are vanishing. Otherwise there exists a range of fragments with non-zero masses.

B-types Bouncing is characterised by two fragments in the final fragment distribution. For bouncing with compaction (B1) the masses are unaltered, i.e. $m_1 = m_\mathrm{t}$ and $m_2 = m_\mathrm{p}$, but the filling factors are increased: $\phi_1 > \phi_\mathrm{t}$ and $\phi_2 > \phi_\mathrm{p}$. For the case of bouncing with mass transfer (B2) the filling factors are also increased but the masses are altered such that $m_1 + m_2 = m_\mathrm{t} + m_\mathrm{p}$ and $m_1 \neq m_\mathrm{t}$ as well as $m_2 \neq m_\mathrm{p}$. By definition, no fragments are produced in the bouncing events such that $m_{\mathrm{pw}} = m_{\mathrm{sr}} = 0$. Also for B2 the filling factors are increased, i.e. $\phi_1 > \phi_\mathrm{t}$ and $\phi_2 > \phi_\mathrm{p}$.

F-types The fragmentation events (F1 to F2 types) are characterised by the fact that the mass of the largest fragment is smaller than the largest mass before the collision, i.e. $m_1 < m_\mathrm{t}$. The distinction between F1 and F2 in terms of the collision outcome is not clear. In both cases a power-law as well as a sub-resolution population is generated, i.e. $m_{\mathrm{pw}} > 0$ and $m_{\mathrm{sr}} > 0$. It seems that for F2 the mass of the target is only reduced by a small amount such that $m_1 \lesssim m_\mathrm{t}$ (Güttler et al. 2010). Also in this reference, F3 is characterised by the fact that the target (solid plate) gains mass, i.e. $m_1 > m_\mathrm{t}$. This is inconsistent with the idea that fragmentation is equivalent to $m_1 < m_\mathrm{t}$. The mass of the second largest fragment has some value $m_2 > 0$ and total masses of the power-law and sub-resolution populations are $m_{\mathrm{pw}} > 0$ and $m_{\mathrm{sr}} > 0$.

The transition between sticking and fragmentation can consequently be characterised by the transition $m_1 > m_\mathrm{t} \rightarrow m_1 < m_\mathrm{t}$, since for the S4 type power-law and sub-resolution population are already present. In contrast, the transition from bouncing (which also includes the change of target and projectile masses by mass transfer in B2) can be defined by the appearance of a power-law and sub-resolution population, i.e. $m_{\mathrm{pw}} = 0 \rightarrow m_{\mathrm{pw}} > 0$ and $m_{\mathrm{sr}} = 0 \rightarrow m_{\mathrm{sr}} > 0$, together with a non-growing target $m_1 \leq m_\mathrm{t}$. These and other transitions are discussed in Sec. 6.4 in more detail.

In this section, I have shown that the four-population model for collision outcomes is capable of encompassing all the sticking, bouncing, and fragmentation sub-types. Furthermore, it was demonstrated that also the transition between these types can be modelled continuously by utilising the masses of each of the four populations.

outcome type	m_1	ϕ_1	m_2	ϕ_2	m_{pw}	m_{sr}
hit & stick (S1)	$m_\mathrm{t} + m_\mathrm{p}$	ϕ_1	0	0	0	0
sticking through surface effects (S2)	$m_\mathrm{t} + m_\mathrm{p}$	$\phi_1 > \phi_\mathrm{t}$	0	0	0	0
sticking by penetration (S3)	$m_\mathrm{t} + m_\mathrm{p}$	$\phi_1 > \phi_\mathrm{t}$	0	0	0	0
mass transfer (S4)	$m_1 > m_\mathrm{t}$	$\phi_1 > \phi_\mathrm{t}$	$m_2 < m_\mathrm{p}$	$\phi_2 > \phi_\mathrm{p}$	$m_\mathrm{pw} \geq 0$	$m_\mathrm{sr} > 0$
bouncing with compaction (B1)	$m_1 = m_\mathrm{t}$	$\phi_1 > \phi_\mathrm{t}$	$m_2 = m_\mathrm{p}$	$\phi_2 > \phi_\mathrm{p}$	0	0
bouncing with mass transfer (B2)	$m_1 \neq m_\mathrm{t}$	$\phi_1 > \phi_\mathrm{t}$	$m_2 \neq m_\mathrm{p}$	$\phi_2 > \phi_\mathrm{p}$	0	0
fragmentation (F1)	$m_1 < m_\mathrm{t}$	$\phi_1 > \phi_\mathrm{t}$	$m_2 > 0$	$\phi_2 > \phi_\mathrm{p}$	$m_\mathrm{pw} > 0$	$m_\mathrm{sr} > 0$
erosion (F2)	$m_1 \lesssim m_\mathrm{t}$	$\phi_1 > \phi_\mathrm{t}$	$m_2 \geq 0$	$\phi_2 > \phi_\mathrm{p}$	$m_\mathrm{pw} \geq 0$	$m_\mathrm{sr} > 0$
fragmentation with mass transfer (F3)	$m_1 > m_\mathrm{t}$	$\phi_1 > \phi_\mathrm{t}$	$m_2 > 0$	$\phi_2 > \phi_\mathrm{p}$	$m_\mathrm{pw} > 0$	$m_\mathrm{sr} > 0$
sticking – fragmentation transition	$m_1 > m_\mathrm{t} \rightarrow m_1 < m_\mathrm{t}$	ϕ_1	$m_2 \geq 0$	ϕ_2	$m_\mathrm{pw} \geq 0$	$m_\mathrm{sr} \geq 0$
bouncing – fragmentation transition	$m_1 \leq m_\mathrm{t}$	ϕ_1	$m_2 \geq 0$	ϕ_2	$m_\mathrm{pw} = 0 \rightarrow m_\mathrm{pw} > 0$	$m_\mathrm{sr} = 0 \rightarrow m_\mathrm{sr} > 0$

Table 6.2. *Mapping sticking, bouncing, and fragmentation to the four-population model.* In this table it is illustrated how the collision outcome types in Sec. 6.1.1 can be mapped to the four-population model using the characteristic quantities mass m and filling factor ϕ as examples. The masses of the largest and second largest fragment, the power-law population, and the sub-resolution population are given by m_1, m_2, m_pw, and m_sr, respectively. I assume for the target mass m_t and projectile mass m_p before the collision $m_\mathrm{t} \geq m_\mathrm{p}$. The filling factors are represented by ϕ_t for the target, ϕ_p for the projectile, ϕ_1 for the largest fragment, and ϕ_2 for the second largest fragment. Examples are given for transition criteria between the types in Sec. 6.1.1. A list of symbols can be found in the appendix and further explanations are given in the text.

6.1.3. Applying the new model to simulation data

numerical setting

In this section, the four-population model is applied to a study of collisions of medium porosity pre-planetesimals with different velocities to demonstrate that the outcomes of pre-planetesimal collisions can be described quantitatively using the model. I carry out 24 simulations of head-on collisions involving spherical dust aggregates with target and projectile radii of $r_\mathrm{t} = 10\,\mathrm{cm}$ and $r_\mathrm{p} = 6\,\mathrm{cm}$ modelled using 238,238 and 51,477 SPH particles, respectively. I choose the initial filling factor of the aggregates to be $\phi = 0.35$ resulting in target and projectile masses of 2.93 and 0.63 kg, respectively. The collision velocity is varied between 0.1 and 27.5 m/s. The initial particle distributions are set up by means of the program `initgrid` (Appx. A.3). Table 6.3 summarises the simulations carried out. The program `fragment` (Appx. A.2) is used to evaluate the final particle distribution. I broadly categorise the simulations by eye into *bouncing*, *sticking*, or *fragmentation* so that a comparison can be made between the results of the four-population model and the categorisations used previously. It is important to note that these broad categorisations are only present to show where the boundaries between these regimes lie and are not used for the quantitative approach of my model.

As discussed in Sec. 6.1.2, the outcome of pre-planetesimal collisions can be quantitatively described by a number of parameters such as the final mass, size, energy, velocity, porosity, and rotation and each of these parameters can be used to describe the four populations. In this preliminary study I focus on the final mass, porosity, and energy of the different populations in the four-population model.

population masses

Figure 6.4 shows how the mass distribution amongst the four populations varies with collision velocity. At low collision velocities, the contact energy and thus the tensile strength is too low to hold the objects together. This results in bouncing causing the overall mass distribution being similar to the initial distribution. The collision with 0.2 m/s shows evidence of mass transfer resulting in a largest fragment smaller than the target. As the collision velocity increases, the energy is dissipated by plastic deformation resulting in sticking such that all the mass is stored in a single object. At even higher collision velocities in which fragmentation is seen, the mass stored in the largest fragment is reduced but is increasingly present in the power-law population. Figure 6.4 also shows how the mass of the largest fragment varies with collision velocity. It can be seen that three distinct regions exist, which justify the broad classification of Tab. 6.3. However, there do not appear to be distinctions within these regions which promote the further division into sticking, bouncing, and fragmentation sub-types. A sharp *transition between the bouncing and sticking* regions exists at ∼ 1 m/s. The velocity threshold for the bouncing-sticking transition varies with object porosity and projectile size. This is shown and discussed in more detail in Sec. 6.4. Above 10.5 m/s, pure sticking no longer occurs and the mass of the largest fragment begins to decrease as the transition between sticking and fragmentation takes place. As a result of very high collision velocities the mass contribution of the sub-resolution population dominates over the largest and second largest fragment indicating violent disruption. I note that the simulation with collision velocity 11.5 m/s still results in collision *growth* but above this velocity the mass gain of the largest fragment is negative.

bouncing-sticking transition

sticking-fragmentation transition

Figure 6.4 clearly shows that at velocities $\gtrsim 11.5$ m/s, pure sticking no longer occurs and a transition into the *fragmentation* regime begins. For the simulation with a collision velocity of 11.5 m/s (see Fig. 6.5, top, for an illustration of the resulting fragments), the mass of the largest fragment clearly increases but according to the model by Güttler et al. (2010) it is unclear whether this simulation would be classed as sticking with mass transfer (S4) or fragmentation with mass transfer

Collision Velocity [m/s]	Broad categorisation
0.1	bouncing
0.2	bouncing
1.0	bouncing
1.25	sticking
1.5	sticking
1.75	sticking
2.0	sticking
2.2	sticking
2.5	sticking
4.0	sticking
5.0	sticking
6.0	sticking
7.5	sticking
10.0	sticking
11.5	fragmentation
12.5	fragmentation
15.0	fragmentation
17.5	fragmentation
25.0	fragmentation
27.5	fragmentation

Table 6.3. *Applying the four-population model – collision velocities and categorisation.* The target and projectile are homogeneous and feature an intermediate porosity ($\phi = 0.35$). These simulations have been carried out to show how the proposed model can quantitatively demonstrate the results of pre-planetesimal collisions. Each simulation is assigned a broad categorisation so that the transition regions between the categories can be investigated.

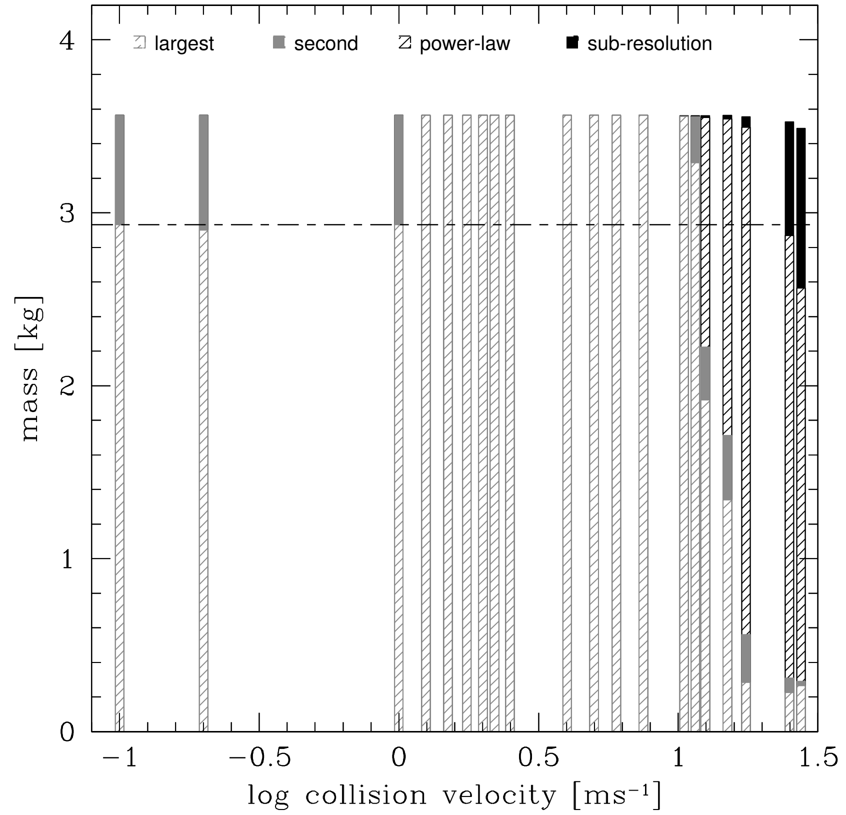

Figure 6.4. *Four-population model IV – population masses.* Cumulative plot of the contributions to the total mass in the system from the largest (grey slashed), second largest (solid grey), power-law (black slashed), and sub-resolution (solid black) populations after the aggregate collisions at various velocities. At low velocities, where bouncing occurs, the mass is wholly within the first and second largest fragments while at intermediate velocities, where sticking occurs, the contribution to the mass is in the largest fragments. At high velocities, the mass contribution from the power-law population becomes significant. To save computing time, particles are removed when they exceed a sphere of 20 m radius around the impact site. The slight drop in mass is visible for the highest collision velocities (figure from Geretshauser et al. 2011).

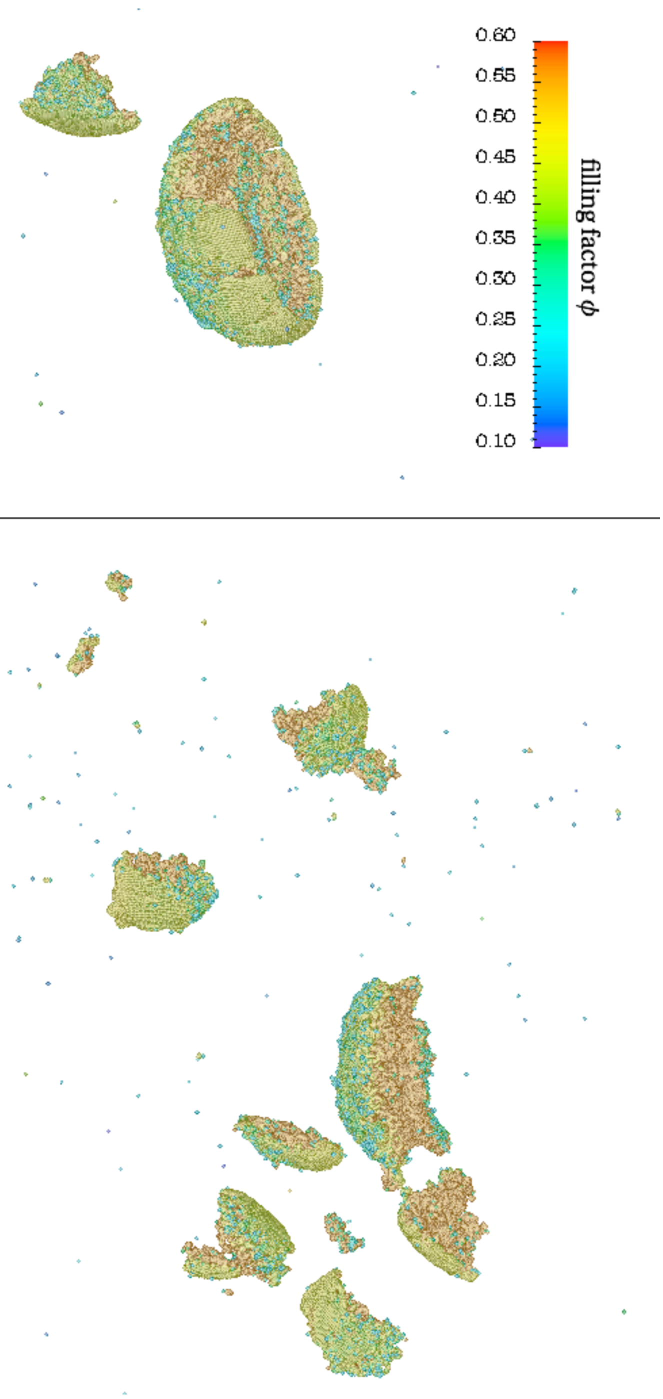

Figure 6.5. *Four-population model V – sticking-fragmentation transition for intermediate porosity.* Outcome of the dust collision simulation with 11.5 m/s (top) and 12.5 m/s (bottom) at a time, t=0.8 s. The collision with 11.5 m/s results in the growth of the target but also a large chunk does break off such that pure sticking does not occur. The situation is adequately mapped with the appearance of a second largest fragment. For 12.5 m/s the target breaks apart and the power-law population becomes as significant as the largest fragment. The transition from sticking to fragmentation occurs in between the presented collision velocities.

(F3). Using our model, such an intermediate region can be described quantitatively. At ~ 12.5 m/s (see Fig. 6.5, bottom, for an illustration), the mass contribution from the power-law population becomes as significant as the contribution from the largest fragment. In this region, the target fragments into a small number of large pieces. I expect that the transition from the sticking to fragmentation regime, described in Sec. 6.1.2, occurs between 11.5 and 12.5 m/s. The sticking-fragmentation threshold depends also on object porosity and projectile size (see Sec. 6.4). In addition there is evidence that for inhomogeneous aggregates the threshold velocity for fragmentation is lowered (Sec. 6.2). Other factors such as impact parameter and rotation might also influence the fragmentation threshold. Further investigation into the factors that determine the fragmentation boundary is crucial to ultimately understand under what conditions fragments may grow to planetesimal sizes. It is important to note that to decrease the computational expense, the SPH particles that move out of a radius of 20 m are removed from the simulation. Therefore, the total mass at the end of the higher velocity simulations is smaller than the initial mass. However, the total mass removed from the simulation is ~ 2% in the highest velocity simulation.

second largest fragment

Figure 6.6 shows how the mass of the *second largest fragment* varies. For low collision velocities it is evident that *bouncing* occurs and the projectile, whose mass is indicated by the dashed line in Fig. 6.6, appears as second largest fragment with unaltered or slightly increased mass in the final distribution. For higher collision velocities the projectile *sticks* to the target and no second largest fragment results, which is indicated by vanishing masses in this regime. As the velocity further increases, the resulting mass of the second largest fragment increases again but is smaller than the projectile mass, which indicates *fragmentation.* The increase is followed by a sharp decrease in the mass of the largest fragment. Such simulations that are reasonably close to the sticking-fragmentation boundary not only cause the two aggregates to fragment, but they also cause mass to be transferred between the target and projectile. At higher velocities still, the impact is sufficiently violent for the second largest fragment to also decrease sufficiently.

power-law population

Figure 6.4 shows that as the collision velocity increases, the contribution to the mass from the *power-law population* also increases. As an outcome of pre-planetesimal collisions, the cumulative mass distribution of the fragments is often described by a power-law

$$m_{\mathrm{cum}}(m_{\mathrm{f}}) = \sum_{m_{\mathrm{f}}<\mu_{\mathrm{pw}}} m_{\mathrm{f}} = \int_0^{m_{\mathrm{f}}} n(m)\, m \,\mathrm{d}m = \left(\frac{m_{\mathrm{f}}}{\mu_{\mathrm{pw}}}\right)^{\kappa}, \tag{6.1}$$

where $n(m)\,\mathrm{d}m$ is the number of fragments within the mass range $[m, m+\mathrm{d}m]$, m_{f} is the fragment mass, and μ_{pw} is the most massive member of the power-law population. The quantities m, m_{f}, and μ_{pw} are normalised by the total mass of the power-law population m_{pw} and κ is the power-law index.

Figure 6.7 shows the cumulative mass distribution $m_{\mathrm{cum}}(m_{\mathrm{f}})$ against the fragment mass normalised by m_{pw}. For higher fragment masses m_{f}, a power-law fit can be obtained which describes the mass distribution of the power-law population. As the velocity increases, the slope of the power-law decreases. This is because at higher collision velocities, the destruction of the dust aggregates is more violent and a larger number of smaller fragments results. At low fragment masses, it is currently unclear whether the deviation from the power-law distribution is physical, or whether it is a result of a low number of SPH particles ($\lesssim 100$) per fragment. Such a deviation is also seen in the experimental results of Güttler et al. (2010).

filling factor

I now consider how much compaction takes place in each of the simulations by considering the

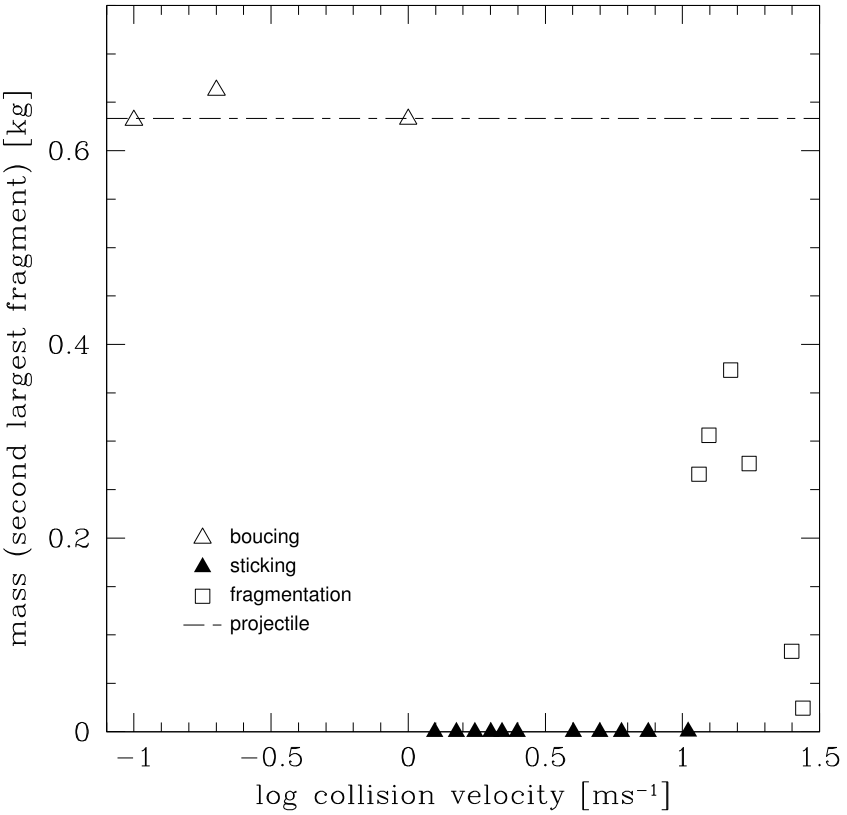

Figure 6.6. *Four-population model VI – mass (second largest fragment).* The broad categorisation into *bouncing* (open triangles), *sticking* (closed triangles), and *fragmentation* (open squares) can be identified by masses of the second largest fragments being approximately the projectile mass (dashed line), nearly vanishing, and smaller than the projectile mass, respectively. For the fragmenting collisions, the mass of the second largest fragment initially increases with collision velocity. However, at higher collision velocities, the fragment mass decreases due to the collision nature of the simulations (figure from Geretshauser et al. 2011).

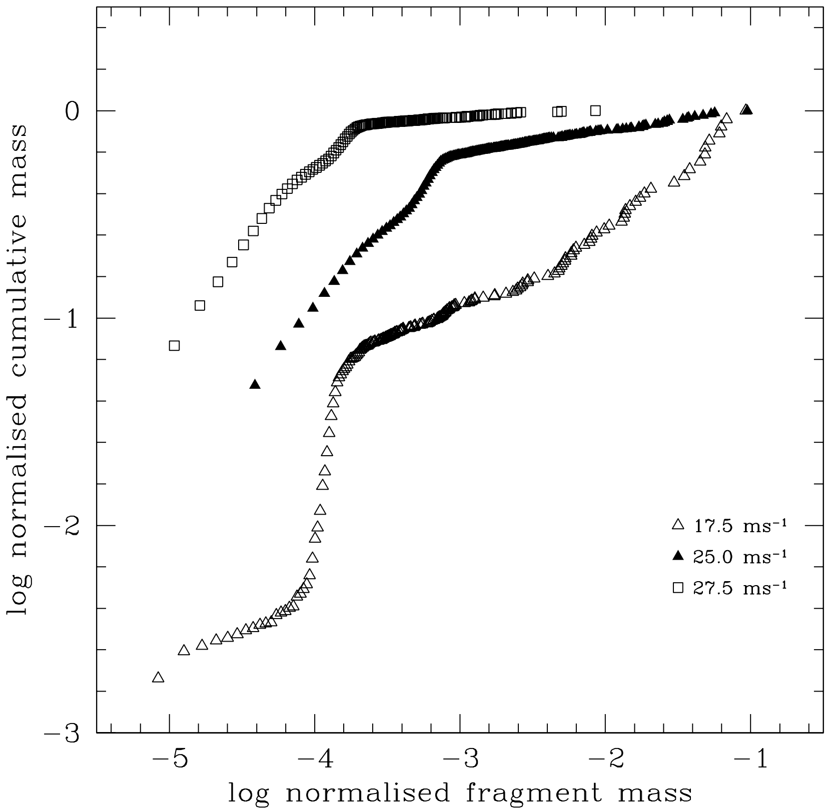

Figure 6.7. *Four-population model VII – mass distribution (power-law population).* Cumulative mass distribution (given by equation 6.1) against fragment mass of the power-law populations resulting from the simulations with 17.5 (open triangles), 25.0 (closed triangles), and 27.5 m/s (open squares). Both axes are normalised by m_{pw}. For high fragment masses, the gradient of the slope decreases with increasing velocity. For low masses, the deviation from the power-law requires further investigation as to whether this is a physical or numerical artefact (figure from Geretshauser et al. 2011).

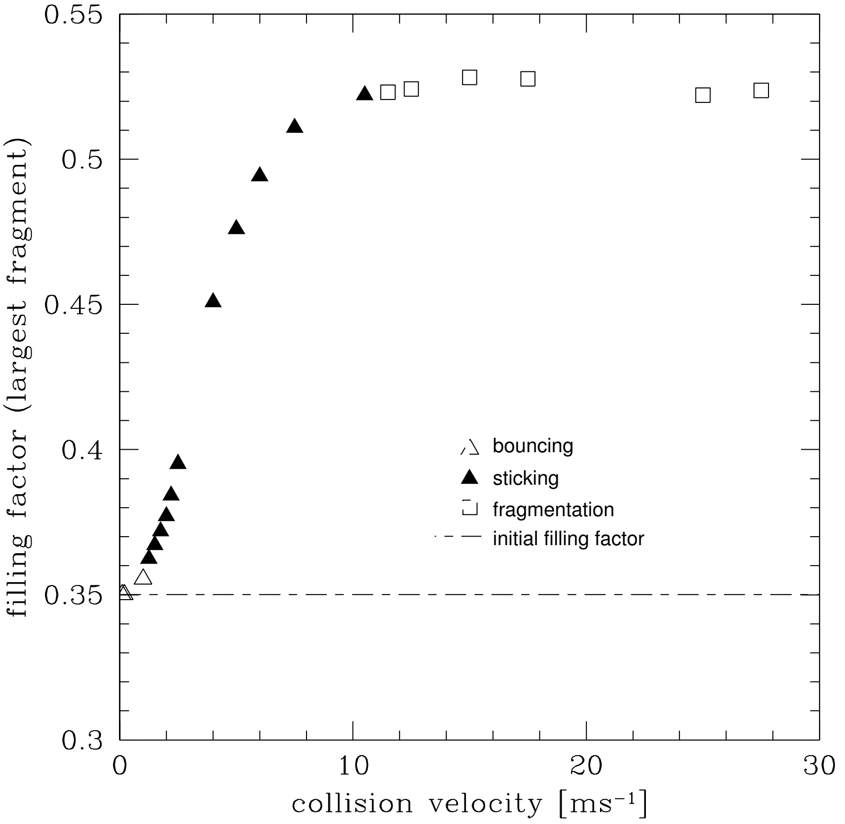

Figure 6.8. *Four-population model VIII – filling factor (largest fragment).* Final average filling factor of the largest fragment in each of the simulations. The simulations have been broadly categorised into bouncing (open triangles), sticking (solid triangles) and fragmentation (open squares). The filling factor varies smoothly as the collision velocity is increased (figure from Geretshauser et al. 2011).

largest fragment resulting *filling factors* of the various populations. Figure 6.8 shows the average filling factor of the *largest fragment*, ϕ_1, compared to the initial filling factor. As the velocity increases the compaction also increases, causing the filling factor to increase with velocity. This forms a smooth curve between the initial filling factor of 0.35 and the maximum filling factor of ~ 0.58 for SiO_2. The curve resembles the Fermi-Dirac shape of the compressive strength relation (Eq. 4.128), which directly links the dynamic pressure to the obtained filling factor. I note that the appearance of fragmenting events coincides with the largest fragment reaching a filling factor close to the maximum filling factor. This suggests that fragmentation sets in when the material is maximally compressed. Furthermore, I stress that the transition of the filling factor is smooth right from the low velocity (bouncing) collisions, through to the medium velocity (sticking) collisions to the high velocity (fragmentation) collisions. For simulations with higher initial filling factors, a transition is expected to occur directly between the bouncing and fragmentation regimes, as discussed in Sec. 6.1.2. Simulation results showing this transition are presented in Sec. 6.4.

The transition is particularly important since for planet formation, one is primarily concerned with the evolution of the largest fragment. This demonstrates that the four-population model can quantitatively capture the results of the collisions over a wide region of velocity parameter space. The preliminary results for the second largest fragment suggest that only a small amount of compaction takes place for the second largest fragment for low velocity *bouncing* simulations such that the final filling factor is very close to the initial filling factor, while for high velocity *fragmentation* simulations, a large amount of compaction takes place resulting in filling factors close to the maximum value of 0.58. Further investigation will be carried out in a future study.

power-law population Figure 6.9 shows the average, maximum and minimum filling factors of the *power-law population*. At higher velocities when more violent fragmentation occurs, the spread in the filling factor is greater than at lower velocities. This suggests that at lower velocities, fragments may be chipped off without too much change to their compaction, whereas in the more violent cases with higher collision velocities, the fragments may get compacted before being chipped off or rupture due to plastic flow occurs where parts of the dust are stretched before they rip off. Figure 6.10 shows the filling factor distribution of the power-law populations resulting from the simulations with 17.5, 25.0, and 27.5 m/s. As the collision velocity increases, the number of fragments increases. In particular, most of the particles have filling factors smaller than the initial value of 0.35. This suggests that during the collision, fragments rip off rather than being compressed before breaking apart.

total energy Finally, the contributions to the total energy (normalised by the initial energies) from the different populations are explored. The total energy is the sum of the energy stored in translation, rotation, and vibration. Figure 6.11 shows that at low velocities the major energy contribution comes from the largest fragment, while at higher velocities the contribution from the power-law population becomes somewhat equally significant (at ~ 12.5 m/s) and is even more significant at even higher velocities. At low velocities the energy is stored in elastic deformation and released into kinetic energy again so that a smaller fraction of the initial energy is dissipated. As the velocity increases plastic deformation occurs causing energy dissipation. At even higher velocities, though energy is still dissipated (since bonds are broken in the fragmentation process), the dissipated energy as a fraction of the initial energy due to bonds being broken is not as large as the energy dissipation due to plastic deformation. For very high impact velocities a considerable amount of energy is stored in the sub-resolution population. Figure 6.12 shows the absolute energy dissipated at each collision velocity as well as the initial energy. The total amount of energy dissipated increases smoothly with increasing velocity, irrespective of the *bouncing*, *sticking* or

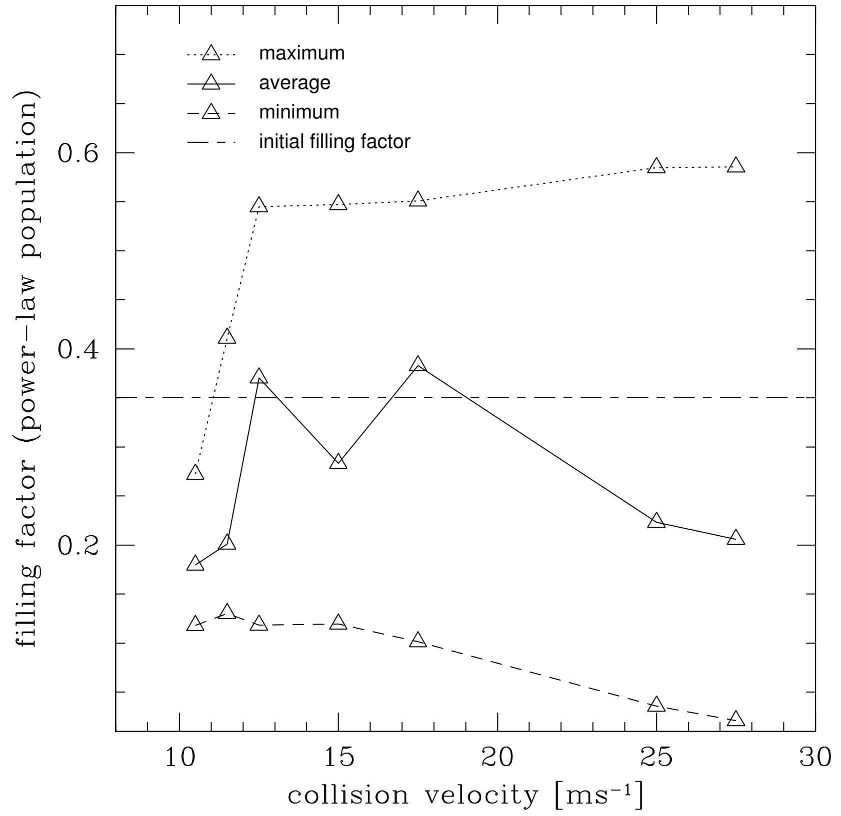

Figure 6.9. *Four-population model IX – average filling factor (power-law population).* Final average filling factor (black line) of the power-law populations in each of the simulations. Also plotted are the maximum (upper grey line) and minimum (lower grey line) filling factors for each simulation as well as the initial filling factor (dashed line). As the collision velocity increases, the range of filling factors for any one simulation increases (figure from Geretshauser et al. 2011).

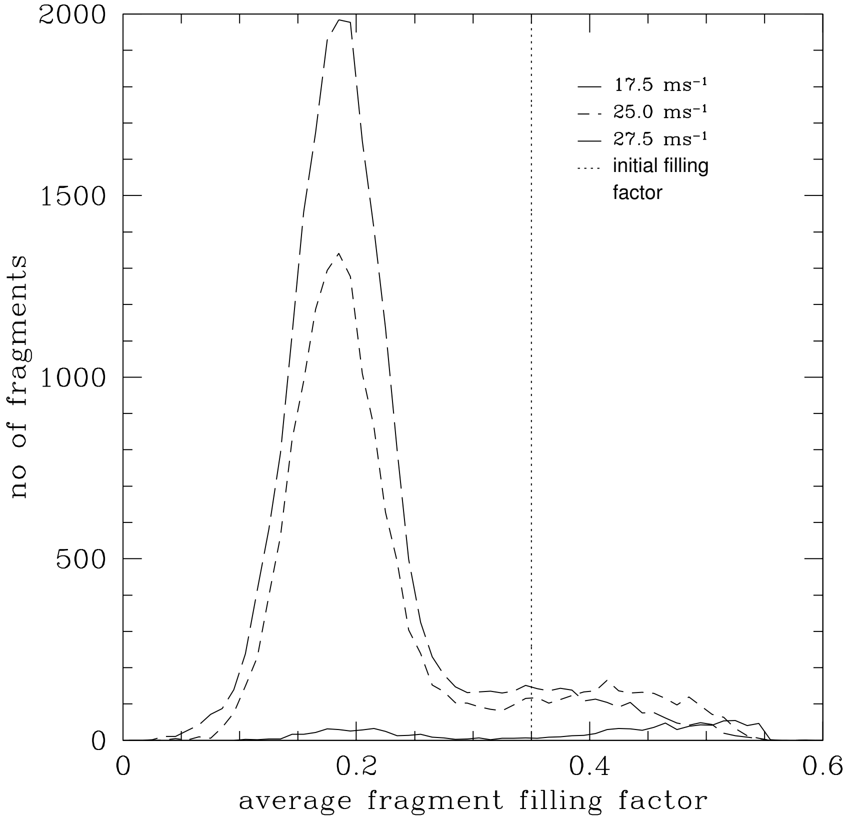

Figure 6.10. *Four-population model X – filling factor distribution (power-law population).* Filling factor distribution for the simulations with 17.5 (solid line), 25.0 (short dashed line) and 27.5 m/s (long dashed line). The size of a filling factor bin is 0.01. As the collision velocity increases, the number of fragments increases. For higher collision velocities, the majority of fragments have lower filling factors than the original value (dotted line) (figure from Geretshauser et al. 2011).

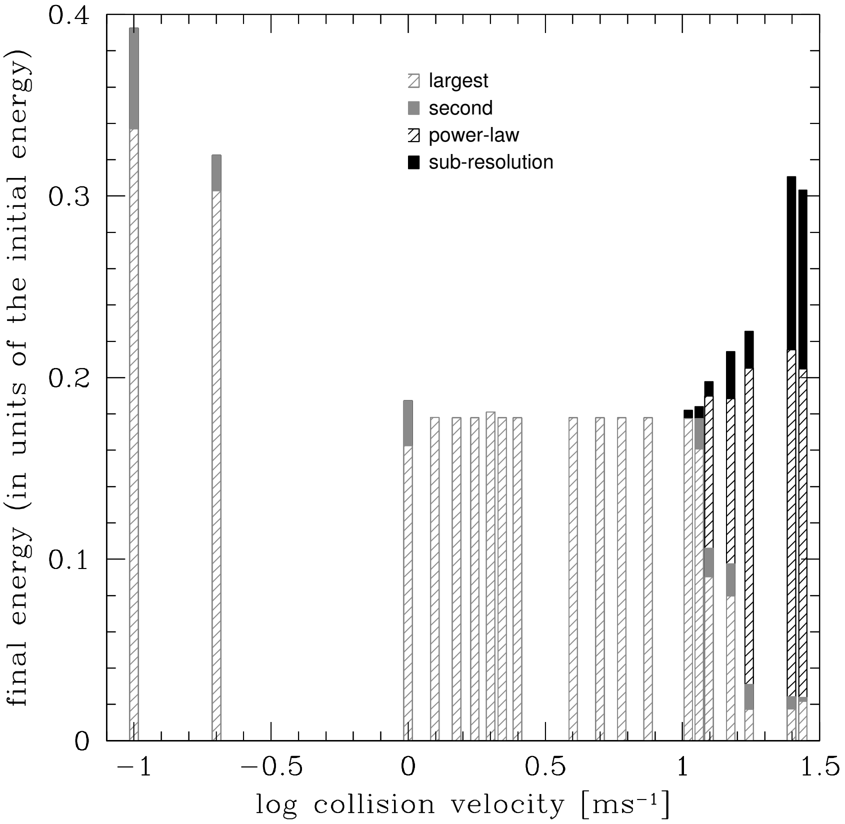

Figure 6.11. *Four-population model XI – total residual energy.* Cumulative plot of the contributions to the total energy in the system from the largest (grey slashed), second largest (solid grey), power-law (black slashed) and sub-resolution (solid black) populations after the aggregate collisions at various velocities. At low velocities, the energy is primarily from the largest fragment whereas at higher collision velocities where more fragments form, the contribution from the power-law population becomes more significant (figure from Geretshauser et al. 2011).

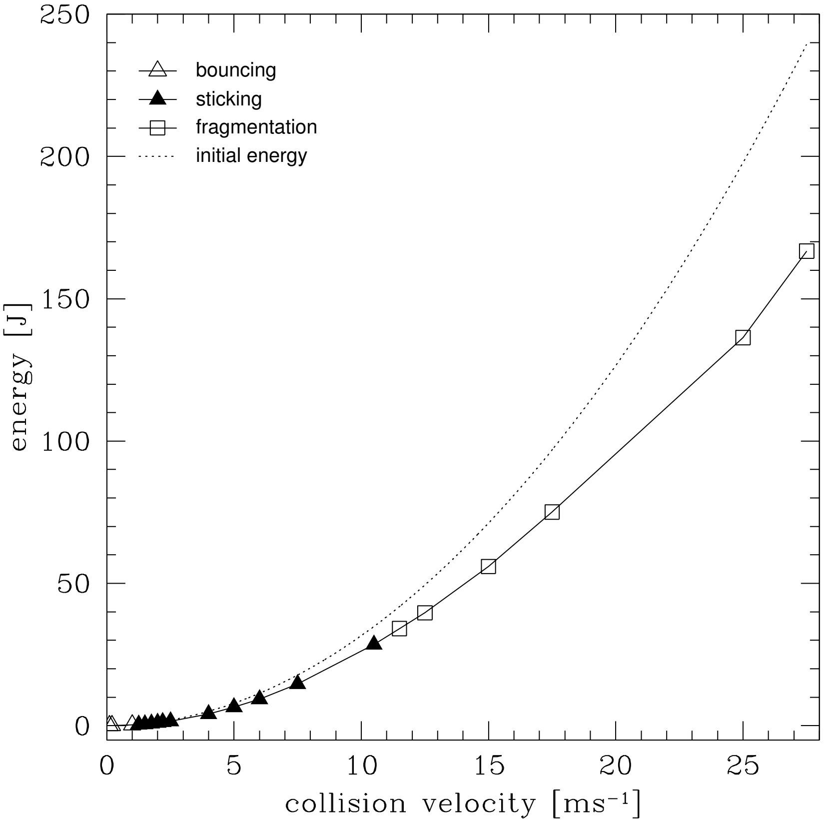

Figure 6.12. *Four-population model XII – dissipated energy.* Initial (dotted line) and dissipated (solid line) energies against the collision velocity. The amount of energy dissipated changes smoothly with collision velocity, regardless of whether the simulations involves bouncing (open triangles), sticking (closed triangles) or fragmentation (open triangles) (figure from Geretshauser et al. 2011).

fragmentation regime. Note that in these examples, the final rotational energies are not very significant since the collisions are head-on. The difference between the rotational and translational energies will become more important in simulations with non-zero impact parameters.

The results presented here are simply a small number of simulations which show that transitions between the *bouncing*, *sticking* and *fragmentation* regions occurs and that the results of pre-planetesimal collisions can be described quantitatively. This can be extended further to explore a vast parameter space of inputs. The four-population model has been shown to not only encompass previous qualitative models (Sec. 6.1.2) but also provides an alternative model that focuses on the quantitative outcome of pre-planetesimal collisions. Furthermore, it can provide an accurate input into global models which may then carry out detailed calculations on the result of pre-planetesimal collisions. In addition, this model provides a powerful aid to determine the region of parameter space that allows growth of pre-planetesimals to occur.

6.1.4. Discussion and Outlook

summary

I have demonstrated that the SPH code, extended and calibrated for the simulation of porous SiO_2 dust, is capable of reproducing all sticking, bouncing, and fragmentation types that appear in collision experiments with macroscopic porous dust aggregates. In addition to the quantitatively correct simulation of laboratory benchmark experiments (see Ch. 5), this consolidates the validity of the applied porosity model and shows its readiness for the application in the field of investigating pre-planetesimal collisions. Since the continuum approach of the SPH method does not place an upper bound on the aggregate size, collision data of a parameter space inaccessible so far in laboratory experiments can now be provided for further use in global coagulation models.

For this transfer, a suitable mapping of collision data has to be chosen, which is accurate enough to quantitatively capture the most important features of any combination of sticking, bouncing, and fragmentation and which is simple enough to be implementable in global coagulation models. I have attempted to map the simulation data to the categorisation by Güttler et al. (2010), which represented the most elaborate collision model available. On the one hand, the distinction between four sticking, two bouncing, and three fragmentation types introduces unnecessary complexity caused by distinguishing between a mixture of qualitative and quantitative attributes and by adhering to the classification into sticking, bouncing, and fragmentation events. On the other hand, I have found collision outcome which could not clearly be attributed to one of the proposed categories.

Because of this ambiguity, I have proposed a new model, which is based on quantitative aspects. For this purpose, I have divided the set of fragments of a collision into four populations: the largest and second largest fragment are described by distinct values for the characteristic quantities of mass, filling factor, and kinetic energy to name only a few. The power-law population is described by distributions and the sub-resolution population by averaged values for the characteristic quantities. The largest fragment indicates growth or erosion, the second largest fragment accounts for bouncing, the power-law population quantitatively describes the amount of fragmentation, and the sub-resolution population gives an upper limit for smaller fragments, which are not captured due to insufficient resolution. Since the SPH code is not restricted to small aggregate sizes, the importance of the sub-resolution population becomes significant for aggregate collisions between objects of approximately metre size and more. Also for growth models which rely on the sweeping up of small particles (Teiser and Wurm 2009a) the sub-resolution population plays an important role. I have demonstrated that this model is in general encompassing the model proposed by Güttler et al. (2010) but is also capable of capturing intermediate events. Finally I have applied the new model to map data for head-on collisions of aggregates with intermediate ($\phi = 0.35$) porosity and varying impact velocity. I have shown that the broad sticking, bouncing, and fragmentation categorisation can still be found in the four-population model. But in addition I also have shown that continuous transitions in the variation of the mass of the largest fragment, the filling factor, and the final kinetic energy of the fragments with collision velocity exhibit a more quantitative description. The ability to capture these transitions justifies the design of the four-population model and demonstrates its descriptive power.

discussion Despite its narrow parameter range, the following conclusions can be drawn from the velocity study presented in Sec. 6.1.3. For the transition between bouncing and sticking a threshold velocity of $\sim 1\,\mathrm{m/s}$ is found and the transition from sticking to fragmentation lies between 11.5 and $12.5\,\mathrm{m/s}$. Since the initial filling factor $\phi = 0.35$ is close to the critical filling factor 0.4, which separates porous from compact aggregates in Güttler et al. (2010), the simulation outcomes cannot be compared directly to their results. For collisions between equally sized highly porous and very compact aggregates they found a direct transition from bouncing to fragmentation at $\sim 1\,\mathrm{m/s}$. However, for collisions between a compact target and a porous projectile of equal size they find a bouncing-sticking transition at $1\,\mathrm{m/s}$ and a transition from sticking to no mass gain at $9.4\,\mathrm{m/s}$. These thresholds resemble my findings for intermediate porosity very well. The simulation results for fragmenting collisions indicate that the power-law index of the fragment mass distribution is velocity dependent. This is supported by the collection of laboratory fragmentation data (Mathis et al. 1977, Davis and Ryan 1990, Blum and Münch 1993, Güttler et al. 2010). Furthermore, it is physically reasonable that in more violent collisions the fraction of smaller fragments increases. This suggests a velocity dependent power-law index.

I note that the results presented in Sec. 6.1.3 are valid for collisions between homogeneous aggregates of intermediate porosity. Increasing inhomogeneity might affect the presented threshold velocities as discussed in Sec. 6.2. Furthermore, rotation of the largest and second largest fragments might cause them to fall apart beyond the simulated time, which eventually affects their final size. The results presented here, in particular for fragmenting collisions, are based on one simulation for each collision velocity. Although I do not expect a large variation in outcome because of the symmetry given by a head-on collision of two spheres, a profound statistical investigation has to be carried out. As a further issue, it has to be investigated whether the deviation of the power-law mass distribution for low fragment masses is a numerical or physical effect. Despite these drawbacks, it has been possible possible to demonstrate the applicability and functionality of the four-population model by means of the simulation results.

outlook Despite increased experimental efforts only small spots of the required parameter space of pre-planetesimal collisions are actually covered by empirical data. In fact, vast regions of these maps are *terra incognita* and collision data for pre-planetesimal sizes larger than centimetre are missing.

With a code calibrated for the simulation of pre-planetesimals (see Ch. 5) and the four-population model as an adequate mapping model, I have established a basis to profoundly investigate all aspects of pre-planetesimal collisions and transferring acquired data to global dust coagulation models. In future works these tools can be utilised to generate a catalogue of pre-planetesimal collisions. Below, the four-population model is applied to investigate the collision behaviour depending on important parameters such as aggregate inhomogeneity (Sec. 6.2) as well as aggregate porosity, mass ratio of the collision partners, and impact velocity. The latter three parameters are considered in the head-on collision study presented in Sec. 6.4. In future work, impact parameter and rotation will be considered. Furthermore, I will assess the statistics of the fragmentation results.

6.2. Inhomogeneity damage model

In this section, simulations are carried out using the inhomogeneity damage model approach presented in Sec. 4.3.5. Inhomogeneity is important for many aspects of investigating pre-planetesimal collisions. (1) Since pre-planetesimals are formed by subsequent collisions with different impact velocities, this collisional history creates an inhomogeneous aggregate. Any realistic simulation of pre-planetesimal collisions must include this effect. (2) It is very likely that inhomogeneity varies with the size of objects of comparable filling factor. Thus including this aspect introduces a length scale into the numerical porosity model. So far, the compressive, tensile, and shear strengths of the latter are scaling with the dimensionless parameter ϕ. For this reason, the fragment distribution resulting from a collision with the same impact velocity scales with the size of the collision partners. The use of a damage model with an inhomogeneity scaling law could tackle this problem. (3) Randomly assigning an inhomogeneity with constant standard deviation to bodies of equal size makes it possible to profoundly investigate statistical fluctuations of fragment distributions. So far, a collision of homogeneous objects with the same input parameters results in the same fragment distribution.

The outline is as follows: in Sec. 6.2.1 I discuss the implementation of the inhomogeneity damage model. Subsequently, I present the results of a series of simulations with varying inhomogeneity and two different impact velocities in Sec. 6.2.2. The velocities are chosen such that the lower lies below and the higher lies above the fragmentation threshold for homogeneous medium porosity ($\phi = 0.35$) aggregates. The simulation outcome is analysed by means of the four-population model presented in Sec. 6.1. To conclude, I summarise the findings, discuss the relevance of inhomogeneity, and give an outlook on future work in Sec. 6.2.3

6.2.1. Implementation issues

generating inhomogeneity

The inhomogeneity is imposed on the simulated aggregate as an *initial condition*. At first, a homogeneous aggregate is generated by assigning an initial filling factor ϕ_i. As a second step, ϕ_i is modified according to a Gaussian distribution with standard deviation ϕ_σ. For this purpose, a particle a is picked randomly and its density is set to a new $\tilde{\phi}_\mathrm{i}{}^a$ following the Gaussian (Eq. 4.157). The same $\tilde{\phi}_\mathrm{i}{}^a$ is assigned to all interaction partners. The mass of all individual SPH particles takes a constant value in the simulation. This value is computed to be consistent with the initial homogeneous aggregate (here $\phi_\mathrm{i} = 0.35$). Therefore, the modification of the density introduces a slight *inconsistency* into the SPH particle distribution. However, as the density is determined by solving the continuity equation and not by the usual approach evaluating the number density of the particles, this inconsistency should be marginal. Moreover, the time evolution of a resting inhomogeneous dust aggregate has been simulated and no spurious particle motion has been detected. In addition, the aggregate *has not shown signs of instabilities* within simulation times much larger than the collision time scale. Consequently, the presented approach produces stable aggregates. Evaluating the generated SPH particle distribution using the particle distribution evaluation tool `sph3deval` (Appx. A.1) yields the resulting filling factor distribution: the num-

inconsistency and stability

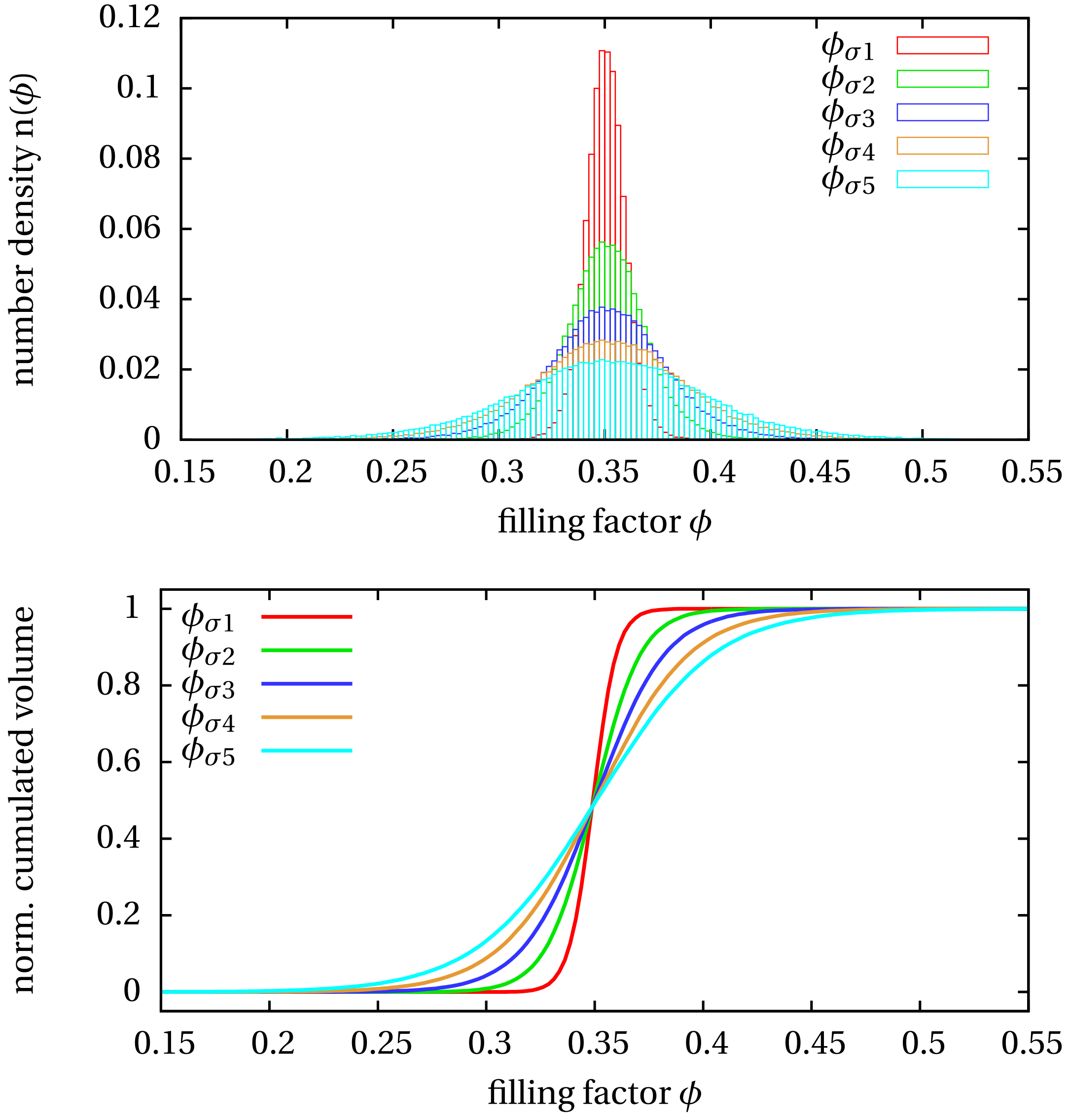

Figure 6.13. *Inhomogeneity model I – initial filling factor distributions.* Initial filling factor distributions of the target and projectile as binned (top) and cumulative (bottom) diagrams. For the binned distribution the number density $n(\phi)$ of volumes with filling factor ϕ, is plotted against ϕ. In the cumulated diagram the cumulated volume with filling factor ϕ is displayed against ϕ. A larger degree of inhomogeneity is characterised by the increasing standard deviation ϕ_σ of the Gaussian (Eq. 4.157) around the initial filling factor ϕ_i of the homogeneous aggregate (here $\phi_\mathrm{i} = 0.35$).

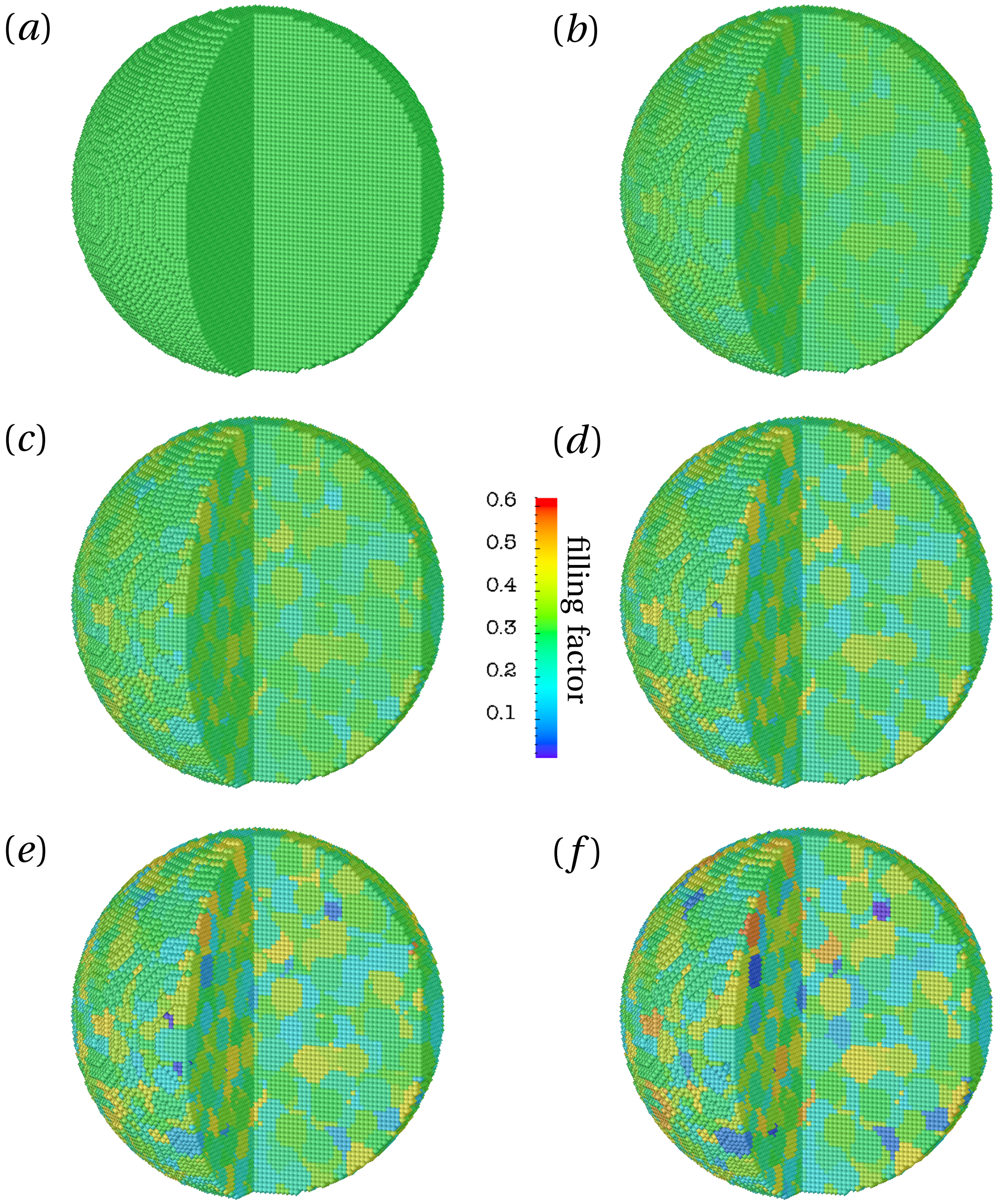

Figure 6.14. *Inhomogeneity model II – inhomogeneous aggregates.* Interior and exterior view of the targets for different inhomogeneities with the filling factor colour coded. The inhomogeneity increases from the homogeneous target (a) to the most inhomogeneous target (f). In particular, the standard deviations are $\phi_\sigma = 0$ (a), $\phi_\sigma = 0.01$ (b), $\phi_\sigma = 0.02$ (c), $\phi_\sigma = 0.03$ (d), $\phi_\sigma = 0.04$ (e), and $\phi_\sigma = 0.05$ (f). All targets have a similar brindle pattern which originates from considering interacting particle passages in the implementation. With increasing ϕ_σ the maximum and minimum filling factor of the different spots increase and decrease, respectively. The projectiles have a similar appearance. The result of collisions among these aggregates with $10\,\mathrm{m/s}$ are depicted in Fig. 6.15.

Symbol	algorithmic value	FWHM value
$\phi_{\sigma 1}$	0.010	0.0085
$\phi_{\sigma 2}$	0.020	0.018
$\phi_{\sigma 3}$	0.030	0.027
$\phi_{\sigma 4}$	0.040	0.034
$\phi_{\sigma 5}$	0.050	0.042

Table 6.4. *Inhomogeneity standard deviations.* Selection of the standard deviations ϕ_σ as they are used in the inhomogeneity algorithm. They are compared with the achieved value deduced from the FWHM of the resulting filling factor distribution in Fig. 6.13.

ber density $n(\phi)$ of the volume fraction with filling factor ϕ is shown in Fig. 6.13 as binned and cumulative plots for various ϕ_σ.

particle packages For a Gaussian distribution of the density of single SPH particles only, i.e. not considering their interaction partners as well, no macroscopic deviation from the initial filling factor ϕ_i is visible after evaluating the particle distribution with `sph3deval` (Appx. A.1). This is because in the evaluation process the contribution from a number of SPH particles is taken into account for computing the density of a physical volume element. However, for Gaussian distributed particle densities this yields ϕ_i. For this reason, a macroscopic density deviation is generated by considering *interacting particle packages.*

These packages with different filling factors are clearly visible in Fig. 6.14, where the density structure of the target is colour coded for different ϕ_σ. The packages are picked randomly but the random pattern is the same for all aggregates to ensure that the results are comparable. Due to the increasing ϕ_σ, the regions with $\phi \neq \phi_\mathrm{i}$ gain higher maximum and lower minimum filling factors. Consequently, the inhomogeneity patterns for $\phi_{\sigma 1}$ and $\phi_{\sigma 2}$ (see Tab. 6.4) are barely visible in Fig. 6.14 (aggregates b and c). In contrast, for $\phi_{\sigma 5}$ the difference between the extreme values of the filling factor create a clearly visible pattern with high contrast.

The standard deviation of the Gaussian filling factor curve ϕ_σ is supplied to the distribution routine as an input parameter. However, because interacting particle packages are considered the real standard deviation computed from the full width at half maximum (FWHM) is smaller than the desired ϕ_σ (algorithmic value). The FWHM values are listed in Tab. 6.4. For the sake of simplicity, I use the algorithmic value in the further course of the analysis.

The algorithm for generating inhomogeneous dust aggregates is implemented in the program `initgrid` (Appx. A.3), which is utilised to set up the initial particle distributions in this chapter.

6.2.2. Simulation results

numerical setting In this section, I perform test simulations with the inhomogeneity damage model. The initial setup consists of two colliding spheres with $\phi_\mathrm{i} = 0.35$. The radii of the target and projectile are $r_\mathrm{t} = 10\,\mathrm{cm}$ and $r_\mathrm{p} = 6\,\mathrm{cm}$, and they consist of 238,238 and 51,477 SPH particles, respectively. I consider two impact velocities $v_0 = 10\,\mathrm{m/s}$ and $v_0 = 12.5\,\mathrm{m/s}$. For homogeneous aggregates, the lower velocity leads to sticking of the projectile to the target (see Fig. 6.15, a). In contrast, the higher velocity results in fragmentation (see also Sec. 6.1.3, in particular Fig. 6.5). For these two collision velocities, the inhomogeneity of both the target and the projectile is defined by the standard deviation of the Gaussian ϕ_σ, which is varied from 0 to 0.05 yielding the distributions depicted in Fig. 6.13. The resulting targets are shown in Fig. 6.14. The projectiles show a similar density pattern. After the collision the resulting SPH particle distribution is evaluated by means of the program `fragment` (Appx. A.2)

For $v_0 = 10\,\mathrm{m/s}$ the final fragment distribution is shown in Fig. 6.15 from the impact direction. For homogeneous aggregates (a) and the small standard deviation ($\phi_\sigma = 0.01$, b) the target remains intact and the target and projectile form one big aggregate. For $\phi_\sigma = 0.01$ some small fragments are visible. For $\phi_\sigma \geq 0.02$ the target fragments and with greater inhomogeneity the largest fragments of the distribution decrease in size.

The first impression from the visual control of the collision outcome is confirmed by the more detailed analysis. For this purpose, I utilise the four-population model presented in Sec. 6.1, which divides the fragment distribution into four fragment populations: the largest and second largest fragment, a power-law population, and a sub-resolution population. The latter represents the limit of our resolution and consists of single SPH particles only, whose masses for the given setup are $1.23 \times 10^{-5}\,\mathrm{kg}$ each.

population masses

The variation of the *masses of each population* with ϕ_σ is shown in Fig. 6.16 as a fraction of the total mass. The upper and the lower plot display the results for $v_0 = 10\,\mathrm{m/s}$ and $v_0 = 12.5\,\mathrm{m/s}$, respectively. The exact values can be found in Tab. 6.6. For the lower collision velocity (Fig. 6.16) and $\phi_\sigma \leq 0.01$ nearly all mass is stored in the largest fragment m_1. For $\phi_\sigma > 0.1$ a second largest fragment and a power-law population appears. With increasing inhomogeneity m_1 rapidly decreases, while the mass of the second largest fragment m_2 only slightly decreases. The masses m_1 and m_2 become comparable in the end. For high inhomogeneity values most of the mass is stored in the power-law population m_{pw}, which will be discussed further below. However, for high inhomogeneities m_{pw} seems to remain fairly constant while the mass of the sub-resolution population m_{sr} increases. For the higher collision value (bottom plot of Fig. 6.16) the evolution is similar but already starting of with $m_{\mathrm{pw}} \neq 0$. The value of m_1 constantly decreases, but not as rapidly as for the low velocity case. The quantity m_2 at first increases, then slightly decreases until the largest and second largest fragments become comparable. The mass of the power-law population rapidly increases for $0.01 \leq \phi_\sigma \leq 0.04$. For larger ϕ_σ the power-law population only slightly increases, whereas m_{sr} increases at a faster rate. The mass evolution with increasing inhomogeneity can be summarised as follows: (1) inhomogeneity leads to fragmentation at collision velocities where homogeneous aggregates do not fragment. (2) For the two investigated velocities, larger ϕ_σ leads to a decrease in mass of the largest and second largest fragments in mass. (3) The masses of the power-law and dust populations are increased with a higher degree of inhomogeneity.

total energy

I turn to the analysis of the distribution of the *residual total energy* after the collision, which is shown in Fig. 6.17 as a fraction of the initial kinetic energy. The residual total energy is the sum of translational energy and the energy stored in the internal degrees of freedom (e.g. rotation, vibration) of the respective populations. The tabulated values can be found in Tab. 6.6. In Fig. 6.17 the low velocity case with $v_0 = 10\,\mathrm{m/s}$ is shown in the upper plot and the high velocity case with $v_0 = 12.5\,\mathrm{m/s}$ in the lower plot. For the former, a large amount E_1 is stored in the largest fragment, but also a considerable amount E_{sr} is stored in the sub-resolution population. While E_1 decreases, the contribution of the second largest fragment at first increases, then decreases slightly with larger ϕ_σ. As for the mass, the energy contribution of the power-law population E_{pw} increases with a higher degree of inhomogeneity. Remarkably, the total energy fraction of these three populations almost remains constant. In contrast, the energy contribution of the sub-resolution population E_{sr} increases more strongly than its mass contribution in Fig. 6.16.

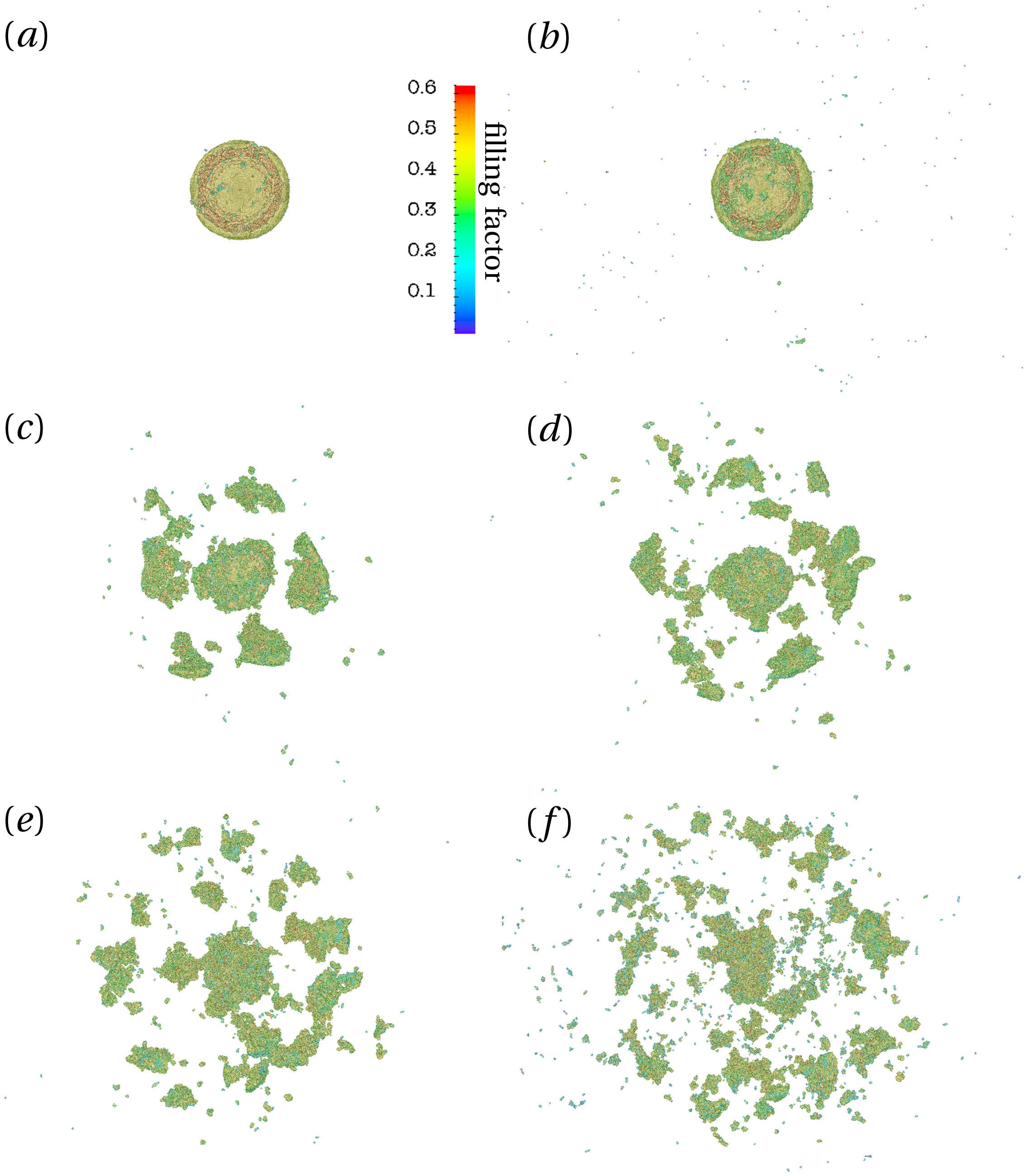

Figure 6.15. *Inhomogeneity model III – collision outcomes.* Outcome of a collision between a target and projectile with the same ϕ_σ for different inhomogeneities. In all cases, the target and projectile radii were $r_t = 10\,\mathrm{cm}$ and $r_p = 6\,\mathrm{cm}$, respectively, and the collision velocity was $v_0 = 10\,\mathrm{m/s}$. Analogous to the initial targets in Fig. 6.14, the standard deviations for the Gaussian were $\phi_\sigma = 0$ (a), $\phi_\sigma = 0.01$ (b), $\phi_\sigma = 0.02$ (c), $\phi_\sigma = 0.03$ (d), $\phi_\sigma = 0.04$ (e), and $\phi_\sigma = 0.05$ (f). The collision outcome is shown in the impact direction. In the homogeneous case (a) and for small inhomogeneities (b) the target stays intact and forms one massive object with the projectile. For $\phi_\sigma \geq 0.02$ the target fragments (c-f). The fragment sizes decrease with increasing ϕ_σ and at the same time the number of fragments increases.

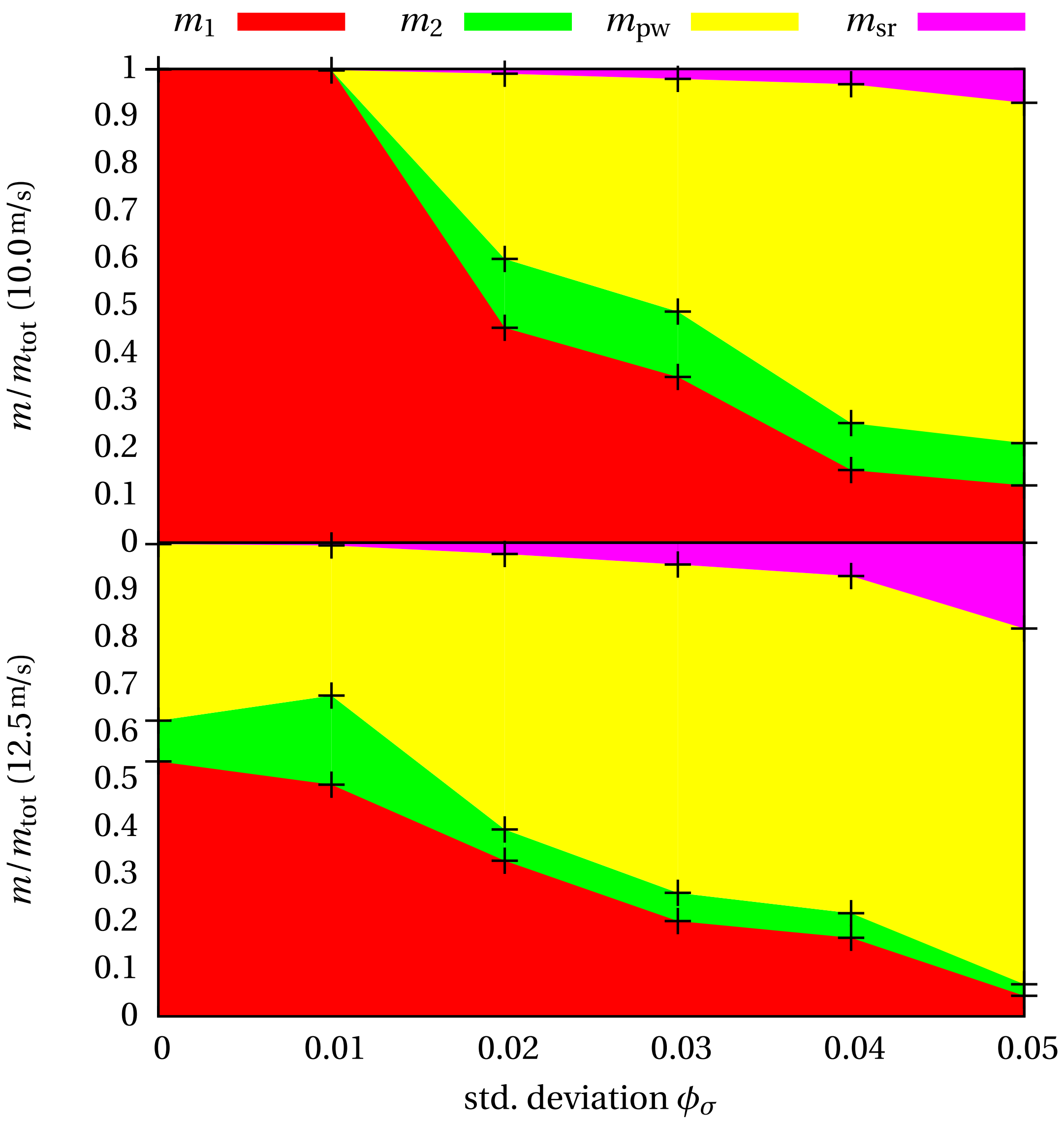

Figure 6.16. *Inhomogeneity model IV – population masses.* Variation of the total masses of the four populations with inhomogeneities measured by ϕ_σ. The collision velocities are $v_0 = 10\,\mathrm{m/s}$ (top) and $v_0 = 12.5\,\mathrm{m/s}$ (bottom). The masses of the largest fragment m_1, of the second largest fragment m_2, of the power-law population m_{pw}, and of the sub-resolution population m_{sr} are stacked up and normalised by the total mass of the system m_{tot}. For both cases m_1 and m_2 decrease with increasing ϕ_σ. Conversely, m_{pw} and m_{sr} increase. For the homogeneous case ($\phi_\sigma = 0$), sticking is found for the low velocity collision, whereas for $v_0 = 12.5\,\mathrm{m/s}$ $m_2 \neq 0$ and $m_{pw} \neq 0$, which indicates fragmentation.

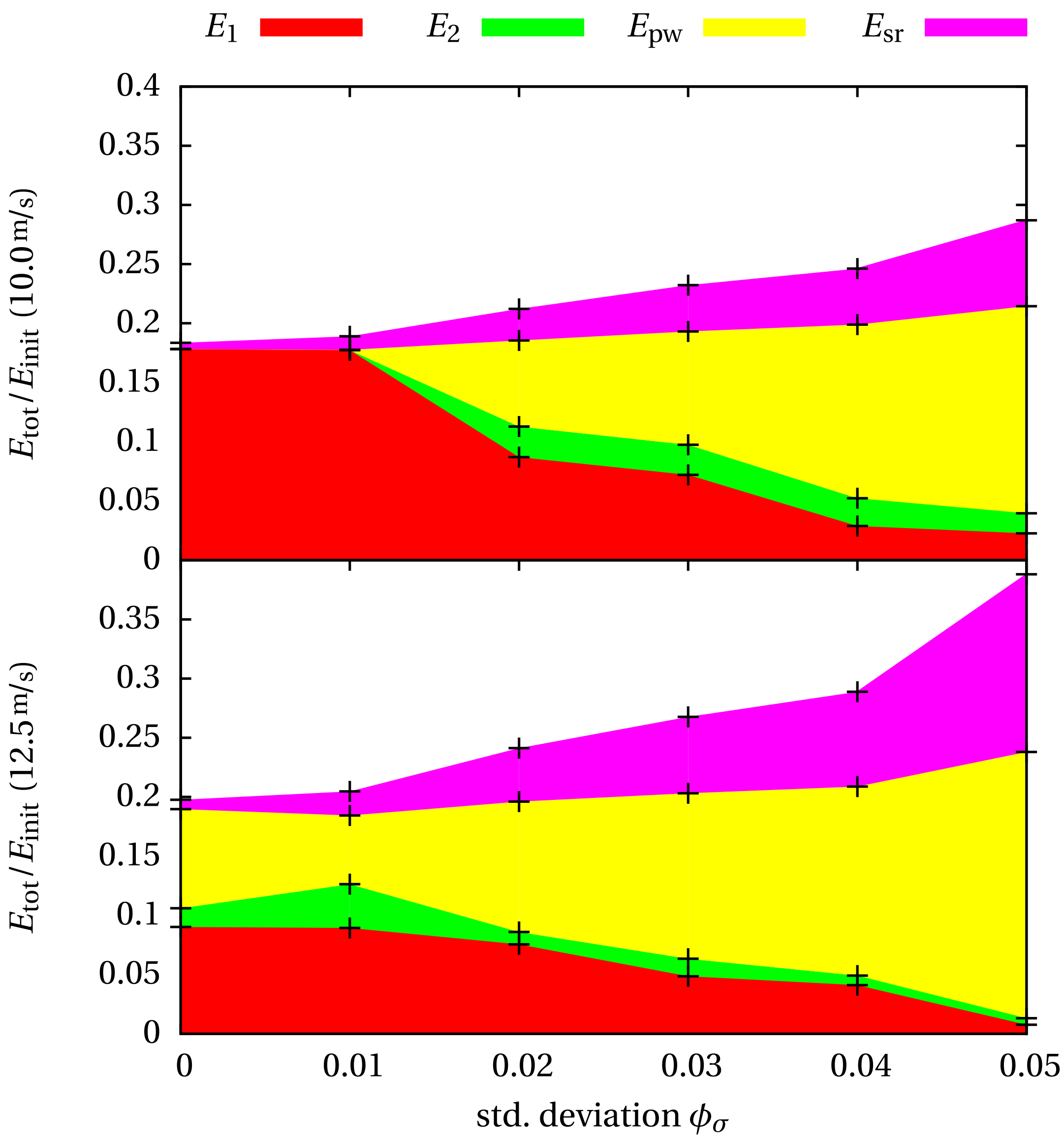

Figure 6.17. *Inhomogeneity model V – residual energy.* Variation of the energy of each population for increasing inhomogeneity parameter ϕ_σ and collision velocity $v_0 = 10\,\mathrm{m/s}$ (top) and $v_0 = 12.5\,\mathrm{m/s}$ (bottom). The energy of each population is the sum of the translational, rotational and vibrational energy and normalised by the initial kinetic energy E_{init} . The latter two energy contributions are negligible for the head-on collisions presented here. Because of the strong correlation with mass, this diagram shows a similar behaviour as Fig. 6.16. The energy contributions are split up into E_1, E_2, E_{pw}, and E_{sr} for the largest and second largest fragments, the power-law and sub-resolution populations, respectively. In both velocity cases E_1 and E_2 decrease with increasing ϕ_σ. In contrast, E_{pw} and E_{sr} increase. In particular the high fraction of kinetic energy stored in the sub-resolution population is remarkable.

The overall residual energy is increasing with a higher degree of inhomogeneity and this energy excess is mostly stored in the sub-resolution population. For the high velocity case (bottom plot of Fig. 6.17) this is even more evident: E_1, E_2, and $E_{\rm pw}$ behave similar to the low velocity case but with $E_2 \neq 0$ and $E_{\rm pw} \neq 0$ for $\phi_\sigma = 0$. Again, with a higher degree of inhomogeneity less energy can be dissipated and the total residual energy of the three largest populations remains nearly constant for increasing ϕ_σ. As a consequence, the residual energy excess is mainly stored in the sub-resolution population for large values of ϕ_σ. The conclusions from the energy analysis are: (1) with increasing impact velocity less energy can be dissipated by the system and the residual energy increases, which was already found in Sec. 6.1.3. (2) With increasing inhomogeneity the ability of energy dissipation decreases for the two investigated velocities. (3) The energy contributions of all populations show a similar dependence on ϕ_σ compared to their mass contributions: the fractions stored in the largest and second largest fragment show a decreasing trend. The contribution of power-law and sub-resolution populations increase. (4) While the overall energy contribution of the largest fragment populations remains nearly constant with ϕ_σ, the fraction stored in the sub-resolution population drastically increases, such that the energy which cannot be dissipated due to increasing inhomogeneity is stored in fast single SPH particles.

filling factor distribution

In comparison to the initial filling factor distribution of Fig. 6.13, the *final filling factor distribution* reveals that the largest mass fraction is compressed to filling factors close to $\phi_{\rm max} = 0.58$ (see Tab. 5.8). Additionally, in Fig. 6.18 I analyse the number distribution of fragments with average filling factor ϕ as a function of ϕ for $v_0 = 10\,{\rm m/s}$ (top) and $v_0 = 12.5\,{\rm m/s}$ (bottom). In the homogeneous cases ($\phi_\sigma = 0$) a slightly bimodal distribution exists for both cases, which is barely visible because of the small fragment numbers. There are a number of fragments which feature the initial filling factor $\phi_{\rm i} = 0.35$. A slightly larger number of fragments possesses filling factors which are distributed around $\phi \sim 0.2$, the rest are distributed around $\phi \sim 0.4$. For a higher degree of inhomogeneity this bimodal distribution is peaked and shifted towards lower filling factors. For both velocity cases the distributions look similar.

power-law population

So far all members of the four-population model have been considered. Now I constrain the analysis to the *power-law population*. Its mass distribution is shown in the cumulative plot of Fig. 6.19 again for $v_0 = 10\,{\rm m/s}$ (top) and $v_0 = 12.5\,{\rm m/s}$ (bottom). The figure shows the cumulated mass $m_{\rm cum}$ over fragment mass $m_{\rm f}$. Both are normalised by the total mass of the power-law population $m_{\rm pw}$, which can be found in Tab. 6.6. As in Sec. 6.1.3, the cumulative distribution is described by a power-law (Eq. 6.1). The cumulative mass distributions of Fig. 6.19 are fitted by this relation. The results are listed in Tab. 6.5. Figure 6.20 shows that the power-law index, or fragmentation parameter, κ slightly decreases with a higher degree of inhomogeneity for both collision velocities indicating shallower slopes in Fig. 6.19. This can be interpreted as the production of smaller fragments with increasing ϕ_σ. Additionally, the κ values for the higher impact velocity ($v_0 = 12.5\,{\rm m/s}$) are systematically below the κ values of the lower velocity ($v_0 = 10.0\,{\rm m/s}$) except for small values of ϕ_σ where a low number of fragments result (see Tab. 6.6) and hence the statistics are insufficient. This finding indicates that a larger fraction of less massive fragments is produced at higher impact velocities, which is expected.

As shown in Fig. 6.21, the normalised mass of the largest member of the power-law population, given by μ, at first increases for larger values of ϕ_σ. It has a maximum at $\phi_\sigma \sim 0.02$ for $v_0 = 10\,{\rm m/s}$ and at $\phi_\sigma \sim 0.01$ for $v_0 = 12.5\,{\rm m/s}$ and then decreases in an exponential fashion. Comparing both velocity cases (see Tab. 6.6), more fragments are produced in the high velocity case. This has already been observed in Sec. 6.1.3. The influence of the inhomogeneity on the power-law population can be summarised as follows: (1) the overall mass of the power-law distribution is

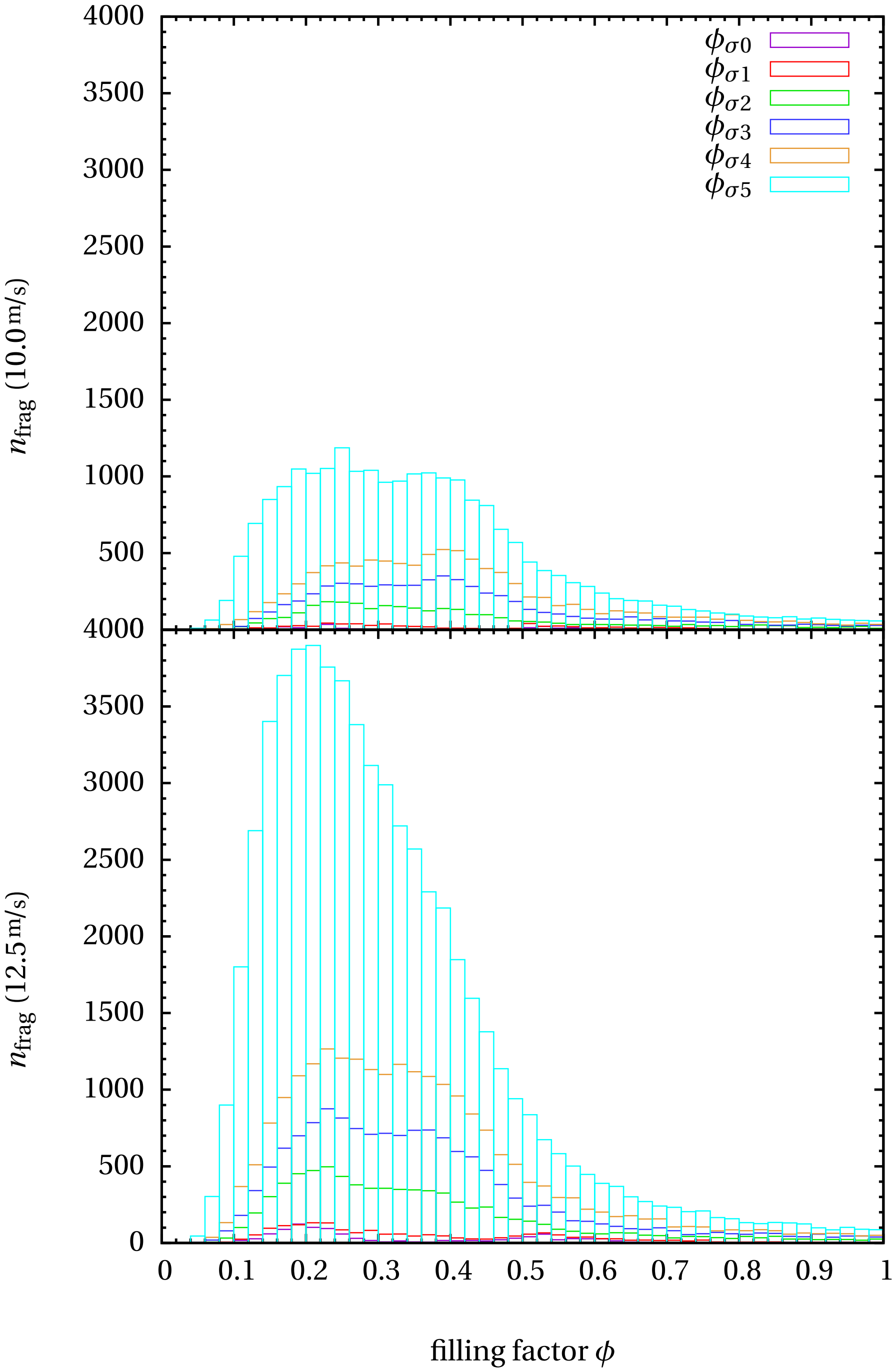

Figure 6.18. *Inhomogeneity model VI – filling factor distribution.* Final filling factor distribution of the number of fragments n_{frag} against average filling factor ϕ for each standard deviation ϕ_σ. The collision velocities are $v_0 = 10\,\mathrm{m/s}$ (top) and $v_0 = 12.5\,\mathrm{m/s}$ (bottom). In the high velocity case the distribution is slightly shifted towards smaller ϕ.

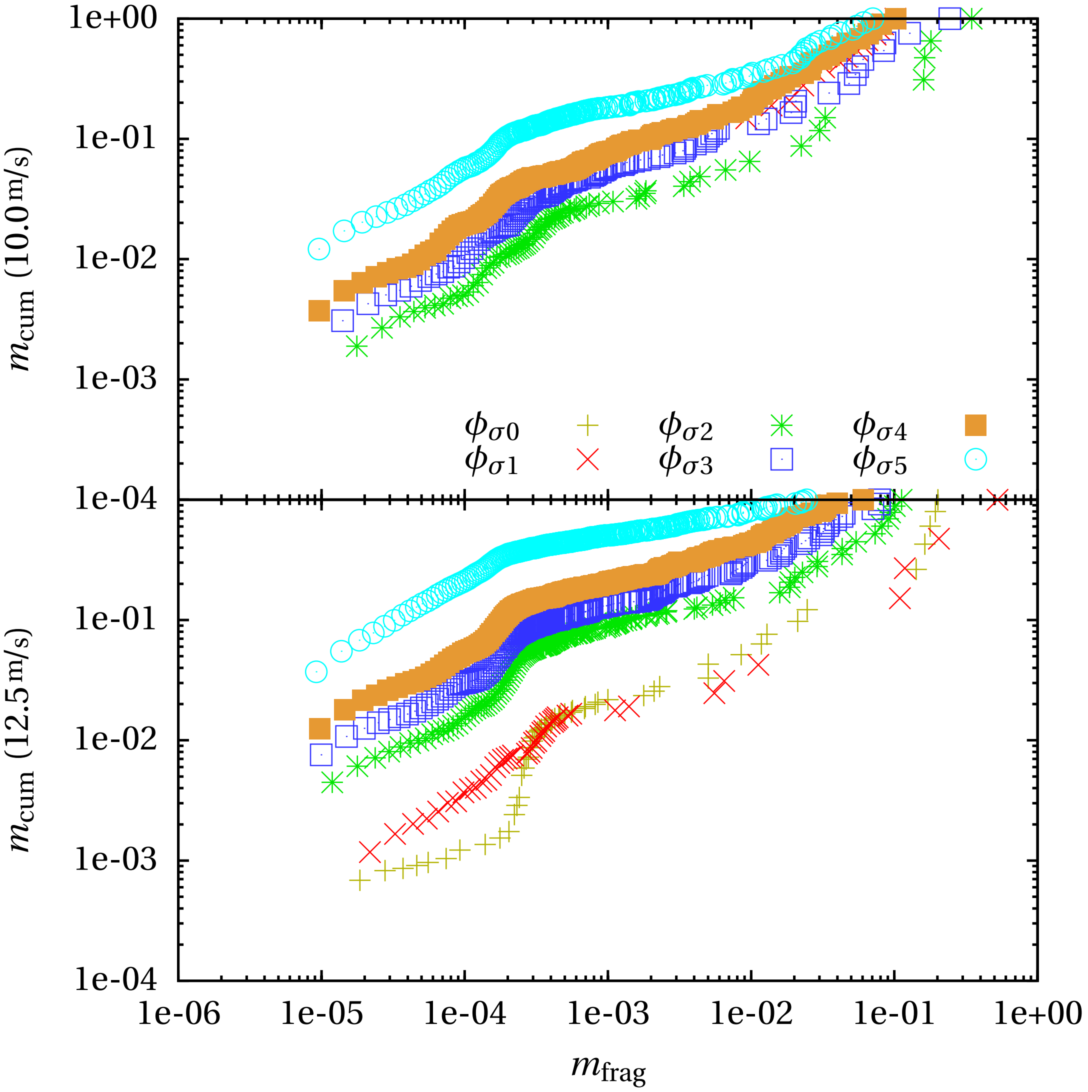

Figure 6.19. *Inhomogeneity model VII – mass distribution (power-law population).* Cumulative mass distribution power-law population for different inhomogeneity parameters ϕ_σ and collision velocities $v_0 = 10\,\mathrm{m/s}$ (top) and $v_0 = 12.5\,\mathrm{m/s}$ (bottom). In both velocity cases the mass of the largest member of the power-law population and the power-law slope decrease. This indicates fragmentation to smaller aggregates for increasing ϕ_σ. For equal ϕ_σ, the slopes are shallower for the higher velocity. The power-law fit parameters can be found in Tab. 6.5.

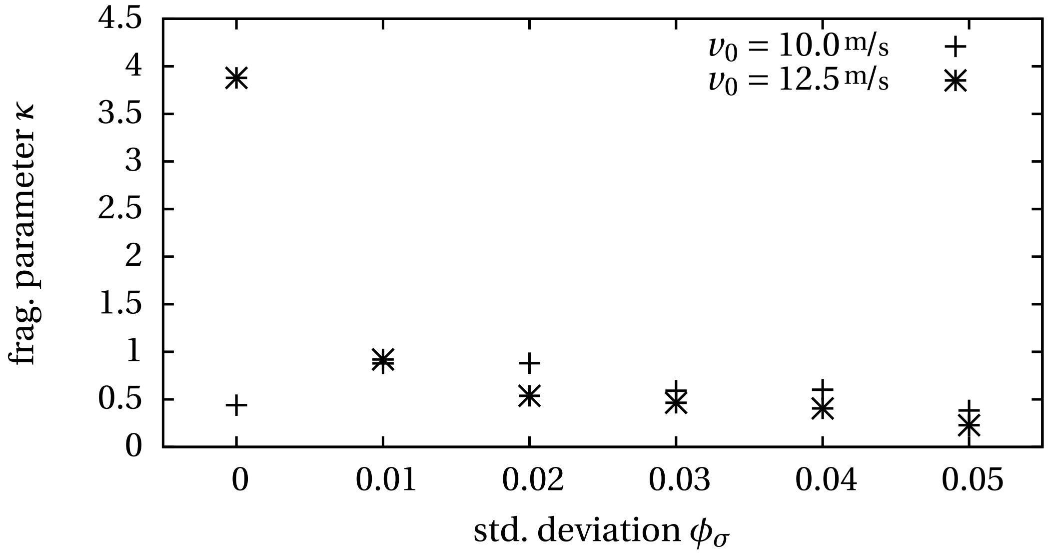

Figure 6.20. *Inhomogeneity model VIII – fragmentation parameter (power-law population).* For increasing inhomogeneity, indicated by the standard deviation ϕ_σ, the fragmentation parameter decreases. This indicates shallower slopes of the power-law mass distribution which is interpreted as an increasing fraction of smaller fragments. For $\phi_\sigma \geq 0.02$, the higher impact velocity results in smaller values of κ.

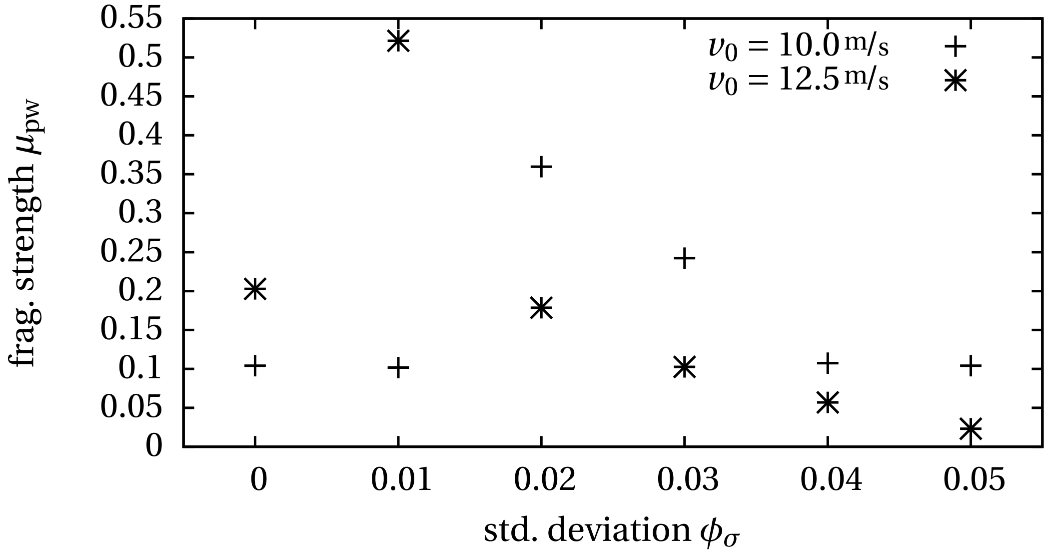

Figure 6.21. *Inhomogeneity model IX – fragmentation strength (power-law population).* The quantity μ represents the normalised mass of the most massive member of the power-law population and serves as an indicator of the fragmentation strength, where a lower value of μ indicates a more destructive collision. For increasing inhomogeneity, represented by larger values of ϕ_σ, μ at first increases and then decreases again. The increase may result from a lack of statistics caused by a low number of fragments.

ϕ_σ	v_0	κ	μ
0	10.0	0.44 ± 0.027	$0.10 \pm 2.4 \times 10^{-3}$
0.01	10.0	0.88 ± 0.035	$0.10 \pm 2.3 \times 10^{-3}$
0.02	10.0	0.88 ± 0.046	0.36 ± 0.012
0.03	10.0	0.59 ± 0.011	$0.24 \pm 6.9 \times 10^{-3}$
0.04	10.0	$0.60 \pm 6.4 \times 10^{-3}$	$0.11 \pm 1.7 \times 10^{-3}$
0.05	10.0	$0.38 \pm 5.4 \times 10^{-3}$	$40.10 \pm 4.0 \times 10^{-3}$
0	12.5	3.88 ± 0.254	$0.20 \pm 1.4 \times 10^{-3}$
0.01	12.5	0.92 ± 0.030	$0.52 \pm 1.0 \times 10^{-2}$
0.02	12.5	0.54 ± 0.017	$0.18 \pm 1.0 \times 10^{-2}$
0.03	12.5	0.46 ± 0.006	$0.10 \pm 3.0 \times 10^{-3}$
0.04	12.5	0.41 ± 0.004	$0.06 \pm 1.3 \times 10^{-3}$
0.05	12.5	0.23 ± 0.003	$0.02 \pm 1.0 \times 10^{-4}$

Table 6.5. *Collisions of inhomogeneous aggregates I – power-law population fits.* Fit values of the power-law population.The quantities κ and μ denote, respectively, the slope of the power-law fit and the mass of the most massive member, which is normalised by the total mass of the power-law population m_{pw}. The standard deviation of the inhomogeneity Gaussian is denoted by ϕ_σ and the impact velocity by v_0.

increased with larger values of ϕ_σ. (2) A higher degree of inhomogeneity leads to the production of smaller fragments. (3) The largest member of the power-law population reaches its largest mass for small ϕ_σ. Then its mass decreases with increasing ϕ_σ.

6.2.3. Discussion and Outlook

summary

In this section I have presented the first damage model which is based on the inhomogeneity of SiO_2 dust aggregates as measured by Güttler et al. (2009). The approach is based on the concept that according to the porosity model (see Sec. 4.3.4) inhomogeneities in the filling factor cause fluctuations in compressive, shear, and tensile strength in the aggregate. These fluctuations can be regarded as flaws in the material. In contrast to previous approaches designed for brittle material (Grady and Kipp 1980), the propagation of these flaws is not explicitly evolved. Instead, the defects in the dust material, which behaves more like a fluid, are determined by the time evolution of the filling factor or - equivalently - the density. The inhomogeneity of an aggregate is imposed on the initial SPH particle distribution as a Gaussian distribution of the filling factor. The measure for the inhomogeneity is the standard deviation ϕ_σ of the Gaussian.

Using this inhomogeneity damage model, I have performed test simulations of collisions between dust aggregates of intermediate porosity. Two collision velocities have been chosen: one below and one above the fragmentation threshold for homogeneous aggregates. The results have been analysed using the four-population model presented in Sec. 6.1. For the lower collision velocity I have shown that inhomogeneity leads to fragmentation. For both velocities the masses of largest and second largest fragment are decreased with a higher degree of inhomogeneity whereas the masses of the power-law and sub-resolution population are increased. Focussing on the power-law population, the number of fragments and the fraction of small fragments increase with increasing ϕ_σ. These findings demonstrate the qualitative and also quantitative functionality of the inhomogeneity approach as a damage model.

discussion The findings indicate that inhomogeneous dust aggregates are weaker than their homogeneous equivalents. A slight inhomogeneity is sufficient to result in catastrophic disruption instead of growth as a result of a dust aggregate collision. Therefore, inhomogeneity might explain the lower velocity thresholds for fragmentation in laboratory experiments ($\sim 1\,\mathrm{m/s}$, see also Sec. 6.1.4 and 6.4.3) compared to a higher value found in simulations.

Furthermore, macroscopic dust aggregates in protoplanetary discs are produced by subsequent impacts of smaller aggregates at different impact velocities, i.e. pre-planetesimals feature a collision history and thus are very likely to be inhomogeneous. With the model presented in this section it is possible to capture this feature. Further studies might be carried out which investigate the inhomogeneity created by subsequent multiple impacts. The result can be classified according to the presented inhomogeneity model.

So far the simulations of collisions between homogeneous aggregates carried out by means of the porosity model described in Sec. 4.3.4 produce the same fragment distribution for the same set of input parameters. By randomly assigning an inhomogeneity pattern it is now possible to profoundly investigate the statistics of a fragment distribution. Statistical fluctuations of the quantities of the four-population model can now be estimated, in particular, for simulations with a low number of fragments.

In high velocity grazing collisions the target is caused to rotate. For highly porous aggregates, which feature a low tensile strength, it is likely that high spinning rates lead to fragmentation of the target. With increasing inhomogeneity this might also be true for aggregates with medium and low porosities. A quantitative investigation of this effect can be carried out by means of the inhomogeneity damage model.

outlook The filling factor distribution of dust aggregates can be determined in the laboratory by X-ray tomography measurements (Güttler et al. 2009). These empirical data can be directly implemented into the inhomogeneity damage model whose input parameters can obtained more easily than the values for the Weibull distribution (Weibull 1939), which is used for brittle material. Besides the successful material calibration of Ch. 5, the obtained inhomogeneity parameters can be used to further improve the realistic simulation of porous dust aggregates. By considering laboratory measurements of a size range of aggregates of the same filling factor, scaling laws of the inhomogeneity with size could be derived. This eventually introduces a length scale for simulations of pre-planetesimals of sizes ranging from centimetre to hundreds of metres.

ϕ_σ	v_0 [m/s]	E_{tot} [J]	m_1 [kg]	E_1 [J]	m_2 [kg]	E_2 [J]	m_{pw} [kg]	E_{pw} [J]	N_{pw}	m_{sr} [kg]	E_{sr} [J]	N_{sr}
0.00	10.0	5.81	3.56	5.64	5×10^{-5}	1×10^{-4}	5×10^{-3}	3×10^{-3}	17	2×10^{-3}	0.17	158
0.01	10.0	5.99	3.55	5.61	3×10^{-4}	7×10^{-4}	3×10^{-3}	0.01	36	0.01	0.36	610
0.02	10.0	6.72	1.62	2.75	0.52	0.82	1.39	2.30	290	0.04	0.84	2854
0.03	10.0	7.35	1.25	2.28	0.49	0.80	1.75	3.03	588	0.07	1.24	6043
0.04	10.0	7.80	0.55	0.91	0.35	0.75	2.55	4.64	1057	0.11	1.50	9292
0.05	10.0	9.09	0.43	0.71	0.32	0.54	2.56	5.54	3056	0.25	2.30	20657
0.00	12.5	9.78	1.92	4.47	0.31	0.78	1.33	4.14	123	0.01	0.39	861
0.01	12.5	10.12	1.74	4.42	0.67	1.83	1.13	2.87	157	0.02	1.00	1650
0.02	12.5	11.93	1.17	3.73	0.23	0.52	2.07	5.45	984	0.08	2.23	6882
0.03	12.5	13.24	0.72	2.40	0.21	0.74	2.47	6.91	1865	0.16	3.19	13285
0.04	12.5	14.29	0.59	2.03	0.18	0.40	2.54	7.90	3180	0.25	3.96	20402
0.05	12.5	19.20	0.15	0.38	0.09	0.27	2.68	11.13	10578	0.65	7.42	52478

Table 6.6. *Collisions of inhomogeneous aggregates II – results.* Simulation results presented according to the four-population classification. The subscripts “1”, “2”, “pw”, “sr”, and “tot” denote the largest and second largest fragments, the power-law, sub-resolution and total fragment populations, respectively. The quantities E, m, and N are the total energy, the mass and the number of fragments, respectively. The standard deviation for the inhomogeneity Gaussian distribution is given by ϕ_σ and the impact velocity by v_0.

6.3. Hard shells and aggregate bouncing

Güttler et al. (2010) divided a collision parameter space ranging from 10^{-11} to 10^{2} g in projectile mass and from 10^{-6} to 10^{2} m/s in collision velocity into sticking, bouncing and fragmentation events. Approximately one third of the logarithmic parameter space for collisions between porous aggregates of comparable size was assumed to yield bouncing. In particular, for collision velocities of 0.01 to 1 m/s and projectile masses ≥ 1 g, bouncing is assumed to be the only outcome. As a consequence, pre-planetesimal growth is halted at aggregates of roughly centimetre size ("bouncing barrier", Sec. 2.3.1). Güttler et al. (2010) based the boundaries of the bouncing regime on theoretical considerations as well as on empirical grounds. According to their theoretical model, the demarcation between sticking and bouncing was estimated by the equality of the contact energy and the rebound energy (Eq. 12 in Güttler et al. 2010). For the estimation of the contact area they assumed elastic deformation. As an empirical basis, two experimental studies were utilised: Blum and Münch (1993) conducted collision experiments with $ZiSiO_4$ aggregates of intermediate porosity (initial filling factor $\phi_i = 0.26$) which bounced for 0.15 up to $v_0 = 1$ m/s and Heißelmann et al. (2007) collided millimetre sized cubes of highly porous SiO_2 ($\phi_i = 0.15$) at $v_0 = 0.4$ m/s, which rebounded (see also Sec. 3.1). Güttler et al. (2010) integrate these experiments into their collision model assuming that the different material has no significant effect on the mechanical properties (see also Sec. 2.2.1).

6.3.1. Homogeneous dust aggregates

In the first study I investigate the influence of porosity on the bouncing and sticking behaviour. This is to assess whether the experiments with intermediate porosity (Blum and Münch 1993) and high porosity (Heißelmann et al. 2007) can be combined into the collision map presented by Güttler et al. (2010). A more detailed investigation on bouncing for different porosities and projectile sizes is carried out in Sec. 6.4.

numerical setting

For this purpose, I conduct simulations for a homogeneous target and projectile and distinguish the cases where both objects either feature an initial filling factor of $\phi_i = 0.15$ (high porosity) or of $\phi_i = 0.35$ (intermediate porosity). The impacting projectile has a radius $r_p = 0.6 \times r_t$ of the target radius r_t, which is roughly one decimetre. For both filling factor cases, the radii are chosen such that the masses of both cases are comparable and thus also the kinetic energy of the impact. The impact velocities v_0 are 0.1, 0.3, 0.5, and 1.0 m/s. The initial particle distribution of the aggregates is created by means of the `initgrid` program (Appx. A.3).

intermediate porosity

The resulting outcomes are shown in Fig. 6.22 for the high (left) and *intermediate porosity cases* (right) as a cross section through the spherical aggregates. For the filling factor $\phi_i = 0.35$ my findings confirm the results of Blum and Münch (1993): all collisions resulted in bouncing except for the lowest velocity, where the aggregates are connected by a few SPH particles. However, this connection can be destroyed very easily, which effectively leads to bouncing. From the figure it can be seen that the filling factor in both the target and projectile is increased to $\phi \sim 0.48$ in a region whose size is increasing with impact velocity. With the latter the contact area is also enlarged, which remains as a flattened spot on the impact site.

high porosity

In contrast to the intermediate porosity case, for the *high porosity* $\phi_i = 0.15$ (Fig. 6.22, left) I cannot confirm the results of Heißelmann et al. (2007): all collisions result in sticking. While for the lowest velocity the contact area between both aggregates is very small and easy to break apart, the contact area for higher impact velocities increases and both aggregates are merged.

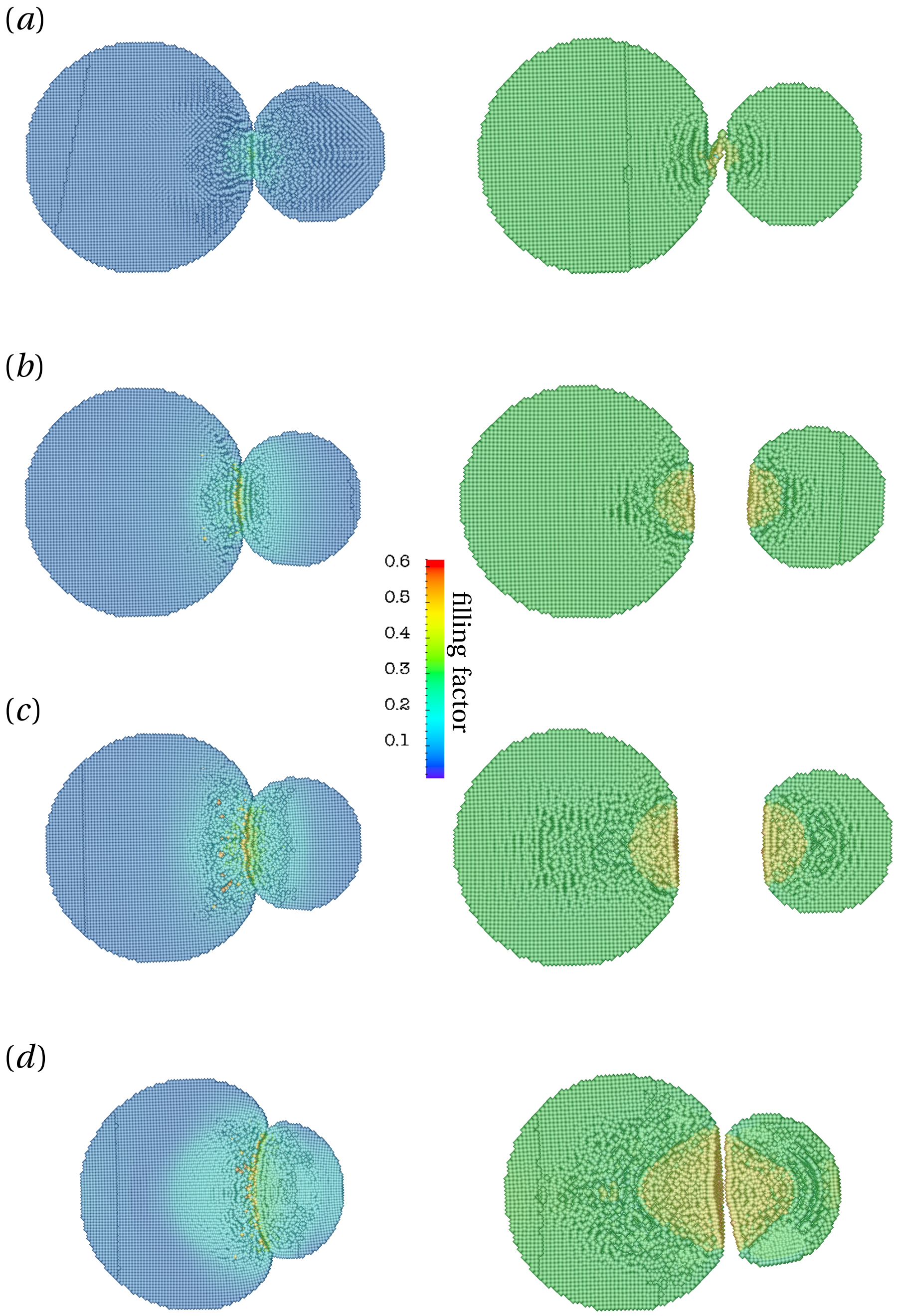

Figure 6.22. *Hard shells I – homogeneous aggregates.* Cross-section through the outcome of collision simulations with homogeneous aggregates for high ($\phi_\mathrm{i} = 0.15$, left) and intermediate porosity ($\phi_\mathrm{i} = 0.35$, right). The projectile radius is $r_\mathrm{p} = 0.6 \times r_\mathrm{t}$ of the target radius. The collision velocities are (a) 0.1, (b) 0.3, (c) 0.5, and (d) 1.0 m/s. For both porosity cases, the aggregates increasingly get compacted with higher velocities. While in the high porosity case all collisions result in sticking, for intermediate porosity aggregates exclusively bouncing occurs (except for the lowest velocity, where the aggregates remain connected by a string of particles). The high porosity target also is deformed considerably, while the intermediate porosity target is only flattened at the impact site.

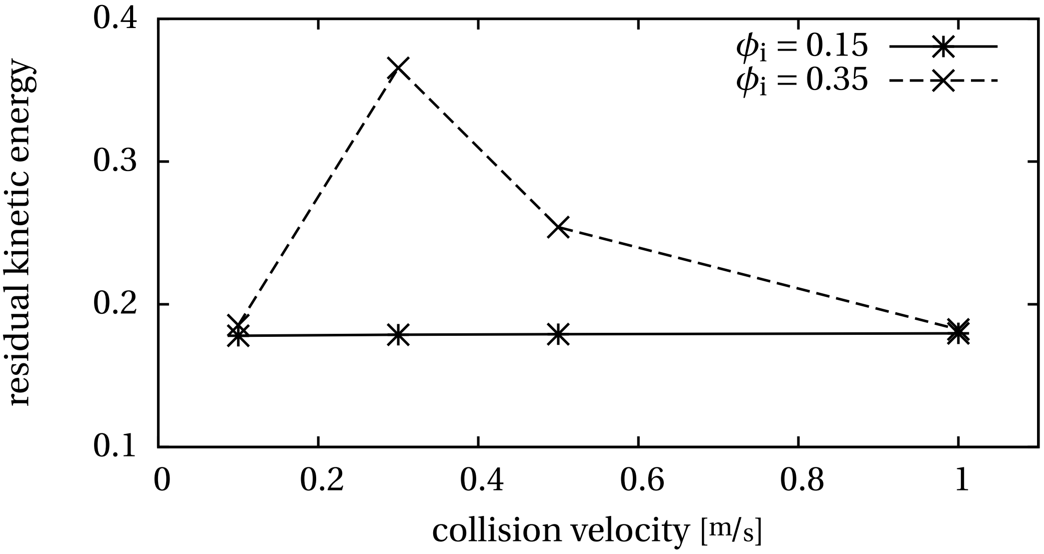

Figure 6.23. *Hard shells II – residual energy (homogeneous).* Residual kinetic energy as fraction of the initial kinetic energy in collisions with homogeneous aggregates as a function of collision velocity v_0. For the high porosity case ($\phi_i = 0.15$) the residual energy hardly changes with v_0. In collisions with aggregates of intermediate porosity ($\phi_i = 0.35$), less energy is dissipated for bouncing events. In contrast, for almost sticking outcomes the dissipation is comparable to the high porosity case.

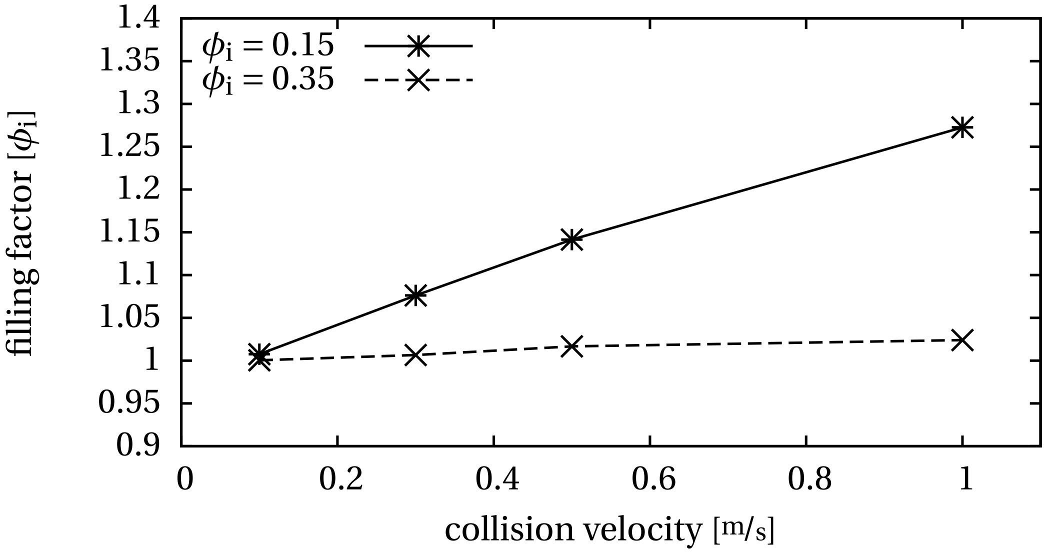

Figure 6.24. *Hard shells III – filling factor (homogeneous).* Filling factor ϕ/ϕ_i for collisions of homogeneous aggregates as a function of collision velocity. For the intermediate porosity case ($\phi_i = 0.35$), ϕ hardly changes with increasing impact velocity. In contrast, for high porosity ($\phi_i = 0.15$) a high degree of plastic deformation takes place and a filling factor of $\sim 1.27\phi_i$ is achieved.

It is particularly interesting to note that for the high porosity case the filling factor in the impact area is also increased to $\phi \sim 0.48$ just as in the intermediate porosity case. According to Eq. 4.129, this leads to an increased tensile strength in this region which prevents the separation of both aggregates. Furthermore, because of the high porosity the compressive strength of the impactor and target is very low, which follows from Eq. 4.128. This leads to a large extent of plastic deformation which becomes evident when comparing the cases with $v_0 = 0.1\,\mathrm{m/s}$ and $v_0 = 1.0\,\mathrm{m/s}$. For the latter the aggregate assumes a kidney shape. The deformation is not as strong in the intermediate porosity case because these aggregates are less plastic.

energy dissipation Since *kinetic energy is dissipated* effectively in plastic deformations, the difference between high and intermediate porosity is also evident looking at the residual kinetic energy for each simulation (Fig. 6.23), which is given by the sum of translation energy and the internal energy (rotation and vibration) of the remaining object(s). It is normalised by the initial kinetic energy. For the high porosity case the remaining energy is nearly constant at ~ 18 %. In the case of bouncing for aggregates of intermediate porosity less energy is dissipated: the residual kinetic energy is ~ 36 % of the initial energy for $v_0 = 0.3\,\mathrm{m/s}$ and ~ 25 % for $v_0 = 0.5\,\mathrm{m/s}$. For the almost sticking cases ~ 18 % of the initial energy remains in the system, just like in the high porosity case.

filling factor I also investigated the average *filling factor* of both objects compared to the initial filling factor ϕ_i. The result is shown in Fig. 6.24. While ϕ hardly increases to $1.024\,\phi_\mathrm{i}$ for the highest collision velocity for the intermediate porosity aggregates, it rises to $1.27\,\phi_\mathrm{i}$ for the high porosity dust. This is because at low collision velocities the dynamic pressure is below the compressive strength for intermediate porosity objects $\Sigma(0.35) = 260\,\mathrm{Pa}$ in most parts of the aggregates and consequently no plastic deformation takes place there. For the high porosity aggregates $\Sigma(0.15) = 7.4\,\mathrm{Pa}$, and as a result even small dynamic pressures cause plastic deformation and consequential filling factor increase in large parts of the aggregate.

discussion The theoretical demarcation between sticking and bouncing by Güttler et al. (2010) makes the following assumptions: (1) elastic deformation of the aggregates, (2) shear strength equals shear modulus where both are constant for all filling factors, and (3) the filling factor in the contact region is not changed in the collision. These assumptions are too simplistic.

(1) The assumption of elastic deformation of the aggregates is only valid for filling factors close to the maximum filling factor. In particular for highly porous aggregates the deformation is highly plastic and as a consequence the contact area between the aggregates is increased compared to elastic contact (see e.g. Fig. 6.22, d).

(2) Firstly, the shear modulus $\mu(\phi)$ governs the elastic properties of an aggregate and cannot be estimated by the shear strength $Y(\phi)$, which is a plasticity quantity. According to Eq. 4.123 $\mu(0.15) = 2250\,\mathrm{Pa}$ and $\mu(0.35) = 4076\,\mathrm{Pa}$, whereas according to Eq. 4.125, 4.128, and 4.129 the shear strength is given by $Y(0.15) = 88\,\mathrm{Pa}$ and $Y(0.35) = 735\,\mathrm{Pa}$. In contrast, Güttler et al. (2010) estimate $\mu = 632\,\mathrm{Pa}$. Secondly, they assume that the shear modulus is constant for all filling factors, but from $\phi = 0.15$ to $\phi = 0.35$ it rises by a factor of more than two. This means that the contact area is larger for aggregates with higher porosity according to their Eq. 12. Thirdly, they apply the static strength quantities, whereas the dynamic shear strength and compressive strength as stated above are more appropriate (see Sec. 5.3.2 and 5.3.3). The incorrect estimate for the shear modulus leads to smaller sticking thresholds. However, the assumption of an elastic deformation is not valid for dust aggregates anyway.

(3) As it can be clearly seen in Fig. 6.22, the filling factor is highly increased in the contact area. This leads to an increased tensile strength in this region (Eq. 4.129). An increased tensile strength, however, also increases the contact energy, which promotes sticking.

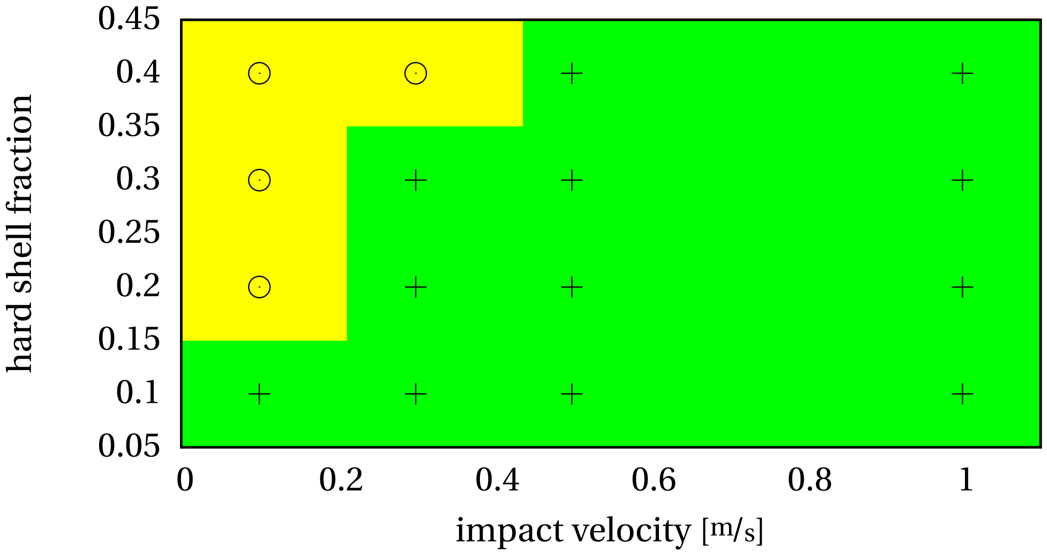

Figure 6.25. *Hard shells IV – sticking and bouncing.* Sticking and bouncing in collisions with hard shells depending on impact velocity v_0 and hard shell fraction. Bouncing only occurs for velocities ≤ 0.2 m/s and intermediate and large thicknesses of hard shells ≥ 0.2 r. For very thick hard shells ≥ 0.4 r bouncing also occurs for $v_0 \geq 0.2$ m/s.

I conclude that because of these effects in particular for highly porous dust aggregates the threshold velocity for sticking is much larger than presented in Güttler et al. (2010). Consequently, the parameter space where bouncing occurs is much smaller than assumed in this reference and sticking dominates for low velocities and low filling factors.

The comparison of collisions with high and intermediate porosity show, that there are significant differences regarding the sticking and bouncing behaviour. While aggregates of intermediate porosity tend to bounce at low collision velocities, highly porous aggregates tend to stick. However, Heißelmann et al. (2007) observed bouncing for the latter. A possible reason for this is the influence of hard shells of porous aggregates, which is presented in the next section.

6.3.2. Hard shell dust aggregates

Heißelmann et al. (2007) found bouncing for aggregates with $\phi_i \sim 0.15$ and collision velocities $v_0 \sim 0.4$ m/s. However, in the preparation process of the dust aggregates for the collision experiments the aggregates are compacted at their boundaries. This compaction creates a shell of increased filling factor around the dust sample, which I refer to as "hard shell". In this section, the influence of hard shells of various thicknesses on the sticking and bouncing behaviour of macroscopic dust aggregates is investigated.

numerical setting

I use the same setup as in the previous section regarding ratio of target and projectile radius and collision velocity. Again, the mass of the projectile is chosen such that the impact energies are comparable to those of the previous section. The thickness of the hard shell given as a fixed fraction of target and projectile radii, respectively, i.e. 0.1, 0.2, 0.3, and 0.4 (see Fig. 6.26 a for an

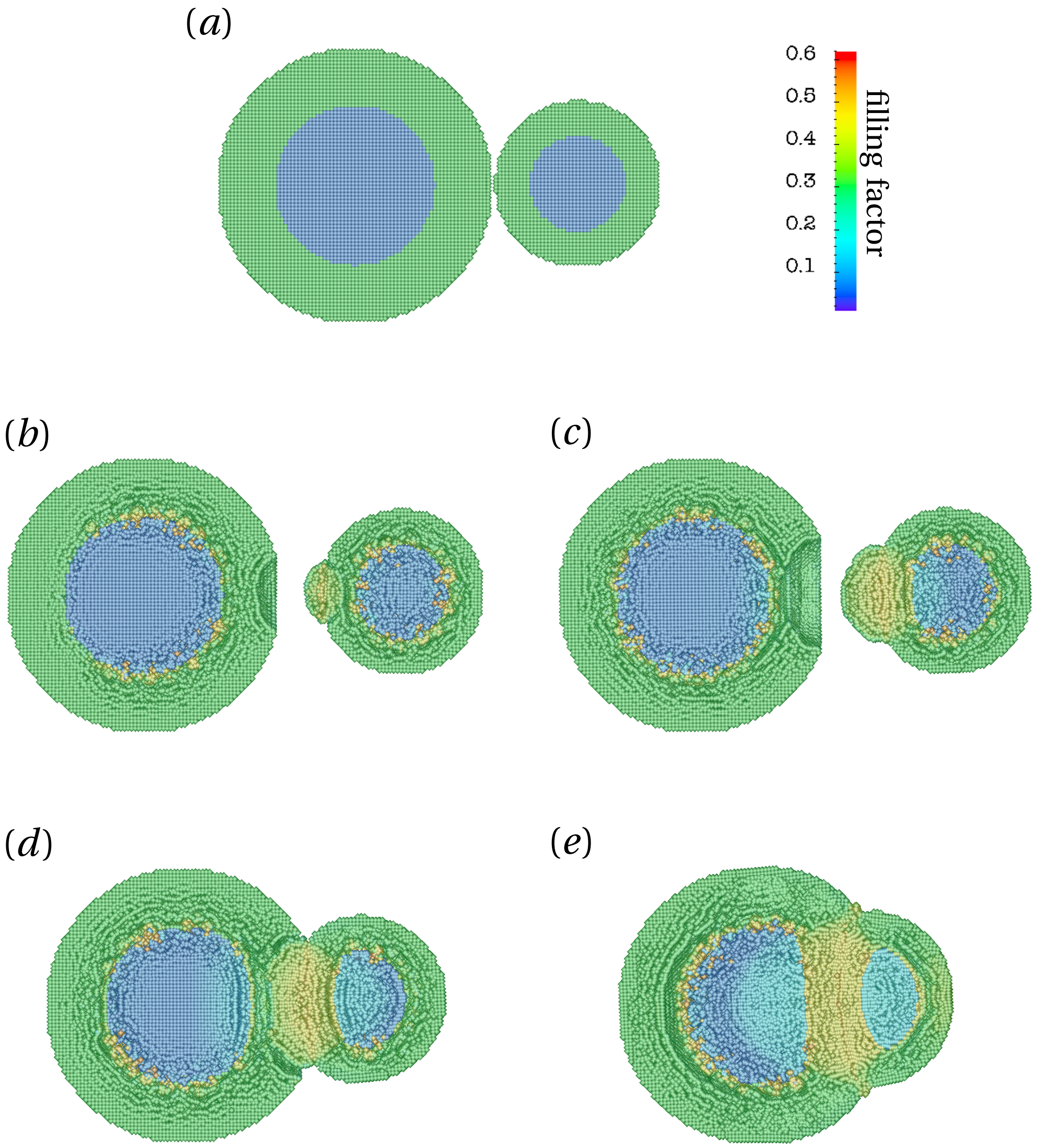

Figure 6.26. *Hard shells V – hard shell aggregates.* Cross-section through aggregates with a hard shell of 0.4 r. The hard shell has an intermediate filling factor ($\phi_h = 0.35$) and the interior is highly porous ($\phi_i = 0.15$). The initial setup is shown in (a). The remaining cross-sections show the situation after the impact with 0.1 (a), 0.3 (b), 0.5 (c), and 1.0 m/s (d). Thus the velocities are comparable to the simulations with homogeneous aggregates in Fig. 6.22.

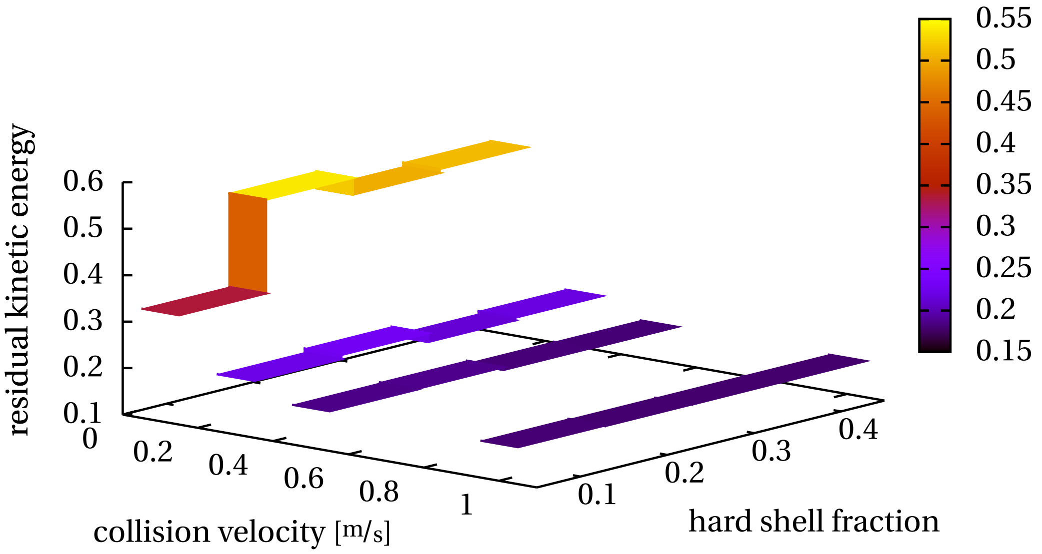

Figure 6.27. *Hard shells VI – residual energy (hard shell).* Residual kinetic energy normalised by the initial kinetic energy in collisions with hard shells. The residual energy is plotted as a function of the hard shell fraction of the aggregates' radii and the collision velocity. In bouncing events less energy is generally dissipated. For sticking events the residual energy is comparable to collisions with homogeneous aggregates.

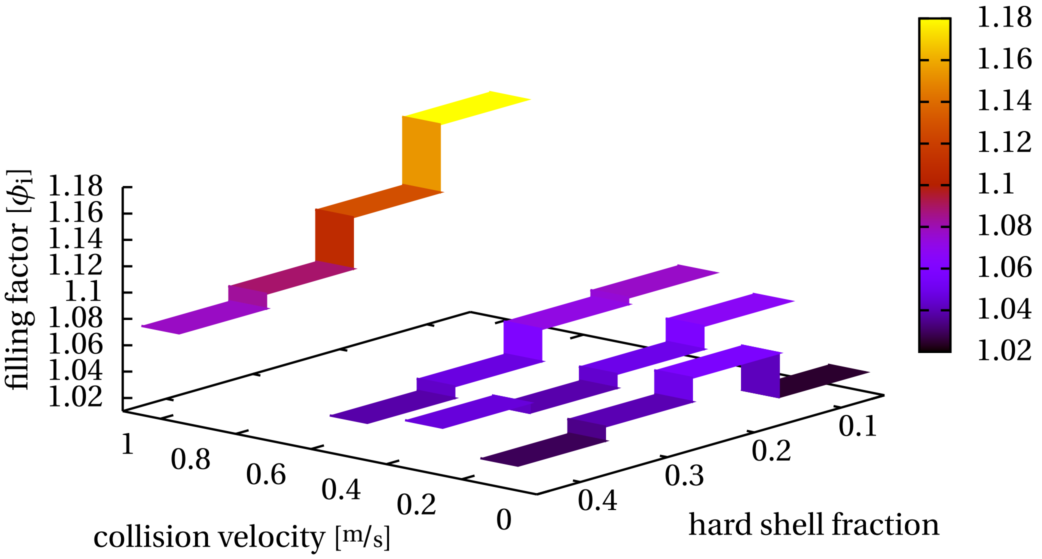

Figure 6.28. *Hard shells VII – filling factor (hard shells).* Filling factor ϕ normalised by the average initial filling factor. Thin hard shells and high collision velocities lead to high filling factors. In general the increase is in between the homogeneous cases.

illustration). The core of both aggregates has a filling factor $\phi_\mathrm{i} = 0.15$, whereas the hard shell is simulated with $\phi_\mathrm{h} = 0.35$. The masses of the target (1.3 kg) and projectile (0.27 kg) were kept fixed to ensure equal impact energies for hard shells of different thicknesses. The aggregates with their hard shells are set up using the `initgrid` particle distribution tool (Appx. A.3).

sticking and bouncing conditions

The simulation either resulted in *sticking* or in *bouncing* as depicted in Fig. 6.25, where bouncing events are represented as circles and sticking events as crosses. The green surface indicates the estimated parameter region for sticking, whereas yellow accounts for bouncing. From the comparison with aggregates without hard shell (homogeneous $\phi_\mathrm{i} = 0.15$), which exclusively resulted in sticking, it is evident that hard shells do have an influence on the bouncing behaviour of dust aggregates. In particular for low collision velocities and thick hard shells bouncing occurs. This is because for homogeneous aggregates with $\phi_\mathrm{i} = 0.15$ the compressive strength is very low $\Sigma(0.15) = 7.4\,\mathrm{Pa}$. As a consequence, nearly the entire kinetic energy of the impact is dissipated by plastic deformation and nearly no elastic loading of the colliding objects is possible.

In contrast, for aggregates with hard shells ($\phi_\mathrm{h} = 0.35$) the plastic deformation threshold is higher for the shell $\Sigma(0.35) = 260\,\mathrm{Pa}$. During the impact, the shell is elastically loaded and the aggregates rebound. However, in the immediate area around the impact site the deformation threshold for the shell is exceeded and plastic deformation takes place in the hard shell. Material there is compressed to filling factors $\phi \sim 0.47$. Therefore, the tensile $T(\phi)$ and shear $Y(\phi)$ strengths are increased in this region and counteract the bouncing. If this region of increased strength is too small, a piece of the target is ripped off and sticks to the projectile. This situation is depicted in Fig. 6.26 for a hard shell fraction of 0.4 and $v_0 = 0.1\,\mathrm{m/s}$ (b) and $v_0 = 0.3\,\mathrm{m/s}$ (c). In the first case, the projectile mass is increased by 2.00 %, in the second case by 12.1 %.

In contrast, if the compressed area is sufficiently large, increased strengths prevent the projectile from rebounding. This result is illustrated in Fig. 6.26 for $v_0 = 0.5\,\mathrm{m/s}$ (d) and $v_0 = 1.0\,\mathrm{m/s}$ (e). For larger velocities I expect sticking until at even higher collision energies the target fragmentation sets in.

From Fig. 6.25 it can be seen that for thin hard shells ($\sim 0.1\,r$) no bouncing occurs at all. For this thickness, two processes lead to sticking: a thin hard shell does not provide enough elastic loading for rebound and the highly porous core gets more compacted. As a result, more kinetic energy is dissipated. For thicker hard shells fractions ($\geq 0.2\,r$), elastic loading is sufficient for bouncing at low collision velocities $v_0 \leq 0.2$.

residual energy

As in the previous section, the *residual kinetic energy* after the impact is the sum of the translation energy and the internal energy in the final state. In Fig. 6.27 it is normalised by the initial energy and plotted as a function of the collision velocity and hard shell fraction. For low collision velocities, the residual energy increases with the thickness of the hard shell. This is because in bouncing collisions the pressure in the largest regions of the dust aggregates stays below the threshold for plastic deformation. Thus, the occurring deformation is mainly elastic and reversible. For higher impact energies, this threshold is exceeded in large parts of the aggregate. Hence, deformation is mainly plastic and irreversible, which leads to a reduced residual energy ($\sim 22\,\%$ of the initial kinetic energy for $v_0 \sim 0.3\,\mathrm{m/s}$ and $\sim 18\,\%$ for $v_0 \geq 0.5\,\mathrm{m/s}$. In bouncing collisions, e.g. for $v_0 = 0.2\,\mathrm{m/s} \sim 50\,\%$ of the kinetic energy is not dissipated. The sticking event with a hard shell thickness of $0.1\,r$ and $v_0 = 0.1\,\mathrm{m/s}$ represents an intermediate state, where the residual energy is $\sim 34\,\%$ of the initial kinetic energy.

filling factor

The *filling factor variation* for the hard shell simulations is displayed in Fig. 6.28 as a function of hard shell thickness and collision velocity. In this plot the filling factor is normalised by the initial filling factor. In general it can be said that for thin hard shells and high collision velocities the filling factor is increased the most (up to ~ $1.18\phi_\mathrm{i}$). For $v_0 = 0.5\,\mathrm{m/s}$ the filling factor ranges from ~ 1.04 to ~ $1.08\phi_\mathrm{i}$. The lowest increase (~ $1.02\phi_\mathrm{i}$) is reached for the thinnest hard shell and the lowest collision velocity.

comparison of homogeneous and hard-shell aggregates

The outcomes of simulations with homogeneous and hard shell aggregates are now compared to understand the influence of the latter:

(1) I take a look on the occurrence of bouncing. While homogeneous highly porous dust aggregates ($\phi_\mathrm{i} = 0.15$) never bounce in the investigated velocity regime ($v_0 = 0.1 - 1.0\,\mathrm{m/s}$), homogeneous intermediate porosity aggregates ($\phi_\mathrm{i} = 0.35$) always rebound. As it can be expected, a a $\phi_\mathrm{i} = 0.15$ aggregate with a hard shell of $\phi_\mathrm{h} = 0.35$ of produces some intermediate behaviour. Indeed, aggregates with a hard shell bounce at low collision velocities. The velocity threshold for bouncing increases with increasing hard shell thickness. In the preparation process of the dust samples, Heißelmann et al. (2007) created a hard shell. If this shell was thick enough it could explain the bouncing events for highly porous dust aggregates although the compressive strength is very low.

(2) A hard shell does not prevent sticking of dust aggregates. While homogeneous intermediate porosity aggregates ($\phi_\mathrm{i} = 0.35$) never stick for the investigated velocity range, the highly porous core lowers the velocity threshold for sticking. For $v_0 \geq 0.5\,\mathrm{m/s}$ the aggregates stick for all eggshell thicknesses. This is because the impact energy is sufficient to plastically deform the highly porous core, where energy is dissipated effectively. Thus, the projectile breaks through the shell in these collisions.

(3) Hard shells seem to promote the ripping out of large chunks of the shell (see Fig. 6.26). The reason for this could be the lower tensile strength $T(\phi)$ of the highly porous core. In the impact process the filling factor is increased in the hard shell which is then bound more strongly to the projectile than to the porous core. Thus, during rebound a piece of the hard shell is ripped off. This behaviour could not be seen in collisions of homogeneous aggregates. There, the contact area is only flattened during the impact (see Fig. 6.22).

(4) In bouncing collisions of hard shell aggregates the residual kinetic energy is much larger than for bouncing of homogeneous aggregates (comparing Figs. 6.23 and 6.27). The dissipated energy for sticking events is nearly equal.

(5) The relative filling factor increase for hard shell aggregates lies in between the maximum defined by homogeneous highly porous aggregates and the minimum defined by homogeneous aggregates of intermediate porosity. This is because of the hybrid nature of the hard shell aggregate with respect to the filling factor.

6.3.3. Discussion and outlook

summary

I have investigated the occurrence of sticking and bouncing for macroscopic and microscopic aggregates. This study has been carried out to assess whether the bouncing regime for similar sized porous aggregates proposed by Güttler et al. (2010) is realistic.

discussion

From collisions between decimetre sized spherical dust aggregates with homogeneous porosity I have shown that bouncing is characteristic for aggregates of intermediate porosity ($\phi_\mathrm{i} = 0.35$) and collision velocities $v_0 \leq 1\,\mathrm{m/s}$. For highly porous aggregates however, sticking is much more frequent than stated by Güttler et al. (2010). This is because their theoretical sticking velocity threshold is based on elastic deformation and a filling factor, which is assumed to be constant during the collision. In particular highly porous aggregates are very plastic. This increases the contact area between the collision parters and hence the contact energy. In addition, the filling factor in the contact region is increased resulting in an increased tensile strength there, which in turn also increases the contact energy. The assumptions of Güttler et al. (2010) are only valid for low or intermediate porosity, which is supported by their empirical basis (Blum and Münch 1993).

There is experimental evidence (Heißelmann et al. 2007) which points to bouncing also of highly porous aggregates. However, the outer regions of these aggregates are compressed while preparing the collision experiment. To assess the effect of this compacted shell, I have carried out simulations of dust aggregates with a hard shell of intermediate porosity and a highly porous core. I have found that for the low collision velocities used by Heißelmann et al. (2007) even a thin hard shell could produce bouncing of the aggregates instead of sticking.

I conclude that in the collision parameter space bouncing is much less frequent than assumed by Güttler et al. (2010) and that the bouncing barrier proposed by Zsom et al. (2010), who rely on the former reference, could be less endangering for planetesimal formation than hypothesised by the authors.

Nevertheless, hard shells may play an important role in the planet formation process. Experimental evidence (Weidling et al. 2009) indicates that hard shells can be created in bouncing collisions of macroscopic dust aggregates. Other experiments (T. Meisner, J. Teiser, and G. Wurm, private communication) show that a highly porous macroscopic aggregate can acquire a hard shell by accreting microscopic fractal aggregates while it moves through the protoplanetary disc. In this process, the relative velocity between macroscopic body and microscopic aggregates determines the filling factor of the hard shell: the higher the impact velocity the higher are the filling factors of the shell. The results indicate that hard shells can be created by multiple sticking and separation of two loosely bound highly porous aggregates.

I have shown that collisions between aggregates with hard shells only yield bouncing for low collision velocities. The thinner the hard shell the lower the collision velocity has to be for the aggregates to rebound. At higher collision velocities the projectile breaks through the hard shell and energy is dissipated by compacting the highly porous core. Such collisions with velocities below the fragmentation threshold result in sticking. Therefore, bouncing due to hard shells is only an obstacle to collisional growth of pre-planetesimals if the collision velocities are low. Furthermore, the velocity threshold between bouncing and sticking is lowered for aggregates with a porous core and an intermediate porosity hard shell compared to homogeneous intermediate porosity aggregates. Therefore, even if dust aggregates acquire a hard shell by one of the mentioned processes and rebound in low velocity collisions, they might stick at slightly higher velocities.

outlook The results of the presented studies encourage further investigation of the quantitative dependence of the bouncing-sticking threshold on hard shell thickness and hard shell filling factor. In addition, the influence of hard shells on the transition from sticking to fragmentation could be investigated.

6.4. Head-on Collisions with Equal Porosity

In this section, I carry out head-on collisions of homogeneous spherical non-rotating pre-planetesimals in the decimetre size regime. This setup represents an idealisation. (1) It is very unlikely that realistic pre-planetesimals have a spherical shape. (2) Perfect head-on collisions are extremely rare events and pre-planetesimal encounters most likely occur with non-zero impact parameter. (3) Macroscopic dust aggregates in the protoplanetary disc feature a collisional history and thus possess an inhomogeneous density structure (see also Sec. 6.2). In addition, the target and projectile are unlikely to have the same porosity. (4) Dust aggregates in the protoplanetary disc environment might be rotating, e.g. because of a preceding grazing collision.

Nevertheless, it is worthwhile considering this idealised setup. (1) Because of its simplicity the setting has a small number of free parameters: I consider porosity, impact velocity, and size ratio of the aggregates. (2) The results from these simulations can be used directly in global dust coagulation models (see Sec. 3.3) as first estimates for parameter ranges which are not accessible by laboratory experiments (see Sec. 3.1). (3) The findings from this study establish a basis from which the effect of other parameters such as inhomogeneity or impact parameter can be studied.

This section has the following outline: in Sec. 6.4.1 I shortly describe the numerical setting and how the final fragment distribution is evaluated. In Sec. 6.4.2 the simulation results are evaluated according to the four-population model developed in Sec. 6.1. Finally, I summarise and discuss the results in Sec. 6.4.3 and give an outlook on future projects.

6.4.1. Numerical setting and evaluation

Using the particle distribution generation tool `initgrid` (Appx. A.3) two spheres are positioned in a distance such that they do not interact, i.e. the distance is $\sim 2h$. The SPH particles of each sphere are placed on a cubic lattice with lattice constant $l_\mathrm{c} = 2.6\,\mathrm{mm}$. According to the findings of Sec. 5.2.2 the smoothing length is set to $h = 3.75 \times l_\mathrm{c} = 9.75\,\mathrm{mm}$. The setup is not perfectly head-on: the projectile is shifted by $0.5\,l_\mathrm{c}$ in the directions perpendicular to the collision axis. This is to avoid particle interpenetration. The lattice planes of both spheres are parallel and perpendicular to each other, respectively. In simulations with low resolutions (C. Schäfer, unpublished data) this symmetry caused fragmentation along the planes. In the resulting particle distributions of fragmenting collisions presented here this behaviour is never observed because a higher resolution is used.

The target radius is fixed at $r_\mathrm{t} = 10\,\mathrm{cm}$ whereas the projectile radius is varied from $r_\mathrm{p} = 2\,\mathrm{cm}$ to $r_\mathrm{p} = 10\,\mathrm{cm}$. The target is resting and the projectile velocity ranges from $v_0 = 0.1\,\mathrm{m/s}$ to $v_0 = 27.5\,\mathrm{m/s}$ which roughly represents the collision velocity range of decimetre sized dust aggregates for various size ratios (J.-F. Gonzales, personal communication, see also Sec. 2.1.3). Both spherical aggregates are homogeneous and feature the same initial filling factor ϕ_i. Three values are considered for this study: $\phi_\mathrm{i} = 0.15$ (high porosity), $\phi_\mathrm{i} = 0.35$ (intermediate porosity), and $\phi_\mathrm{i} = 0.55$ (low porosity). The filling factor of the high porosity case is close to the minimum filling factor $\phi_\mathrm{min} = 0.12$ of the ODC compressive strength (Eq. 5.4) and the low porosity case is close to its maximum filling factor $\phi_\mathrm{max} = 0.58$. According to their filling factors and sizes the target and projectiles have the masses and particle numbers specified in Tab. 6.7. The dust material is simulated by means of the porosity model presented in Sec. 4.3.4 with the calibrated parameters of Ch. 5, in particular Tab. 5.8. In total 160 simulations are carried out for this study.

The end times of the simulations are chosen by visual control, i.e. a point in time is determined when changes in the fragment distribution seize. Larger fragments are considered to be stable when their internal SPH particle velocities are low. These estimations are qualitative and a more quantitative criterion has to be found which is left to future work. For collisions with $v_0 \lesssim 7.5\,\mathrm{m/s}$, which covers most of the sticking and bouncing regimes, five times the crossing time is used as a rough estimate for the simulated time. In the fragmentation regime with $v_0 \gtrsim 7.5\,\mathrm{m/s}$ the simulation is run for 0.7 to 1 s. The final particle distribution is evaluated by means of the pro-

Initial filling factor	$\phi_\mathrm{i} = 0.15$
Target radius	$r_\mathrm{t} = 10\,\mathrm{cm}$
Target mass	$m_\mathrm{t} = 1.26\,\mathrm{kg}$
No. SPH part. target	238,238
SPH particle mass	$5.27 \times 10^{-6}\,\mathrm{kg}$

projectile radius r_p	projectile mass m_p	SPH particles projectile
2	0.0100	1,905
4	0.0803	15,234
5	0.157	29,794
6	0.271	51,477
8	0.643	121,979
10	1.26	238.238

Initial filling factor	$\phi_\mathrm{i} = 0.35$
Target radius	$r_\mathrm{t} = 10\,\mathrm{cm}$
Target mass	$m_\mathrm{t} = 2.93\,\mathrm{kg}$
No. SPH part. target	238,238
SPH particle mass	$1.23 \times 10^{-5}\,\mathrm{kg}$

projectile radius r_p	projectile mass m_p	SPH particles projectile
2	0.0234	1,905
4	0.187	15,234
5	0.366	29,794
6	0.633	51,477
10	2.93	238,238

Initial filling factor	$\phi_\mathrm{i} = 0.55$
Target radius	$r_\mathrm{t} = 10\,\mathrm{cm}$
Target mass	$m_\mathrm{t} = 4.60\,\mathrm{kg}$
No. SPH part. target	238,238
SPH particle mass	$1.93 \times 10^{-5}\,\mathrm{kg}$

projectile radius r_p	projectile mass m_p	SPH particles projectile
2	0.0368	1,905
4	0.294	15,234
6	0.995	51,477
10	4.60	238,238

Table 6.7. *Initial parameters of the head-on collision series.* The table lists the initial properties of the spherical homogeneous non-rotating targets and projectiles used for the head-on collision simulations in Sec. 6.4. The target and projectile masses change with their initial filling factors $\phi_\mathrm{i} = 0.15$ (top), $\phi_\mathrm{i} = 0.35$ (middle), and $\phi_\mathrm{i} = 0.55$ (bottom).

gram `fragment` (see Appx. A.2). The resulting fragment distribution is categorised according to the four-population model presented in Sec. 6.1, i.e. according to their mass the fragments are classed as the largest fragment, the second largest fragment, a member of the power-law population, or a member of the sub-resolution population.

6.4.2. Simulation results

The results of this broad study are shown as the final mass against collision velocity for the largest fragment (Fig. 6.32), second largest fragment (Fig. 6.34), the power-law population (Fig. 6.35), and the sub-resolution population (Fig. 6.36). The masses are normalised in a suitable way. The figures are divided into the results for dust material of high porosity ($\phi_\mathrm{i} = 0.15$, top), intermediate porosity ($\phi_\mathrm{i} = 0.35$, middle), and low porosity ($\phi_\mathrm{i} = 0.55$, bottom). The different curves indicate collisions with different projectile radii. In Fig. 6.33 the normalised mass of the largest fragment is plotted over the momentum of the initial projectile for reasons of comparison. In the following discussion I will identify the most important features of each fragment population with the main focus on the effect of porosity.
Besides the analysis according to the four-population model I present snapshots of collisions with different projectile radii in Fig. 6.29 ($\phi_\mathrm{i} = 0.15$), Fig. 6.30 ($\phi_\mathrm{i} = 0.35$), and Fig. 6.31 ($\phi_\mathrm{i} = 0.55$). In Sec. 6.1 I have already pointed out that in any collision an interplay between sticking, bouncing, and fragmentation processes takes place. While in the preceding sections these more illustrative terms have been used, I abandon them in this section. Instead I define a *gain regime*, where the largest fragment is more massive than before the collision, a *neutral regime* where the largest fragment possesses approximately the same mass as before the collision, and finally a *loss regime* where the largest fragment has lost mass. The terms “sticking”, “bouncing”, and “fragmentation” will exclusively be used for the respective physical processes from now on.

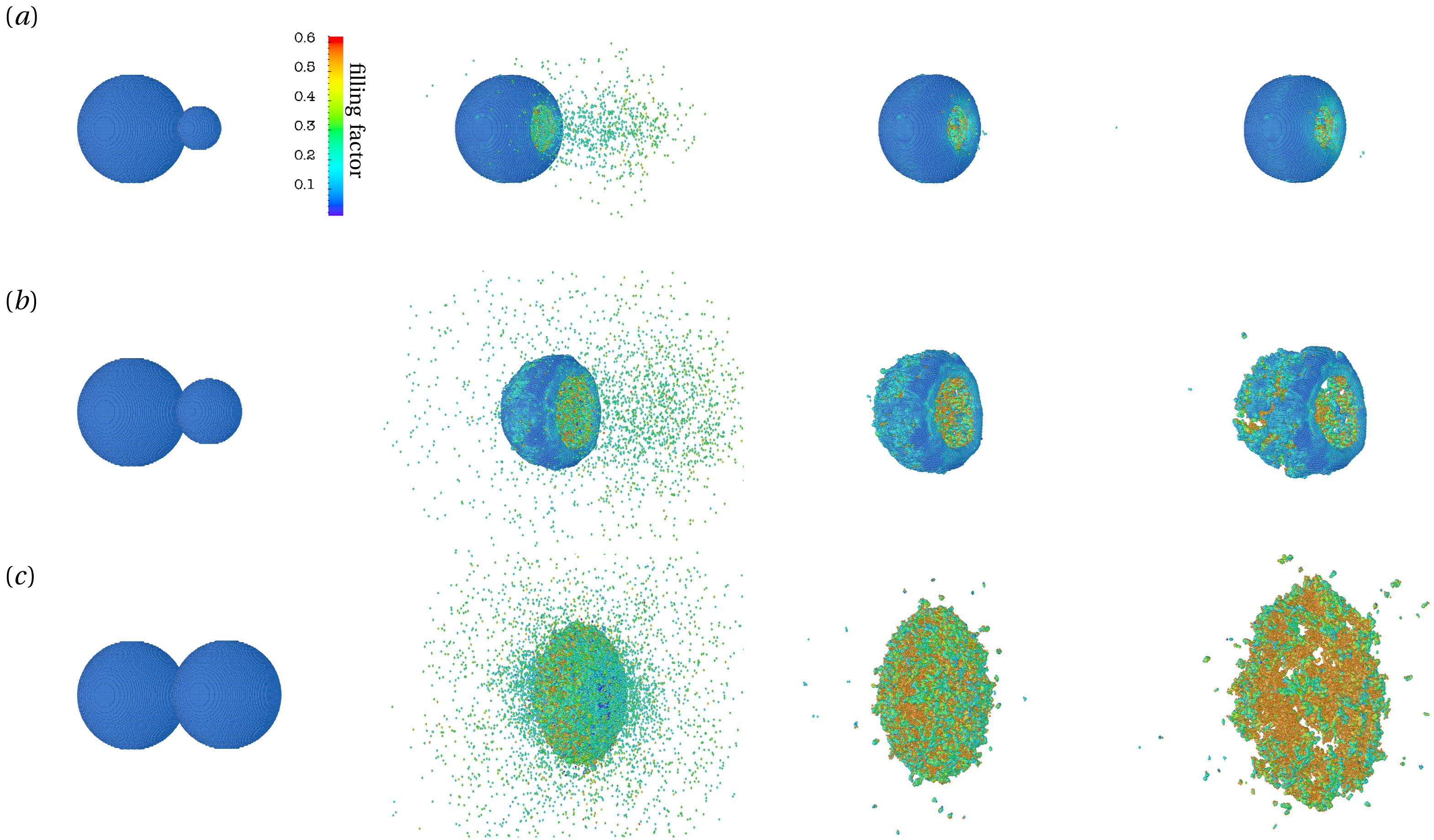

Figure 6.29. *Head-on collisions I – high porosity collision sequences.* The homogeneous aggregates have an initial filling factor of $\phi_\mathrm{i} = 0.15$. The projectiles with radii $r_\mathrm{p} = 4\,\mathrm{cm}$ (a), $r_\mathrm{p} = 6\,\mathrm{cm}$ (b), and $r_\mathrm{p} = 10\,\mathrm{cm}$ (c) hit a 10 cm target with a collision velocity of $v_0 = 7.5\,\mathrm{m/s}$. From the left to the right the simulation times are 0, 40, 80, and 160 ms. For the latter two panels, single SPH particles are removed for the purpose of visibility. The filling factor is colour coded in this figure.

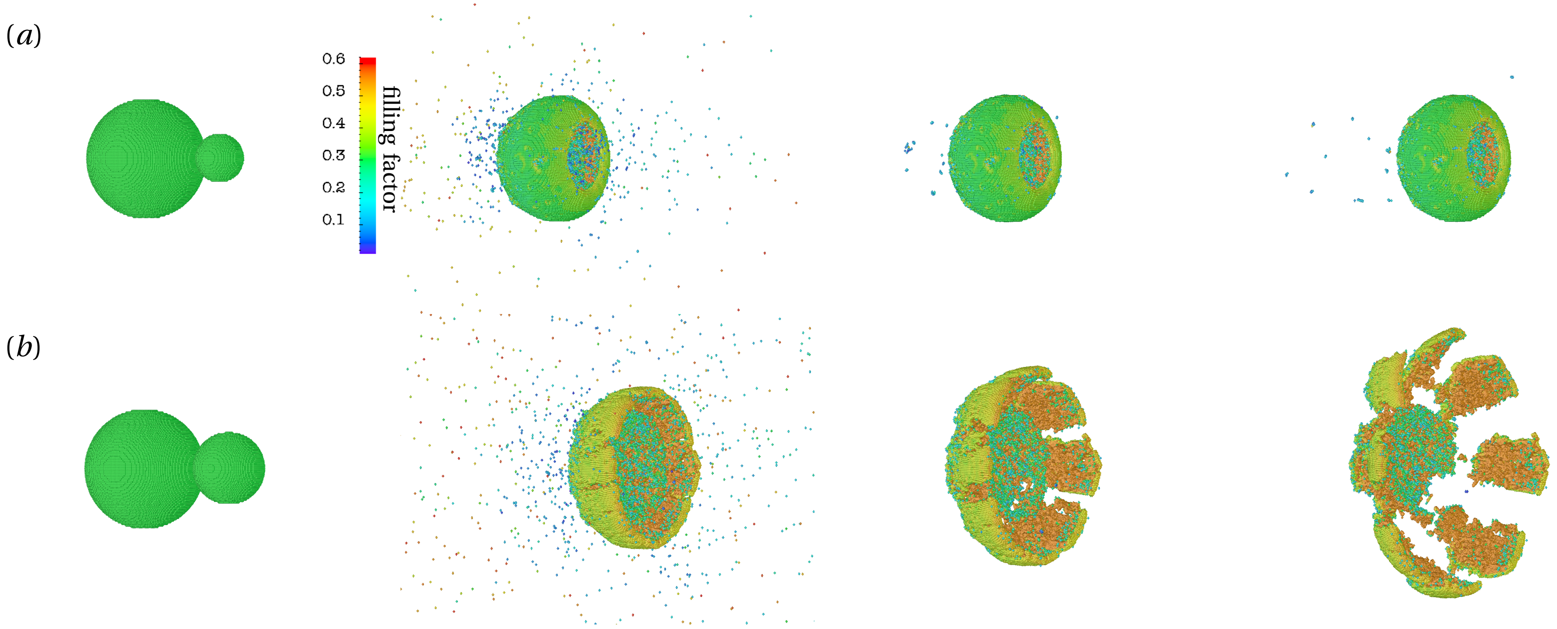

Figure 6.30. *Head-on collisions II – intermediate porosity collision sequences.* The homogeneous aggregates have an initial filling factor of $\phi_\mathrm{i} = 0.35$. The projectiles with radii $r_\mathrm{p} = 4\,\mathrm{cm}$ (a) and $r_\mathrm{p} = 6\,\mathrm{cm}$ (b) hit a 10 cm target with a collision velocity of $v_0 = 15\,\mathrm{m/s}$. From the left to the right the simulation times are 0, 40, 80, and 160 ms. For the latter two panels, single SPH particles are removed for the purpose of visibility. The filling factor is colour coded in this figure.

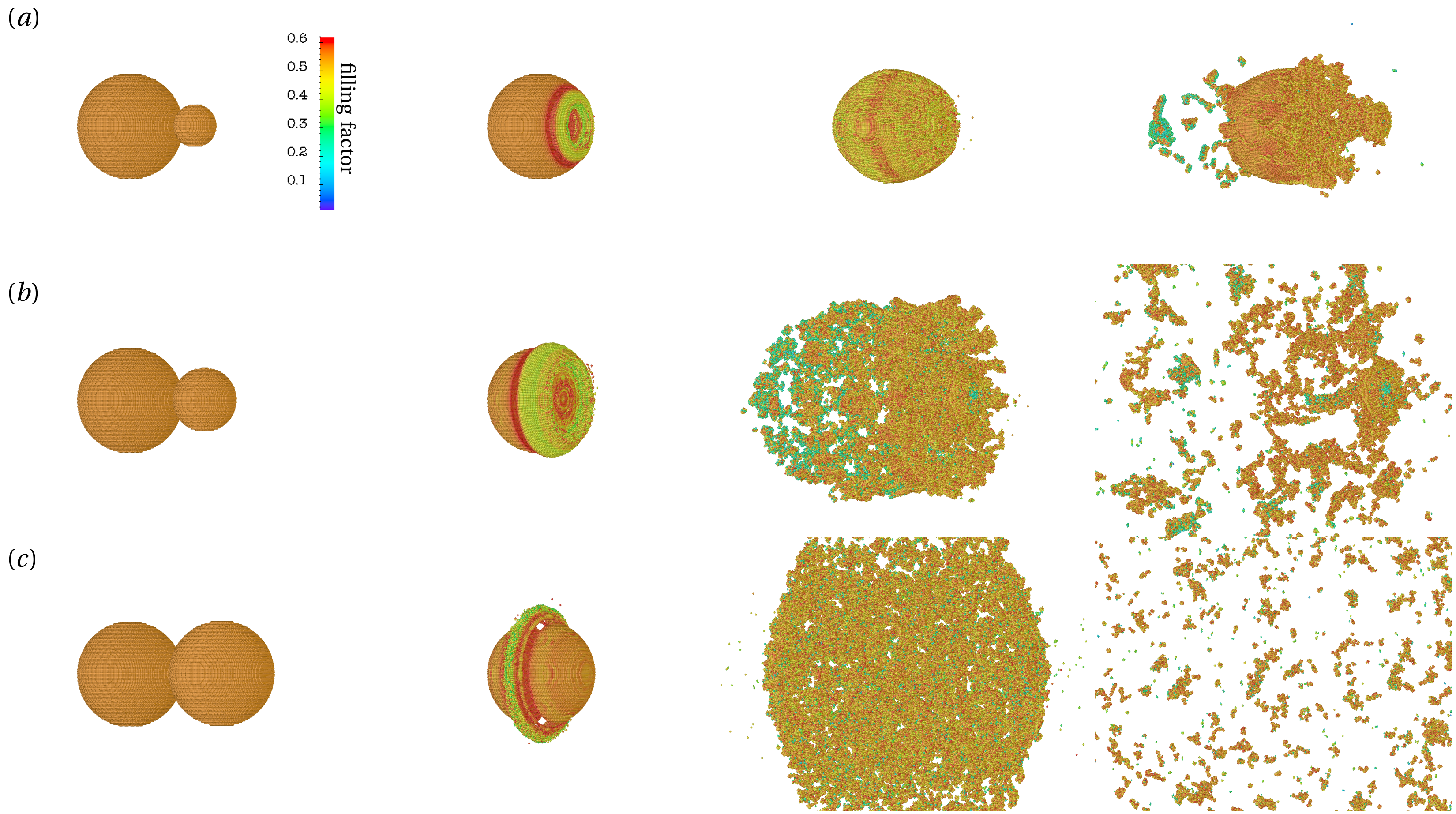

Figure 6.31. *Head-on collisions III – low porosity collision sequences.* The homogeneous aggregates have an initial filling factor of $\phi_\mathrm{i} = 0.55$. The projectiles with radii $r_\mathrm{p} = 4\,\mathrm{cm}$ (a), $r_\mathrm{p} = 6\,\mathrm{cm}$ (b), and $r_\mathrm{p} = 10\,\mathrm{cm}$ (c) hit a 10 cm target with a collision velocity of $v_0 = 5\,\mathrm{m/s}$. From the left to the right the simulation times are 0, 40, 160, and 560 ms. For the latter two panels, single SPH particles are removed for the purpose of visibility. The filling factor is colour coded in this figure.

Largest fragment

mass normalisation

I start with the variation of the mass of the largest fragment m_1 with collision velocity v_0 in Fig. 6.32. The value of m_1 is normalised by the target mass m_t. In this representation the gain regime is indicated by $m_1\, m_\mathrm{t}^{-1} > 1$, the loss regime by $m_1\, m_\mathrm{t}^{-1} < 1$, and the neutral regime by $m_1\, m_\mathrm{t}^{-1} = 1$.

high porosity

In collisions with aggregates of *high porosity* (top) growth occurs in all collisions with $v_0 \lesssim 7.5\,\mathrm{m/s}$. In this *gain regime* the resulting mass is simply given by the sum of target and projectile mass. However, at very low impact velocities the aggregates only touch each other and become connected loosely (see also Sec. 6.3.1, in particular Fig. 6.22). The gain regime is explored explicitly for collisions with projectile radii of 2, 6, and 10 cm and it can be assumed that the outcome will be similar for other projectile radii. At $v_0 \sim 6\,\mathrm{m/s}$ to $8\,\mathrm{m/s}$ all curves (except $r_\mathrm{p} = 2\,\mathrm{cm}$) start to drop rapidly below $m_1\, m_\mathrm{t}^{-1} = 1$. In this velocity range the transition from the gain regime to the *loss regime* occurs. The transition starts where $m_1 < m_\mathrm{t} + m_\mathrm{p}$. There is a trend that larger projectiles produce smaller largest fragments at the same impact velocity. The *gain-loss transition* velocity seems to decrease with increasing impact velocity. Projectiles with radius 2 cm intrude deeply into the target. At high impact velocities they cause material to be ejected from the impact site and opposite to it. Although the projectile does not pierce the target, the impact launches elastic waves which cause the ejection of material opposite to the impact site. This behaviour was already seen in high velocity impact experiments (Paraskov et al. 2007).

intermediate porosity

In the *intermediate porosity* case (middle) a *neutral regime* appears for collision velocities $v_0 \lesssim 1\,\mathrm{m/s}$. As already discussed in Sec. 6.1.1, the aggregate bouncing in the neutral regime is never fully growth neutral and a small amount of mass is always transferred between the collision partners. This effect causes small deviations from $m_1\, m_\mathrm{t}^{-1} = 1$, which are marginal compared to the target and projectile masses. The *transition* from the *neutral to the gain regime* starts where $m_1 \gtrsim m_\mathrm{t}$. From the given simulations it can not be assessed whether the neutral-gain transition velocity depends on the projectile size. For higher velocities it is succeeded by a *gain regime*. The *transition* from the *gain to the loss regime* is more spread out than in the high porosity case. For the $\phi_\mathrm{i} = 0.35$ aggregates all curves (except $r_\mathrm{p} = 2\,\mathrm{cm}$ again) drop below $m_1\, m_\mathrm{t}^{-1} = 1$ at velocities between $v_0 \sim 10\,\mathrm{m/s}$ and $15\,\mathrm{m/s}$. As in the high porosity case, the gain-neutral transition velocity decreases with increasing impact velocity.

low porosity

Finally, in the *low porosity* case (bottom) one encounters a third type of transition: the *neutral-loss transition*. In the velocity regime $v_0 \leq 1\,\mathrm{m/s}$ nearly growth neutral bouncing occurs for all projectile sizes. Between $v_0 \sim 1\,\mathrm{m/s}$ and $3\,\mathrm{m/s}$ the neutral-loss transition takes place for all projectile sizes. For large projectiles (6 and 10 cm) the target and projectile shatter, whereas for the smaller projectile some parts of the projectile stick to the target. However in the latter collisions, more mass is eroded from the target by ejection at and opposite the impact site such that mass loss of the target results. In particular these simulations show that sticking processes do not necessarily lead to pre-planetesimal growth. This issue has already been discussed in Sec. 6.1.

To assess the influence of the projectile mass on the mass of the largest fragment Fig. 6.33 shows the variation of $m_1\, m_\mathrm{t}^{-1}$ with the momentum of the projectile p_p. This representation reveals that all transitions, i.e. the gain-loss transition in the high and intermediate porosity case, the neutral-gain transition in the intermediate porosity case, and also the neutral-loss transition in the low porosity case depend strongly on the mass of the projectile. The transition momentum increases with increasing projectile size. Since in the context of planet formation the collision velocity is the quantity which is most frequently used, I stick to this representation furtheron.

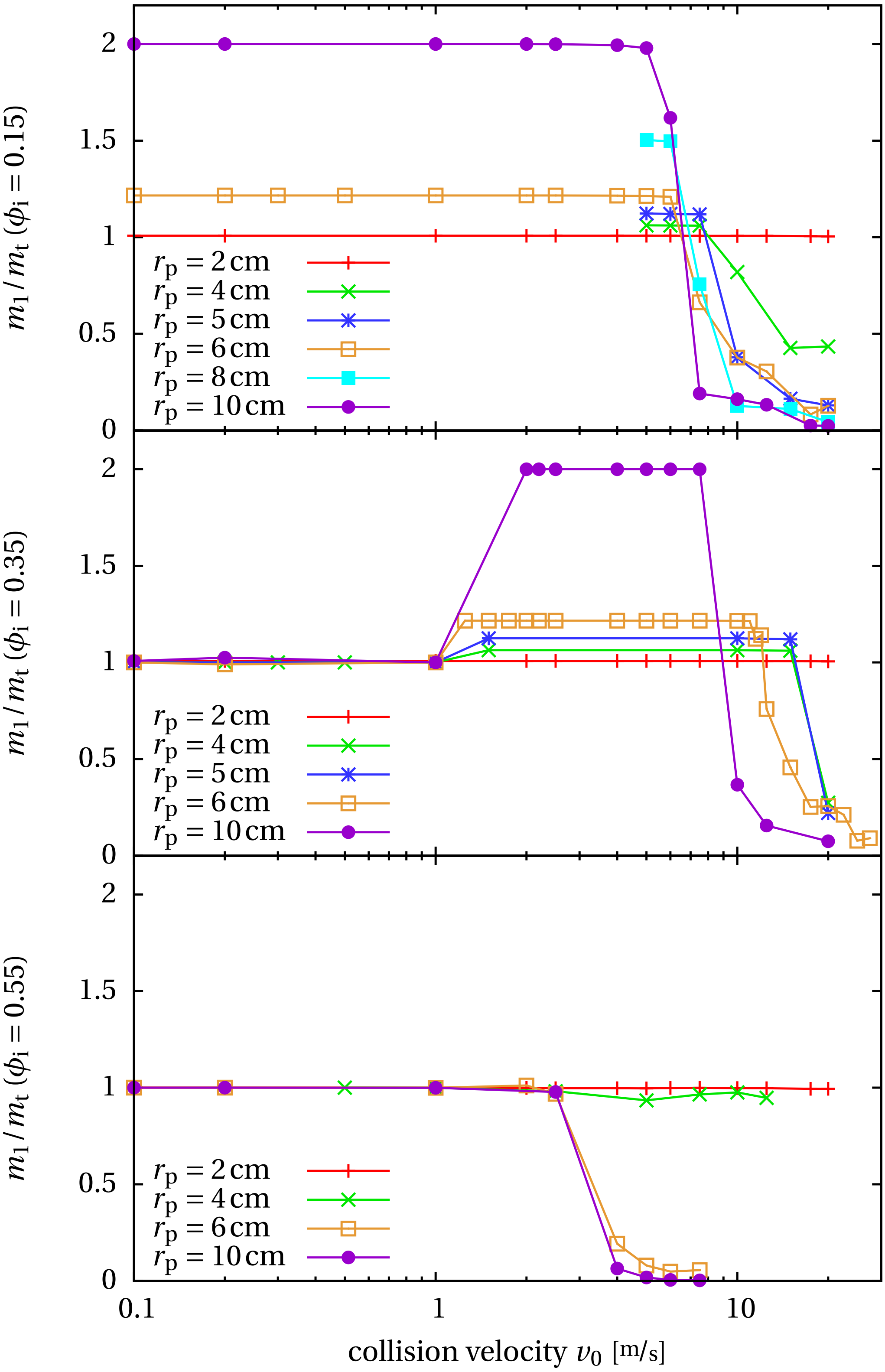

Figure 6.32. *Head-on collisions IV – mass against collision velocity (largest fragment).* The mass of the largest fragment m_1 is normalised by the target mass m_t. The projectile radii r_p and other initial parameters are listed in Tab. 6.7. The homogeneous aggregates have an initial filling factor $\phi_i = 0.15$ (top), $\phi_i = 0.35$ (middle), and $\phi_i = 0.55$ (bottom).

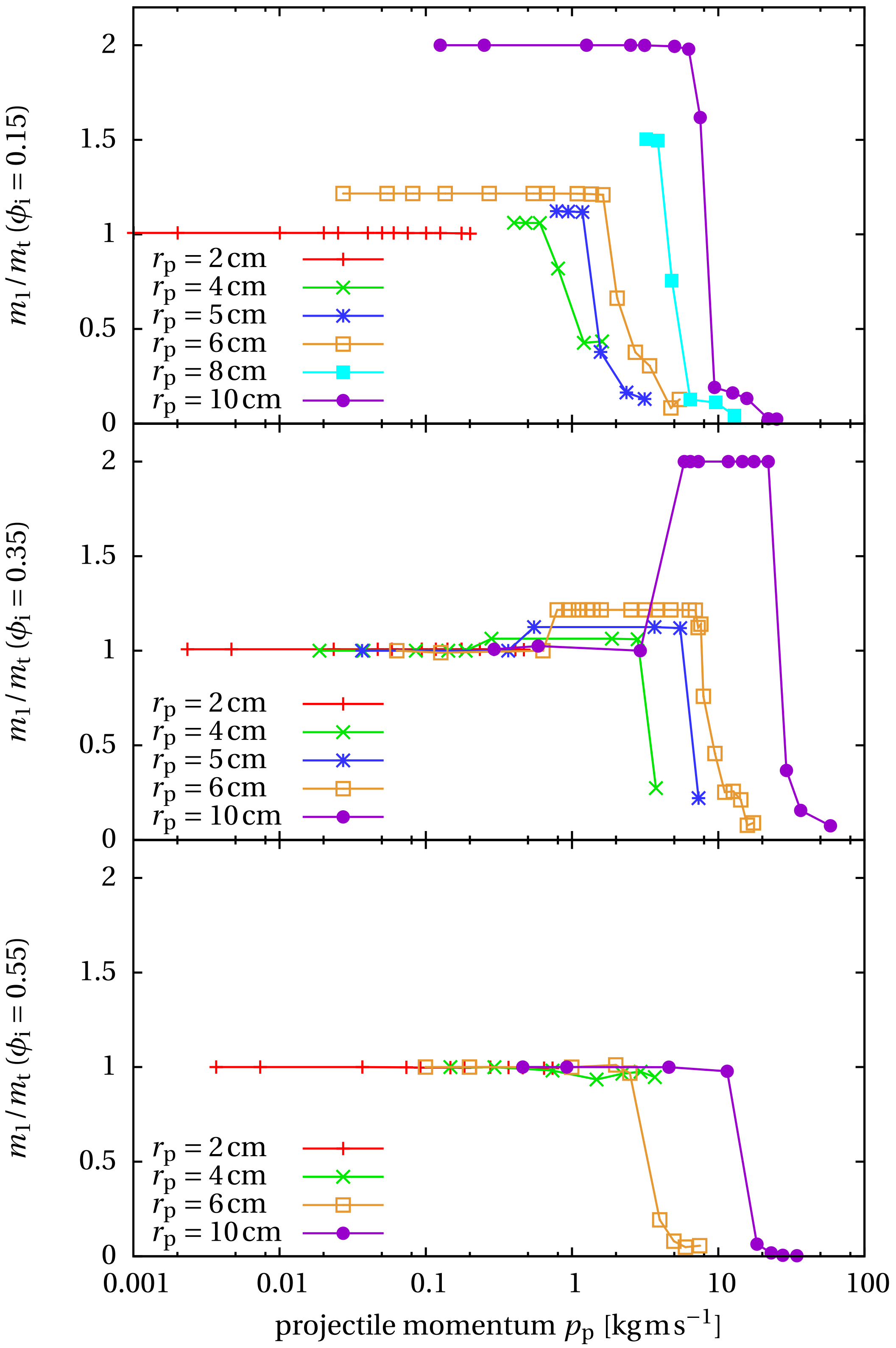

Figure 6.33. *Head-on collisions V – against projectile momentum (largest fragment).* The mass of the largest fragment m_1 is normalised by the target mass m_t. The projectile radii r_p and other initial parameters are listed in Tab. 6.7. The homogeneous aggregates have an initial filling factor $\phi_i = 0.15$ (top), $\phi_i = 0.35$ (middle), and $\phi_i = 0.55$ (bottom).

Second largest fragment

mass normalisation

The most important features for pre-planetesimal growth are already identified in the figures of the largest fragment. These turn up again in Fig. 6.34, which shows how the second largest fragment varies with collision velocity. It is again split up into the high porosity (top), intermediate porosity (middle), and low porosity (bottom) cases. The purpose of the second largest fragment is the accurate mapping of bouncing collisions (see Sec. 6.1.2). For this reason the mass of the second largest fragment m_2 is normalised by the mass of the projectile m_p. The neutral regime where bouncing occurs is then represented by $m_2\, m_\mathrm{p}^{-1} \sim 1$. Pure sticking events without any fragmentation can be identified by $m_2\, m_\mathrm{p}^{-1} \sim 0$.

high porosity

Regarding the *high porosity* case, there is no second largest fragment in the gain regime $0.1\,\mathrm{m/s} < v_0 \lesssim 6\,\mathrm{m/s}$. This is because the projectile sticks to the target in this regime and no fragments are produced. The *gain-loss transition* is characterised by the appearance of a second largest fragment. For radii $r_\mathrm{p} \leq 6\,\mathrm{cm}$ and $v_0 \sim 10\,\mathrm{m/s}$ the projectile pierces the target and the second largest fragment is the projectile which has accreted material from the target (Fig. 6.29, b). For this reason the second largest fragment is more massive than the initial projectile, i.e. $m_2 > m_\mathrm{p}$. For larger projectile radii the target and projectile shatter and $m_2 < m_\mathrm{p}$. There is a trend that the mass of the second largest fragment decreases with increasing projectile radius.

intermediate porosity

At low impact velocities $v_0 \leq 1\,\mathrm{m/s}$ the *intermediate porosity* case starts of with a neutral regime where the projectile rebounds from the target with little mass transfer, so $m_2 \sim m_\mathrm{p}$. Entering the gain regime m_2 drops to zero indicating that the projectile sticks to the target. This marks the *neutral-gain transition* at $\sim 1\,\mathrm{m/s}$. Similar to the high porosity case the *gain-loss transition* can be identified by the re-appearance of a second largest fragment. For all projectile radii the second largest fragment is a product of a collision where the target and projectile shatter. As in the high porosity case the mass of the second largest fragment decreases with increasing projectile size.

low porosity

In the *low porosity* case the projectile rebounds with nearly unaltered mass and appears as the second largest fragment for $v_0 \leq 1\,\mathrm{m/s}$ and all projectile radii. This represents the neutral regime. For higher collision velocities the projectile rebounds from the target and due to induced elastic waves both objects shatter (see also Fig. 6.31, in particular panel a). The mass of the second largest fragment drops below $m_2\, m_\mathrm{p}^{-1} \sim 1$. The second largest fragment may consist of any fragment of the shattered fragment distribution and is not necessarily identical to a part of the rebounded and shattered projectile.

Power-law population

mass normalisation

I now turn to the variation of the mass of the power-law population with impact velocity in Fig. 6.35. The figure displays the three porosity cases again. The mass of the power-law population is a suitable measure for the degree of fragmentation. For this reason I normalise m_pw by the total mass of the system m_tot to assess the mass fraction of the masses smaller than the mass of the second largest fragment.

In all porosity cases the appearance of a power-law population indicates the onset of fragmentation. As already seen in the discussions for the largest and second largest fragments, fragmentation sets in at different collision velocities for different projectile radii. The larger the projectile the lower the velocity for the transition to the loss regime. From the power-law population diagram it is not evident whether this transition comes from the gain or neutral regime. For the low porosity case, m_pw at first increases and then decreases for the two largest projectile radii with

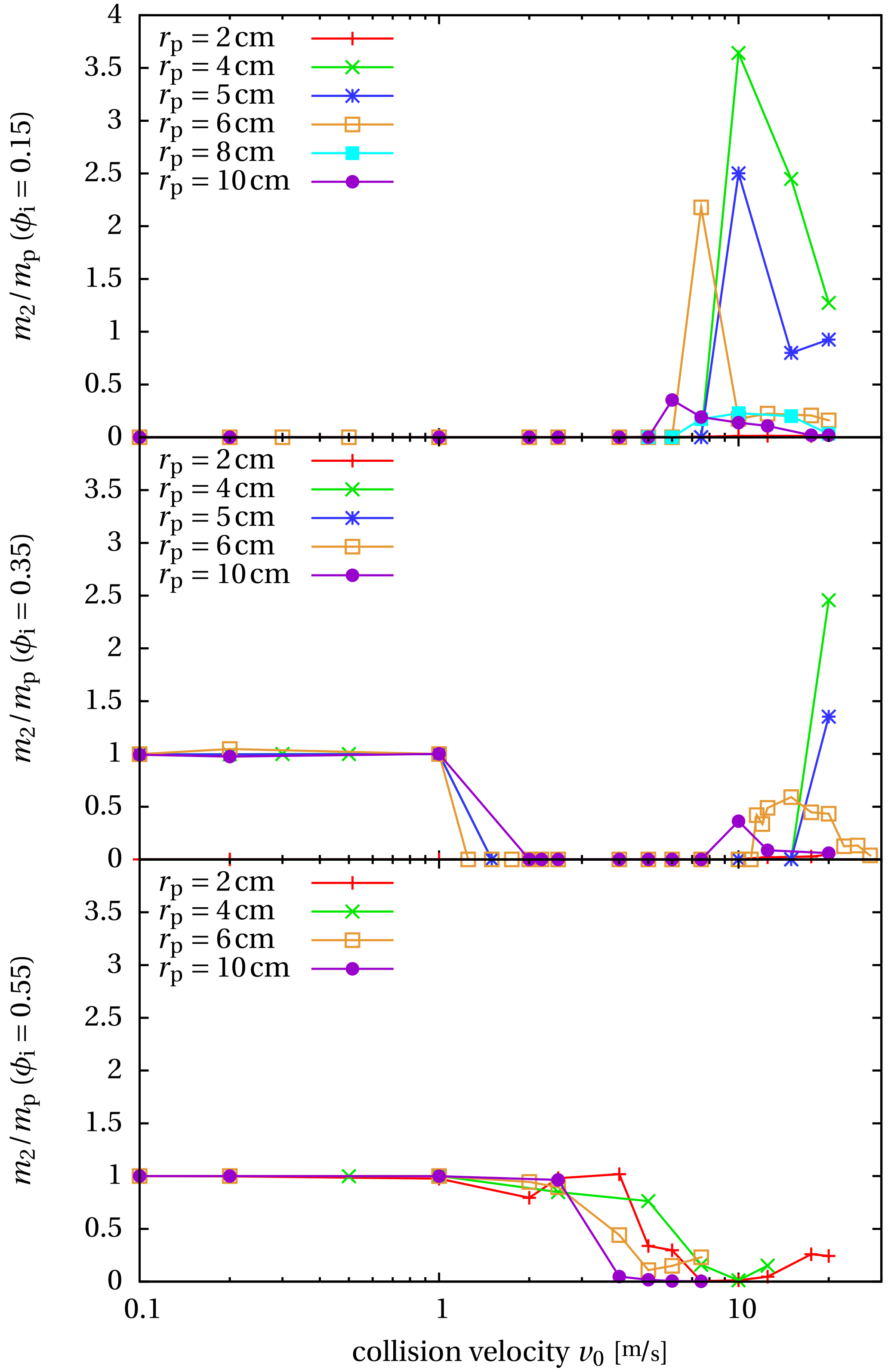

Figure 6.34. *Head-on collisions VI – mass against collision velocity (second largest fragment).* The mass of the second largest fragment m_2 is normalised by the projectile mass m_p. The projectile radii r_p and other initial parameters are listed in Tab. 6.7. The homogeneous aggregates have an initial filling factor $\phi_i = 0.15$ (top), $\phi_i = 0.35$ (middle), and $\phi_i = 0.55$ (bottom).

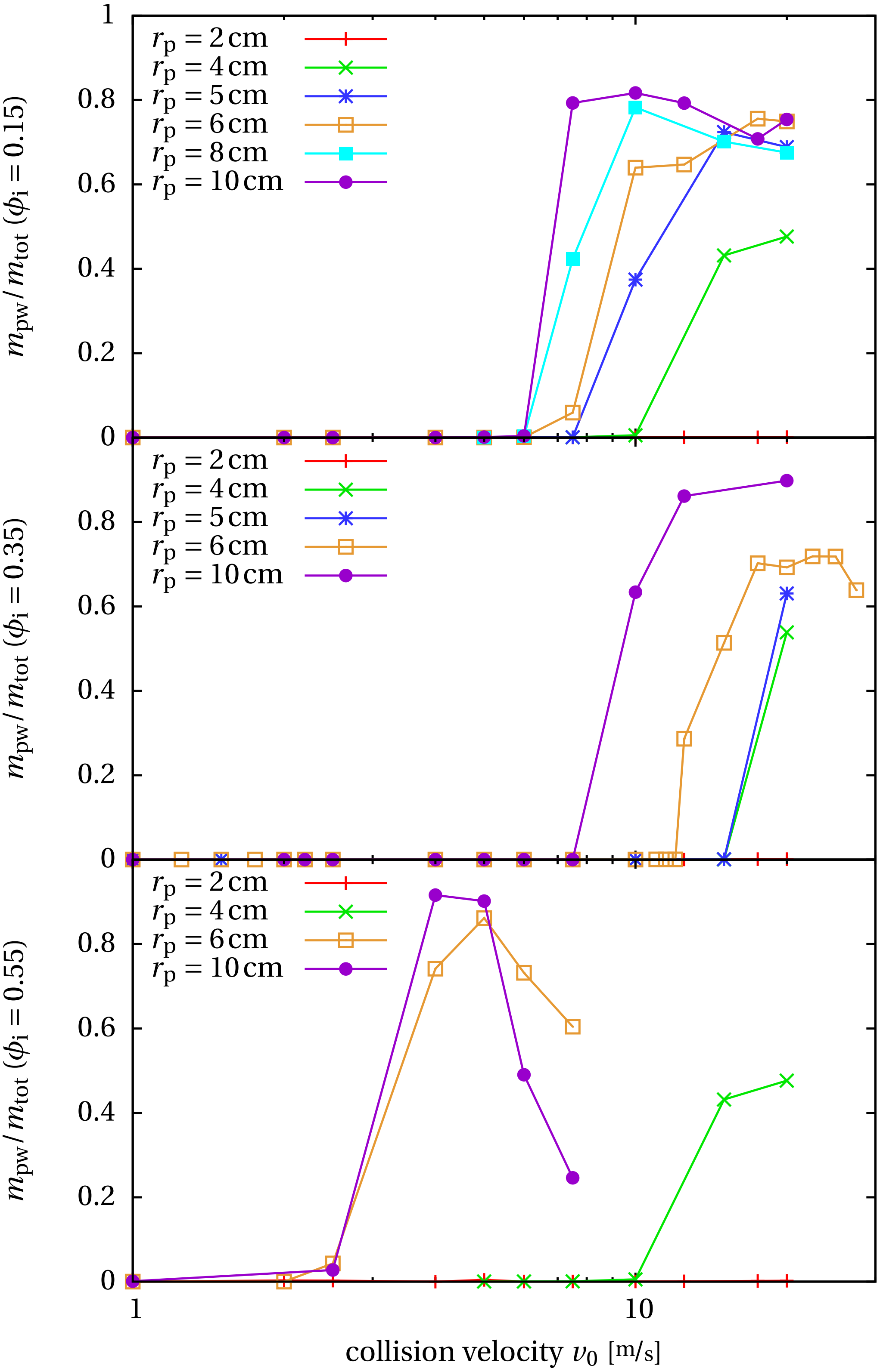

Figure 6.35. *Head-on collisions VII – mass against collision velocity (power-law population).* The mass of the power-law population m_{pw} is normalised by the total mass m_{tot}. The projectile radii r_p and other initial parameters are listed in Tab. 6.7. The homogeneous aggregates have an initial filling factor $\phi_i = 0.15$ (top), $\phi_i = 0.35$ (middle), and $\phi_i = 0.55$ (bottom).

higher impact velocity. The curve for the 6 cm projectile in the intermediate porosity case shows the same trend but a plateau appears in between the increase and decrease. At these impact energies the target and projectile are shattered to a very large degree such that the fragments reach the lower resolution limit and a large number of single SPH particles are produced. Their mass appears in the sub-resolution population as discussed below. In the high porosity case the curves roughly saturate at a plateau value. For projectiles with $r_\mathrm{p} \geq 5\,\mathrm{cm}$ this value is $\sim 0.7\,\mathrm{m}_\mathrm{tot}$. However, for higher collision velocities I expect the mass of the power-law population to decrease transferring its mass to the sub-resolution population. The same increase-plateau-decrease behaviour is also expected for the intermediate porosity case. It is remarkable that hardly any mass is stored in the power-law population in collisions with $r_\mathrm{p} = 2\,\mathrm{cm}$ in all porosity cases.

Sub-resolution population

At the end of this description I draw the reader's attention to the variation of the sub-resolution population with impact velocity in Fig. 6.36. The sub-resolution population is an indication of sufficient resolution as well as an upper mass limit for the dust produced in the collision (see Sec. 6.1.2). The figure shows the result of collisions for high porosity (top), intermediate porosity (middle), and low porosity (bottom) again.

I note that a significant sub-resolution population appears at collision velocities larger than the transition velocities to the loss regime in the other diagrams. This is because at lower collision energies the fragments tend to break apart upon collision and contribute to the power-law population. With higher impact velocities the objects shatter more and more which results in an increasing sub-resolution population. For the same collision velocity, the mass of the produced sub-resolution population increases with increasing projectile radius which is particularly evident in the low porosity case. Again for collisions with the smallest projectile hardly any mass ends up in the sub-resolution population. Only for the low porosity case is a significant amount visible.

6.4.3. Discussion and outlook

In pre-planetesimal collisions kinetic energy is dissipated by breaking molecular bonds (see Sec. 2.2.3, 2.2.4 and 3.2). Macroscopically this is achieved by compacting and fragmenting an aggregate. Since the compressive strength for most of the filling factor regime is smaller then the (absolute value of the) tensile strength (see Fig. 5.24) the preferred way of energy dissipation for aggregates of high and intermediate porosity is compaction. For filling factors where the compressive strength exceeds the tensile strength fragmentation sets in. This filling factor is close to maximum compaction.

gain regime

In the preceding description of pre-planetesimal collisions three different regimes could be distinguished: the gain, neutral, and loss regime. The *gain regime* is only seen for high and intermediate porosity aggregates. This is because the initial filling factor, which is significantly below the maximum filling factor, permits compaction of the aggregates. The kinetic energy of the projectile is low enough such that most of the kinetic energy can be dissipated by compaction. The compaction leads to increased filling factors at the contact area of both aggregates which causes the projectile to stick to the target (see also Sec. 6.3, in particular Fig. 6.22, left, and Fig. 6.26, d and e). In the low porosity case where the filling factor is close to the maximum, little energy can be dissipated by compaction which prevents the sticking of aggregates.

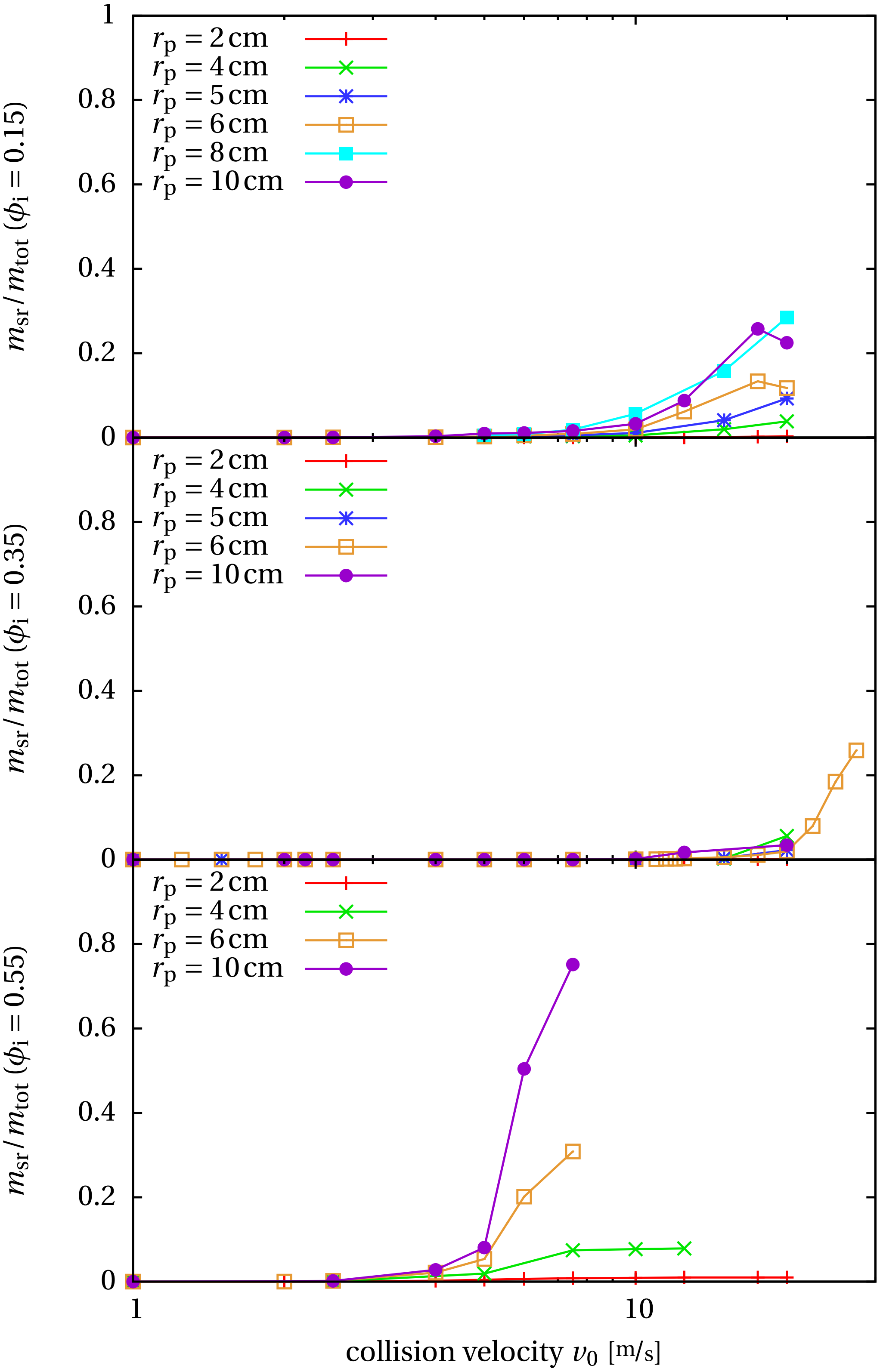

Figure 6.36. *Head-on collisions VIII – mass against collision velocity (sub-resolution population).* The mass of the sub-resolution population m_{sr} is normalised by the total mass m_{tot}. The projectile radii r_p and other initial parameters are listed in Tab. 6.7. The homogeneous aggregates have an initial filling factor $\phi_i = 0.15$ (top), $\phi_i = 0.35$ (middle), and $\phi_i = 0.55$ (bottom).

neutral regime

The *neutral regime* is visible in the intermediate and low porosity case. This is because this regime is characterised by the rebound of the projectile. Bouncing requires a sufficient elastic loading of the target and projectile without fragmentation. In both porosity cases the neutral regime can be found at low collision energies. In the intermediate porosity case the collision energy is not sufficient for a compaction of the aggregates, which eventually leads to sticking, and in the low porosity case the energy is too low to shatter the target and projectile.

loss regime

The *loss regime* is present for all porosity cases. This is because at high collision velocities the kinetic energy cannot entirely be dissipated by compaction. The energy excess has to be dissipated by fragmentation, which causes the loss regime.

Given the three regimes gain, neutral, and loss, six transitions are theoretically possible. However, the loss-gain and loss-neutral transitions are physically not reasonable. This is evident from the above discussion. Fragmentation is the result of high velocity collisions and even smaller fragments are produced at higher collision velocities.

neutral-gain transition

The *neutral-gain transition* can be seen for aggregates of intermediate porosity at $v_0 \sim 1\,\mathrm{m/s}$. It can also be regarded as a transition from bouncing to sticking collisions. At sufficiently low collision velocities only a small fraction of the projectile energy is dissipated by compaction and a large part is stored in elastic loading, which is released in the rebound of the projectile. This can be seen from the residual energy of the system (Fig. 6.11). With higher collision velocities the contact area of the collision partners increases as well as the filling factors in this region. Together with the fact that less energy is stored in elastic loading and is not available for rebound, the transition to sticking occurs (see also Sec. 6.3). Neutral-gain transitions can be expected for all initial filling factors in an intermediate regime. I expect the transition velocity to decrease with the initial filling factor because the compaction threshold is lowered. This threshold velocity might also vary slightly with projectile radius.

gain-loss transition

The *gain-loss transition* only exists for aggregates of high and intermediate porosity. This is because only these aggregates can be sufficiently compressed to allow for sticking and hence a gain regime. As discussed above, the transition occurs when there is more kinetic energy than the amount that can be dissipated by compaction. The energy excess leads to shattering and the system enters the loss regime. The threshold velocity varies with projectile size for the same filling factor and it is important to note that it also varies with initial filling factor. Very porous aggregates can be compressed easily but they also fragment more easily. Aggregates of intermediate porosity are more stable and feature higher gain-loss thresholds.

neutral-loss transition

The *neutral-loss transition* is only visible for aggregates of low porosity. This is because only low-porosity aggregates lack the ability to be compacted. This transition is characterised by a rebounding projectile but the elastic waves induced in both objects cause them to shatter. It is important to note that the neutral-loss transition velocity is much lower than the gain-loss transition velocities of the high and intermediate porosity cases.

gain-neutral transition

In the velocity and size range of the simulations presented no *gain-neutral transition* could be identified. This might be because the minimum collision velocity $v_0 = 0.1\,\mathrm{m/s}$ of the considered velocity range is too large. Güttler et al. (2010) assume a sticking-bouncing (gain-neutral) transition for $v_0 \sim 1 \times 10^{-5}\,\mathrm{m/s}$ for comparable projectile sizes. However, this value is based on theoretical considerations and might be much larger (see Sec. 6.3.1).

Since Güttler et al. (2010) presented the most comprehensive collection of laboratory experiments with SiO_2 dust, I compare the simulation results to their findings of nearly equal sized aggregates. For the sake of simplicity they do not distinguish between different filling factors but categorise their aggregates into “porous” with $\phi_\mathrm{i} \leq 0.40$ and “compact” with $\phi_\mathrm{i} > 0.40$. For collisions of a porous projectile with a porous target, of a compact projectile with a compact target, and of a compact projectile with a porous target they assume a bouncing-fragmentation (neutral-loss) collision velocity of $v_0 \sim 1\,\mathrm{m/s}$. The type of transition and the threshold velocity more resemble my findings for aggregates with low porosity. I note that the inhomogeneity of the aggregates might affect the velocity thresholds as shown in Sec. 6.2.

However, Güttler et al. (2010) find a bouncing-sticking (neutral-gain) transition at $v_0 \sim 1\,\mathrm{m/s}$ and a sticking-fragmentation (gain-loss) transition at $v_0 \sim 10\,\mathrm{m/s}$ for collisions of a porous projectile and a compact target. It remains unexplained why these results are different from the case of a compact projectile hitting a porous target. From the symmetry of the system one would expect the same transition thresholds. Nevertheless, these results resemble my collision outcomes for aggregates of intermediate porosity (see also Sec. 6.1).

The simulation results of this section reveal that the assumptions by Güttler et al. (2010) are to be revised. It is not sufficient to distinguish between porous and compact aggregates. The simulated collisions show that not only do the threshold values for the transitions vary with the filling factor, but so do transition. In addition the gain-loss transition threshold velocity, which is the most important for pre-planetesimal growth, also varies with projectile size, which is most evident in the intermediate porosity case. The simulations also indicate that the gain-loss threshold might be much higher than estimated by Güttler et al. (2010). This might be sufficient for pre-planetesimals to break through the fragmentation barrier (see Sec. 2.3.1).

A more detailed and quantitative analysis of these data is left to future work. This has the following reasons: (1) a detailed analysis requires more simulations, in particular in the transition regions. (2) In the loss regime fragmentation is dominant. Especially for the sizes of the largest and second largest fragment in the transition regions, errors of the masses have to be estimated to establish a profound collision model. This is because slight numerical fluctuations might determine the masses of these objects. To assess the statistics simulations with different lattice types, lattice orientations, and also different resolutions have to be carried out for selected collisions. The inhomogeneity damage model outlined in Sec. 6.2 might be useful for this investigation. (3) It is still problematic to determine the end time of a fragmenting collision. Fragments might break apart due to rotation on timescales larger than the collision time scale. Simulation runs with a long time frame have to be carried out to assess the evolution of the fragments, in particular the mass distribution of the power-law population. On the basis of these example runs, the error due to termination of the simulation can be estimated.

Once these issues are settled satisfactorily, a detailed collision model can be constructed. With the aid of the velocity thresholds for the respective transitions, the mass variation for the largest and second largest fragment with collision velocity can be determined with respect to the projectile size and filling factor. In particular the curves in the loss regime can be fitted with power-laws. Similar fit functions should be found for the masses of the power-law and sub-resolution population. For the former the mass distribution can be fitted by a power-law and the dependence of the fit parameters on projectile size and filling factor can be estimated. In this way the simplifying assumptions of Güttler et al. (2010) can be improved and a detailed collision model can be constructed.

7. Conclusions

7.1. Summary and discussion

The subject of this thesis is the realistic simulation of pre-planetesimal material, the production of a catalogue of pre-planetesimal collisions, and the design of a suitable transfer method of the acquired data to global dust coagulation models in protoplanetary discs. This is to understand the formation of kilometre sized planetesimals which are the seedlings for the planet formation process. For this purpose I have reviewed the state of the art knowledge of planet formation in Ch. 2. In particular, it has been pointed out that the existence of planetesimals is essential for both the accretion and the gravitational instability hypothesis of planet formation. Thus, the topic of this thesis is at the basis of any planet formation theory. In the further course it has been demonstrated that pre-planetesimals of centimetre size are porous objects composed of protoplanetary dust which are created from dust monomers by hit-and-stick, restructuring, and compaction mechanisms. A suitable analogue for protoplanetary material is monodisperse spherical SiO_2 dust. Because of increasing collision velocities the colliding pre-planetesimals encounter three barriers on their way to planetesimals: the drift, bouncing, and fragmentation barriers. The latter two are addressed in this thesis. In the course of the review it became evident that the right mixture of sticking, bouncing, and fragmentation events is necessary to explain both the dust features of late T Tauri discs and the formation of planets.

To explore a suitable method for the investigation of pre-planetesimal collisions and to assess the potential ways of information transfer in this field I have reviewed some neighbouring methods in Ch. 3. Laboratory experiments yield valuable material parameters for the porosity model of this thesis but the direct investigation of pre-planetesimal collisions is limited by the size of the experimental apparatus. Molecular dynamics (MD) simulations directly simulate the interactions between dust monomers and may also be a valuable source for material parameters, in particular those which are hard to measure in the laboratory. However, because of limited computational resources MD simulations are constrained to aggregates well below millimetre size. Global dust coagulation models provide the big picture of planet formation in a protoplanetary disc by simulating the size evolution from dust grains to planets using the laws for particle-gas interaction. These simulations essentially lack data on the outcome of pre-planetesimal collisions. Smoothed particle hydrodynamics (SPH) has been identified as the most suitable method to investigate pre-planetesimal collisions. Because of the continuum approach it possesses no upper size limit for the simulated objects and due to its Lagrangian and particle nature it establishes a natural frame of reference for fragmentation.

In Ch. 4 I have reviewed the SPH method. Since this thesis is concerned with the simulation of solid material I have put a strong focus on solid body mechanics and its SPH implementation. In the same chapter I have also described the applied porosity model. This model is based on the approach by Sirono (2004) but has been significantly improved in this thesis. The compressive strength and tensile strength relations were adopted by Sirono as simple power-laws derived from toner particle measurements. Sirono utilised these relations for the simulation of a different material, namely porous ice. In this thesis the material relations have been replaced by more realistic data from laboratory measurements for SiO_2 dust. Sirono's damage model, which was originally developed for brittle material, has been replaced by a different approach involving the tensile strength. I have also shown that this approach makes the damage restoration model by Sirono unnecessary. Since the strength quantities of the porosity model depend on the filling factor, which is a dimensionless parameter, no length scale is introduced for the simulated objects. Therefore, I have proposed a new damage model which is based on the inhomogeneity of the dust aggregates. The input parameter, which is simply the Gaussian distribution of the filling factors, can be measured in the laboratory which was already demonstrated by Güttler et al. (2009). Since pre-planetesimals are very likely to be inhomogeneous, this approach also improves the realistic simulation of these objects.

To validate the porosity model and to test the correct functionality of the code (Ch. 5), I have performed an intensive calibration process with the aid of three benchmark experiments. At the same time these have been carried out in the laboratory by collaborators. Firstly, the compaction properties have been tested by a glass sphere dropped into a dust sample. Secondly, the elastic properties have been checked by a dust sphere rebounding from a solid surface. Thirdly, the correct reproduction of fragmentation has been verified by a dust sphere shattering at a solid surface. In the calibration process it has turned out that some empirical material relations could not be measured and others were measured statically which has made them inapplicable to dynamic pre-planetesimal collisions. For this reason the benchmark experiments have been used to determine the missing relations by means of parameter studies. In this course, the dynamic compressive strength, the dynamic shear strength, and the bulk modulus, which are hard to measure empirically, have been determined with the aid of numerical simulations. As a byproduct, this procedure may serve as an example of how empirically inaccessible material parameters become accessible by joining computational and laboratory methods. For this determination a number of benchmark features had to be sacrificed. However, the number of benchmark features were larger than the material relations to determine. The remaining attributes have been used to validate the porosity model. Eventually, the three benchmark experiments, which test for very different physical properties (compaction, bouncing, fragmentation), could by simulated quantitatively correct with one consistent set of material relations. This result has been considered as a sufficient criterion for a successful calibration. The harvest of this validation process is the only functional code and porosity model currently available, which is capable of the quantitatively correct simulation of bouncing, compaction, and fragmentation of highly porous dust in the astrophysical context. In particular, rebounding macroscopic dust aggregates have been simulated for the first time. The results of this fruitful collaboration between numerics and laboratory physics yielded two publications (Güttler et al. 2009, Geretshauser et al. 2010).

In Ch. 6 I have presented results which are directly relevant for pre-planetesimal collisions. For the transfer of collision data to global coagulation models a suitable format has to be chosen. Since for planetesimal formation the right mixture of sticking, bouncing, and fragmentation events might be crucial, this format has to be accurate enough to capture the most important collision outcome features but at the same time simple enough to be implementable in coagulation models. In Sec. 6.1 I have mapped existing simulation data to the most elaborate collision format available, which distinguishes between several types of sticking, bouncing, and fragmentation events. However, the analysis of my simulation data has revealed that sticking, bouncing, and fragmentation can occur in the very same collision because they are physical processes. I have come to the conclusion that the existing categorisation represents a too qualitative ap-

proach to classify collision data. For this reason I have developed a more quantitative model, the four-population model. By their mass I distinguish between the largest fragment, the second largest fragment, a power-law population, and a sub-resolution population. I have shown that the four-population model encompasses previous classification attempts in a closed format. In addition transitions between previous rigid categories can be mapped with the new quantitative approach, which demonstrates the high accuracy of the four-population model. Finally, I have applied this format to my simulation data and showed the applicability and functionality of the new model. The four-population model with its closed form is a simple and accurate mapping format for any method producing collision data such as laboratory experiments, molecular dynamics simulations, and numerical continuum methods. It has the potential to significantly improve the information transfer between the latter disciplines and global dust coagulation models.
In Sec. 6.2 I have presented the first results from simulations with the inhomogeneity damage model. I have demonstrated that inhomogeneous dust aggregates are more prone to fragmentation. In particular a collision which has resulted in the growth of the aggregate for the homogeneous case has yielded catastrophic disruption for a small degree of inhomogeneity. I have analysed the data by means of the four-population model. This has confirmed that smaller fragments result for a larger degree of inhomogeneity, which has exhibited the correct functionality of the damage model. It is very likely that pre-planetesimals have a collisional history and thus are inhomogeneous. The simulations have suggested that the collisional history might lead to more fragile aggregates. This has to be considered in pre-planetesimal collisions. The inhomogeneity damage model might be used to introduce a length scale to the current porosity model and solve its scaling problem. Furthermore, the input parameters of the proposed damage model are easier to determine in the laboratory than for other damage models.
The bouncing barrier possibly represents a serious obstacle to planetesimal formation. Section 6.3 has been devoted to this topic. The discovery of this bouncing barrier is based on a collision model originating from a collection of laboratory experiments, which were extrapolated by theoretical considerations. I have shown that the laboratory data on which this barrier is founded might overestimate the occurrence of rebound events. This is because bouncing as collision outcome strongly depends on the filling factor, which is not sufficiently taken into account in the previous collision model. Furthermore, my discussion exhibits that simplistic assumptions in the theoretical considerations lead to a bias with respect to bouncing. I have also demonstrated that hard shells have a strong influence on the bouncing properties of an aggregate. Hard shells, created unintentionally in the preparation of highly porous aggregates for the experiments, might lead to a wrong picture regarding bouncing. The results from this section show that the bouncing barrier might be caused by a spurious bias of the laboratory experiments and that rebound might not seriously endanger planetesimal formation.
Concluding Ch. 6, I have performed a large number of head-on collision simulations of homogeneous aggregates in Sec. 6.4. The analysis of this data has been performed by means of the four-population model. I have distinguished between simulations which lead to pre-planetesimal growth ("gain"), which are growth neutral ("neutral"), and which lead to catastrophic disruption ("loss"). I have shown that depending on the filling factor of the aggregates there exist different types of transitions: gain-loss, neutral-gain, and neutral-loss. I have also demonstrated that the thresholds for these transitions strongly depend on the filling factor and on the projectile size. Both have not yet been taken into account in global dust coagulation simulations although it is of crucial importance for planetesimal formation.
In conclusion, this thesis has developed two powerful tools for the investigation of pre-plane-

tesimal collisions: a code and porosity model, which have been calibrated to a high degree of accuracy and which includes an extension for inhomogeneity, and a simple and accurate mapping model to classify the produced simulation outcome. These tools have been applied to assess the danger of the bouncing barrier for planetesimal formation and the influence of the inhomogeneity of dust aggregates on the collision outcome. In addition, a large dataset of the collision outcome of head-on collisions has been produced and quantitatively classified according to the four-population model. All investigations emphasise the importance of considering the filling factor of pre-planetesimals in dust coagulation models.

7.2. Outlook

This thesis offers many prospects for future work. Continuing the analysis of Sec. 6.4.2, all tools offered by the four-population model can be applied to the existing dataset of head-on collisions. After estimates for the respective errors are found, the variation of each population with collision velocity can be modelled using suitable fit functions. In addition, the mass distributions of the resulting power-law populations can be determined. In particular the parameter region around the threshold velocities of the transitions should be studied in more detail. Expanding the parameter space, more filling factors should be studied and the variation of the transition thresholds as well as the variation of the fragment population features with filling factor should be investigated. It is very likely that pre-planetesimal collisions occur off-centre and that both aggregates possess a different filling factor. Therefore, the effect of a non-zero impact parameter (Fig. 7.1) and different porosities can be studied building on a reliable basis of head-on collisions. In addition, the rotation of aggregates produced in off-centre collisions might affect the collision outcome: spinning pre-planetesimals might fall apart due to their rotation and even the head-on collision of two rotating aggregates might produce a fragment distribution which is different from the non-rotating case.

Since the number of laboratory experiments with SiO_2 dust is constantly increasing, other benchmark tests could be carried out to further validate the porosity model. In particular high-velocity impacts could be carried out to explore the limits of the current isothermal model. Using the existing porosity model and the calibration method developed in this thesis, the code could be calibrated for the simulation of other dust materials such as irregular SiO_2 or diamond dust (Blum et al. 2006b). Simulations with these new materials could be carried out and classified by means of the four-population model. This is to assess the effect of different materials on the outcome of pre-planetesimal collisions. The results could be compared to those presented in this thesis and delivered to global coagulation simulations. In turn, global coagulation models could constrain collision outcomes in critical parameter ranges which allow for planetesimal formation. Utilising the solid body SPH code, material parameters could be varied until these desired collisional outcomes are produced. Approaching this “inverse problem”, it could be assessed whether planetesimal formation by coagulation is possible with a realistic material and what the properties of this material must be. The four-population model should be adopted for categorising experiments and simulations to assess its value for the information transfer between dust coagulation models and dust collisions.

A major improvement of the existing porosity model would be the inclusion of proper thermodynamics. This is the basis of the realistic simulation of phase transitions such as sintering, freezing, melting, and vaporisation. The thermodynamic expansion allows supersonic impacts to be

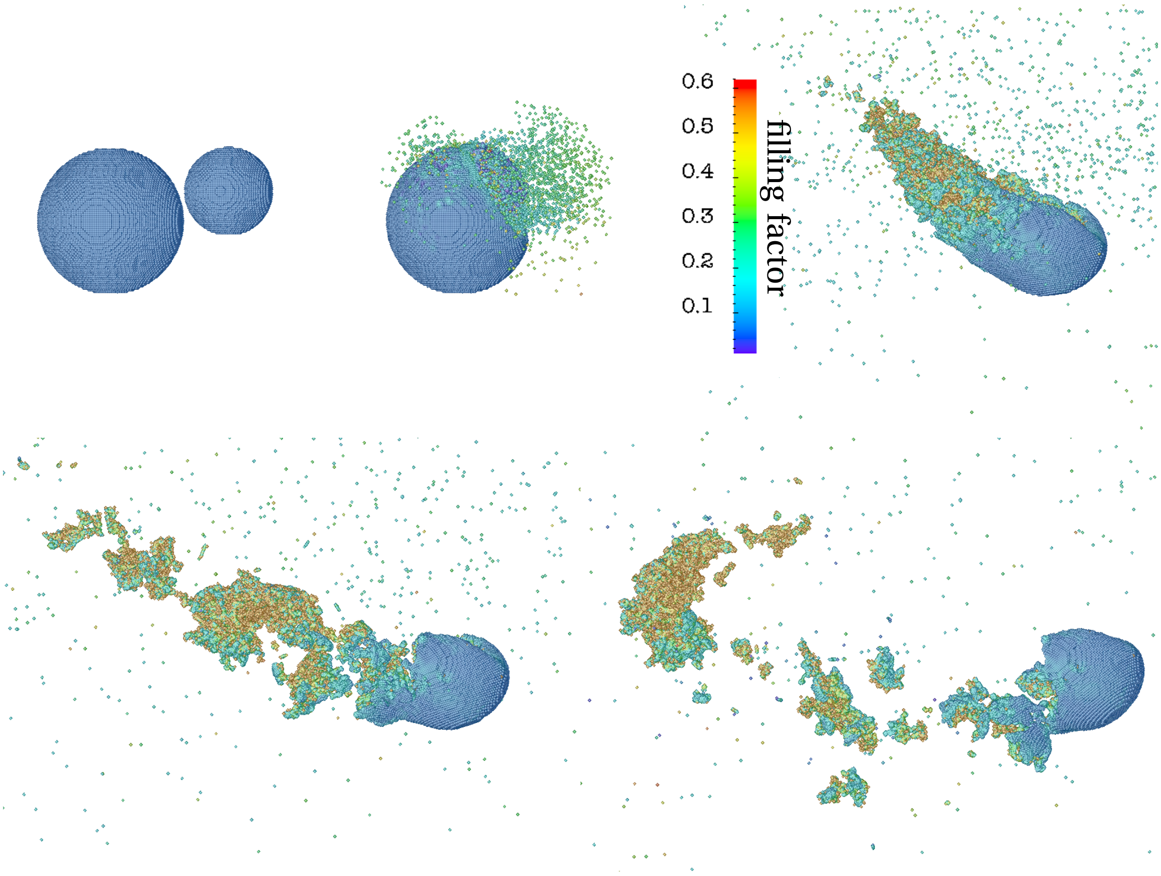

Figure 7.1. *Collision with impact parameter.* The homogeneous aggregates have an initial filling factor of $\phi_\mathrm{i} = 0.15$. The projectile with radius $r_\mathrm{p} = 6\,\mathrm{cm}$ hits a 10 cm target with a collision velocity of $v_0 = 7.5\,\mathrm{m/s}$. The impact parameter in this collision is $b = 4\,\mathrm{cm}$. From the top left to the bottom right the simulation times are 0, 40, 200, 400 and 800 ms. The filling factor is colour coded in this figure.

considered as well as different protoplanetary disc environments very close and very far from the host star. The enhanced porosity model can then be calibrated for the simulation of porous ice and dust-ice mixtures. Due to its static dipoles ices might increase the sticking properties of pre-planetesimals and support planetesimal formation. The correct functionality might be tested by comparison with laboratory benchmark experiments as well as numerical results from simulations with different porosity models. After sufficient testing, the new porosity model can be applied to investigate the collision outcome of ices, ice-silicate mixtures, and ice-coated dust aggregates and compare them to results involving pure dust aggregates. This allows a profound study of pre-planetesimal collisions in promoting regions, such as near or outside the snowline, to be carried out.

A. Computer programs and evaluation tools

A.1. Particle distribution evaluation tool `sph3Deval`

The evaluation program by Roland Speith transforms an SPH particle distribution back into the frame of continuous physical quantities. This is achieved by averaging the values of the contributing SPH particles on a user defined grid. The contributing particles are found by a nearest neighbour search for the given grid point where the smoothing length is taken into account. The evaluation methods include computing the arithmetic mean and averaging according to the SPH algorithm. The evaluation grids can be 1D, 2D, or 3D. The user can choose between cartesian, cylindrical, and polar coordinates. The evaluation parameters are specified in the file `eval.grid`. The program expects ASCII input from standard input in the format presented in Tab. A.1. The output is directed to standard output in the format shown in Tab. A.2.

dim	x	y	z	m_{SPH}	h	ρ	f_1	…	f_n
1D	1			2	3	4	5	…	$n+4$
2D	1	2		3	4	5	6	…	$n+5$
3D	1	2	3	4	5	6	7	…	$n+6$

Table A.1. *Input format of the particle distribution evaluation tool `sph3deval`.* The quantities x, y, and z are the cartesian coordinates of the SPH particles, m_{SPH} their mass, h the smoothing length and ρ their density. $f_1 \ldots f_n$ are additional functional values to be evaluated.

dim	x_{g}	y_{g}	z_{g}	$\bar{\rho}$	$\bar{f}_1$	…	$\bar{f}_n$
1D	1			2	3	…	$n+2$
2D	1	2		3	4	…	$n+3$
3D	1	2	3	4	5	…	$n+4$

Table A.2. *Output format of the particle distribution evaluation tool `sph3deval`.* The barred values represent the averages at the specified grid points which have the coordinates x_{g}, y_{g}, and z_{g}.

A.2. Fragment distribution evaluation tool `fragment`

The fragment evaluation tool `fragment` by Roland Speith is based on the program `sph3deval` of Appx. A.1. It is designed to evaluate an SPH particle distribution originating from a collision.

Fragments are identified by their constituting sets of SPH particles which interact due to smoothing length overlap. The program computes the physical quantities of each fragment and writes them to the output file. The code accepts 1D, 2D, and 3D particle distributions.
From the standard input `fragment` expects the SPH particle distribution in the format presented in Tab. A.3. The output is written to `fragment.dat` in the format shown in Tab. A.4.

dim	x	y	z	v_x	v_y	v_z	m_{SPH}	h	f_1	…	f_n
1D	1			2			3	4	5	…	$n+4$
2D	1	2		3	4		5	6	7	…	$n+6$
3D	1	2	3	4	5	6	7	8	9	…	$n+7$

Table A.3. *Input format of the fragment evaluation tool* `fragment`. The quantities x, y, and z denote the SPH particle positions and v_x, v_y, and v_z the velocity components of each particle. The SPH particle mass is represented by m_{SPH}. The value of h is the smoothing length. The functional values $f_1 \dots f_n$ are particle properties which are to be averaged over each fragment.

dim	n^{f}	n^{f}_p	x^{f}	y^{f}	z^{f}	v^{f}_x	v^{f}_y	v^{f}_z	m^{f}	L^{f}_x	L^{f}_y	L_zf	$E^{\mathrm{f}}_{\mathrm{rot}}$	$\bar{f}_1$	…	$\bar{f}_n$
1D	1	2	3			4			5	6			7	8	…	$n+7$
2D	1	2	3	4		5	6		7	8	9		10	11	…	$n+10$
3D	1	2	3	4	5	6	7	8	9	10	11	12	13	14	…	$n+13$

Table A.4. *Output format of the fragment evaluation tool* `fragment`. The quantities n^{f} and n^{f}_p denote the fragment number and number of SPH particles of each fragment, respectively. The cartesian coordinates of the centre of mass of each fragment are denoted by x^{f}, y^{f}, and z^{f}. Its velocity components are v^{f}_x, v^{f}_y, and v^{f}_z. The quantities L^{f}_x, L^{f}_y, and L^{f}_z represent the angular momentum of each fragment with respect to the centre of mass. The total fragment mass is given by m^{f} and $E^{\mathrm{f}}_{\mathrm{rot}}$ stands for the internal kinetic energy stored in rotational and vibrational degrees of freedom. The values $\bar{f}_1 \dots \bar{f}_n$ stand for other properties which are to be averaged over the fragment, e.g. the density.

A.3. Particle distribution tool initgrid

The particle distribution tool `initgrid` was developed for this thesis. It creates the initial SPH particle distribution for `parasph` (Appx. A.4). The SPH particles can be positioned on a cubic, face-centred, and body-centred lattice in 3D, on a square and triangular lattice in 2D, and on a line in 1D. The average distance of the particles is determined by the lattice constant. The program features different object geometries such as sphere, hemisphere, box, and cylinder in 3D and circle, hemicircle, and rectangle in 2D. The geometrical objects can be assigned different positions, velocities, and spins about an arbitrary axis. The material parameters of the objects include porous, bulk, and critical densities, material flags, and bulk modulus to suite the porosity model implementation of `parasph`. In particular the density and mass of an SPH particle are constructed to be consistent with the SPH sum. Each object can be assigned a fixed boundary on an arbitrary side. The boundary may be rigid or a region of smoothly increasing artificial viscosity. All objects can be coated with hard or soft shells. The transition between core and shell may be continuous or discontinuous. Objects of homogeneous density may be created as well as inhomogeneous objects where the filling factor distribution assumes the shape of a Gaussian. The standard deviation of the Gaussian is supplied as an input parameter. The output of `initgrid` is a file in ASCII or HDF5 format.

A.4. Parallel SPH code `parasph`

The parallel SPH code `parasph` was developed by M. Hipp and already described by Hipp and Rosenstiel (2004) and Schäfer (2005). It is based on the ParaSPH library by Bubeck et al. (1998, 1999). This is a set of routines developed for an easier and faster handling of parallel particle codes. By means of this library the physical problem and the parallel implementation are clearly separated. ParaSPH features domain decomposition, load balancing, nearest neighbour search, and inter-node communication. The adaptive Runge-Kutta-Cash-Karp integrator has been used for the simulations presented in this thesis. The parallel implementation utilises the Message Passing Interface (MPI) library. Test simulations yielded a speedup of 120 on 256 single core processors of a Cray T3E and of 60 on 128 single core processors on a Beowulf-Cluster. The code is described in detail by M. Hipp (PhD thesis, in prep.).

Schäfer (2005) extended the code by M. Hipp for the simulation of elasticity and plasticity including the time evolution of the deviatoric stress tensor, which costs a large amount of computing time. He also implemented the first version of the porosity model after Sirono (2004) and the Murnaghan and Tillotson equation of state. With respect to numerics an adaptive second order Runge-Kutta, and an Euler integrator was added. Moreover, the SPH enhancements such as additional artificial stress and XSPH were implemented.

Within the frame of this thesis, I corrected and improved the porosity model implementation and added a treatment of fixed boundaries. HDF5 was included as a compressed input and output file format with increased accuracy, which decreases the amount of required storage space considerably. I described the flags and parameters of `parasph` in detail in Geretshauser (2006).

The modified porosity model contains the following parameters for a problem with the dimension *dim*:

description	symbol	Type	variable (*P.parts. …*)
position	$\mathbf{r}$	vector(dim)	p
velocity	$\mathbf{v}$	vector(dim)	v
mass	m	scalar	m
density	ρ	scalar	rho
reference density	ρ_0'	scalar	rho_0prime
upper critical density	ρ_c^+	scalar	rho_c_pos
lower critical density	ρ_c^-	scalar	rho_c_neg
bulk density	ρ_0	scalar	rho_0
pressure	p	scalar	press
smoothing length	hsml	scalar	hsml
number of interaction partners	noip	scalar	noip
intrinsic energy	e	scalar	e
material type	mt	scalar	mt
damage	d	scalar	damage
	noaf	scalar	noaf
local strain	ε_{loc}	scalar	local_strain
bulk modulus	K	scalar	K
deviatoric stress tensor	S	matrix(dim × dim)	S
number of flaws	nof	scalar	nof
flaws	flaw	vector(nof)	flaw
Acceleration due to:			
physical viscosity	visk	vector(dim)	visk
artificial viscosity	artvisk	vector(dim)	artvisk
stress tensor	accσ	vector(dim)	accelS
hydrostatic pressure	accP	vector(dim)	accP
deviatoric stress tensor	accDST	vector(dim)	accDST

Table A.5. *Input and output quantities of the particle distribution files.* These values are specified for each particle of the SPH particle distribution.

dim	**r**			**v**			m	ρ	ρ'_0	ρ_c^+	ρ_c^-	ρ_0	e	mt	d	K	S	nof	flaw
	r_x	r_y	r_z	v_x	v_y	v_z													
1D	1			2			3	4	5	6	7	8	9	10	11	12	13	14	15
2D	1	2		3	4		5	6	7	8	9	10	11	12	13	14	15…18	19	20
3D	1	2	3	4	5	6	7	8	9	10	11	12	13	14	15	16	17…25	26	27

dim	**r**			**v**			m	ρ	ρ'_0	ρ_c^+	ρ_c^-	ρ_0	p	hsml	noip	e	mt	d	noaf	$\varepsilon_{\mathrm{loc}}$	K	S	nof	flaw
	r_x	r_y	r_z	v_x	v_y	v_z																		
1D	1			2			3	4	5	6	7	8	9	10	11	12	13	14	15	16	17	18	19	20
2D	1	2		3	4		5	6	7	8	9	10	11	12	13	14	15	16	17	18	19…22	23	24	25
3D	1	2	3	4	5	6	7	8	9	10	11	12	13	14	15	16	17	18	19	20	21…29	30	31	32

dim	visk			artvisk			accσ			accP			accDST		
	x	y	z	x	y	z	x	y	z	x	y	z	x	y	z
1D	1			2			3			4			5		
2D	1	2		3	4		5	6		7	8		9	10	
3D	1	2	3	4	5	6	7	8	9	10	11	12	13	14	15

Table A.6. *Structure of the* `parasph` *particle distribution files.* The table shows the structure of the input (top), output (middle), and acceleration (bottom) files of the SPH particle distribution. The quantities are explained in Tab. A.5.

List of Figures

2.1. SED of a protoplanetary disc and vertical disc structure(from Dullemond et al. 2007) 19
2.2. Collision velocities for various disc models (after Weidling et al. 2009) 22
2.3. Fractal aggregates (with data from J. Blum and S. Carstens) 29
2.4. Aggregate compaction (from Paszun and Dominik 2009) 32
2.5. Grinding growth model (from Teiser and Wurm 2009a) 37
2.6. Radial drift velocities (from Cuzzi and Weidenschilling 2006) 39

3.1. Laboratory dust experiments (from Blum and Wurm 2008) 53
3.2. Degrees of freedom in MD simulations (from Dominik and Tielens 1997) 56

4.1. Schematic stress-strain relation 82
4.2. Porosity model yield conditions 85
4.3. Porosity model 91

5.1. Laboratory compaction setup (from Güttler et al. 2009) 105
5.2. Numerical compaction setup 106
5.3. Numerical bouncing setup 110
5.4. Numerical fragmentation setup 113
5.5. Influence of dust sample size and shape on the compaction calibration setup 115
5.6. Convergence study of spatial resolution I 117
5.7. Convergence study of spatial resolution II 118
5.8. Convergence study of numerical resolution 119
5.9. Verification of the 2D-3D correction factor 122
5.10. Artificial viscosity study for the vertical density profile 123
5.11. Artificial viscosity study for various quantities 124
5.12. Shear strength models 128
5.13. Dynamic compressive strength models 131
5.14. Mean pressure study of the ODC compressive strength I 134
5.15. Mean pressure study of the ODC compressive strength II 135
5.16. Slope study of the ODC compressive strength 136
5.17. Comparison with benchmark experiments I – deceleration curve 138
5.18. Comparison with benchmark experiments II – density profile and distribution . . . 139
5.19. Comparison with benchmark experiments III – vertical density cross-section 140
5.20. Bouncing sequence 142
5.21. Bouncing for different bulk moduli 143
5.22. Fragmentation sequence 147
5.23. Fragmentation for different bulk moduli 148
5.24. Calibrated strength curves 150

6.1. Four-population model I – outcome classification (from Güttler et al. 2010) 154
6.2. Four-population model II – reproducing sticking, bouncing, and frag. types. 156
6.3. Four-population model III – illustration 160
6.4. Four-population model IV – population masses (from Geretshauser et al. 2011) . . . 166
6.5. Four-population model V – sticking-fragmentation transition 167
6.6. Four-population model VI – mass (snd. largest) (from Geretshauser et al. 2011) . . . 169
6.7. Four-population model VII – mass distr. (pwlw) (from Geretshauser et al. 2011) . . . 170
6.8. Four-population model VIII – ϕ (largest) (from Geretshauser et al. 2011) 171
6.9. Four-population model IX – average ϕ (pwlw) (from Geretshauser et al. 2011) 173
6.10. Four-population model X – ϕ distribution (pwlw) (from Geretshauser et al. 2011) . . 174
6.11. Four-population model XI – total residual energy (from Geretshauser et al. 2011) . . 175
6.12. Four-population model XII – dissipated energy (from Geretshauser et al. 2011) . . . 176
6.13. Inhomogeneity model I – initial filling factor distributions 180
6.14. Inhomogeneity model II – inhomogeneous aggregates. 181
6.15. Inhomogeneity model III – collision outcomes 184
6.16. Inhomogeneity model IV – population masses 185
6.17. Inhomogeneity model V – residual energy 186
6.18. Inhomogeneity model VI – filling factor distribution 188
6.19. Inhomogeneity model VII – mass distribution (power-law population) 189
6.20. Inhomogeneity model VIII – fragmentation parameter (power-law population). . . . 190
6.21. Inhomogeneity model IX – fragmentation strength (power-law population) 190
6.22. Hard shells I – homogeneous aggregates. 195
6.23. Hard shells II – residual energy (homogeneous) 196
6.24. Hard shells III – filling factor (homogeneous) 197
6.25. Hard shells IV – sticking and bouncing. 199
6.26. Hard shells V – hard shell aggregates 200
6.27. Hard shells VI – residual energy (hard shell) 201
6.28. Hard shells VII – filling factor (hard shells) 201
6.29. Head-on collisions I – high porosity snapshots 208
6.30. Head-on collisions II – intermediate porosity snapshots 209
6.31. Head-on collisions III – low porosity snapshots 210
6.32. Head-on collisions IV – mass against collision velocity (largest fragment) 212
6.33. Head-on collisions V – mass against projectile momentum (largest fragment) 213
6.34. Head-on collisions VI – mass against collision velocity (second largest fragment) . . 215
6.35. Head-on collisions VII – mass against collision velocity (power-law population) . . . 216
6.36. Head-on collisions VIII – mass against collision velocity (sub-resolution population) 218

7.1. Collision with impact parameter 225

List of Tables

3.1. Submillimetre aggregate collision thresholds 57
3.2. Local dust coagulation models 59

5.1. Selected parameters for the compaction calibration setup 108
5.2. Numerical parameters for the bouncing calibration setup 111
5.3. Numerical parameters for the fragmentation calibration setup 114
5.4. Parameters of the convergence study regarding numerical resolution 116
5.5. Results of the bouncing calibration setup for $p_\mathrm{m} = 1.3\,\mathrm{kPa}$ 144
5.6. Results of the bouncing calibration setup for $p_\mathrm{m} = 0.26\,\mathrm{kPa}$ 144
5.7. Results of the fragmentation calibration setup 146
5.8. Selection of numerical and material parameters after the completed calibration . . . 150

6.1. Parameters for reproduction of collision types 158
6.2. Mapping sticking, bouncing, and fragmentation to the four populations-model . . . 163
6.3. Applying the four-population model – collision velocities and categorisation 165
6.4. Inhomogeneity standard deviations 182
6.5. Collisions of inhomogeneous aggregates I – power-law population fits 191
6.6. Collisions of inhomogeneous aggregates II – results 193
6.7. Initial parameters of the head-on collision series 206

A.1. Input format of the particle distribution evaluation tool `sph3deval` 227
A.2. Output format of the particle distribution evaluation tool `sph3deval` 227
A.3. Input format of the fragment evaluation tool `fragment` 228
A.4. Output format of the fragment evaluation tool `fragment` 228
A.5. Input and output quantities of the particle distribution files 230
A.6. Structure of the `parasph` particle distribution files 231

Bibliography

Andrews, S.M., Williams, J.P., 2005. Circumstellar Dust Disks in Taurus-Auriga: The Submillimeter Perspective. The Astrophysical Journal 631, 1134.

Andrews, S.M., Williams, J.P., 2007. High-Resolution Submillimeter Constraints on Circumstellar Disk Structure. The Astrophysical Journal 659, 705.

Arena, S.E., Speith, R., 2010. Pore surface energy corrected P-alpha like models and the anomalous behavior of porous materials, in: Bertin, G., de Luca, F., Lodato, G., Pozzoli, R., Romé, M. (Eds.), Plasmas in the laboratory and in the universe, American Inst. of Physics. pp. 294–299.

Arena, S.E., Speith, R., 2011. Porosity models for pre-planetesimals: I. choice of the distension relation and correction for the surface energy of the pores in $P-\alpha$-like hydrostatic models , in prep.

Balbus, S.A., Hawley, J.F., 1991. A powerful local shear instability in weakly magnetized disks: I - Linear analysis. The Astrophysical Journal 376, 214–222.

Barge, P., Sommeria, J., 1995. Did planet formation begin inside persistent gaseous vortices? Astronomy and Astrophysics 295, L1–L4.

Barrière-Fouchet, L., Gonzalez, J.F., Murray, J.R., Humble, R.J., Maddison, S.T., 2005. Dust distribution in protoplanetary disks. Astronomy and Astrophysics 443, 185–194.

Benz, W., 1990. Smooth Particle Hydrodynamics - a Review, in: Buchler, J.R. (Ed.), The Numerical modelling of nonlinear stellar pulsations. Kluwer Academic Publishers, Dordrecht, Boston. volume 302 of *NATO ASI series. Series C, Mathematical and physical sciences*, p. 269.

Benz, W., 2000. Low Velocity Collisions and the Growth of Planetesimals. Space Science Reviews 92, 279–294.

Benz, W., Asphaug, E., 1994. Impact Simulations with Fracture. I. Method and Tests. Icarus 107, 98–116.

Benz, W., Asphaug, E., 1995. Simulations of brittle solids using smooth particle hydrodynamics. Computer Physics Communications 87, 253–265.

Benz, W., Asphaug, E., 1999. Catastrophic Disruptions Revisited. Icarus 142, 5–20.

Benz, W., Jutzi, M., 2007. Collision and impact simulations including porosity, in: Milani, A., Valsecchi, G.B., Vokrouhlický, D. (Eds.), Near Earth objects, our celestial neighbors, Cambridge Univ. Press. pp. 223–232.

Birnstiel, T., Dullemond, C.P., Brauer, F., 2009. Dust retention in protoplanetary disks. Astronomy and Astrophysics 503, L5–L8.

Birnstiel, T., Ricci, L., Trotta, F., Dullemond, C.P., Natta, A., Testi, L., Dominik, C., Henning, T., Ormel, C.W., Zsom, A., 2010. Testing the theory of grain growth and fragmentation by millimeter observations of protoplanetary disks. Astronomy and Astrophysics 516, L14.

Blum, J., Bruns, S., Rademacher, D., Voss, A., Willenberg, B., Krause, M., 2006a. Measurement of the Translational and Rotational Brownian Motion of Individual Particles in a Rarefied Gas. Phys. Rev. Lett. 97, 230601.

Blum, J., Münch, M., 1993. Experimental Investigations on Aggregate-Aggregate Collisions in the Early Solar Nebula. Icarus 106, 151–167.

Blum, J., Schräpler, R., 2004. Structure and Mechanical Properties of High-Porosity Macroscopic Agglomerates Formed by Random Ballistic Deposition. Phys. Rev. Lett. 93, 115503.

Blum, J., Schräpler, R., Davidsson, B.J.R., Trigo-Rodriguez, J.M., 2006b. The Physics of Protoplanetesimal Dust Agglomerates. I. Mechanical Properties and Relations to Primitive Bodies in the Solar System. The Astrophysical Journal 652, 1768–1781.

Blum, J., Wurm, G., 2000. Experiments on Sticking, Restructuring, and Fragmentation of Preplanetary Dust Aggregates. Icarus 143, 138–146.

Blum, J., Wurm, G., 2008. The Growth Mechanisms of Macroscopic Bodies in Protoplanetary Disks. Annual Review of Astronomy and Astrophysics 46, 21–56.

Blum, J., Wurm, G., Kempf, S., Poppe, T., Klahr, H., Kozasa, T., Rott, M., Henning, T., Dorschner, J., Schräpler, R., Keller, H.U., Markiewicz, W.J., Mann, I., Gustafson, B.A.S., Giovane, F., Neuhaus, D., Fechtig, H., Grün, E., Feuerbacher, B., Kochan, H., Ratke, L., El Goresy, A., Morfill, G., Weidenschilling, S.J., Schwehm, G., Metzler, K., Ip, W.H., 2000. Growth and Form of Planetary Seedlings: Results from a Microgravity Aggregation Experiment. Phys. Rev. Lett. 85, 2426.

Blum, J., Wurm, G., Poppe, T., Heim, L.O., 1998. Aspects of Laboratory Dust Aggregation with Relevance to the Formation of Planetesimals. Earth, Moon, and Planets 80, 285–309.

Blum, J., Wurm, G., Poppe, T., Kempf, S., Kozasa, T., 2002. First results from the cosmic dust aggregation experiment codag. Advances in Space Research 29, 497–503.

Bonnor, W.B., 1956. Boyle's Law and Gravitational Instability. Monthly Notices of the Royal Astronomical Society 116, 351–359.

Brauer, F., Dullemond, C.P., Henning, T., 2008a. Coagulation, fragmentation and radial motion of solid particles in protoplanetary disks. Astronomy and Astrophysics 480, 859–877.

Brauer, F., Dullemond, C.P., Johansen, A., Henning, T., Klahr, H., Natta, A., 2007. Survival of the mm-cm size grain population observed in protoplanetary disks. Astronomy and Astrophysics 469, 1169–1182.

Brauer, F., Henning, T., Dullemond, C.P., 2008b. Planetesimal formation near the snow line in MRI-driven turbulent protoplanetary disks. Astronomy and Astrophysics 487, L1–L4.

Bubeck, T., Hipp, M., Huettemann, S., Kunze, S., Ritt, M., Rosenstiel, W., Ruder, H., Speith, R., 1999. SPH test simulations on a portable parallel environment, in: Proceedings of the Workshop on Physics and Computer Science, Spring meeting of the DPG. pp. 139–155.

Bubeck, T., Hipp, M., Hüttemann, S., Kunze, S., Ritt, M., Rosenstiel, W., Ruder, H., Speith, R., 1998. Parallel SPH on Cray T3E and NEC SX-4 using DTS, in: Krause, E., Jäger, W. (Eds.), High Performance Computing in Science and Engineering '98, Springer-Verlag. pp. 396–410.

Chambers, J.E., 2004. Planetary accretion in the inner Solar System. Earth and Planetary Science Letters 223, 241–252.

Chiang, E.I., Youdin, A.N., 2010. Forming Planetesimals in Solar and Extrasolar Nebulae. Annual Review of Earth and Planetary Sciences 38, 493–522.

Chokshi, A., Tielens, A.G.G.M., Hollenbach, D., 1993. Dust coagulation. The Astrophysical Journal 407, 806–819.

Ciesla, F.J., Cuzzi, J.N., 2006. The evolution of the water distribution in a viscous protoplanetary disk. Icarus 181, 178–204.

Clarke, C.J., Lodato, G., 2009. Limits on the location of planetesimal formation in self-gravitating protostellar discs. Monthly Notices of the Royal Astronomical Society: Letters 398, L6–L10.

Clayton, G.C., Wolff, M.J., Sofia, U.J., Gordon, K.D., Misselt, K.A., 2003. Dust Grain Size Distributions from MRN to MEM. The Astrophysical Journal 588, 871.

Cuzzi, J.N., Dobrovolskis, A.R., Champney, J.M., 1993. Particle-Gas Dynamics in the Midplane of a Protoplanetary Nebula. Icarus 106, 102–134.

Cuzzi, J.N., Hogan, R.C., Paque, J.M., Dobrovolskis, A.R., 2001. Size-selective Concentration of Chondrules and Other Small Particles in Protoplanetary Nebula Turbulence. The Astrophysical Journal 546, 496.

Cuzzi, J.N., Weidenschilling, J.S., 2006. Particle-Gas Dynamics and Primary Accretion, in: Lauretta, D.S., McSween, H.Y. (Eds.), Meteorites and the early solar system II. University of Arizona Press, Tucson. The University of Arizona space science series, pp. 353–381.

Davis, D.R., Ryan, E.V., 1990. On collisional disruption: Experimental results and scaling laws. Icarus 83, 156–182.

Desch, S.J., 2007. Mass Distribution and Planet Formation in the Solar Nebula. The Astrophysical Journal 671, 878–893.

Dobrovolskis, A.R., Dacles-Mariani, J.S., Cuzzi, J.N., 1999. Production and damping of turbulence by particles in the solar nebula. J. Geophys. Res. 104, 30805–30815.

Dominik, C., Blum, J., Cuzzi, J.N., Wurm, G., 2007. Growth of Dust as the Initial Step Toward Planet Formation, in: Reipurth, B., Jewitt, D., Keil, K. (Eds.), Protostars and Planets V. University of Arizona Press, Tucson, pp. 783–800.

Dominik, C., Tielens, A.G.G.M., 1995. Resistance to rolling in the adhesive contact of two elastic spheres. Philosophical Magazine A 72, 783–803.

Dominik, C., Tielens, A.G.G.M., 1996. Resistance to sliding on atomic scales in the adhesive contact of two elastic spheres. Philosophical Magazine A 73, 1279–1302.

Dominik, C., Tielens, A.G.G.M., 1997. The Physics of Dust Coagulation and the Structure of Dust Aggregates in Space. The Astrophysical Journal 480, 647.

Dullemond, C.P., Dominik, C., 2004. The effect of dust settling on the appearance of protoplanetary disks. Astronomy and Astrophysics 421, 1075–1086.

Dullemond, C.P., Dominik, C., 2005. Dust coagulation in protoplanetary disks: A rapid depletion of small grains. Astronomy and Astrophysics 434, 971–986.

Dullemond, C.P., Hollenbach, D., Kamp, I., D'Alessio, P., 2007. Models of the Structure and Evolution of Protoplanetary Disks, in: Reipurth, B., Jewitt, D., Keil, K. (Eds.), Protostars and Planets V. University of Arizona Press, Tucson, pp. 555–572.

Dullemond, C.P., Monnier, J.D., 2010. The inner regions of protoplanetary disks. Annual Review of Astronomy and Astrophysics 48, 205–239.

Dzyurkevich, N., Flock, M., Turner, N.J., Klahr, H., Henning, T., 2010. Trapping solids at the inner edge of the dead zone: 3-D global MHD simulations. Astronomy and Astrophysics 515, A70.

Ebert, R., 1957. Zur Instabilität kugelsymmetrischer Gasverteilungen. Zeitschrift für Astrophysik 42, 263–272.

Eringen, A.C., 1962. Nonlinear theory of continuous media. McGraw-Hill.

Flaig, M., Kissmann, R., Kley, W., 2009. Growth of the MRI in accretion discs - the influence of radiation transport. Monthly Notices of the Royal Astronomical Society 394, 1887–1896.

Forgan, D., Rice, K., Stamatellos, D., Whitworth, A., 2009. Introducing a hybrid radiative transfer method for smoothed particle hydrodynamics. Monthly Notices of the Royal Astronomical Society 394, 882–891.

Gail, H.P., 2004. Radial mixing in protoplanetary accretion disks. Astronomy and Astrophysics 413, 571–591.

Gammie, C.F., 1996. Layered Accretion in T Tauri Disks. The Astrophysical Journal 457, 355–362.

Geretshauser, R., Meru, F., Speith, R., Kley, W., 2011. The four-population model: a new classification scheme for pre-planetesimal collisions. Astronomy and Astrophysics , in press.

Geretshauser, R.J., 2006. Modifying, Testing and Calibrating a Smooth Particle Hydrodynamics Code for Simulations of Planetesimal Growth. Diploma thesis. Universität Tübingen. Tübingen.

Geretshauser, R.J., Speith, R., Güttler, C., Krause, M., Blum, J., 2010. Numerical simulations of highly porous dust aggregates in the low-velocity collision regime: Implementation and calibration of a smooth particle hydrodynamics code. Astronomy and Astrophysics 513, A58.

Gingold, R.A., Monaghan, J.J., 1977. Smoothed particle hydrodynamics - Theory and application to non-spherical stars. Monthly Notices of the Royal Astronomical Society 181, 375–389.

Goldreich, P., Lithwick, Y., Sari, R., 2004a. Final Stages of Planet Formation. The Astrophysical Journal 614, 497.

Goldreich, P., Lithwick, Y., Sari, R., 2004b. Planet Formation by Coagulation: A Focus on Uranus and Neptune. Annual Review of Astronomy and Astrophysics 42, 549–601.

Goldreich, P., Ward, W.R., 1973. The Formation of Planetesimals. The Astrophysical Journal 183, 1051–1062.

Gomes, R., Levison, H.F., Tsiganis, K., Morbidelli, A., 2005. Origin of the cataclysmic Late Heavy Bombardment period of the terrestrial planets. Nature 435, 466–469.

Goodman, J., Pindor, B., 2000. Secular Instability and Planetesimal Formation in the Dust Layer. Icarus 148, 537–549.

Grady, D.E., Kipp, M.E., 1980. Continuum modelling of explosive fracture in oil shale. International Journal of Rock Mechanics and Mining Sciences & Geomechanics Abstracts 17, 147–157.

Greenberg, R., Wacker, J.F., Hartmann, W.K., Chapman, C.R., 1978. Planetesimals to planets: Numerical simulation of collisional evolution. Icarus 35, 1–26.

Gurson, A.L., 1977. Continuum theory of ductile rupture by void nucleation and growth: Part I: Yield criteria and flow rules for porous ductile media. Journal of Engineering Materials and Technology , 2–15.

Güttler, C., Blum, J., Zsom, A., Ormel, C.W., Dullemond, C.P., 2010. The outcome of protoplanetary dust growth: pebbles, boulders, or planetesimals? - I. Mapping the zoo of laboratory collision experiments. Astronomy and Astrophysics 513, A56.

Güttler, C., Krause, M., Geretshauser, R.J., Speith, R., Blum, J., 2009. The Physics of Protoplanetesimal Dust Agglomerates. IV. Toward a Dynamical Collision Model. The Astrophysical Journal 701, 130–141.

Hartmann, L., 2009. Accretion processes in star formation. volume 47 of *Cambridge astrophysics series*. Cambridge Univ. Pr. and Cambridge University Press, Cambridge, New York. 2. ed. edition.

Hayashi, C., 1981. Formation of the planets, in: Sugimoto, D., Lamb, D.Q., Schramm, D.N. (Eds.), Fundamental Problems in the Theory of Stellar Evolution, pp. 113–126.

Hayashi, C., Nakazawa, K., Nakagawa, Y., 1985. Formation of the solar system, in: Black, D.C., Matthews, M.S. (Eds.), Protostars & Planets II. University of Arizona Press, Tucson. Space Science Series, pp. 1100–1153.

Heim, L.O., Blum, J., Preuss, M., Butt, H.J., 1999. Adhesion and Friction Forces between Spherical Micrometer-Sized Particles. Physical Review Letters 83, 3328–3331.

Heißelmann, D., Fraser, H.J., Blum, J., 2007. Experimental Studies on the Aggregation Properties of Ice and Dust in Planet-Forming Regions. International Astronautical Congress Abstracts 58, 1–6.

Henning, T., Meeus, G., 2010. Dust Processing and Mineralogy in Protoplanetary Accretion Disks, in: Garcia, P.J.V. (Ed.), Physical Processes in Circumstellar Disks around Young Stars. Univ. of Chicago Press, Chicago. Theoretical astrophysics, p. in press.

Herrmann, W., 1969. Constitutive Equation for the Dynamic Compaction of Ductile Porous Materials. Journal of Applied Physics 40, 2490–2499.

Hipp, M., Rosenstiel, W., 2004. Parallel hybrid particle simulations using mpi and openmp, in: Danelutto, M., Vanneschi, M., Laforenza, D. (Eds.), Euro-Par, Springer. pp. 189–197.

Ida, S., Makino, J., 1993. Scattering of Planetesimals by a Protoplanet: Slowing Down of Runaway Growth. Icarus 106, 210–227.

Ilgner, M., Nelson, R.P., 2006. On the ionisation fraction in protoplanetary disks. Astronomy and Astrophysics 445, 205–222.

Jaumann, G., 1911. Geschlossenes System physikalischer und chemischer Differentialgesetze. Sitzungsbericht der kaiserlichen Akademie der Wissenschaften, Wien IIa.

Johansen, A., Brauer, F., Dullemond, C., Klahr, H., Henning, T., 2008. A coagulation-fragmentation model for the turbulent growth and destruction of preplanetesimals. Astronomy and Astrophysics 486, 597–611.

Johansen, A., Henning, T., Klahr, H., 2006a. Dust Sedimentation and Self-sustained Kelvin-Helmholtz Turbulence in Protoplanetary Disk Midplanes. The Astrophysical Journal 643, 1219.

Johansen, A., Klahr, H., 2005. Dust Diffusion in Protoplanetary Disks by Magnetorotational Turbulence. The Astrophysical Journal 634, 1353.

Johansen, A., Klahr, H., Henning, T., 2006b. Gravoturbulent Formation of Planetesimals. The Astrophysical Journal 636, 1121.

Johansen, A., Oishi, J.S., Low, M.M.M., Klahr, H., Henning, T., Youdin, A., 2007. Rapid planetesimal formation in turbulent circumstellar disks. Nature 448, 1022–1025.

Johansen, A., Youdin, A., Low, M.M.M., 2009. Particle Clumping and Planetesimal Formation Depend Strongly on Metallicity. The Astrophysical Journal Letters 704, L75.

Johnson, K.L., Kendall, K., Roberts, A.D., 1971. Surface Energy and the Contact of Elastic Solids. Proceedings of the Royal Society of London. A. Mathematical and Physical Sciences 324, 301–313.

Jutzi, M., Benz, W., Michel, P., 2008. Numerical simulations of impacts involving porous bodies: I. Implementing sub-resolution porosity in a 3D SPH hydrocode. Icarus 198, 242–255.

Jutzi, M., Michel, P., Benz, W., Richardson, D.C., 2009a. The formation of the Baptistina family by catastrophic disruption: Porous versus non-porous parent body. Meteoritics and Planetary Science 44, 1877–1887.

Jutzi, M., Michel, P., Benz, W., Richardson, D.C., 2010. Fragment properties at the catastrophic disruption threshold: The effect of the parent body's internal structure. Icarus 207, 54–65.

Jutzi, M., Michel, P., Hiraoka, K., Nakamura, A.M., Benz, W., 2009b. Numerical simulations of impacts involving porous bodies: II. Comparison with laboratory experiments. Icarus 201, 802–813.

Kachanov, L.M., 1971. Foundations of the theory of plasticity. volume 12 of *North-Holland series in applied mathematics and mechanics*. North-Holland [u.a.], Amsterdam.

Kempf, S., Pfalzner, S., Henning, T.K., 1999. N-Particle-Simulations of Dust Growth: I. Growth Driven by Brownian Motion. Icarus 141, 388–398.

Klahr, H., Bodenheimer, P., 2006. Formation of Giant Planets by Concurrent Accretion of Solids and Gas inside an Anticyclonic Vortex. The Astrophysical Journal 639, 432.

Klahr, H., Henning, T., 1997. Particle-Trapping Eddies in Protoplanetary Accretion Disks. Icarus 128, 213–229.

Kley, W., Bitsch, B., Klahr, H., 2009. Planet migration in three-dimensional radiative discs. Astronomy and Astrophysics 506, 971–987.

Kokubo, E., Ida, S., 1996. On Runaway Growth of Planetesimals. Icarus 123, 180–191.

Kokubo, E., Ida, S., 1998. Oligarchic Growth of Protoplanets. Icarus 131, 171–178.

Kokubo, E., Ida, S., 2000. Formation of Protoplanets from Planetesimals in the Solar Nebula. Icarus 143, 15–27.

Kornet, K., Stepinski, T.F., Róyczka, M., 2001. Diversity of planetary systems from evolution of solids in protoplanetary disks. Astronomy and Astrophysics 378, 180–191.

Krause, M., Blum, J., 2004. Growth and Form of Planetary Seedlings: Results from a Sounding Rocket Microgravity Aggregation Experiment. Phys. Rev. Lett. 93, 021103.

Kretke, K.A., Lin, D.N.C., 2007. Grain Retention and Formation of Planetesimals near the Snow Line in MRI-driven Turbulent Protoplanetary Disks. The Astrophysical Journal Letters 664, L55.

Laibe, G., Gonzalez, J.F., Fouchet, L., Maddison, S.T., 2008. SPH simulations of grain growth in protoplanetary disks. Astronomy and Astrophysics 487, 265–270.

Landau, L.D., Lifshitz, E.M., 1966. Fluid mechanics. Course of theoretical physics, Pergamon Press.

Langkowski, D., Teiser, J., Blum, J., 2008. The Physics of Protoplanetesimal Dust Agglomerates. II. Low-Velocity Collision Properties. The Astrophysical Journal 675, 764–776.

Larson, R.B., 2003. The physics of star formation. Reports on Progress in Physics 66, 1651.

Leinhardt, Z.M., Richardson, D.C., Lufkin, G., Haseltine, J., 2009. Planetesimals to protoplanets - II. Effect of debris on terrestrial planet formation. Monthly Notices of the Royal Astronomical Society 396, 718–728.

Li, A., Greenberg, J.M., 1997. A unified model of interstellar dust. Astronomy and Astrophysics 323, 566–584.

Libersky, L.D., Petschek, A.G., 1991. Smooth Particle Hydrodynamics with Stength of Materials, in: Trease, H., Fritts, M.J., Crowley, W.P. (Eds.), Advances in the Free-Lagrange method: including contributions on adaptive gridding and the smooth particle hydrodynamics method, Springer.

Libersky, L.D., Petschek, A.G., Carney, T.C., Hipp, J.R., Allahdadi, F.A., 1993. High Strain Lagrangian Hydrodynamics: A Three-Dimensional SPH Code for Dynamic Material Response. Journal of Computational Physics 109, 67–75.

Libersky, L.D., Randles, P.W., Carney, T.C., Dickinson, D.L., 1997. Recent improvements in SPH modeling of hypervelocity impact: Hypervelocity Impact. International Journal of Impact Engineering 20, 525–532.

Lissauer, J.J., Stewart, G.R., 1993. Growth of planets from planetesimals, in: Levy, E.H., Lunine, J.I. (Eds.), Protostars and planets, Univ. of Arizona Press. pp. 1061–1088.

Lucy, L.B., 1977. A numerical approach to the testing of the fission hypothesis. The Astronomical Journal 82, 1013–1024.

Lufkin, G., Quinn, T., Wadsley, J., Stadel, J., Governato, F., 2004. Simulations of gaseous disc-embedded planet interaction. Monthly Notices of the Royal Astronomical Society 347, 421–429.

Lynden-Bell, D., Pringle, J.E., 1974. The evolution of viscous discs and the origin of the nebular variables. Monthly Notices of the Royal Astronomical Society 168, 603–637.

Mathis, J.S., Rumpl, W., Nordsieck, K.H., 1977. The size distribution of interstellar grains. The Astrophysical Journal 217, 425–433.

McKee, C.F., Ostriker, E.C., 2007. Theory of Star Formation. Annual Review of Astronomy and Astrophysics 45, 565–687.

Meglicki, Z., Wickramasinghe, D., Bicknell, G.V., 1993. 3D structure of truncated accretion discs in close binaries. Monthly Notices of the Royal Astronomical Society 264, 691–704.

Melosh, H.J., 1989. Impact cratering: A geologic process. Oxford monographs on geology and geophysics, Oxford Univ. Pr. [u.a.], New York.

Michel, P., Benz, W., Richardson, D.C., 2003. Disruption of fragmented parent bodies as the origin of asteroid families. Nature 421, 608–611.

Michel, P., Benz, W., Richardson, D.C., 2004. Catastrophic disruption of pre-shattered parent bodies. Icarus 168, 420–432.

Michel, P., Tanga, P., Benz, W., Richardson, D.C., 2002. Formation of Asteroid Families by Catastrophic Disruption: Simulations with Fragmentation and Gravitational Reaccumulation. Icarus 160, 10–23.

Mizuno, H., 1989. Grain growth in the turbulent accretion disk solar nebula. Icarus 80, 189–201.

Mizuno, H., Markiewicz, W.J., Völk, H.J., 1988. Grain growth in turbulent protoplanetary disks. Astronomy and Astrophysics 195, 183–192.

Monaghan, J.J., 1992. Smoothed Particle Hydrodynamics. Annual Review of Astronomy and Astrophysics 30, 543–574.

Monaghan, J.J., 2000. SPH without a Tensile Instability. Journal of Computational Physics 159, 290–311.

Monaghan, J.J., 2005. Smoothed particle hydrodynamics. Reports on Progress in Physics 68, 1703.

Monaghan, J.J., Gingold, R.A., 1983. Shock simulation by the particle method SPH. Journal of Computational Physics 52, 374–389.

Monaghan, J.J., Lattanzio, 1985. A refined particle method for astrophysical problems. Astronomy and Astrophysics 149, 135–143.

Morbidelli, A., Levison, H.F., Tsiganis, K., Gomes, R., 2005. Chaotic capture of Jupiter's Trojan asteroids in the early Solar System. Nature 435, 462–465.

Morris, J.P., 1996. Analysis of SPH with Applications. Ph.D. thesis. Monash University. Monash.

Nakagawa, Y., Nakazawa, K., Hayashi, C., 1981. Growth and sedimentation of dust grains in the primordial solar nebula. Icarus 45, 517–528.

Natta, A., Testi, L., Calvet, N., Henning, T., Waters, R., Wilner, D.J., 2007. Dust in Proto-Planetary Disks: Properties and Evolution, in: Reipurth, B., Jewitt, D., Keil, K. (Eds.), Protostars and Planets V. University of Arizona Press, Tucson, pp. 767–781.

von Neumann, J., Richtmyer, R.D., 1950. A Method for the Numerical Calculation of Hydrodynamic Shocks. Journal of Applied Physics 21, 232–237.

Omang, M., Børve, S., Trulsen, J., 2006. SPH in spherical and cylindrical coordinates. Journal of Computational Physics 213, 391–412.

Omang, M., Børve, S., Trulsen, J., 2007. Shock collisions in 3D using an axi-symmetric regularized smoothed particle hydrodynamics code. Shock Waves 16, 467–475.

Ormel, C.W., Cuzzi, J.N., 2007. Closed-form expressions for particle relative velocities induced by turbulence. A&A 466, 413–420.

Ormel, C.W., Dullemond, C.P., Spaans, M., 2010a. A new condition for the transition from runaway to oligarchic growth. The Astrophysical Journal Letters 714, L103–L107.

Ormel, C.W., Dullemond, C.P., Spaans, M., 2010b. Accretion among preplanetary bodies: the many faces of runaway growth. Icarus 210, 507–538.

Ormel, C.W., Paszun, D., Dominik, C., Tielens, A.G.G.M., 2009. Dust coagulation and fragmentation in molecular clouds: I. How collisions between dust aggregates alter the dust size distribution. Astronomy and Astrophysics 502, 845–869.

Ormel, C.W., Spaans, M., Tielens, A.G.G.M., 2007. Dust coagulation in protoplanetary disks: porosity matters. Astronomy and Astrophysics 461, 215–232.

Papaloizou, J.C.B., Nelson, R.P., Kley, W., Masset, F.S., Artymowicz, P., 2007. Disk-Planet Interactions During Planet Formation, in: Reipurth, B., Jewitt, D., Keil, K. (Eds.), Protostars and Planets V. University of Arizona Press, Tucson, pp. 655–668.

Paraskov, G., Wurm, G., Krauss, O., 2007. Impacts into weak dust targets under microgravity and the formation of planetesimals. Icarus 191, 779–789.

Paszun, D., Dominik, C., 2006. The influence of grain rotation on the structure of dust aggregates. Icarus 182, 274–280.

Paszun, D., Dominik, C., 2008. Numerical determination of the material properties of porous dust cakes. Astronomy and Astrophysics 484, 859–868.

Paszun, D., Dominik, C., 2009. Collisional evolution of dust aggregates. From compaction to catastrophic destruction. Astronomy and Astrophysics 507, 1023–1040.

Poppe, T., Blum, J., Henning, T., 2000. Analogous Experiments on the Stickiness of Micron-sized Preplanetary Dust. The Astrophysical Journal 533, 454–471.

Pringle, J.E., 1981. Accretion discs in astrophysics. Annual Review of Astronomy and Astrophysics 19, 137–162.

Rafikov, R.R., 2003. The Growth of Planetary Embryos: Orderly, Runaway, or Oligarchic? The Astronomical Journal 125, 942.

Randles, P.W., Libersky, L.D., 1996. Smoothed Particle Hydrodynamics: Some recent improvements and applications. Computer Methods in Applied Mechanics and Engineering 139, 375–408.

Rice, W.K.M., Lodato, G., Pringle, J.E., Armitage, P.J., Bonnell, I.A., 2004. Accelerated planetesimal growth in self-gravitating protoplanetary discs. Monthly Notices of the Royal Astronomical Society 355, 543–552.

Rosswog, S., 2009. Astrophysical smooth particle hydrodynamics. New Astronomy Reviews 53, 78–104.

Safronov, V.S., 1969. Evolution of the protoplanetary cloud and formation of the earth and planets. Nauka, Moscow.

Schäfer, C., 2005. Application of Smooth Particle Hydrodynamics to selected Aspects of Planet Formation. Ph.D. thesis. Universität Tübingen. Tübingen.

Schäfer, C., Speith, R., Kley, W., 2007. Collisions between equal-sized ice grain agglomerates. Astronomy and Astrophysics 470, 733–739.

Schäfer, C., Speith, S., Hipp, M., Kley, W., 2004. Simulations of planet-disc interactions using SmoothedÂ ParticleÂ Hydrodynamics. Astronomy and Astrophysics 418, 325–335.

Schmitt, W., Henning, T., Mucha, R., 1997. Dust evolution in protoplanetary accretion disks. Astronomy and Astrophysics 325, 569–584.

Seizinger, A., 2010. Numerical simulation of particle agglomerates. Diploma thesis. Universität Tübingen. Tübingen.

Sekiya, M., 1983. Gravitational Instabilities in a Dust-Gas Layer and Formation of Planetesimals in the Solar Nebula. Progress of Theoretical Physics 69, 1116–113.

Sekiya, M., 1998. Quasi-Equilibrium Density Distributions of Small Dust Aggregations in the Solar Nebula. Icarus 133, 298–309.

Shakura, N.I., Sunyaev, R.A., 1973. Black Holes in Binary Systems. Observational Appearance. Astronomy and Astrophysics 24, 337–355.

Sirono, S., 2004. Conditions for collisional growth of a grain aggregate. Icarus 167, 431–452.

Smoluchowski, M.V., 1916. Drei Vortrage über Diffusion, Brownsche Bewegung und Koagulation von Kolloidteilchen. Zeitschrift für Physik 17, 557–585.

Speith, R., 1998. Untersuchung von Smoothed Particle Hydrodynamics anhand astrophysikalischer Beispiele. Ph.D. thesis. Universität Tübingen. Tübingen.

Speith, R., 2007. Improvements of the numerical method Smoothed Particle Hydrodynamics. Habilitation thesis. Universität Tübingen. Tübingen.

Stamatellos, D., Whitworth, A.P., Bisbas, T., Goodwin, S., 2007. Radiative transfer and the energy equation in SPH simulations of star formation. Astronomy and Astrophysics 475, 37–49.

Stellingwerf, R.F., Wingate, C.A., 1994. Impact Modelling with SPH (Invited paper). Memorie della Società Astronomia Italiana 65, 1117.

Stone, J.M., Balbus, S.A., 1996. Angular Momentum Transport in Accretion Disks via Convection. The Astrophysical Journal 464, 364–372.

Supulver, K.D., Bridges, F.G., Tiscareno, S., Lievore, J., Lin, D.N.C., 1997. The Sticking Properties of Water Frost Produced under Various Ambient Conditions. Icarus 129, 539–554.

Suyama, T., Wada, K., Tanaka, H., 2008. Numerical Simulation of Density Evolution of Dust Aggregates in Protoplanetary Disks. I. Head-on Collisions. The Astrophysical Journal 684, 1310.

Swegle, J.W., Hicks, D.L., Attaway, S.W., 1995. Smoothed Particle Hydrodynamics Stability Analysis. Journal of Computational Physics 116, 123–134.

Teiser, J., Wurm, G., 2009a. Decimetre dust aggregates in protoplanetary discs. Astronomy and Astrophysics 505, 351–359.

Teiser, J., Wurm, G., 2009b. High-velocity dust collisions: forming planetesimals in a fragmentation cascade with final accretion. Monthly Notices of the Royal Astronomical Society 393, 1584–1594.

Thommes, E.W., Duncan, M.J., Levison, H.F., 2003. Oligarchic growth of giant planets. Icarus 161, 431–455.

Tillotson, J.H., 1962. Metallic equations of state for hypervelocity impact. San Diego.

Toomre, A., 1964. On the gravitational stability of a disk of stars. The Astrophysical Journal 139, 1217–1238.

Truesdell, C., Noll, W., 1965. The non-linear field theories of mechanics. volume III/3 of *Encyclopedia of Physics*. Springer, Berlin.

Tscharnuter, M.W., Schönke, J., Gail, H.P., Trieloff, M., Lüttjohann, E., 2009. Protostellar collapse: rotation and disk formation. Astronomy and Astrophysics 504, 109–113.

Tsiganis, K., Gomes, R., Morbidelli, A., Levison, F.H., 2005. Origin of the orbital architecture of the giant planets of the Solar System. Nature 435, 459–461.

Valverde, J.M., Ramos, A., Castellanos, A., Watson, P.K., 1998. The tensile strength of cohesive powders and its relationship to consolidation, free volume and cohesivity. Powder Technology 97, 237–245.

Völk, H.J., Jones, F.C., Morfill, G.E., Röser, S., 1980. Collisions between grains in a turbulent gas. Astronomy and Astrophysics 85, 316–325.

Wada, K., Tanaka, H., Suyama, T., Kimura, H., Yamamoto, T., 2007. Numerical Simulation of Dust Aggregate Collisions. I. Compression and Disruption of Two-Dimensional Aggregates. The Astrophysical Journal 661, 320.

Wada, K., Tanaka, H., Suyama, T., Kimura, H., Yamamoto, T., 2008. Numerical Simulation of Dust Aggregate Collisions. II. Compression and Disruption of Three-Dimensional Aggregates in Head-on Collisions. The Astrophysical Journal 677, 1296.

Wada, K., Tanaka, H., Suyama, T., Kimura, H., Yamamoto, T., 2009. Collisional Gowth Conditions for Dust Aggregates. The Astrophysical Journal 702, 1490.

Wegner, J.L., Haddow, J.B., 2009. Elements of continuum mechanics and thermodynamics. Cambridge Univ. Press, Cambridge.

Weibull, W., 1939. A statistical theory of the strength of materials. volume 151 of *Ingeniörsvetenskapsakademiens handlingar*. Generalstabens litografiska anstalts förlag, Stockholm.

Weidenschilling, J.S., 1977a. The distribution of mass in the planetary system and solar nebula. Astrophysics and Space Science 51, 153–158.

Weidenschilling, S.J., 1977b. Aerodynamics of solid bodies in the solar nebula. Monthly Notices of the Royal Astronomical Society 180, 57–70.

Weidenschilling, S.J., 1980. Dust to planetesimals: Settling and coagulation in the solar nebula. Icarus 44, 172–189.

Weidenschilling, S.J., 1984. Evolution of grains in a turbulent solar nebula. Icarus 60, 553–567.

Weidenschilling, S.J., 1995. Can Gravitational Instability Form Planetesimals? Icarus 116, 433–435.

Weidenschilling, S.J., 1997. The Origin of Comets in the Solar Nebula: A Unified Model. Icarus 127, 290–306.

Weidenschilling, S.J., 2000. Formation of Planetesimals and Accretion of the Terrestrial Planets. Space Science Reviews 92, 295–310.

Weidenschilling, S.J., 2003. Radial drift of particles in the solar nebula: implications for planetesimal formation. Icarus 165, 438–442.

Weidenschilling, S.J., 2006. Models of particle layers in the midplane of the solar nebula. Icarus 181, 572–586.

Weidenschilling, S.J., 2008. Accretion of planetary embryos in the inner and outer solar system. Physica Scripta 2008, 1–11.

Weidenschilling, S.J., 2010. Particles in the nebular midplane: Collective effects and relative velocities. Meteoritics and Planetary Science 45, 276–288.

Weidenschilling, S.J., Cuzzi, J.N., 1993. Formation of planetesimals in the solar nebula, in: Levy, E.H., Lunine, J.I. (Eds.), Protostars and planets, Univ. of Arizona Press. pp. 1031–1060.

Weidling, R., Güttler, C., Blum, J., Brauer, F., 2009. The Physics of Protoplanetesimal Dust Agglomerates. III. Compaction in Multiple Collisions. The Astrophysical Journal 696, 2036.

Wetherill, G.W., Stewart, G.R., 1989. Accumulation of a swarm of small planetesimals. Icarus 77, 330–357.

Whipple, F.L., 1972. On certain aerodynamic processes for asteroids and comets, in: Elvius, A. (Ed.), From plasma to planet, Almqvist & Wiksell. p. 211.

Whitehouse, S.C., Bate, M.R., 2006. The thermodynamics of collapsing molecular cloud cores using smoothed particle hydrodynamics with radiative transfer. Monthly Notices of the Royal Astronomical Society 367, 32–38.

Wünnemann, K., Collins, G.S., Melosh, H.J., 2006. A strain-based porosity model for use in hydrocode simulations of impacts and implications for transient crater growth in porous targets. Icarus 180, 514–527.

Wurm, G., 2003. The formation of terrestrial planets, in: Lacoste, H., Fridlund, M., Henning, T. (Eds.), Procceedings of the Conference on Towards Other Earths - DARWIN/TPF and the Search for Extrasolar Terrestial Planets, ESA Publications Div.. pp. 151–161.

Wurm, G., Blum, J., 1998. Experiments on Preplanetary Dust Aggregation. Icarus 132, 125–136.

Wurm, G., Blum, J., 2000. An Experimental Study on the Structure of Cosmic Dust Aggregates and Their Alignment by Motion Relative to Gas. The Astrophysical Journal Letters 529, L57.

Wurm, G., Blum, J., Colwell, J.E., 2001a. A New Mechanism Relevant to the Formation of Planetesimals in the Solar Nebula. Icarus 151, 318–321.

Wurm, G., Blum, J., Colwell, J.E., 2001b. Aerodynamical sticking of dust aggregates. Phys. Rev. E 64, 046301.

Wurm, G., Paraskov, G., Krauß, O., 2004. On the Importance of Gas Flow through Porous Bodies for the Formation of Planetesimals. The Astrophysical Journal 606, 983.

Wurm, G., Paraskov, G., Krauss, O., 2005a. Ejection of dust by elastic waves in collisions between millimeter- and centimeter-sized dust aggregates at 16.5 to 37.5 m/s impact velocities. Phys. Rev. E 71, 021304.

Wurm, G., Paraskov, G., Krauss, O., 2005b. Growth of planetesimals by impacts at 25 m/s. Icarus 178, 253–263.

Youdin, A.N., 2004. Obstacles to the Collisional Growth of Planetesimals, in: Johnstone, D., Adams, F.C., Lin, D.N.C., Neufeeld, D.A., Ostriker, E.C. (Eds.), Star Formation in the Interstellar Medium: In Honor of David Hollenbach, p. 319.

Youdin, A.N., Goodman, J., 2005. Streaming Instabilities in Protoplanetary Disks. The Astrophysical Journal 620, 459.

Youdin, A.N., Shu, F.H., 2002. Planetesimal Formation by Gravitational Instability. The Astrophysical Journal 580, 494.

Zsom, A., Dullemond, C.P., 2008. A representative particle approach to coagulation and fragmentation of dust aggregates and fluid droplets. Astronomy and Astrophysics 489, 931–941.

Zsom, A., Ormel, C.W., Güttler C., Blum, J., Dullemond, C.P., 2010. The outcome of protoplanetary dust growth: pebbles, boulders, or planetesimals? II. Introducing the bouncing barrier. Astronomy and Astrophysics 513, A57.

Acknowledgements

The work presented in this thesis was funded by the DFG Research Unit FOR 759 “Formation of Planets” (Kl 650/8-1). The simulations were carried out on the university cluster of the computing centre (ZDV) of the University of Tübingen, the bwGriD clusters in Karlsruhe, Stuttgart, and Tübingen, and the national supercomputer NEC Nehalem Cluster of the High Performance Computing Centre Stuttgart (HLRS) under project grant SPH-PPC/12848.

First of all I wish to thank my supervisor PD Dr. Roland Speith for sharing his vast knowledge on SPH with me, for providing me with an intensive and highly qualified supervision, and for many interesting and entertaining discussions on scientific and non-scientific topics on countless business trips. Many ideas of this thesis were developed on long train journeys. Thank you for the great time, Roland!

I also wish to thank Prof. Dr. Willy Kley for providing me with funding, particularly in the (extended) late stages of this thesis. I am also grateful for his patience in the early stages when philosophical and interdisciplinary studies took their time. Many illuminating discussions with him brought me back from material science to the realm of astrophysics.

For the intensive and fruitful collaboration on the material calibration I am indebted to Prof. Dr. Jürgen Blum, Dr. Carsten Güttler, Maya Krause, and the rest of the IGEP group at the TU Braunschweig. Many visits and grill sessions, a joint meeting in the wilderness of the Harz mountains made it possible to simulate dust material with SPH now. I am grateful for the relaxed and scientifically stimulating atmosphere, the illuminating discussions, and the contribution to two publications.

I would also like to thank Prof. Dr. Gerhard Wurm and Dr. Jens Teiser for their hospitality and for sharing their knowledge about high velocity dust collisions with me.

I am indebted to Prof. Dr. Willy Benz and his group at the University of Bern for the input and discussions at the Bern-Tübingen SPH symposia. Many fruitful ideas were born in this round.

I wish to thank Dr. Farzana Meru for her language expertise in thoroughly reading the manuscript of this thesis and for many critical comments which helped to shape the text. I am also grateful for many illuminating discussions and her contribution to one publication. I will not forget the entertaining and productive atmosphere in our office with us either chatting or being in our “zones”. As another office-mate I wish to thank Dr. Serena Arena for many discussions on material physics, her expertise on thermodynamics and the Italian flair in our ufficio.

The CPT group created a lovely and relaxed working atmosphere at the institute. I particularly would like to thank Dipl. phys. Simeon Carstens for sharing the office with me, for many mathematical discussions and chats on molecular dynamics, for many climbing events, and introducing me to the wonderful world of rock climbing.

Meinen Sandlfreunden Markus und Stephan danke ich für die Mittagsrunden, die gemeinsamen Urlaube, die vielen Gespräche über Gott und die Welt, den gemeinsamen Weg im Studium und die vielen gemeinsam gesammelten Lebenspunkte.

Mein ganz besonderer Dank gilt denen, die mir in den turbulenten und aufwühlenden Zeiten in und außerhalb der Dissertation beigestanden sind und mich durch sie hindurch getragen haben. Für ihre Freundschaft, ihre Geduld, ihr offenes Ohr und ihren Rat danke ich Eva Wruck und Jochen Friedl. Meiner Familie danke ich für die geduldige und treue Unterstützung in allen Lebenslagen.